Identifying Explosive Transients and Implications for Gravitational Wave Followup

by

Vahid Zachary Golkhou

A Dissertation Presented in Partial Fulfillment
of the Requirements for the Degree
Doctor of Philosophy

Approved June 2017 by the
Graduate Supervisory Committee:

Nathaniel R. Butler, Chair
Judd Bowman
Rolf A. Jansen
Jennifer Patience
Evan Scannapieco

ARIZONA STATE UNIVERSITY

August 2017

ABSTRACT

High-energy explosive phenomena, Gamma-Ray Bursts (GRBs) and Supernovae (SNe), provide unique laboratories to study extreme physics and potentially open up the new discovery window of Gravitational-wave astronomy.

Uncovering the intrinsic variability of GRBs constrains the size of the GRB emission region, and ejecta velocity, in turn provides hints on the nature of GRBs and their progenitors. We develop a novel method which ties together wavelet and structure-function analyses to measure, for the first time, the actual minimum variability timescale, $\Delta t_{\rm min}$, of GRB light curves. Implementing our technique to the largest sample of GRBs collected by *Swift* and *Fermi* instruments, reveals that only less than 10% of GRBs exhibit evidence for variability on timescales below 2 ms. Investigation on various energy bands of the Gamma-ray Burst Monitor onboard *Fermi* shows that the tightest constraints on progenitor radii derive from timescales obtained from the hardest energy channel of light curves (299–1000 keV). Our derivations for the minimum Lorentz factor, $\Gamma_{\rm min}$, and the minimum emission radius, $R = 2\,c\,\Gamma^2_{\rm min}\Delta t_{\rm min}/(1+z)$, find $\Gamma \gtrsim 400$ which imply typical emission radii $R \approx 1 \times 10^{14}$ cm for long-duration GRBs and $R \approx 3 \times 10^{13}$ cm for short-duration GRBs (sGRBs).

I present the Reionization and Transients InfraRed (RATIR) followup of LIGO/Virgo Gravitational-wave events especially for the G194575 trigger. I show that expanding our pipeline to search for either optical *riZ* or near-infrared *YJH* detections (3 or more bands) should result in a false-alarm-rate $\approx 1\%$ (one candidate in the vast 100 deg^2 LIGO error region) and an efficiency $\approx 90\%$.

I also present the results of a 5-year comprehensive SN search by the Palomar Transient Factory aimed to measure the SN rates in the local Luminous Infrared Galaxies. We find that the SN rate of the sample, $0.05 \pm 0.02\,yr^{-1}$/galaxy, is consistent with that expected from the theoretical prediction, $0.060 \pm 0.002\,yr^{-1}$/galaxy.

To my parents, with gratitude.

ACKNOWLEDGMENTS

Though only my name appears on the title page of this dissertation, a great many people have contributed, in various ways, to its completion. I would like to thank them for their help and support throughout my graduate studies at ASU.

The choice to work with my Ph.D. advisor, Prof. Nathaniel R. Butler, is the single best decision that I have made during graduate school. I thank Nat for introducing me to the wonderful world of gamma-ray bursts and for leading by example every single day. I thank him for his guidance and support of my efforts throughout the Ph.D. program. I thank him also for his optimism that was invaluable in the most challenging periods, and his generosity with opportunities that encouraged my growth as a scientist. I could not have asked for a better and more inspiring Ph.D. advisor.

I heartily thank my thesis committee members: Prof. Judd Bowman, Dr. Rolf A. Jansen, Prof. Sangeeta Malhotra, Prof. Jennifer Patience, Prof. James Rhoads, and Prof. Evan Scannapieco, for their constructive advice and comments that improved the clarity of this work.

Visiting Caltech and the Infrared Processing and Analysis Center (IPAC) and working with Dr. Jason Surace has been an enriching and exciting experience, one that I will always look back upon as a valuable component in my development as a professional. I thank Jason, my advisor at Caltech/IPAC, for his contagious love of astrophysics and Star Trek and his mentorship and support. I also would like to thank the scientists and staff at IPAC and the PTF team and in particular Drs. Lee Armus, Eric Bellm, Sean Carey, Russ Laher, and Frank Masci for their advice and support of my PTF SNe project. I acknowledge support from IPAC Graduate Student Fellowship Program and also wish to thank the IPAC for their hospitality.

I have been fortunate to be a member of the RATIR GRBs and LVC teams and I want to thank them all for their expertise, and collaboration. Though by no means

an exhaustive list, I want to mention Drs. Brad Cenko, Antonino Cucchiara, Neil Gehrels, Alexander Kutyrev, William H. Lee, Carlos G. Román-Zúñiga, Eleonora Troja, and Alan M. Watson. I also want to thank the staff of the Observatorio Astronómico Nacional on Sierra San Pedro Mártir.

I would like to thank my colleagues in Butler's group: Ian Chute, Becky Jackson, Robert Strausbaugh, Zhenya Zheng, and in particular Owen Littlejohns for all of their help and collaboration during the last 5 years.

Last but certainly, not least, I would like to thank (among others) my friends and colleagues at School of Earth and Space Exploration (SESE) - ASU: Teresa Ashcraft, Sean Bryan, George Che, Seth Cohen, Kimberly Emig, Wanda Feng, Ehsan Gharib-Nezhad, Alicia Gonzalez, Bhavin Joshi, Anusha Kalyaan, Duho Kim, Piyanat (Boom) Kittiwisit, Karen Knierman, Kelley Liebst, Nikhil Monga, Jacqueline Monkiewicz, Thomas Mozdzen, Karen Olsen, Genady Pilyavsky, Karen Rieck, Rick Sarmento, Brent Smith, Michael Veto, Kimberly Ward-Duong, and in particular Mohammadtaher Safarzadeh and thank them for all of their help over the years.

Finally, I would not be where I am today without the tremendous sacrifices of my family. I cannot thank you enough for your love and support.

TABLE OF CONTENTS

CHAPTER Page

CHAPTER Page

CHAPTER Page

CHAPTER Page

LIST OF TABLES

LIST OF FIGURES

Figure Page

Figure Page

Chapter 1

INTRODUCTION

High energy transients make up a diverse and exotic class of objects, from terrestrial lightning to Gamma-ray Bursts (GRBs) at cosmological distances. In this review, I provide a detailed look at some of the more exciting transients relevant to this work, GRBs observed by *Swift* and *Fermi* satellites, Supernovae surveyed with the Palomar Transient Factory (PTF), and Electromagnetic counterparts to the Laser Interferometer Gravitational-wave Observatory (LIGO) gravitational wave events followed with the Reionization and Transients InfraRed (RATIR) telescope.

1.1 Gamma-Ray Bursts

GRBs produce tenths to hundreds of seconds of temporally irregular gamma-ray emission with smooth spectra peaking in the hundreds of keV. This initial "prompt" emission is followed by a long-wavelength afterglow that fades over several weeks. Redshift measurements of afterglows have confirmed that GRBs are located at cosmological distances, making them the most luminous objects in the universe. Decades of study have narrowed potential theories of GRB progenitors and emission mechanisms, but many questions remain open.

1.1.1 GRB Phenomenology

1.1.1.1 Prompt Emission

The "prompt" gamma-ray emission of GRBs was discovered serendipitously in 1967 by the Vela satellites monitoring Soviet compliance with the Nuclear Test Ban Treaty

(Klebesadel et al., 1973). The characteristic multi-peaked, variation in burst duration, and irregular temporal structure were readily observed (Figure 1.1). A larger sample of GRB light curves and spectra obtained by observers during the 1970s and 1980s and theories of GRB origins began to proliferate. However, significant progress could not be made due to the challenges of localizing such short-lived transients.

The Burst and Transient Experiment (BATSE; Fishman et al. 1989) onboard the Compton Gamma-Ray Observatory (CGRO) provided degree-scale localization of a large burst sample and improved energy spectra. The sample's spatial inhomogeneity and angular isotropy provided evidence for cosmological models of the burst origin (Meegan et al., 1992). Bimodality in the distribution of burst duration – defined by the T_{90} spanning the time interval in which 5% - 95% of the total observed counts are obtained – suggested two classes of burst progenitors (Kouveliotou et al., 1993). The observed correlation between duration and spectral hardness introduced the classification of "short–hard" and "long–soft" bursts, with a division at about 2-3 seconds [1] (see Figure 1.2).

BATSE spectral analysis of GRBs showed smooth, apparently non-thermal spectra with νF_ν peak energies, $E_{\rm peak}$, of several hundred keV (Band et al., 1993). The peak energy is correlated with intensity and typically shows a hard-to-soft temporal evolution.

In 1997, the discovery of the first afterglows (van Paradijs et al., 1997; Costa et al., 1997; Frail et al., 1997) and the measurement of GRB redshifts (Metzger et al., 1997) confirmed the cosmological origin of GRBs. Arcminute-precision localization by BeppoSAX (Boella et al., 1997), HETE-2, and the Interplanetary Network enabled

[1] The discovery of short bursts with tens to hundreds of seconds of soft extended emission following the initial hard spike has complicated this temporal division (Norris & Bonnell, 2006), and the proportion of bursts observed in each class varies with detector bandpass and triggering algorithm.

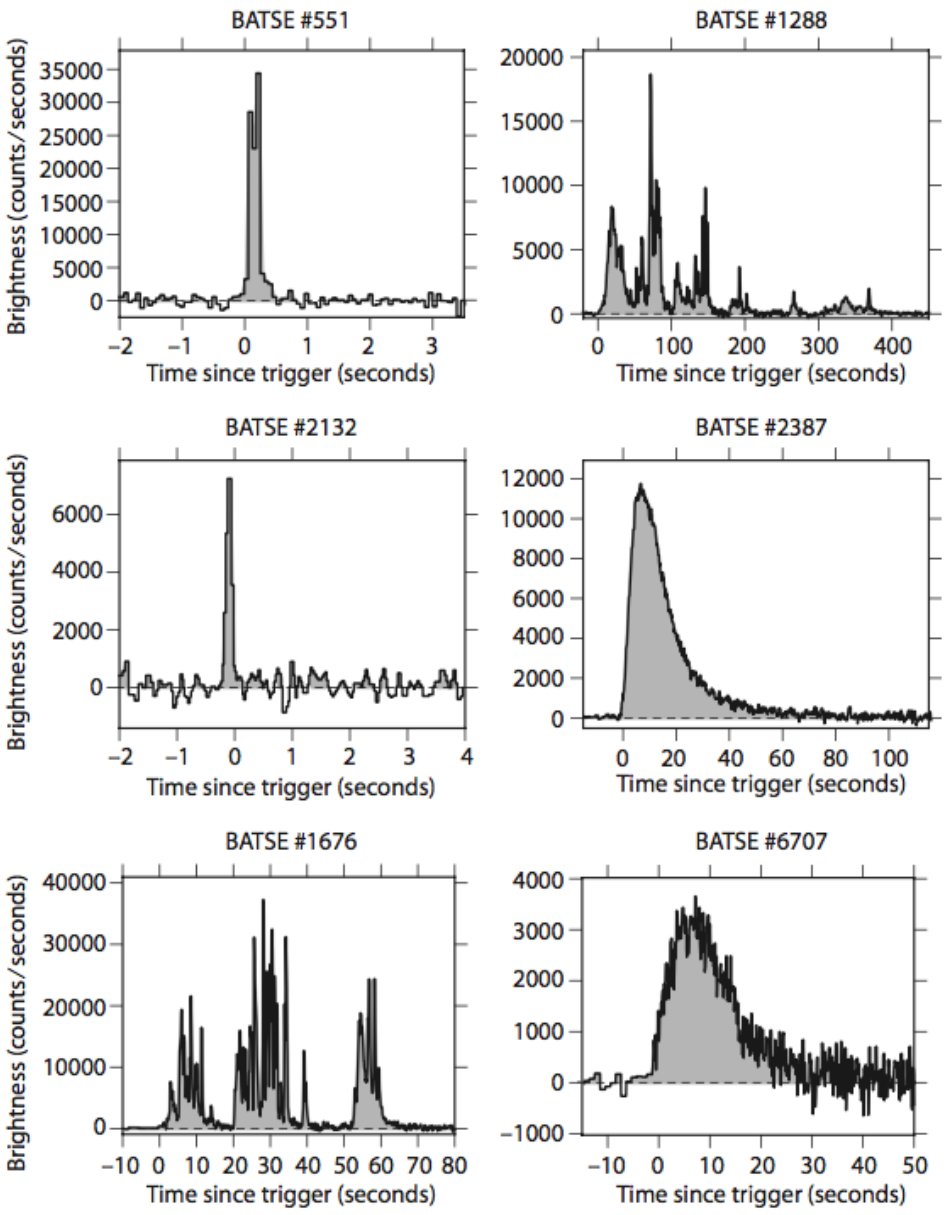

Figure 1.1: GRB light curves. The count rate in all four BATSE energy channels (30 keV - 2 MeV) as a function of time for 6 different GRBs. Note the large diversity in shape and duration, as well as the rapid variability seen in many bursts. (Adopted from Bloom 2011.)

detection of long-wavelength counterparts for increasing number of GRBs. The *Swift* satellite (Gehrels et al., 2004), launched in 2004, has localized about 100 bursts per year with its rapid slewing capability. Table 1.1 gives an overview of major GRB-

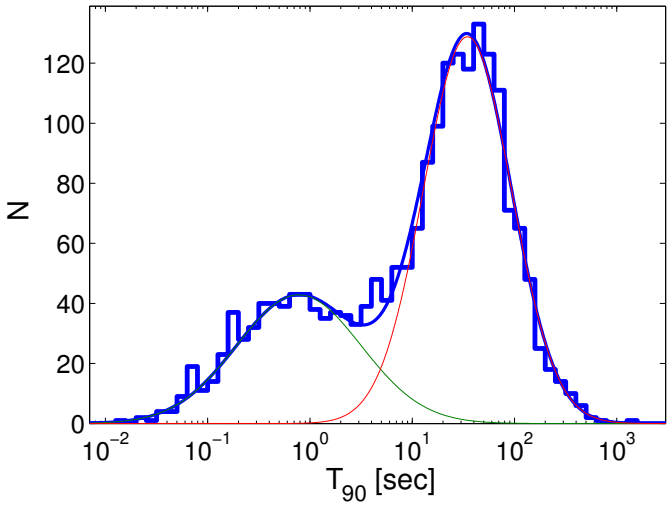

Figure 1.2: The bimodal duration distribution of BATSE GRBs. The decomposition into two log-normal distributions, as determined by Horváth (2002) (thin solid lines), together with the sum of the two distributions (thick solid line), are shown here superposed on the observed histogram. Adopted from Nakar (2007).

detecting missions (see Bellm, 2011).

The availability of GRB positions has enabled searches for prompt emission components in bands other than the gamma-ray. Simultaneous detections have been rare however, and determining whether such simultaneous multi-wavelength data is due to prompt or afterglow emission presents a significant interpretive challenge.

Searches for the GRBs' prompt emission components in bands other than the gamma-ray became possible by the precise localizations of GRBs' positions. The first detection of the optical counterpart to GRB 990123 was recorded by Akerlof et al. (1999) using the ROTSE-I robotic imager. GRB 041219a was detected in the optical (Vestrand et al., 2005) and infrared (Blake et al., 2005). The small precursor of GRB 061121 triggered *Swift*/BAT and enabled UVOT observations during the primary burst phase (Page et al., 2007). GRB 080319B known as the "naked-eye" GRB (the peak magnitude: 5.3 mag) detected by *Swift* which enabled high-cadence optical observations contemporaneous with the prompt gamma-rays (Bloom et al., 2009; Racusin et al., 2008). For all these bursts, the optical/IR light curves showed general

Table 1.1: Major GRB-detecting Satellites.

Mission	Years of operation	Instrument	Energy Band (keV)	Major Results
Vela	1965-1984	multiple satellite	200-1500	GRB discovery and prompt morphology
CGRO	1991-2000	BATSE	20-8000	Largest GRB sample, isotropy
		EGRET	20 MeV - 80 GeV	long and short-duration bursts, Band function spectra
BeppoSAX	2001-2006	GRBM	40-700	Localization of first afterglows
		WFC	2-25	
		NFI	0.1-300	
HETE-2	2001-2006	FREGATE	6-400	GRB-SN conncetion
		WXM	2-25	
		SXC	0.5-10	
Swift	2004-	BAT	15-50	Best-localized sample at a range of redshifts
		XRT	0.2-10	
		UVOT 170-650		
Fermi	2008-	GBM	3 keV - 30 MeV	
		LAT	20 MeV $-$ > 300 GeV	Properties of GeV emission

correspondence with the prompt gamma-rays; however, the detailed variability in the two bands showed less correlation. In other cases, such as GRBs 060124 (Romano et al., 2006) and 091024 (Gruber et al., 2011), the behavior of the optical emission is generally independent of the prompt gamma-rays.

Hurley et al. (1994) observed GeV photons simultaneous with and up to 5700 seconds after the long GRB 940217 using the EGRET pair telescope onboard CGRO. Additionally, for some bright bursts, EGRET observed hard high-energy (10-200 MeV) spectral features (González et al., 2003; Kaneko et al., 2008).

Fermi/LAT (Atwood et al., 2009) has observed those GRBs and confirmed the high energy components in the spectra of the brightest long (Abdo et al., 2009a; Ackermann et al., 2011) and short-duration (Ackermann et al., 2010) GRBs. For the bright GRB 080916c, however, the data were consistent with a Band-only spectrum (Abdo et al., 2009b). Notably, the high energy component of GRB 090926A showed evidence of a cutoff at 1.4 GeV (Ackermann et al., 2011).

1.1.1.2 Afterglow Emission

The production of long-wavelength emission is a natural consequence of the relative inefficiency in converting the kinetic energy of the outflow into gamma-ray radiation as the outflow sweeps up and shocks the ambient circumburst medium (CBM). Given the long-lived, fading nature of this emission, these counterparts are called "afterglows".

The first long-wavelength afterglows of long-duration GRBs ("lGRBs") were observed in 1997 (van Paradijs et al., 1997; Costa et al., 1997; Frail et al., 1997) and have been observed regularly since then. Short-duration GRB ("sGRB") afterglows were first observed in 2005 (Gehrels et al., 2005; Fox et al., 2005; Hjorth et al., 2005; Berger et al., 2005), as they are generally dimmer by an order of magnitude (Nakar, 2007). GRB afterglows have less temporal and spectral variability than the prompt

emission and fade smoothly over a period of weeks to months. Afterglow observations continue to enable new insights into the complex physics of GRBs, including studies of their redshift distribution, their connection to SNe, their host galaxies, and their interaction with the CBM.

1.1.1.2.1 X-ray

BeppoSAX (Costa et al., 1997) was the first instrument to observe the X-ray afterglows of lGRBs. However, *Swift*'s rapid slewing capability provided the large sample of early-time afterglows, which revealed a complex but characteristic behavior (Nousek et al., 2006, Figure 1.3). A steep ($\propto t^{-2}$ or steeper) initial flux decline lasting hundreds of seconds follows the end of the prompt phase before slowing into a plateau phase ($\propto t^{-0.5}$ to t^{-1}) typically lasting $10^3 - 10^4$ s. The steep-to-plateau transition is typically marked by a change in the spectral index. After the plateau, the light curve enters a shallow decay phase ($\propto t^{-1}$ to $t^{-1.5}$) lasting until late times. The final decay phase sometimes breaks and steepens.

In some cases, large X-ray flares interrupt the smooth decay. Generally the flares appear to be late, soft spikes similar to the prompt emission (Butler & Kocevski, 2007; Krimm et al., 2007). The low-energy sensitivity of HETE-2 enabled earlier observations of X-Ray Flashes (XRFs) and identified X-Ray Rich GRBs (XRRs) (Sakamoto et al., 2005) in similar numbers as typical GRBs. This might suggest that even in the classical prompt phase the observed dominance of gamma-ray emission over X-ray emission may be influenced by detector thresholds. For short-duration bursts, the X-ray afterglow typically begins with an X-ray tail lasting $\sim$100 s; sometimes the tail produces extended emission in the gamma-ray band (Norris & Bonnell, 2006). A fast decay phase then transitions into a gradual ($\sim t^{-1}$) decay similar to that observed for long bursts, with X-ray flares and late temporal breaks occasionally observed (see

Figure 1.3).

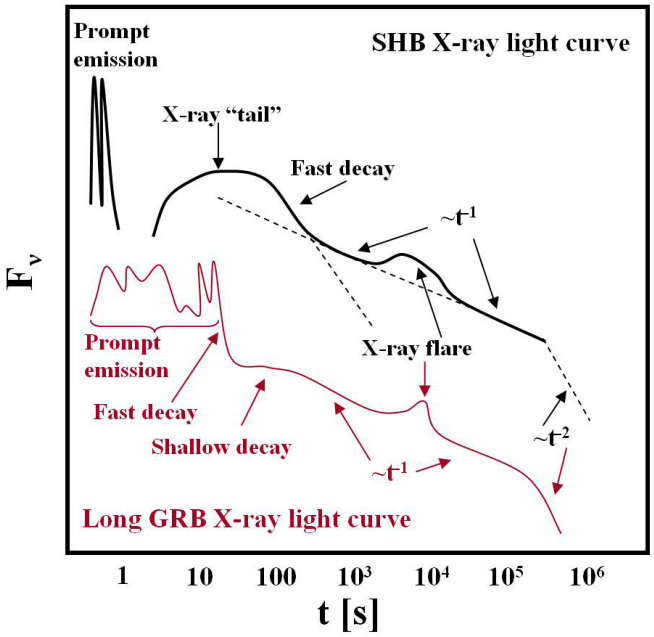

Figure 1.3: Characteristic X-ray afterglow light curves for short (black) and long (red) duration bursts (Adopted from Nakar 2007, Figure 7).

1.1.1.2.2 Optical

In the optical bands, lGRB afterglows characteristically show several hundred seconds of flat or rising emission followed by gradual power-law decays $t^{-\alpha}$, with decay indices of $-0.5 < \alpha \lesssim -1.2$ (Oates et al., 2009). Power-law spectra are also the norm. Typical visual magnitudes of long-duration bursts one day after the burst are 19-20 mag.

Some optical light curves show temporal breaks to steeper slopes $\alpha \approx 2.0$ in the days after the burst. Previous theoretical expectations and early observations (e.g., Harrison et al., 1999) suggested that the decaying afterglow light curves should show breaks in all bands at the same time, i.e., "achromatic breaks." Interestingly, chromatic breaks are commonly observed instead, with breaks occurring at different times or not at all in the various bands (e.g., Liang et al., 2008). Accounting for chromatic breaks poses a significant challenge for existing GRB jet models.

A notable fraction of GRBs, known as "optically dark" have no detected optical counterparts. About forty percent of the *Swift* GRB sample have no reported optical detection by *Swift*/UVOT or ground-based telescopes despite the early-time observations (Roming et al., 2009). Perley et al. (2009) suggested that dust extinction is the primary cause of the dark bursts rather than high-redshift or observational biases.

1.1.1.2.3 Radio

Radio afterglow measurements are obtained less frequently than observations in other bands due to constraints on available telescope time. However, radio measurements have enabled significant advances in understanding the physics of the afterglow emission such as identifying signatures of relativistic motion. Radio observations have also played a key role in detailed broadband afterglow models of bright GRBs (e.g., Chandra et al., 2008).

1.1.1.2.4 GeV-TeV Gamma Rays

Very high-energy gamma-rays (tens of MeV-GeV) occur contemporaneously with the MeV prompt emission with temporal correlations suggesting some of the emission has a common origin (e.g., Ackermann et al., 2011). However, observations of high energy components which persist after the prompt emission may complicate the division of prompt and afterglow emission. Hurley et al. (1994) observed an 18 GeV photon 5700 seconds after GRB 940217. González et al. (2003) found the high-energy spectral component of GRB 941017 increased in strength as the MeV prompt component weakened. Ultimately, *Fermi*/LAT has observed that emission in the LAT band (20 MeV to > 300 GeV) starts later and lasts longer than that at lower energies (Ackermann et al., 2011, and references therein). No afterglow detections at TeV energies have been made yet (Aharonian et al., 2009; Jarvis et al., 2010); however, it has

remained an active research area by many groups such as the IceCube Collaboration.

1.1.2 Theories of GRBs

The complexity of GRB phenomenology has made it challenging to build predictive, unified theories of GRBs. Some features of an eventually unified GRB theory would be established by strong evidence, such as the presence of relativistic jets and the connection between lGRBs and Type Ibc SNe.

1.1.2.1 Jets and Energetics

Several independent pieces of evidence indicate that GRB emission is the product of relativistic jets. The presence of a significant flux of (apparently) non-thermal radiation at MeV energies and above creates a so-called "compactness problem." If a non-relativistic source emits photons with temporal features of size δt, it requires the physical size of the emitting region to be $\lesssim c\delta t$. The corresponding optical depth of MeV photons to $\gamma\gamma \rightarrow e^{\pm}$ is enormous: $\tau_{\gamma\gamma} \sim 10^{15}$ (Piran, 2004, and references therein). If the prompt emitting region is moving relativistically with a bulk Lorentz factor Γ, consequently two effects could alleviate the compactness problem. In the source frame, the energies of the photons are lower than those observed by a factor of Γ. Also, the size of the emitting region increases to $\Gamma^2\, c\delta t$. Observations of prompt GRB emissions, therefore, can be used to set constraints on the minimum Lorentz factor, $\Gamma_{\rm min} \approx 100$ (e.g., Lithwick & Sari, 2001).

Direct measurement of relativistic expansion rates was made with observations of radio scintillation in GRB afterglows. Taylor et al. (2004) used the VLBI to resolve images of the radio afterglow of GRB 030329 between 20 and 100 days after the burst, finding its size and proper motion consistent with a relativistic outflow. Given the presence of GRBs at cosmological distances, it became apparent that the implied

energetics were pushing the limits of stellar-mass progenitors. The energy in prompt gamma-rays assuming isotropic emission, $E_{\rm iso}$, for some bursts was $10^{53} - 10^{54}$ erg (e.g., Kulkarni et al., 1998, 1999).

If the GRB emission were collimated in relativistic jets, therefore this problem would be avoided: Rhoads (1997) found that the isotropic energy release would be reduced by the fraction of the solid angle subtended by the jet. The jet model predicted achromatic temporal breaks in the afterglow light curve: initially, relativistic beaming would restrict afterglow observations to a subset of the jet. As the jet slowed, eventually the edge of the jet would become visible, and the decay index would increase. This transition occurs when $\Gamma \sim 1/\theta_j$, where θ_j is the jet opening angle. By measuring the time of the afterglow breaks, the jet opening angles could be inferred (Sari et al., 1999). Early results found that the beaming-corrected energies, E_γ, of lGRBs clustered tightly at 10^{51} erg (Frail et al., 2001; Bloom et al., 2003), suggesting a single class of stellar-mass progenitors. *Swift*'s observations challenged the initial clarity of this picture of GRB jets and energetics. First, the overwhelming majority of GRBs show afterglow breaks that are chromatic between the X-ray and optical bands, with the X-ray breaks occurring earlier (e.g., Liang et al., 2008).

These results are difficult to reconcile within standard jet models. Multiple-component jets have been proposed to accommodate some observations (Racusin et al., 2008). Another possibility is that the observed breaks in the X-ray light curves are due to effects other than jet physics, and that the actual jet breaks are occurring at late times and are undetected (Kocevski & Butler, 2008). Second, some bursts with measured jet breaks appear sub- or super-energetic compared to initial estimates. Detailed broadband modeling of bright *Swift* GRBs has found several bursts with collimation-corrected energy release greater than 10^{52} erg (Chandra et al., 2008; Bellm et al., 2008; Cenko et al., 2010). The nearest GRBs, however, have energetics

orders of magnitude lower than typical GRBs (Bloom et al., 2001; Soderberg et al., 2006). The classical analytic jet models which assume an on-axis observer may impose distortions. Recent simulations suggest that the true energy of a burst measured by an off-axis observer can be as much as a factor of four smaller than that implied by on-axis models (van Eerten et al., 2010). Furthermore, jet breaks in the radio regime should be delayed relative to the X-ray/optical breaks due to self-absorption effects, creating chromatic breaks (van Eerten et al., 2011).

1.1.2.2 Progenitors

1.1.2.2.1 Long-duration GRBs: lGRBs

Observational evidence connecting lGRBs with core-collapse SNe emerged soon after the first afterglow detections (for a review, see Woosley & Bloom 2006). Galama et al. (1998) reported the first indication of such connection based on the temporal and spatial coincidence of GRB 980425 and SN 1998bw. Late-time bumps observed in some afterglows beginning with GRB 980326 (Bloom et al., 1999) suggested emerging SN light curves. However, re-brightening due to dust effects was also plausible (Esin & Blandford, 2000; Waxman & Draine, 2000). Spectroscopic observations of the GRB 030329 afterglow confirmed the link (Stanek et al., 2003): the spectral evolution of the associated SN 2003dh manifested clear correspondence to SN 1998bw (Hjorth et al., 2003). Since then, associated SNe have been regularly detected for nearby GRBs (e.g., Malesani et al., 2004; Campana et al., 2006; Starling et al., 2011). Two nearby bursts, GRBs 060505 and 060614, showed no underlying SNe to deep limits (Gehrels et al., 2006); however, their prompt emission might be construed as that of a short-duration burst (060505) or a short-duration burst with extended emission (060614) (Nakar, 2007, and references therein).

1.1.2.2.2 Short-duration GRBs: sGRBs

One of the greatest mysteries of GRB astronomy – prior to the launch of *Swift* – was the nature of sGRBs. Although more than 50 lGRBs had afterglow detections, no afterglow had been found for any short burst. Finally, in 2005 *Swift* and HETE-2 precisely located three sGRBs for which afterglow observations were obtained. This led to a breakthrough in our understanding of short bursts (Gehrels et al., 2005; Bloom et al., 2006; Barthelmy et al., 2005a; Berger et al., 2005; Fox et al., 2005; Hjorth et al., 2005; Villasenor et al., 2005). At the time of writing this dissertation, *Swift*/BAT has detected 107 sGRBs, $\sim$70% of which have XRT detections, and 23 of which have measured redshifts.

In contrast to long-duration bursts, the evidence is that sGRBs typically originate in host galaxies with a broad range of star formation properties, including low formation rate. Their host properties are substantially different than those of long-duration bursts (Leibler & Berger, 2010; Fong et al., 2010) indicating a different origin. Also, nearby sGRBs show no evidence for simultaneous supernovae (Nakar, 2007, and references therein), very different than long bursts. Taken together, these results support the interpretation that sGRBs arise from old populations of stars and are due to mergers of compact objects (i.e., double neutron star (NS) or NS - black hole (BH)) (Nakar, 2007; Eichler et al., 1989; Paczynski, 1991). However, it is probable that there exists a subpopulation of high-redshift, high-luminosity sGRBs with a completely different origin (Zhang et al., 2009; Bromberg et al., 2012).

Constraining limits on beaming from light curve break searches has been difficult due to the typically weak afterglow of sGRBs. Because of large uncertainties associated with small number statistics, the distribution of beaming angles for sGRBs seems to range from $\sim 5^\circ$ to $> 25^\circ$ (Burrows et al., 2006; Fong et al., 2012), roughly consistent but perhaps somewhat larger than that of lGRBs (Gehrels & Razzaque,

2013).

Recent observations of the afterglows and host galaxies of sGRBs 100625A, 101219A, and 110112A by Fong et al. (2013), demonstrated the diversity of sGRB environments. Given their moderate physical offsets and low inferred densities, they interpreted these as evidence for a compact binary progenitor of sGRBs. Fong & Berger (2013) showed a median sGRB projected physical offset of 4.5 kpc relative to the host centers, about 3.5 times larger than that for lGRBs. They also found that ≈25% of sGRBs have offsets of $\gtrsim 10$ kpc. Therefore, they concluded that sGRBs do not occur in regions of star formation or even trace stellar mass.

1.1.2.3 Central Engines

The central engines which power GRBs must generate colossal energy releases, $\sim 10^{51}$ erg within timescales of a few to tens of seconds. They require to produce collimated, relativistic outflows which are expected from the high Lorentz factors observed.

There are two major models for the energy source and release: (1) gravitational, produced by rapid accretion onto a newly-formed BH and (2) magneto-rotational, produced by outflows from a highly magnetized, rapidly rotating proto-neutron star ("millisecond magnetar"). Woosley (1993) proposed the "collapsar" scenario based on failed SNe Ib. This model developed further in the context of highly-energetic "hypernovae" like SN 1998bw (MacFadyen & Woosley, 1999; MacFadyen et al., 2001).

A fast-rotating massive star explodes as the SN produces a BH either directly or after a period of fallback accretion onto an NS (Woosley & Heger, 2006). Accretion onto a newly formed BH may also occur after binary mergers, potentially producing sGRBs (Lee & Ramirez-Ruiz, 2007). Due to the fast rotation, an optically thick, neutrino-cooled accretion disk forms around the BH and produces jets carrying some fraction of the energy released by rapid accretion. Many of the details of the accre-

tion disk formation and cooling remain uncertain, and the viability of the process is sensitive to the assumed initial conditions (e.g., Lee & Ramirez-Ruiz, 2007; Taylor et al., 2011, and references therein).

Simulations initiated after a BH formation show that collapsar jets can break out of the stellar envelope, potentially generating the observed GRB emission (MacFadyen & Woosley, 1999; MacFadyen et al., 2001). Some simulations have suggested that accretion onto the NS formed after core collapse may not produce a BH (e.g., Dessart et al., 2008). Instead, the NS loses mass through a magnetically driven baryonic jet. This result could potentially challenge the fundamental assumption of BH formation in the collapsar model.

Usov (1992) noticed that a newly born rapidly rotating magnetar could produce a relativistic electron-positron fireball leading to the observed emission. The original model proposed that the NS formed due to the accretion-induced collapse (AIC) of a white dwarf (WD). Other scenarios may be relevant for short-duration bursts including WD AIC and WD-WD or NS-NS binary mergers (Metzger et al., 2008).

We should note that the "inner engine" that produces the relativistic energy flow is hidden from direct observations. However, the observed temporal structure reflects directly this "engine's" activity. This model requires a compact internal "engine" that produces a wind – a long energy flow (long compared to the size of the "engine" itself) – rather than an explosive "engine" that produces a "fireball" whose size is comparable to the size of the "engine" (Piran, 1999).

1.1.2.4 Prompt Emission Mechanisms

"Internal shocks" (Rees & Meszaros, 1994) are the most popular dissipation mechanism in models containing non-magnetized "fireball" outflows. In the internal shocks scenario, variable activity from the "central engine" produces shells of ejecta with

varying Lorentz factors. Faster shells overtake slower ones and collide. Fermi acceleration due to repeated shock crossings during the resulting collisionless shocks produces populations of accelerated electrons which may then radiate. The internal shocks model is capable of producing the observed variability of GRB light curves (Sari & Piran, 1997), and the central engine activity which produces the shells could produce late X-ray flares. However, the low efficiency of the internal shocks model ($\sim$1%; Kumar 1999) requires a larger energy budget from the central engine.

Synchrotron emission is the obvious candidate for the prompt emission mechanism (Meszaros et al., 1994; Lloyd & Petrosian, 2000), given the apparently non-thermal spectra and the likelihood that the source region contains magnetic fields and a population of relativistic electrons. A challenge for pure synchrotron models is that some observed low-energy spectral slopes ($\alpha > -2/3$ Preece et al., 1998; Ghirlanda et al., 2002) are impossible to achieve with optically thin synchrotron emission (Katz, 1994; Ghisellini et al., 2000). Compton scattering may modify a source synchrotron spectrum. Even moderate Inverse-Compton cooling of the source electrons may produce low-energy spectral indices in line with observations (Daigne et al., 2011).

1.1.2.5 Afterglow Emission Mechanisms

Since the emission processes producing the prompt emission do not dissipate all of the energy of the burst, the final stage of a GRB occurs when the outflow collides with the CBM, eventually slowing. This "external shock" interaction produces a "forward shock" of the ejecta on the CBM as well as a "reverse shock" on the ejecta itself. The forward shock is expected to generate the late-time afterglow emission (Mészáros & Rees, 1997). After an initial radiative phase (Cohen et al., 1998), the shock becomes adiabatic and its propagation is described by the relativistic self-similar solution of Blandford & McKee (1976).

Various effects may complicate this picture, including late-time energy injection ("refreshed shocks") (Rees & Mészáros, 1998), an inhomogeneous external medium (e.g., Lazzati et al., 2002), or structure or inhomogeneity within the jet itself (e.g., Mészáros et al., 1998; Zhang & Mészáros, 2002; Nakar et al., 2003; Racusin et al., 2008).

Synchrotron emission is the likely afterglow emission mechanism. The observed power-law spectra and light curves may be interpreted naturally in terms of the hydrodynamic evolution of the shock and the spectral break frequencies of the synchrotron emission (Sari et al. 1998; for a detailed review, see Piran 2004).

1.1.2.6 The Internal-External Models

It is widely accepted that GRBs are produced by "internal shocks" while the afterglows are produced by "external shocks" (Figure 1.4). There is some observational evidence in favor of the internal-external picture. First, the fact that afterglows are not scaled directly to the GRB suggests that the two are not produced by the same phenomenon. Second, while most GRBs show very irregular time structure and are highly variable; all afterglows observed so far show smooth power-law decay with minimal or no variability (Sari & Piran, 1999).

Butler et al. (2006) employed an early-time broadband modeling of GRB 051111 to study when internal shocks end and external shocks begin. They obtained data using the KAIT robotic optical telescope, Lulin, and PAIRITEL to test the constancy of microphysical parameters in the internal-external shock paradigm and to carefully trace the flow of energy from the GRB to the surrounding medium.

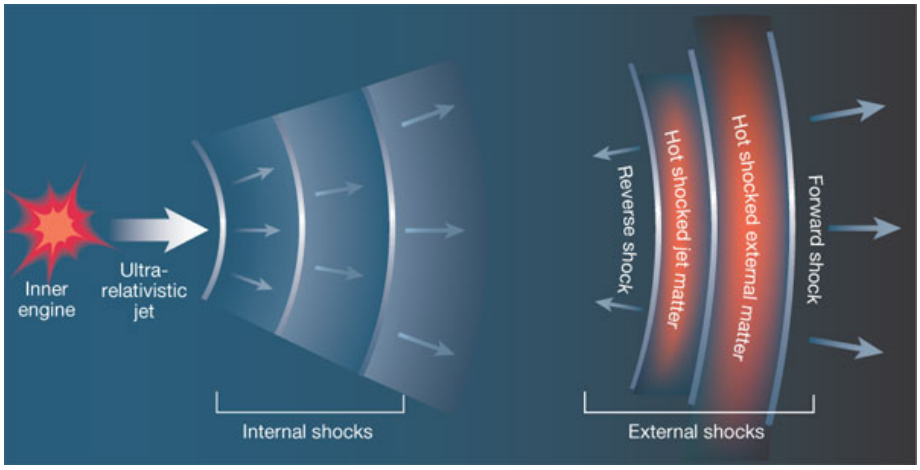

Figure 1.4: A GRB is thought to be driven by an "inner engine", a cataclysmic event such as the collapse of a massive star. Inside an ultra-relativistic jet of particles thrown out from the explosion, internal shocks release a vast amount of energy in a burst of gamma-rays. When the jet is slowed down by surrounding matter, external shocks are created: the forward shock that propagates further into space, and the reverse shock that is reflected back against the relativistic flow. Both types of shock waves heat the surrounding matter, producing an afterglow to the GRB. Adopted from Piran (2003).

1.1.3 The Swift GRB Explorer

Progress in the field of GRBs has come predominantly through two means: (1) new satellite missions capable of providing more accurate localizations for larger numbers of GRBs with smaller delay times; and (2) followup afterglow observations at earlier times, with larger telescopes, and/or in new regimes of the electromagnetic spectrum. Some of the work in this thesis builds off discoveries made by the *Swift* GRB Explorer, a NASA satellite dedicated to GRB science (Gehrels et al., 2004). For this reason, I outline the salient characteristics of *Swift* below.

The *Swift* has three instruments onboard: the wide-field (2 sr) Burst Alert Telescope (BAT; Barthelmy et al., 2005b), a hard X-ray (15-150 keV) coded-mask imager; the X-ray Telescope (XRT; Burrows et al., 2005), a 2-10 keV X-ray imaging telescope; and the Ultra-Violet/Optical Telescope (UVOT; Roming et al., 2005), providing imaging from 1700-6500 Å. The XRT and UVOT slew to BAT-discovered GRBs, typically

beginning observations of the afterglow within 100 s of the burst. Initial results from all three instruments are relayed to ground-based observers in real-time (i.e., time lag of only seconds) so that they may coordinate observations of the afterglow as well. The relevant characteristics of all three *Swift* instruments are outlined in Table 1.2.

On Oct. 27, 2015, *Swift*'s BAT detected the $1{,}000^{th}$ GRB (GRB 151027B) from a location toward the constellation Eridanus. *Swift* has remained as one of the most prolific GRB explorers with an annual average rate of ∼90 per year.

Table 1.2: *Swift* Instrument Overview

Instrument	Effective Area	Detector	FoV	Localization Accuracy	Energy Range
BAT	5200 cm^2	CdZnTe	2 sr	$\approx 3'$	15 - 150 keV
XRT	135 cm^2	XMM EPIC CCD	$23' \times 23'$	$\approx 3''$	0.2 - 10 keV
UVOT	30 $cm^\star$	Intensified CCD	$17' \times 17'$	$\approx 0.3''$	1700 - 6500 Å

(⋆): Mirror diameter

1.1.4 The Fermi GRB Explorer

Fermi Gamma-Ray Space Telescope, formerly GLAST, is a major NASA mission dedicated to observations of high energy gamma rays. Launched on June 11 2008, its main instrument, the Large Area Telescope (LAT; Atwood et al., 2009), provides unprecedented sensitivity to gamma-rays in the energy range of about 20 MeV to about 300 GeV. The Gamma-ray Burst Monitor (GBM; Meegan et al., 2009) complements the LAT in its observations of transient sources and is sensitive to X-rays and gamma-rays with energies between 8 keV and 30 MeV. The combination of the GBM and the LAT provides a powerful tool for studying GRBs, particularly for time-resolved spectral studies over a very large energy band. The GBM, an all-sky monitor, consists of 12 detectors made of sodium iodide to detect X-rays and low-energy gamma rays, and two detectors made of bismuth germanate (BGO) for high-energy gamma rays.

The salient characteristics of *Fermi* are outlined in Table 1.3.

Table 1.3: *Fermi* Instrument Overview

Instrument	Effective Area	Detector	FoV	Localization Accuracy	Energy Range
LAT	$8000\,\mathrm{cm}^2$		2.4 sr	$< 1^\circ$	$\sim$20 MeV to $>$ 300 GeV
GBM	$12 \times 126\,\mathrm{cm}^2$	NaI	> 8 sr	$\sim 5^\circ$	8 keV - 1 MeV
	$2 \times 126\,\mathrm{cm}^2$	GBO			150 keV - 30 MeV

The GBM detects GRBs at a rate of $\sim$ 300 per year, of which on average 20% are short bursts. This makes the *Fermi*/GBM the most prolific sGRBs detector. The LAT detects bursts at a rate of $\sim$ 10 per year. The LAT detects only $\sim 10\%$ of the bursts triggered by the GBM which were in the common GBM-LAT field of view. This may be related to the fact that the LAT-detected GRBs, both long and short, are generally among the highest fluence bursts, as well as being among the intrinsically most energetic GRBs.

1.1.5 Gravitational Waves from GRBs

Binary mergers of NS-NS and NS-BH, the most popular model for sGRBs, are the strongest candidate sources of gravitational waves (GWs) with a total energy reaching $\sim 10^{54}$ ergs (Kochanek & Piran, 1993; Ruffert & Janka, 1999). The luminosity of GW from lGRBs, originating from core-collapse of massive stars, is highly model-dependent (Fryer et al., 2001). Recent numerical calculations of GW emission from lGRBs range from pessimistic (Ott et al., 2011) to modest (Kiuchi et al., 2011) predictions. The expected detection rates of GW from compact binary mergers in coincidences with sGRBs have been estimated to be several per year (Abadie et al., 2010b) for the advanced LIGO and Virgo. Coordinated detection of GW with electromagnetic signal helps to reduce background significantly if sGRBs are the sources. Combining sub-threshold signal from electromagnetic, neutrino and GW observatories

can also lead to significant detection (Smith et al., 2013).

1.1.6 GRB Temporal Analysis

Uncovering the intrinsic variability of GRBs can constrain the size of the GRB emission region, and ejecta velocity, in turn providing hints on the nature of GRBs and their progenitors. After more than four decades of observations, several questions regarding the GRB prompt light curve variability still remain open including:

- ⋆ What is the shortest timescale of intensity variations in GRBs, $\Delta t_{\rm min}$?
- ⋆ How is it possible to distinguish between observable and measurable variability timescales?
- ⋆ Is there an inconsistency between $\Delta t_{\rm min}$ of *Swift* GRB light curves and those from *Fermi*?
- ⋆ Are there variability classes among GRBs?
- ⋆ Are variability timescales dependent on the energy ranges?
- ⋆ What is the fastest timescale for GRBs?
- ⋆ Can $\Delta t_{\rm min}$ be used to discriminate between progenitor models?
- ⋆ Is there any evidence for time dilation in the GRB time series?

GRBs are present over a very broad redshift range, hence the signature of time dilation – and perhaps of any evolution in GRB time structure with redshift – should be present in GRB time series. However, finding the signature of time dilation in GRBs has remained elusive. The fact that extracting such a signature is a crucial step towards potentially using GRBs for cosmological applications at redshifts far exceeding those of SNe Ia will make this effort highly rewarding.

In this thesis, I address some of the above questions. In Chapter 2, we develop a robust technique to determine the minimum variability timescale for GRB light curves

and also implement our technique to the large sample of *Swift*/BAT GRB gamma-ray light curves. In Chapter 3, we expand our methodology and apply it to the large sample of *Fermi*/GBM GRB gamma-ray light curves. The broad *Fermi*/GBM energy coverage enables us to standardize a measure of the minimum variability timescale by studying the energy evolution and evaluating the minimum timescale in a fixed rest-frame bandpass.

1.2 The Palomar Transient Factory

The PTF is a fully-automated, wide-field survey aimed at a systematic exploration of the optical transient sky. PTF utilizes a 7.1 deg^2 camera on the Palomar 48-inch Oschin Schmidt telescope to survey the sky in the optical band at a rate of 1000–3000 deg^2 per night. Observations are mainly performed in one of two broadband filters (Mould-R, SDSS-g0). Under typical seeing conditions (1.1″ at Palomar) the camera achieves a full width at half-maximum intensity (FWHM) $\sim$ 2.0″, and 5σ limiting magnitudes of $R \approx 21.0$, $g' \approx 21.6$ and H$\alpha \approx 18$ mag can be reached in a 60 s exposure (Law et al., 2009). There are more than 3 million images in the R-band available in the PTF Archive (Surace et al., 2015). The data are used to detect and study transient and moving objects such as GRBs, SNe, and asteroids as well as variable phenomena such as quasars and Galactic stars. I refer the reader to Rau et al. (2009) for a review of PTF science and observing strategies, and Law et al. (2009) for performance and technical information concerning PTF.

The Zwicky Transient Facility (ZTF; Bellm, 2014), the successor of PTF, is planned to have its first light in 2017. Using a new 47 deg^2 survey camera, ZTF will survey more than an order of magnitude faster than PTF to discover rare transients and variables. ZTF will provide the best characterization of the bright to moderate-depth ($m \lesssim 21$) transient and variable sky and pave the way for the Large

Synoptic Survey Telescope (LSST; Abell et al., 2009) deeper survey.

1.2.1 SN Rate in Starbursts Using the PTF

The rate of core-collapse SNe is a fundamental key in astrophysics. Measurements of the SN rate and its evolution over cosmic time provide valuable information on the chemical evolution of galaxies, the kinematics and composition of the interstellar medium, the production of cosmic rays, sheds light on various types of SNe progenitors and their mass ranges, and provides constraints for stellar evolution theories. Extreme star-forming galaxies are expected to have high supernova rates, yet direct observational evidence has remained elusive.

In Chapter 4, I explore the search for SNe in extreme star-forming galaxies in the local Universe, i.e., "luminous infrared galaxies" (LIRGs), using the PTF. The wealth of studies on these objects by the GOALS team at IPAC and access to the full PTF archive have allowed us to conduct the first comprehensive SNe search in local LIRGs.

1.3 The Reionization Transients and Infra-Red (RATIR) Instrument

The RATIR is a simultaneous optical/NIR multi-band imaging camera which is 100% time-dedicated to the followup of GRBs. The camera is mounted on the Harold L. Johnson 1.5-meter telescope of the Mexican Observatorio Astronómico Nacional on Sierra San Pedro Mártir (SPM) in Baja California. With rapid slew capability and autonomous interrupt capabilities, the system images GRBs in 6 bands (r, i, Z, Y, J, and H; Figure 1.5) within minutes of receiving a satellite position, detecting optically faint afterglows in the NIR and quickly alerting the community to potential GRBs at high redshift ($z > 6 - 10$). RATIR is capable of responding to a *Swift* trigger within 30 s, providing rapid early-time optical and NIR photometry. The optical cameras

have $5.3' \times 5.3'$ fields-of-view, while the NIR cameras have larger, but vertically split $10' \times 10'$ fields-of-view.

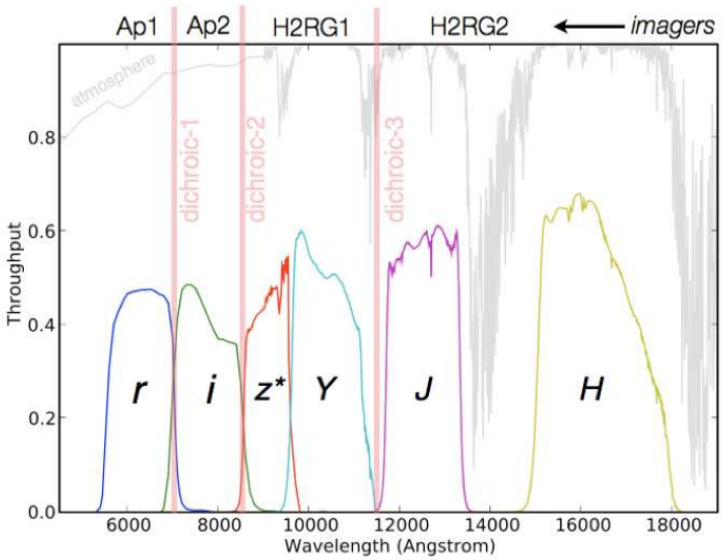

Figure 1.5: The RATIR filters span a broad range in wavelength and are well-suited to peering through the sky at SPM. Three dichroics split the incoming light first between the IR and optical channels and then within those channels to corral the light in the *r, i, Z, Y , J,* and *H* bands.

1.4 Gravitational Waves and the Advanced-LIGO

GWs are 'ripples' in the fabric of space-time caused by some of the most violent and energetic processes in the Universe. Albert Einstein predicted the existence of GWs in 1916 in his general theory of relativity. The capacity to detect GW offers us the possibility to understand astrophysical systems such as binary BHs that can not be observed at any wavelength of the EM spectrum.

The existence of GWs was first demonstrated indirectly in the 1970s and 80s by Joseph Taylor, Jr., and colleagues. Hulse & Taylor discovered in 1974 a binary system composed of a pulsar in orbit around a NS (PSR 1913+16). Taylor & Weisberg in 1982 found that the orbit of the pulsar was slowly shrinking over time consistent with the release of energy in the form of GWs.

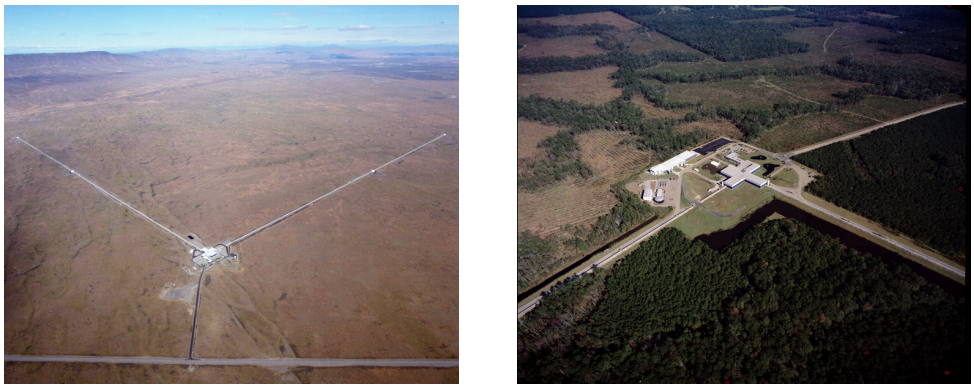

Figure 1.6: Aerial views of LIGO Hanford (left) and Livingston (right) Observatories. Pictures adopted from the LIGO webpage.

Direct detection of GWs is complicated by the extremely small effect they would produce on an Earth-based detector since the wave amplitude decreases inversely proportional with the distance to the source. Important progress has been made over the past couple of decades with the commissioning of kilometer-scale interferometric GW observatories, such as LIGO (in the US) and the Virgo detector (in Italy). Constant upgrades to these detectors laid the path to advanced detectors.

LIGO operates two GW observatories at two different sites: the LIGO Livingston Observatory in Livingston, Louisiana and the LIGO Hanford Observatory in Richland, Washington (Figure 1.6). These sites are separated by 3,002 km (Abadie et al., 2010a). At each observatory, the 4 km long L-shaped LIGO interferometer uses laser light split into two beams that travel back and forth down the arms. The beams are used to monitor the distance between mirrors precisely positioned at the ends of the arms. According to Einstein's theory, the distance between the mirrors changes by an infinitesimal amount when a GW passes by the detector (LIGO can detect a change in the lengths of the arms smaller than 10^{-19} m.)

Advanced-LIGO (LIGO Scientific Collaboration et al., 2015) began operations in 2015 (Abbott et al., 2016a) and almost immediately recorded the first ever direct

GW signal (Figure 1.7) from a binary BH merger, GW 150914 (Abbott et al., 2016b). Based on the observed signals, it was estimated that the source lies at a luminosity distance of 410^{+160}_{-180} Mpc corresponding to a redshift $z = 0.09^{+0.03}_{-0.04}$. In the source frame, the initial BH masses were 36^{+5}_{-4} $M_\odot$ and 29^{+4}_{-4} $M_\odot$which gave a final BH mass of 62^{+4}_{-4} $M_\odot$, with $3.0^{+0.5}_{-0.5}$ $M_\odot c^2$ radiated in GWs (Abbott et al., 2016b).

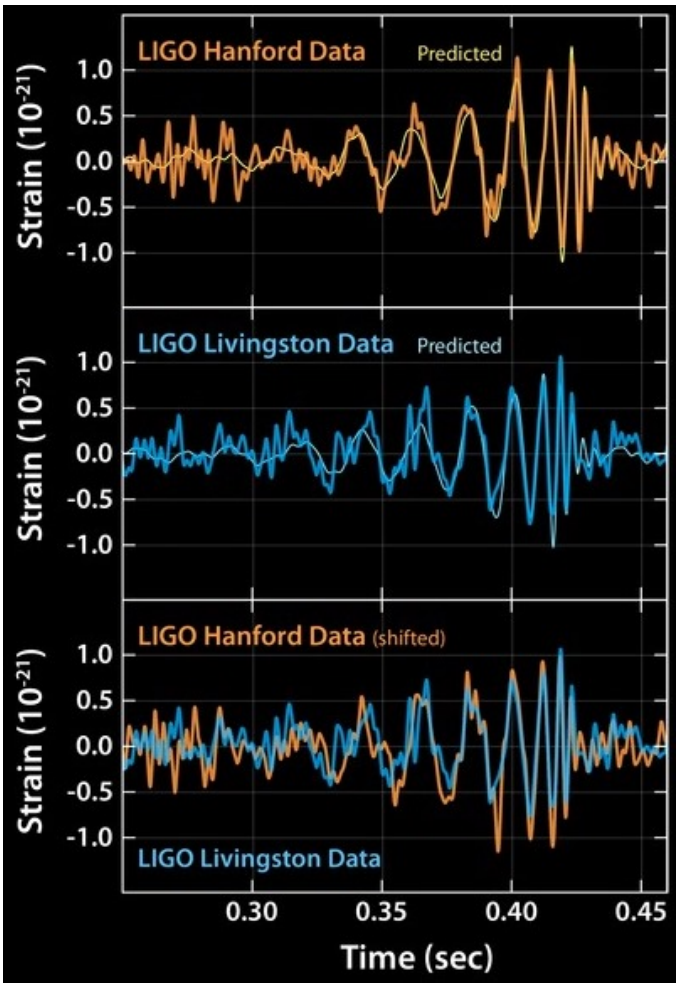

Figure 1.7: Signals of GWs detected by the twin LIGO observatories at Livingston, Louisiana, and Hanford, Washington. The signals came from two merging BHs, each about 30 times the mass of our sun, lying 1.3 billion light-years away. Picture adopted from the LIGO webpage.

1.4.1 The EM Counterparts of LIGO Gravity Wave Events

Many potential sources of transient GW signals will emit EM counterparts detectable by existing and planned astronomical instruments (see Predoi et al., 2010; Metzger & Berger, 2012, and references therein). A joint EM-GW detection would provide some of the most compelling evidence for the unambiguous direct detection of GW, as well as provide valuable information on the nature of the progenitor system. The photometric discovery of the EM counterpart will give a precise location, and a spectrum of the host galaxy will give a precise redshift. This will enable a more accurate measurement of fundamental astrophysical properties such as the luminosity and energetics of this strong-field gravity event. If the spectrum is timely, it may also solve the long-standing mystery of the unknown sites of r-process nucleosynthesis (Kasliwal et al., 2016). However, identifying a counterpart is remarkably challenging due to the LIGO inherently weak localization of GW events ($\sim$ a few hundred deg^2).

Compact binary coalescence (CBC) events represent powerful engines for the production of gravitational, EM and neutrino radiation. In the CBC model for sGRBs, a NS and compact companion in an otherwise stable orbit lose energy to GWs (e.g., Ramirez-Ruiz & Fenimore, 2000; Nakar, 2007). Disruption of the NS(s) provides matter, which can be ejected in relativistic jets. sGRBs provide our best potential link to gravity wave sources. If these events are due to collapse-object mergers (e.g., Nakar, 2007), copious gravity waves are expected, and these can be detected by advanced-LIGO if the source is sufficiently nearby. Indeed, due to beaming, the LIGO rate should be significantly larger (factor 10, Chen & Holz 2013) than the observed sGRB rate.

Finding the rapidly fading afterglow of a GW source requires essentially to engage any available facilities for a fast response time. Many facilities around the world,

such as the RATIR, have participated in the search for the EM counterparts of LIGO GW events – in the optical, X-ray, and radio bands – and have reported their followup strategies to the community (e.g., Connaughton et al., 2016; Evans et al., 2016; Kasliwal et al., 2016; Smartt et al., 2016; Soares-Santos et al., 2016).

1.4.2 RATIR LIGO Followup

As the RATIR team, we are engaged in a search to find the EM counterparts to LIGO gravity wave triggers. In Chapter 5, I discuss the design of an automated pipeline for detection of EM counterparts to LIGO GW sources and also outline our search strategy to achieve low false-alarm-rates.

In Chapter 6, I present concluding remarks and provide some of the fruitful future directions to take in the context of current and future facilities.

Chapter 2

UNCOVERING THE INTRINSIC VARIABILITY OF GAMMA-RAY BURSTS

V. Zach Golkhou & Nathaniel R. Butler

2.1 Abstract

We develop a robust technique to determine the minimum variability timescale for Gamma-ray Burst light curves, utilizing Haar wavelets. Our approach averages over the data for a given GRB, providing an aggregate measure of signal variation while also retaining sensitivity to narrow pulses within complicated time-series. In contrast to previous studies using wavelets, which simply define the minimum timescale in reference to the measurement noise floor, our approach identifies the signature of temporally-smooth features in the wavelet scaleogram and then additionally identifies a break in the scaleogram on longer timescales as signature of a true, temporally-unsmooth light curve feature or features. We apply our technique to the large sample of *Swift* GRB Gamma-ray light curves and for the first time – due to the presence of a large number of GRBs with measured redshift – determine the distribution of minimum variability timescales in the source frame. We find a median minimum timescale for long-duration GRBs in the source frame of $\Delta t_{\rm min} = 0.5$ s, with the shortest timescale found being on the order of 10 ms. This short timescale suggests a compact central engine (3×10^3 km). We discuss further implications for the GRB fireball model and present a tantalizing correlation between minimum timescale and redshift, which may in part be due to cosmological time-dilation.

A version of this chapter has been published previously in *The Astrophysical Journal*, Volume 787, Issue 1, article id. 90, 9 pp. (2014).

2.2 Introduction

Gamma-Ray Burst (GRB) light curves show a remarkable morphological diversity. While a significant number of bright long bursts ($\sim 15\%$) exhibit a single smooth pulse structure, in most cases GRBs appear to be the result of a complex, seemingly random distribution of several pulses. Burst pulses are commonly described as having fast-rise exponential-decay (FRED) shapes (e.g., Fenimore et al., 1996). Parameterized analyses of pulse profiles have shown broad log-normal distributions among different bursts and even within a single burst (see e.g., Norris et al., 1996; Bhat et al., 2012).

Several approaches have been utilized to characterize the distribution of power versus timescale for GRBs and other astrophysical sources. These include structure function (SF) analyses (Trevese et al., 1994; Hook et al., 1994; Cristiani et al., 1996; Aretxaga et al., 1997), autocorrelation function (ACF) analyses (Link et al., 1993; Fenimore et al., 1995; in 't Zand & Fenimore, 1996; Borgonovo, 2004; Chatterjee et al., 2012), and Fourier power spectral density (PSD) analyses (Beloborodov et al., 2000; Chang, 2001; Abdo et al., 2010). In principle, the ACF contains the same information as the PSD, since one is the Fourier transform of the other (the Wiener-Khinchin theorem, Chatfield, 2003). The SF is mathematically very similar to the ACF.

As Hawkins (2002) summarizes, the SF, ACF, and PSD – when calculated for a given dataset – are not completely equivalent because of time-windowing effects and the presence of measurement noise. For long runs of evenly spaced data, the PSD is used in preference to the ACF, as it can be easier to interpret and understand errors. In cases of short or inhomogeneous data sets, the ACF can provide a more stable measurement. However, as ACF values at different time lags are not statistically independent of each other, the ACF interpretation may not be simple.

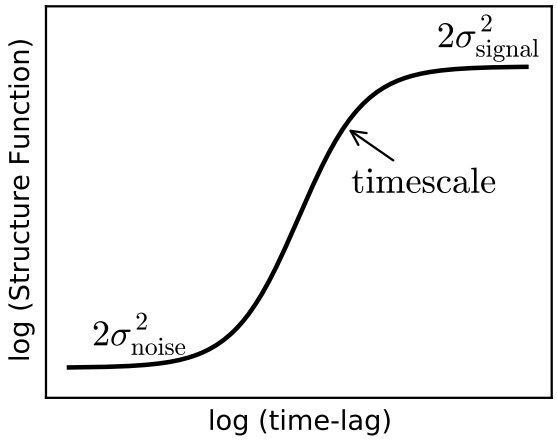

Figure 2.1: Schematic showing a typical SF for a time-series, from Hughes et al. (1992). At short lag-times, the SF flattens due to the measurements error. At long lag-times, the SF again flattens out at a level corresponding to the total variance in the signal. Between these lag-times, the slope of the SF depends on the noise properties of the signal and can be used to identify timescales of interest.

The first-order SF was introduced in astronomy by Simonetti et al. (1985). It has been widely used in the analysis of quasar light curves (e.g., Trevese et al., 1994; Hawkins, 2002) and microlensing statistics (e.g., Wyithe & Turner, 2001). Compared to power-spectral analyses, the SF approach is less dependent on the time sampling (Paltani, 1999). Following these studies, we define the first-order SF as a measure of the mean square difference of a signal $X(t)$ on timescale (or "lag") τ:

$$\mathrm{SF}(\tau) = \left\langle [X(t) - X(t+\tau)]^2 \right\rangle \tag{2.1}$$

Here, $\langle . \rangle$ denotes an averaging over t. In Figure 2.1, we reproduce the typical shape of an SF, from Hughes et al. (1992).

We will be primarily interested below in using the SF to infer the shortest timescale at which a GRB exhibits *uncorrelated temporal variability*. In a seminal study, Walker et al. (2000) (and more recently, MacLachlan et al., 2013) utilize Haar wavelet scaleograms to measure minimum timescales. Wavelets are a set of mathematical functions, which form an orthonormal basis to compactly describe narrow time features

(e.g., Daubechies, 1992; Norris et al., 1994; Kolaczyk, 1997; Scargle et al., 2013). Making the connection between the Haar wavelet scaleogram and the SF, as we do below in mathematical detail, sheds new light on prior work, allowing for a more rigorous analysis and better physical interpretation of the signal power versus timescale. We also exploit the large sample of *Swift* GRBs with measured redshifts to perform this analysis, for the first time, in the GRB source frame.

A general feature we observe in our scaleograms, provided there is sufficient signal-to-noise ratio (SNR), is a linear rise phase relative to the Poisson noise floor on the shortest timescales (see e.g., Figures 2.3 and 2.4). We take this to indicate a typical smoothness on the shortest observed timescales. We thus make an essential distinction – not made in prior studies – between correlated variability (i.e., smooth or continuous) and uncorrelated variability (e.g., pulses or changes in sign). For example, an exponentially decaying GRB light curve pulse with a fairly long time constant (say 100 s) will still exhibit power (i.e., yield a non-zero SF) on much shorter timescales (say 1 s), provided the SNR is sufficiently large for this to be measured. In contrast, the meaningful timescale (in this case $\approx$ 100 s and not 1 s) is the shortest timescale at which the signal becomes uncorrelated.

A simple Taylor expansion of the SF assuming a temporally-smooth signal $X(t)$, shown in Equation 2.2, elucidates how the minimum timescale for uncorrelated variability is connected to the scaleogram linear-rise phase.

$$X(t+\tau) = X(t) + \tau X'(t)|_\tau + ..., \tag{2.2}$$

Substituting Equation 2.2 into Equation 2.1 and ignoring higher order terms produces Equation 2.3:

$$\sqrt{\mathrm{SF}(\tau)} \propto \tau \tag{2.3}$$

which shows that for timescales where the signal is smoothly varying, we expect a

linear dependence on the time lag τ. When the variation becomes non-smooth, SF flattens, providing a signature of the true GRB minimum timescale. Previous studies (Walker et al., 2000; MacLachlan et al., 2013) – which overlook the importance of the SF $\propto \tau$ region – incorrectly interpret the GRB minimum as the shortest timescale at which the SF is first non-zero (after subtracting the measurement noise level), potentially under-estimating the true variability timescales.

In this chapter, we begin with a more detailed description of our method – the Haar wavelet structure function – which exploits a non-decimated, discrete Haar wavelet transform to estimate the SF and, in turn, the minimum variability timescale for a large number GRBs. We discuss the robustness of the structure function in extracting this timescale even in the case of complex GRBs containing multiple, overlapping pulses and we demonstrate self-consistency as the SNR is varied. Next, we apply the methodology to the full sample of GRBs observed by *Swift* BAT, summarizing the derived timescales for the population in the observer and GRB source frames. We conclude by discussing how these minimum variability timescales can elucidate the GRB central engine, help constrain models for the emission mechanism, and potentially also enable a measurement of cosmological time-dilation.

2.3 Method: A Structure Function Estimated Using Haar Wavelets

The technique developed in this section was first used in Kocevski et al. (2007) to study the time-structure of X-ray flares following *Swift* GRBs. It is applicable to a broad range of time-series. Consider a time-series of length N that can be regarded as one portion of one realization from the stochastic process $\{X_t, t = 0, \pm 1, ..., T\}$ (considering a unit sampling interval). Let

$$\bar{X}_t(\tau) = \frac{1}{\tau} \sum_{n=0}^{\tau-1} X_{t-n} \tag{2.4}$$

represent the sample average of τ consecutive observations, the latest one of which is X_t. The Allan (1966) variance at scale τ is denoted by $\sigma^2_X(\tau)$ and is defined to be half the mean square difference between adjacent non-overlapping $\bar{X}_t(\tau)$'s; i.e.,

$$\sigma^2_X(\tau) = \frac{1}{2}\left\langle [\bar{X}_t(\tau) - \bar{X}_{t-\tau}(\tau)]^2 \right\rangle \tag{2.5}$$

Note that the *Allan* variance at scale τ is a measure of the extent to which averages over length τ change from one time period of length τ to the next (Percival & Walden, 2006). Comparing Equation 2.5 to Equation 2.1, we see that the *Allan* variance is related to the SF of the smoothed signal $\bar{X}_t$.

In order to see how Haar wavelets can be used to estimate the SF (see Figure 2.2), we will now relate the Haar wavelet coefficients to the averages calculated in determining the *Allan* variance. Consider the discrete Haar wavelet transform (Percival & Walden, 2006) of the time-series $X_1, ..., X_N$, where we assume that the sample size N is a power of 2 so that $N = 2^q$ $(q > 0)$. By definition, this transformation consists of $N - 1$ "detail" coefficients and one "smooth" coefficient $s_1 = \sum_{t=1}^{N} \frac{X_t}{N}$. The detail coefficients $d_{j,k}$ are defined for scales $k = 1, 2, 4, 8, ..., N/2$ and - within the kth scale - for indices $j = 1, 2, 3, ..., N/2k$ as

$$d_{j,k} \equiv \frac{1}{\sqrt{2k}} \left[\sum_{n=0}^{k-1} X_{2jk-n} - \sum_{n=0}^{k-1} X_{2jk-k-n} \right] \tag{2.6}$$

We can now state the relationship between the *Allan* variance and the Haar wavelet coefficients $d_{j,k}$. Using Equations 2.6, we have

$$d_{j,k} = (\frac{k}{2})^{(1/2)} \left[\bar{X}_{2jk}(k) - \bar{X}_{2jk-k}(k) \right] \tag{2.7}$$

Under the assumption that $E\{d_{j,k}\} = 0$ so that the variance of $d_{j,k}$ is equal to $E\{d^2_{j,k}\}$, an average of the wavelet coefficients squared on scale k provides a natural estimator

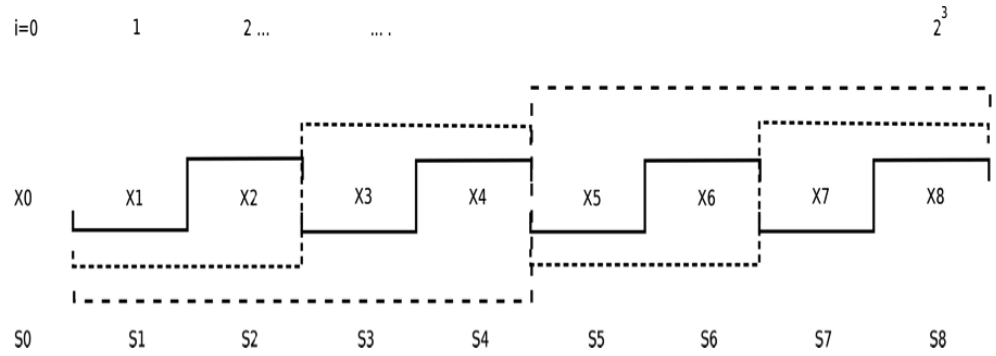

Figure 2.2: A schematic representation of relation between the Haar wavelet coefficients (Equation 2.6) and the first-order structure function. The Haar mother wavelet as shown step function (with different style) operates using scaling and dilation on a time-series: $\{X_i | i = 0..8\}$. $S_i = \sum_0^i X_i$.

for the *Alan* variance:

$$\begin{aligned} \mathrm{var}\{\mathrm{d_{j,k}}\} = \langle \mathrm{d_{j,k}^2} \rangle = \frac{\mathrm{k}}{2} \left\langle \left[\bar{\mathrm{X}}_{\mathrm{2jk}}(\mathrm{k}) - \bar{\mathrm{X}}_{\mathrm{2jk-k}}(\mathrm{k}) \right]^2 \right\rangle \\ = \tau \sigma_X^2(\tau) \end{aligned} \tag{2.8}$$

We will redefine our wavelet coefficients (Equation 2.6) by dividing out another factor of $\sqrt{k/2}$, eliminating the k dependence in Equation 2.8.

2.3.1 Data Analysis and Haar-SF Implementation

In this section, we further develop our algorithm and discuss its application to GRB data captured by NASA's *Swift* satellite (Gehrels et al., 2004). Our automated pipeline at Arizona State University is used to download the *Swift* data in near real time from the *Swift* Archive [1] and quicklook site. We use the calibration files from the 2008-12-17 BAT database release. We establish the energy scale and mask weighting for the BAT event mode data by running the `bateconvert` and `batmaskwtevt` tasks from the HEASoft 6.12 software release [2] . Light curves are extracted in the 15–350

[1] `ftp://legacy.gsfc.nasa.gov/swift/data`

[2] `http://swift.gsfc.nasa.gov/docs/software/lheasoft/download.html`

keV band using the `batbinevt` tool with 100 μs time bins, applying a uniform random deviate on the same timescale to undo artifacts associated with the data capture [3] . The burst duration intervals are determined automatically as described in Butler et al. (2007).

Next, we group together adjacent time bins in the light curve until each composite bin has a fixed SNR of 5, dividing by the exposure time contained with each composite bin to produce the count rate versus time. We then apply our analysis to the natural log of the binned light curve so that the error per light curve bin is approximately constant. For homoscedastic errors – as we now have – the orthogonality properties of the Haar wavelets lead to approximate statistical independence of the wavelet coefficients (see e.g., Percival & Walden, 2006). We find that working with binned data with approximately constant errors from point to point leads to the most stable SF estimates.

Producing a scaleogram using the logarithm of the count rate can be interpreted as yielding the average *fractional* change in the signal versus timescale. We believe such a measure allows for more physical insight into the emission mechanism than a measure of absolute change versus timescale. We note that the time binning will no longer be uniform. This is not a problem for the analysis, provided we propagate the true time difference associated with each wavelength coefficient through the analysis. We call the resulting scaleogram the Haar wavelet structure function, and we will denote it as $\sigma_{X,\Delta t}$ below. To improve statistics, we calculate $\sigma_{X,\Delta t}$ using not just one discrete Haar transform, but averaging $\sigma_{X,\Delta t}$ over the N transforms resulting from cyclic permutations of the data of length N (i.e., the non-decimated Haar transformation).

[3]See `http://swift.gsfc.nasa.gov/docs/swift/analysis/bat_digest.html`

2.3.2 A Sample Burst: The "Naked-Eye" GRB 080319B

We now implement the Haar structure function on a real GRB light curve. The prompt BAT Gamma-ray light curve for GRB 080319B (see e.g., Bloom et al., 2009, and references therein) and our derived $\sigma_{X,\Delta t}$ curve are shown in Figure 2.3. To guide the eye, several lines of constant $\sigma_{X,\Delta t} \propto \Delta t$ are also plotted. The expected measurement error has been subtracted away, leaving only the fractional flux variation expected for the GRB. On timescales where this net variation is greater than zero at the 3σ confidence level, we plot data points. Otherwise we plot upper limits.

Although there is excess signal present on timescales as short as 20 ms in Figure 2.3 (bottom), these timescales correspond to a region of the plot where $\sigma_{X,\Delta t} \propto \Delta t$ and should be interpreted as being due to temporally-smooth variations in a signal which is varying in an unsmooth fashion on longer timescales. The $\sigma_{X,\Delta t}$ points pull away significantly (2σ level from a $\Delta\chi^2$ test) from the $\sigma_{X,\Delta t} \propto \Delta t$ curve at $\Delta t_{\rm min} = 40 \pm 10$ ms. This is the timescale of interest, describing the minimum variability time for uncorrelated variations in the GRB.

Beyond this timescale, $\sigma_{X,\Delta t}$ is flatter than $\sigma_{X,\Delta t} \propto \Delta t$, indicating the presence of pulses with typical durations on these timescales. On a timescale of about 1 s, the $\sigma_{X,\Delta t}$ begins turning over due to a lack of signal variation between this timescale and the timescale (tens of seconds) describing the emission envelope. We are not concerned here with those longer timescale structures, although we do note that $\sigma_{X,\Delta t}$ provides a rich, aggregate description of this temporal activity.

In the inset to Figure 2.3 (top), we show a zoom-in on the narrowest time structure present in the signal. It can be seen that the approximate rise-time of this pulse corresponds nicely to our derived minimum timescale.

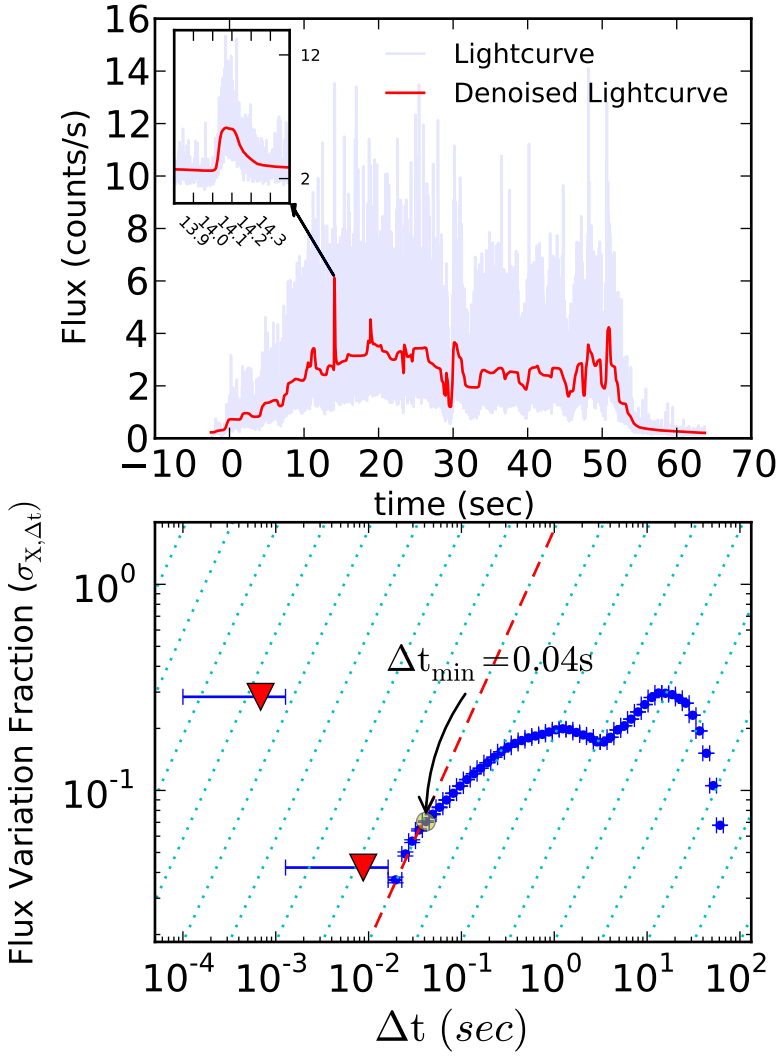

Figure 2.3: (Top) *Swift* BAT light curve (15–350 keV band) of the "Naked Eye" GRB 080319B. Overplotted is a denoised version of the light curve (Kolaczyk, 1997; Quilligan et al., 2002), highlighting the true signal variation that would be observed were there no Poisson error on the measurement. (Bottom) The Haar wavelet scaleogram $\sigma_{X,\Delta t}$ vs. timescale Δt for GRB 080319B. We show only 3σ excesses over the power associated with Poisson fluctuations and report lower values as 3σ upper limits using red triangles. We derive a minimum timescale of 40 ± 10 ms (Section 2.3.2), corresponding to the shortest timescale at which $\sigma_{X,\Delta t}$ departs from $\sigma_{X,\Delta t} \propto \Delta t$. The corresponding light curve structure can be seen clearly in the top panel inset.

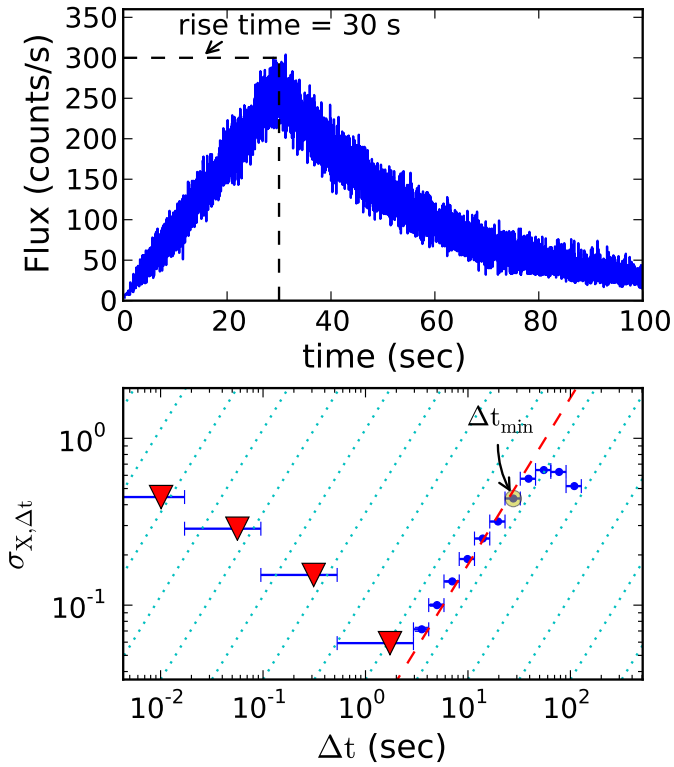

Figure 2.4: A simulated FRED pulse with a rise time of 30 s (Top) and the corresponding Haar wavelet scaleogram $\sigma_{X,\Delta t}$ vs. timescale Δt (Bottom). The expected Poisson noise level has been subtracted. The scaleogram rises linearly on short timescales corresponding to regions of the light curve where the signal is varying smoothly, falling away from the $\sigma_{X,\Delta t} \propto \Delta t$ trend on a timescale ($\approx$ 30 s). This minimum timescale can be robustly measured, provided there is sufficient SNR for the linear region preceding it to be well identified.

2.3.3 Simulated GRBs

The above example demonstrates that $\sigma_{X,\Delta t}$ can be used to extract a minimum timescale from a bright GRB with a rich temporal profile. How robust would the recovery of this timescale be for fainter GRBs? We examine this question using simulated pulses. Figure 2.4 displays a simulated GRB, consisting of a single pulse with FRED profile. The minimum timescale – corresponding to the rise of the pulse – can be correctly identified because there is sufficient SNR to identify the $\sigma_{X,\Delta t} \propto \Delta t$ region of the plot preceding that timescale.

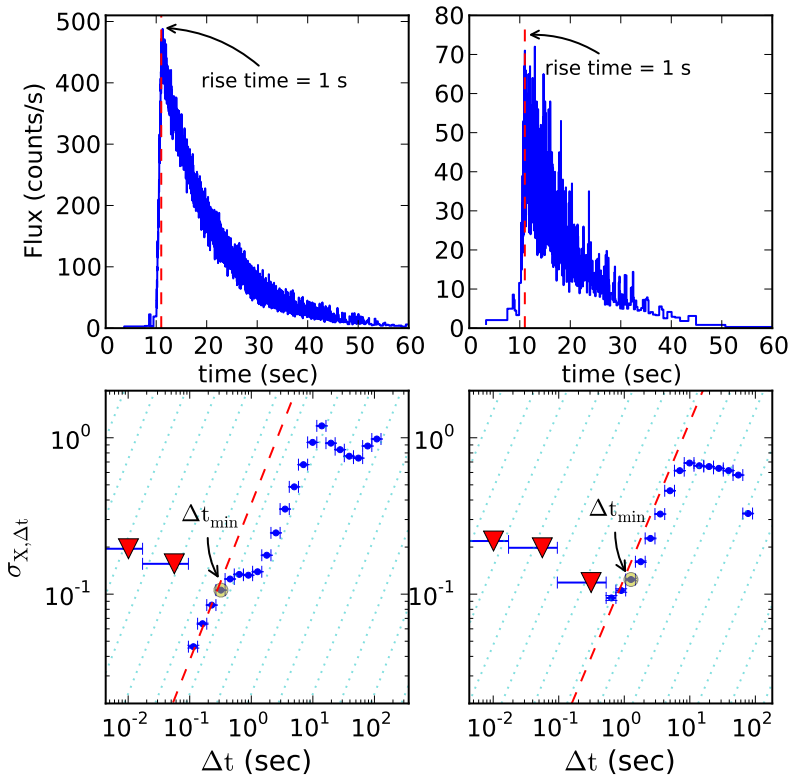

Figure 2.5: Simulated FRED pulses with a rise time of 1 s (Top). The left pulse is an order of magnitude brighter than the right pulse. The bottom panels show the corresponding Haar wavelet scaleogram $\sigma_{X,\Delta t}$ vs. timescale Δt. The expected level for Poisson noise has been subtracted. It is clear that fine-time structure can be missed in the low SNR limit; however the $\sigma_{X,\Delta t}$ measurements remain consistent.

We now consider a pulse with markedly different rise-time $T_{\rm rise}$ and total duration $T_{\rm tot}$, over a range of possible brightness. Figure 2.5 shows a simulated GRB (single pulse) with $T_{\rm rise}/T_{\rm tot} \sim 1/100$. The left panel shows a pulse which is an order of magnitude brighter than that in the right panel. The bottom panels of Figure 2.5 display the corresponding fractional flux variation $\sigma_{X,\Delta t}$ as a function of timescale Δt. The derived minimum timescale in case of brighter light curve is close to the rise-time of 1 s.

When we decrease the pulse SNR, the linear rise phase spans less of the plot and is harder to identify (Figure 2.5 (right)); it becomes more difficult to identify the

minimum timescale. In this example, $\Delta t_{\rm min}$ is still identified correctly for 10 times lower SNR. We note that the y-axis levels ($\sigma_{X,\Delta t}$) in the low and high SNR plots are consistent: we infer the correct fractional signal power at each Δt in each case.

With further decreasing SNR levels, the linear rise phase in $\sigma_{X,\Delta t}$ due to the pulse rise will become absent. If the first non-zero $\sigma_{X,\Delta t}$ values lies on a line flatter than linear, the associated $\Delta t_{\rm min}$ value must be regarded as an upper limit. We will follow this convention below: if a linear rise phase on the shortest timescales cannot be confirmed, $\Delta t_{\rm min}$ will be taken as an upper limit.

At very low SNR levels, our analysis will tend to miss the linear rise phase in $\sigma_{X,\Delta t}$ associated with the pulse rise time and will instead identify the pulse decay time (or total GRB duration) as the minimum timescale. Because actual GRB pulses tend to be asymmetric like this simulated pulse, we expect our $\sigma_{X,\Delta t}$ analysis to correctly identify true minimum timescale if is within an order of magnitude (or so) of the lowest measurable timescale. Care will have to be taken when considering faint GRBs with $\sigma_{X,\Delta t}$ of order unity and with $\Delta t_{\rm min}$ comparable to the event duration.

We conclude from this that the measurement of a linear rise phase in $\sigma_{X,\Delta t}$, followed by a flattening, will allow us to infer the presence of a characteristic timescale describing the transition from smooth (correlated) to unsmooth (uncorrelated) variability. However, we will not generally be able to rule on the presence of uncorrelated variability on much shorter (i.e. factor 10-100) timescales. We stress again that the shortest timescale exhibiting a net $\sigma_{X,\Delta t}$ over the Poisson level (called $\Delta t_{\rm snr}$ below), is not a timescale with intrinsic meaning independent of the noise level.

2.4 Discussion and Results

We analyze the *Swift* data set up until October 27, 2013, which consists of 744 GRBs, 251 with measured redshifts. We only consider those GRBs with total light

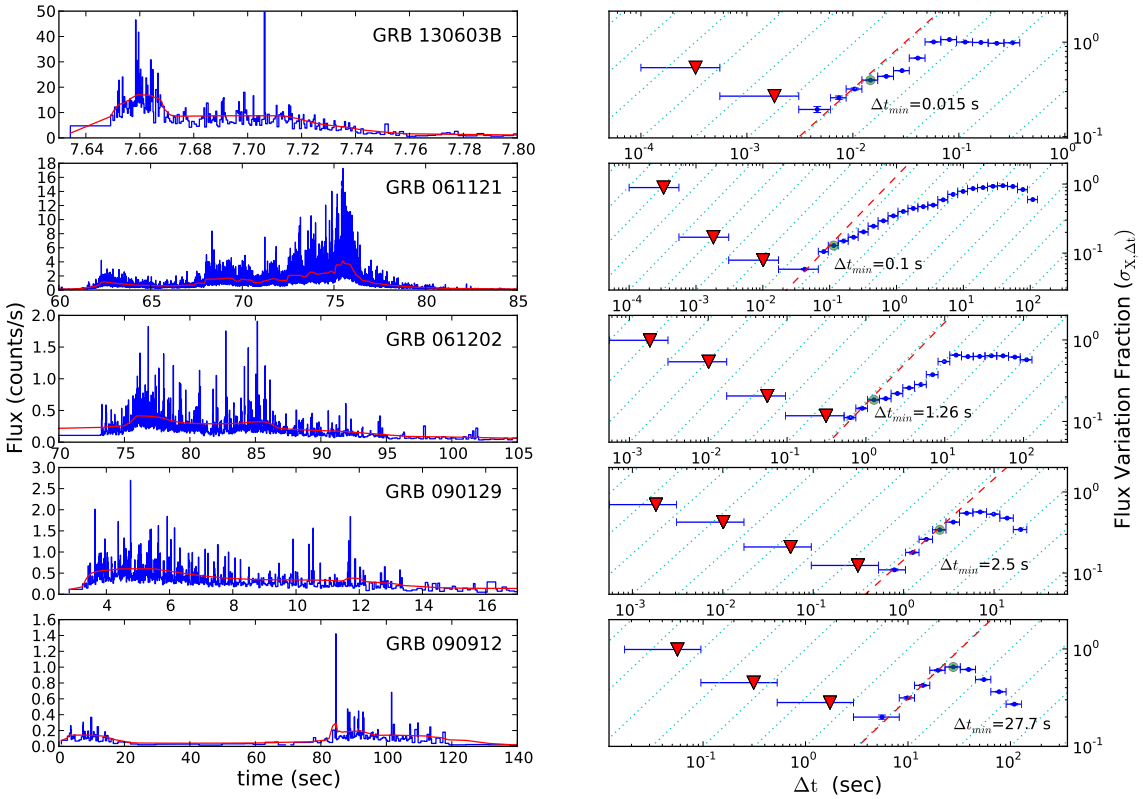

Figure 2.6: A gallery of Haar scaleograms $\sigma_{X,\Delta t}$, spanning a range of minimum variability timescale $\Delta t_{\rm min}$. The left panel shows the light curve in blue, with a denoised red curve to guide the eye. The corresponding Haar scaleogram plot is shown in the right panel. In each of these, the red dashed-line represents the temporally-smooth ($\sigma_{X,\Delta t} \propto \Delta t$) region and the green circle marks the extracted $\Delta t_{\rm min}$.

curve SNR $\geq$ 10, leaving 517 GRBs. Of these, we are able to confirm the presence of a linear rise phase in $\sigma_{X,\Delta t}$ on short timescales for 281 GRBs. We quote upper-limit values for the remainder. Most (256) of the bursts in this compiled subsample are long-duration ($T_{90} > 3$ s) GRBs. In the compiled subsample, 98 GRBs in the compiled subsample have measured redshift. The temporal specifications of all 517 GRBs discussed here are determined using fully-automatic software and are presented in Appendix A (Table A.1). Light curves and Haar scaleograms are shown for a subset of the GRBs in Figure 2.6.

Figure 2.7 displays our minimum variability timescale, $\Delta t_{\rm min}$, versus the GRB

duration, T_{90}. The short and long-duration GRBs are shown with diamond and circle symbols, respectively. In this plot the relative size of symbols is set by the ratio between minimum variability and SNR timescale ($\Delta t_{\rm min}/\Delta t_{\rm snr}$). As described above, $\Delta t_{\rm snr}$ represents the first statistically significant timescale in the Haar wavelet scaleogram. The color of the points in Figure 2.7 corresponds to the fractional flux variation level ($\sigma_{X,\Delta t}$) at $\Delta t_{\rm min}$. A curved black line is also plotted to show a typical value for the minimum observable time ($\Delta t_{\rm snr}$) versus T_{90}.

We first note from the colors in Figure 2.7, that GRBs with $\Delta t_{\rm min}$ close to T_{90} tend to have flux variation fractions of order unity. These are bursts with simple, single-pulse time profiles. As can be seen from the range of point sizes in Figure 2.7, most are not simply low SNR events where fine time structure cannot be observed. Also, we see that there are GRBs with both high and low SNR which have complex time-series ($\Delta t_{\rm min} \ll T_{90}$). Based again on the point colors, this short-timescale variation tends occur at a small fractional level in the signal ($\sigma_{X,\Delta t} \approx$ 1–10 %), at least for the long-duration GRBs.

From a Kendall's τ-test (Kendall, 1938), we find only marginal evidence that $\Delta t_{\rm min}$ and T_{90} are correlated ($\tau_k = 0.38$, 1.5σ above zero). The $\Delta t_{\rm min}$ values in Figure 2.7 are bound from above by T_{90}, and they do not strongly correlate with T_{90} within the allowed region of the plot. Recently, MacLachlan et al. (2013) have studied faint Fermi GBM GRBs and do find evidence for a correlation. We can reconcile our conclusions by identifying low SNR as the driving force in any apparent correlation. If we perform a truncated Kendall's τ test which only compares GRBs above one-another's threshold (Lloyd-Ronning & Petrosian, 2002), the correlation strength drops precipitously ($\tau_k = 0.14$ with 0.5σ). We, therefore, believe there is no strong evidence supporting a real correlation between $\Delta t_{\rm min}$ and T_{90}.

Figure 5.4 (left) shows histograms for the *Swift* GRBs with reliable $\Delta t_{\rm min}$ (in blue)

measurement and also the GRBs for which only upper limits on $\Delta t_{\rm min}$ could be derived (in red). The distributions have consistent mean values. (We discuss discrepancies between the tails of the distributions below.) We find a median minimum timescale for long-duration (short-duration) GRBs in the observer frame of 2.5 s (0.2 s). In the source frame, we find a median minimum timescale for long-duration (short-duration) GRBs of 0.5 s (2.1 s).

From Figure 5.4, we observe that the $\Delta t_{\rm min}$ distribution of long-duration GRBs is displaced from that of short-duration GRBs (8σ, t-test). This finding is consistent with the findings of MacLachlan et al. (2013), but not those of Walker et al. (2000) who find statistically indistinguishable distribution centers. We do note that the distribution centers appear to be consistent when viewed in the source frame (Figure 5.4 (right)), although the number of short-duration GRBs with redshift is low. The reason for the observer frame discrepancy is likely the fact that short-duration GRBs tend to be detected only at low-redshift, unlike long-durations GRBs which span a broad range of redshifts.

Examining the dispersion in $\log(\Delta t_{\rm min})$ values, shows no strong evidence for dissimilar values for the long and short-duration samples ($< 1.5\sigma$, F-test). This finding is fully consistent with MacLachlan et al. (2013), where it was also found (using a larger sample of short-duration GRBs) that the two histograms are quite broad and very similar in dispersion.

We have a large sample of GRBs for which no $\Delta t_{\rm min}$ could be calculated or for which only upper limits on $\Delta t_{\rm min}$ were obtainable. To account for the relative frequencies of such GRBs, we employ a survival analysis (see e.g., Feigelson & Nelson, 1985). Figure 2.9 displays the Kaplan-Meier estimator curves, which combine the detections and upper limits. There are two thin curves (green and red) in each panel of Figure 2.9. The green curve is calculated including the derived upper limits for

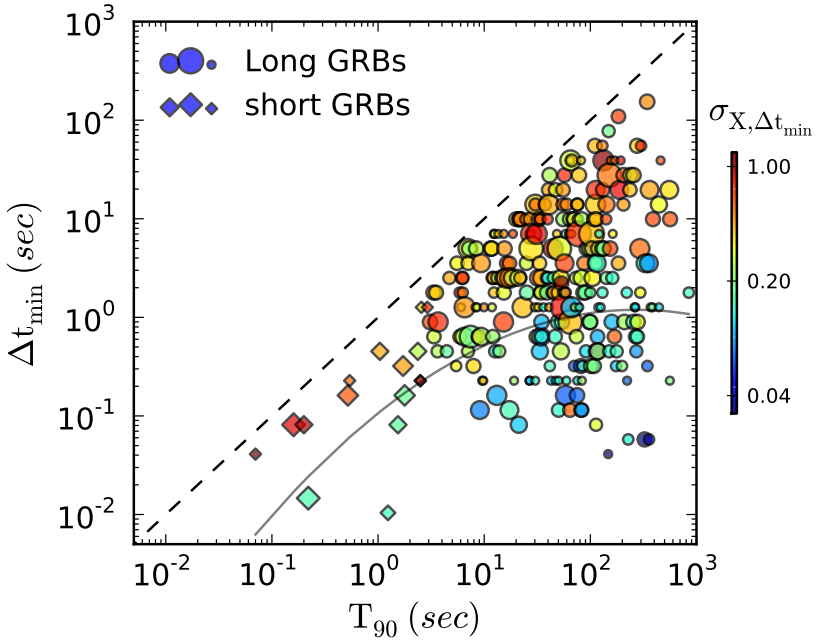

Figure 2.7: Our GRB minimum time $\Delta t_{\rm min}$ plotted versus the GRB T_{90} duration. Circles (diamonds) represent long-duration (short-duration) GRBs. The point color represent the fractional flux variation level ($\sigma_{X,\Delta t_{\rm min}}$) at $\Delta t_{\rm min}$. Also plotted as a curved line is the typical minimum observable $\Delta t_{\rm min}$ as a function of T_{90}. The symbol sizes are set by the ratio of $\Delta t_{\rm min}$ to the actual minimum observable time ($\Delta t_{\rm snr}$) for each GRB.

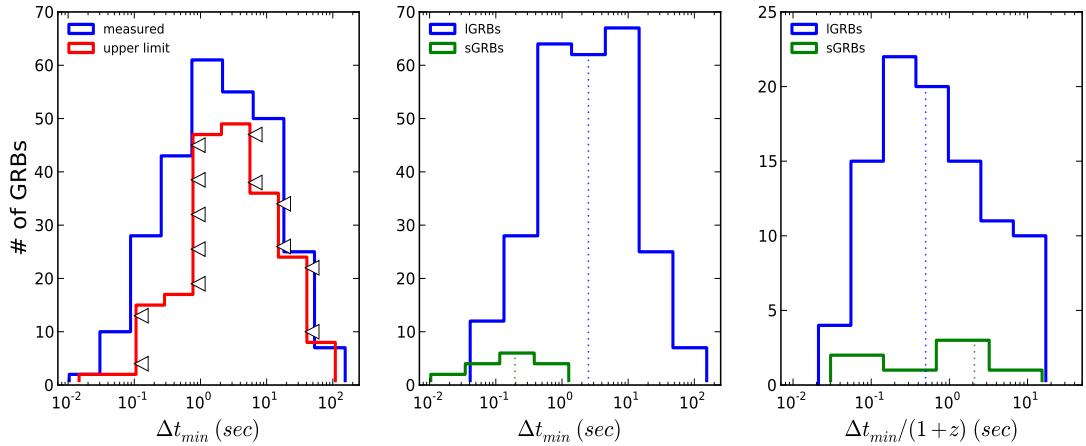

Figure 2.8: The histograms of $\Delta t_{\rm min}$ with reliable measurement (blue) and for GRBs allowing for upper limits only (red). In observer frame (middle panel) the median minimum timescale for long-duration GRBs is: $\Delta t_{\rm min} = 2.5$ s, and for short-duration GRBs is $\Delta t_{\rm min} = 0.2$ s. The same quantities in source frame (right panel) are: $\Delta t_{\rm min} = 0.5$ s and $\Delta t_{\rm min} = 2.1$ s.

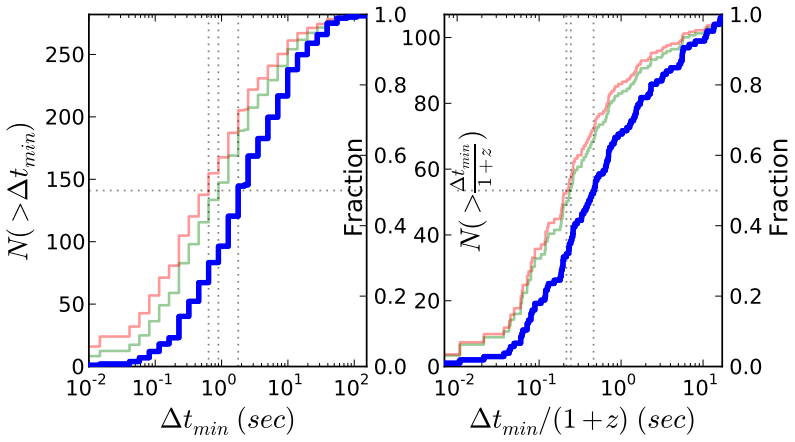

Figure 2.9: Cumulative distributions in the observer frame (left) and source frame (right) for $\Delta t_{\rm min}$ for GRBs with well measured values (blue). The Kaplan-Meier estimator (Feigelson & Nelson, 1985) is used to also include GRBs with upper limits on $\Delta t_{\rm min}$ (green and red curves). The median minimum timescale for GRBs with long and short-durations in the observer frame is: $\Delta t_{\rm min} = 1.8$ s, and in source frame is: $\Delta t_{\rm min} = 0.5$ s.

$\Delta t_{\rm min}$ when SF fitting was possible. The red curve includes these as well as $\Delta t_{\rm min}$ estimates for the remaining GRBs, where we take T_{90} as the limiting value of $\Delta t_{\rm min}$ when no SF fitting was possible. The median minimum timescale for GRBs (long and short-duration) in the observer frame is $\Delta t_{\rm min} = 1.8$ s. In the source frame, the median is $\Delta t_{\rm min} = 0.5$ s. The survival analysis does not strongly affect these median values.

Walker et al. (2000), using BATSE data, report that most GRBs appear to exhibit millisecond variability. Claims have also been made for the presence of sub-millisecond variability (Bhat et al., 1992), and even micro-second variability (Mitrofanov (1989), but see Schaefer et al. (1993); Deng & Schaefer (1997)). In contrast, we find that only 0.4% of *Swift* BAT GRBs with well-measured $\Delta t_{\rm min}$ have $\Delta t_{\rm min} < 10$ ms (observer frame). If we include all *Swift* GRBs using the survival analysis, we still find a fraction below 6%. In the source frame, the numbers are 1% (well-measured) and 4% (all). Of 517 bursts where 1 ms variability could have been measured, none show such short-timescale variability. We conclude that millisecond variability may be quite rare.

2.4.1 Evidence for Time-Dilation?

Given that we can derive a robust GRB minimum timescale and that redshifts have been measured for many of our GRBs, it is interesting to test whether these quantities are correlated. As GRBs are present over a very broad redshift range the signature of time-dilation ought to be present in GRB time-series. However, finding such a signal has remained elusive (Norris et al. (1994); Kocevski & Petrosian (2013), but see e.g., Zhang et al. (2013)).

In Figure 2.10, we plot $\Delta t_{\rm min}$ as a function of redshift. Redshift values are taken from Butler et al. (2007, 2010, and references therein). The blue crosses in Figure 2.10 correspond to geometric averages for sets of 10 bursts of similar redshift. The unbinned data are plotted in the background. We find that the binned data can be well-fitted by a line $\Delta t_{\rm min} = 0.3(1+z)^{1.6\pm0.4}$, possibly indicating the presence of time-dilation, although with a larger best-fit power-law index than would naively be expected.

The purity of this relation comes into question, however, when we perform a similar fit to the minimum observable timescale. We find that this quantity also correlates with redshift, as $\Delta t_{\rm snr} = 0.2(1+z)^{1.2\pm0.3}$. This must be the result of selection effects: more distant GRBs are fainter, thus permitting measurement of only long variability timescales. The power-law indices of the two fits are statistically consistent (1-σ level). For the unbinned data, we find $\tau_k = 0.24$ (3.6σ), but this drops to $\tau_k = -0.02$ accounting for the limits. Given the clear role the threshold plays in defining the correlation strength, we cannot be confident that time-dilation is being uniquely measured by $\Delta t_{\rm min}$.

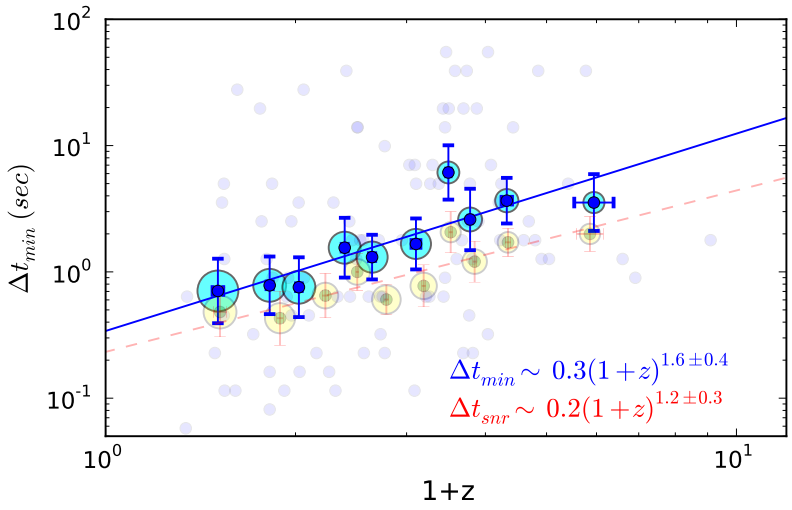

Figure 2.10: Minimum variability timescale in the observer frame versus redshift z. The blue crosses show geometric averages of $\Delta t_{\rm min}$ with 10 bursts in each bin and red crosses show geometric averages of $\Delta t_{\rm snr}$ with 18 bursts in each bin. Cyan and yellow circles correspond to the average of SNR of bursts in each bin. The faint blue circles show all GRBs with measured $\Delta t_{\rm min}$ and known z.

2.5 Conclusions

Using a technique based on Haar wavelets, we have studied the temporal properties of a sample of GRB hard X-ray, prompt-emission light curves captured by the BAT instrument on *Swift* prior to October 27, 2013. Our approach averages over the time-series captured for a given GRB, providing robust measures of minimum variability timescales.

In contrast to previous studies (Walker et al., 2000; MacLachlan et al., 2013; Bhat, 2013), which simply define the minimum timescale in reference to the measurement noise floor, our approach identifies the signature of temporally-smooth features in the wavelet scaleogram and then additionally identifies a break in the scaleogram on longer timescales as signature of a true, temporally-unsmooth light curve feature or features. We find that this timescale ($\Delta t_{\rm min}$) tends to correspond to the rise-time of the narrowest GRB pulse (see also, Bhat, 2013).

We find a median minimum timescale for long-duration GRBs in the source (observer) frame of $\Delta t_{\rm min} = 0.5$ s ($\Delta t_{\rm min} = 2.5$ s). A consistent value in the source-frame for short-duration GRBs may indicate a common central engine.

We find that very few (at most 6%) of *Swift* GRBs can have minimum timescales below 10 ms. Our timescales are thus considerably longer than the millisecond variability timescales found by Walker et al. (2000) to be common in bright BATSE GRBs. Partial explanation for this discrepancy must come from the fact that *Swift* BAT operates in a lower photon energy range than BATSE, and GRB pulses are known to be more narrow in higher energy bandpasses (e.g., Norris et al., 1996; Fenimore et al., 1995, 1996). Nonetheless, we note that the variability found in Walker et al. (2000) is not linked to the presence of discernible features in a given light curve (e.g., the pulse rise-time, which it is actually stated to be considerably less than). Given our new distinction between a Walker et al. (2000) type timescale (which we call $\Delta t_{\rm snr}$) – the minimum possible observable $\Delta t_{\rm min}$ for a GRB of given brightness and not necessarily the true $\Delta t_{\rm min}$ – it is natural to expect that Walker et al. (2000) have under-estimated their minimum timescales.

2.5.1 Constraints on the Fireball Model

The standard fireball model postulates the release of a large amount of energy by a central engine into a concentrated volume (Cavallo & Rees, 1978; Piran, 2004), which causes the resulting outflow to expand and quickly become relativistic (Paczynski, 1986). These relativistic expanding shells – with different Lorentz factors – in general collide, resulting in Gamma-ray flares and potentially rich temporal structure. Our extracted timescales ($\Delta t_{\rm min}$) should provide a diagnostic on the central engine power and its evolution. The size of the central engine is limited to $R < c\,\Delta t_{\rm min}$, which for the smallest minimum variability timescale derived above (~ 10 ms; see also, Nakar &

Piran, 2002) is $R < 3 \times 10^3$ km. Typical $\Delta t_{\rm min}$ values from above lead to $R < 2 \times 10^5$ km. For the first time, due to a large sample of GRBs with measured redshift, we are able to perform these calculations in the source frame.

In the source frame, we are not able to confirm that the minimum variability timescale of short-duration GRBs is substantially shorter than that of long-duration. Hence, we cannot demonstrate that short-duration GRBs have a more condensed central engine of the former (see Bhat, 2013).

We can derive additional constraints on the GRB emission region, following the discussion in Walker et al. (2000).

In the "external shock" picture, shells of material produced by the GRB impact material in the external medium. The physical dimension of clouds and their patchiness – in the direction perpendicular to the expansion of the shell – is constrained by $\Delta t_{\rm min}$. If we assume a single shell expanding at very close to light speed, the arrival time for photons from the shell will be calculated as the summation of travel time of the shell to the radius of impact and the travel time of the Gamma-rays to Earth. Photons from off-axis regions of the relativistic expanding shell experience a purely geometrical delay compared with photons from on-axis regions (Piran, 2004) reaching the observer. The observed delay depends only on the radius of the shell R at the time of impact with a cloud in the external medium and the angular radius of the Gamma-ray emission region as subtended from the burst site ($\Delta\Theta$).

Walker et al. (2000) report millisecond variability superposed on pulses of significantly longer rise-times. High cloud patchiness can potentially explain this modulation. We would have $\Delta\Theta < \Delta t_{\rm min}/(2\Gamma\, T_{\rm rise}) < 0.0002$, where Γ is the bulk Lorentz factor. Only $\sim 5 \times 10^{-3}$ of the emitting shell is active at a given time (also, Fenimore et al., 1999). However, for the bursts in our sample, with typical minimum variability timescale $\sim 0.1\, s$, $T_{\rm rise} > 1\, s$, and assuming $\Gamma > 100$, we find that $\Delta\Theta < 5 \times 10^{-3}$

radians which is comparable with the typical surface filling factor (Fenimore et al., 1999).

In terms of the external shock scenario, the extracted $\Delta t_{\rm min}$ can circumscribe the size scale of the impacted cloud along the line of sight. For a thin shell, the Gamma-ray radiation will start when the relativistic shell hits the inner boundary of the cloud with the peak flux produced as the shell reaches the densest region or center of the cloud. The size scale of the impacted cloud is limited by $2\Gamma^2 c\,\Delta t_{\rm min}$ since the shock is moving near light speed (Fenimore et al., 1996). For the smallest $\Delta t_{\rm min}$ found ~ 10 ms, and assuming $\Gamma < 1000$, the cloud size must be smaller than 40 AU.

In the "internal shock" scenario (e.g., Rees & Meszaros, 1994), the relativistic expanding outflow released from a central engine is assumed to be variable, consisting of multiple shells of differing Γ. These shells propagate and expand adiabatically until a faster shell collides with a slower one, resulting in a measurable rise time. This rise time to an outside observer would appear as: $\Delta t_{r1} \approx \Delta R/2c\Gamma_1^2$, where ΔR and Γ_1 are the thickness and resulting Lorentz factor of the merged shell (e.g., Kocevski et al., 2007). Assuming the same scenario but for two other shells yields $\Delta t_{r2} \approx \Delta R/2c\Gamma_2^2$. Writing $\Delta\Gamma = \Gamma_1 - \Gamma_2$, we have $\Delta\Gamma/\Gamma \approx 1/2\,(\Delta t_{\rm min}/T_{\rm rise})$. In Walker et al. (2000), the ratios $\Delta t_{\rm min}/T_{\rm rise}$ were argued to be small, implying a narrow dispersion in Γ. We, however, find $\Delta t_{\rm min} \sim T_{\rm rise}$, suggesting instead a broad range of possible Lorentz factors.

Finally, we find evidence that our minimum timescales correlate with redshift, possibly providing indication of cosmological time-dilation. However, the measurement threshold also appears to correlate strongly with redshift. This indicates that threshold effects likely dominate the apparent correlation and that the correlation may not be real. It is possible that additional features present in the Haar scaleogram (slopes, breaks on longer timescales) – which richly describe the full GRB light curve and

not just the minimum timescale – may yield correlations with intrinsic quantities like redshift. We will study this further in future work.

Chapter 3

THE ENERGY-DEPENDENCE OF GRB MINIMUM VARIABILITY TIMESCALES

V. Zach Golkhou, Nathaniel R. Butler, & Owen M. Littlejohns

3.1 Abstract

We constrain the minimum variability timescales for 938 GRBs observed by the *Fermi*/GBM instrument prior to July 11, 2012. The tightest constraints on progenitor radii derived from these timescales are obtained from light curves in the hardest energy channel. In the softer bands – or from measurements of the same GRBs in the hard X-rays from *Swift* – we show that variability timescales tend to be a factor 2–3 longer. Applying a survival analysis to account for detections and upper limits, we find median minimum timescale in the rest frame for long-duration and short-duration GRBs of 45 ms and 10 ms, respectively. Fewer than 10% of GRBs show evidence for variability on timescales below 2 ms. These shortest timescales require Lorentz factors $\gtrsim 400$ and imply typical emission radii $R \approx 1{\times}10^{14}$ cm for long-duration GRBs and $R \approx 3{\times}10^{13}$ cm for short-duration GRBs. We discuss implications for the GRB fireball model and investigate whether GRB minimum timescales evolve with cosmic time.

A version of this chapter has been published previously in *The Astrophysical Journal*, Volume 811, Issue 2, article id. 93, 11 pp. (2015).

3.2 Introduction

Gamma-Ray Bursts (GRBs) are the most luminous explosions in the Universe, originating at cosmological distances and releasing $\sim 10^{51}$ ergs over timescales of seconds to tens of seconds. The gargantuan energy release is accompanied by a very rapid and stochastic temporal variability in the gamma-ray emission. The *Swift* (Gehrels et al., 2004) and *Fermi* Space Telescopes (Meegan et al., 2009) have deepened immensely our understanding of these cosmological beacons (e.g., Gehrels & Razzaque, 2013).

The pulses observed in prompt GRB light curves often have a Fast Rising Exponential Decay (FRED) profile (Norris et al., 1996). The time profiles can have a broad morphological diversity in both the number of and duration of these pulses. In the external shock model for GRBs, shells of material produced by the GRB impact material in the circumburst medium (e.g., Rees & Meszaros, 1992). Unless the circumburst medium is highly-clumped (Fenimore et al., 1999), this process tends to produce a smooth GRB light curve in contrast to the rapid temporal variability observed in many GRBs. Under the internal shock mechanism (Rees & Meszaros, 1994), a variable central engine emits a relativistic outflow comprised of multiple shells with different Lorentz factors, Γ. As faster shells collide with slower shells, kinetic energy is converted to radiation, and multiple shell collisions can lead to a complex GRB light curve (e.g., Rees & Meszaros, 1994).

Traditional duration measures such as T_{90} (Kouveliotou et al., 1993), which describes the time during which the central 90% of prompt gamma-ray counts are received, only describe bulk emission properties of the burst. Such a duration does not capture information concerning individual collisions between shells. Instead, detailed temporal analyses that probe variability over a function of timescales are required.

A variety of time series analyses have previously been used to explore the rich properties of prompt GRB light curves. These include structure function (SF) analyses (Trevese et al., 1994; Hook et al., 1994; Cristiani et al., 1996; Aretxaga et al., 1997), autocorrelation function (ACF) analyses (Link et al., 1993; Fenimore et al., 1995; in 't Zand & Fenimore, 1996; Borgonovo, 2004; Chatterjee et al., 2012), and Fourier power spectral density (PSD) analyses (Beloborodov et al., 2000; Chang, 2001; Abdo et al., 2010; Guidorzi et al., 2012; Dichiara et al., 2013). Compared to power-spectral analyses, the SF approach is less dependent on the time sampling (Paltani, 1999). In, Golkhou & Butler (2014), Paper I hereafter, we developed and applied a fast (i.e. linear) and robust SF estimator, based on non-decimated Haar wavelets, to measure the minimum variability timescale, $\Delta t_{\rm min}$, of *Swift* GRBs. We used the first-order SF of light curves as measured by the *Swift* Burst Alert Telescope (BAT; Barthelmy et al. 2005b) to infer the shortest timescale at which a GRB exhibit *uncorrelated temporal variability*.

One limitation of the work presented in Paper I is that we only consider the variability timescale using light curves measured over the narrow 15–350 keV energy band of *Swift*/BAT. A fixed and narrow energy band in the observer frame would probe different regions of the intrinsic GRB spectra, because GRBs are known to occur over a wide range of redshifts (see e.g. Salvaterra et al. 2009; Tanvir et al. 2009; Cucchiara et al. 2011; Jakobsson et al. 2012). Previous studies have shown that GRB pulses vary in duration as a function of energy, with harder energy channels having a lower observed duration (Fenimore et al., 1995; Norris et al., 1996). Working at higher energies – where pulses are narrower – also has the potential to provide tighter limits on variability timescales.

We wish to use the broad *Fermi* Gamma-ray Burst Monitor (GBM;Meegan et al. 2009) energy coverage to overcome this limitation and to effectively standardize a

measure of the minimum variability timescale by studying the energy evolution and/or evaluating the minimum timescale in a fixed rest frame bandpass. Broad energy coverage can potentially also allow us to disentangle the role the ejecta velocity plays in relating radius to minimum timescale and to understand how minimum timescales measured for different instruments should be compared (see e.g., Sonbas et al., 2015). Also, it is important to note that the GBM provides very fine time resolution (2μs) event mode data for the full GRB and not just the first 1–2 s as was the case for *BATSE* (e.g., Walker et al., 2000).

In the discussion below, we begin with a brief application and summary of the method outlined in detail in Paper I. We then investigate how $\Delta t_{\rm min}$ depends on energy for a large sample of *Fermi*/GBM GRBs (Section 3.4.1). We compare $\Delta t_{\rm min}$ estimates from *Swift* and *Fermi* for bursts detected in common to demonstrate stability and accuracy of error estimates (Section 3.4.2). We then use spectral hardness to standardize the $\Delta t_{\rm min}$ estimate (Section 3.4.4) and conclude by deriving constraints on the sample Lorentz factors and emission radii (Section 3.4.5) and by investigating potential evolution of $\Delta t_{\rm min}$ with cosmic time (Section 3.4.6).

3.3 Data

We consider 949 GRBs published in the second *Fermi*/GBM GRB catalog (von Kienlin et al., 2014), spanning the first four years of the *Fermi* mission (between 2008 July 14$^{\rm th}$ and 2012 July 11$^{\rm th}$, inclusive). Event lists for 942 of these bursts were downloaded from the online *Fermi*/GBM burst catalog [1] .

We analyze the *Fermi*/GBM Time-Tagged Event (TTE) data for each of the 12 sodium iodide scintillators. We only consider those detectors in which each GRB was brightest, as listed in column 2 of Table 7 in von Kienlin et al. (2014). Typically,

[1] `http://heasarc.gsfc.nasa.gov/W3Browse/fermi/fermigbrst.html`

this entails using event lists for three detectors for each GRB. Following MacLachlan et al. (2013), we extract 200 μs binned light curves in the full (8 keV – 1 MeV) energy range. We also extract light curves in four energy channels of an equal logarithmic width (8–26, 26–89, 89–299 and 299–1000 keV). These channels are referred to as channels 1, 2, 3, and 4 below.

To remove background counts from the *Fermi*/GBM we employ a two-pass procedure. Using the estimates of T_{90} from Table 7 of von Kienlin et al. (2014), we bin each light curve at a resolution of $T_{90}/100$ and fit a linear background model. The background is initially determined considering two regions of each light curve, both T_{90} in length, occurring immediately before and after the identified period of burst emission. Using the background subtracted light curve, we then estimated T_{100} by accumulating a further 5% of the T_{90} interval counts outward from both the beginning and end of T_{90}. The second pass at fitting a linear background is then conducted, masking out all bins included in the total T_{100} region. This second background fit is then scaled to subtract the predicted background counts in the fine-time-resolution light curve. Our analysis – which identifies variations on timescales short compared to the overall burst durations – does not require the fitting of background models more complex than linear.

We analyze the background-subtracted burst counts in the full T_{100} region following the procedure outlined in Paper I. One change is made to the algorithm to optimize for the detection of signal variations on short timescales: instead of rebinning the 200 μs light curve to a fixed S/N per bin, we weight the unbinned light curve by the denoised (following, Kolaczyk, 1997) signal. This zeros-out portions of the light curve containing no signal and permits use of the full T_{100} region without adversely affecting our ability to identify variations on much shorter timescales.

For 109 bursts in the second *Fermi*/GBM GRB catalog which also have *Swift* high-

energy prompt coverage, the *Swift*/BAT data were obtained from the *Swift* Archive [2] . Using calibration files from the 2008-12-17 BAT data release, we construct 100 μs light curves, in the full 15–350 keV BAT energy range. We use the standard *Swift* software tools: BATECONVERT, BATMASKWTEVT and BATBINEVT. Further details regarding the extraction of the *Swift*/BAT light curves can be found in Paper I.

3.4 Discussion and Results

In Paper I, we demonstrate the power of a novel, wavelet-based method – the Haar-Structure Function (denoted $\sigma_{X,\Delta t}$) – to robustly extract the shortest variability timescale of GRBs detected by *Swift*/BAT. In this work, we implement our technique on GRBs detected by the *Fermi*/GBM instrument, which is sensitive to a much broader range of energies. We obtain constraints on the minimum variability timescales for 938 of 949 GRBs reported in the second *Fermi*/GBM GRB catalog (von Kienlin et al., 2014). Of these, we are able to confirm the presence of a linear rise phase (see Section 3.4.1) in the Haar-Structure Function on short timescales for 528 GRBs. We quote upper-limit values for the remainder. Most (421) of the bursts in this sub-sample are long-duration ($T_{90} > 3$ s) GRBs. In this sub-sample, 24 GRBs have measured redshift, z. The temporal specifications of all 938 GRBs discussed here are determined using fully-automatic software and are presented in Appendix B (Table B.1).

3.4.1 Studying the Energy-Dependence of $\Delta t_{\rm min}$

It has been recognized for decades (e.g., Fenimore et al., 1995; Norris et al., 1996) that a defining feature of GRB emission is a narrowing of pulse profiles observed in increasingly higher energy bands. As a result, durations measured by different instru-

[2] `ftp://legacy.gsfc.nasa.gov/swift/data`

ments can be different (e.g., Virgili et al., 2012). Durations also appear to depend on redshift, perhaps as a result of the dependence on bandpass: recently, Zhang et al. (2013) have found evidence that T_{90} duration – when z is known and used to evaluate the GRB duration in a fixed rest frame energy band – may correlate linearly with redshift as is expected from cosmological time dilation. This result is quite sensitive to the particular choice of binning in the analysis (see Littlejohns & Butler, 2014). Here, we seek to understand whether our measure of shortest duration in GRBs is also highly-dependent upon the observed energy band, and on the instrument detecting the GRB, in particular.

The prompt GBM Gamma-ray light curve for GRB 110721A, split in 4 energy bands, and our derived $\sigma_{X,\Delta t}$ curve for each channel are shown in Figure 3.1. There is a clear evolution in $\Delta t_{\rm min}$ with bandpass, decreasing from the softest to the hardest energy band. To guide the eye, several lines of constant $\sigma_{X,\Delta t} \propto \Delta t$ are also plotted. The expected Poisson level (i.e., measurement error) has been subtracted away, leaving only the flux variation expected for each channel.

Briefly, we review here how our $\Delta t_{\rm min}$ is identified. A general feature observed in our GRB scaleograms, provided there is sufficient signal-to-noise ratio (S/N), is a linear rise phase relative to the Poisson noise. Poisson noise sets a floor on the shortest measurable timescale (denoted $\Delta t_{\rm S/N}$, with $\Delta t_{\rm S/N} \approx 0.1$ s for channels 2 and 3 in Figure 3.1, bottom). Unlike previous studies by other authors (Bhat, 2013; MacLachlan et al., 2013; Walker et al., 2000), we do not implicate the shortest *observable* timescale as $\Delta t_{\rm min}$. Instead, we recognize that pulses can be temporally smooth on short timescales. The departure from this smoothness creates a break in the scaleogram, and this in turn defines our timescale $\Delta t_{\rm min}$ for temporally un-smooth variability. Naturally, this timescale also corresponds to a length-scale, which must be reconciled with GRB progenitor models (Section 3.4.5).

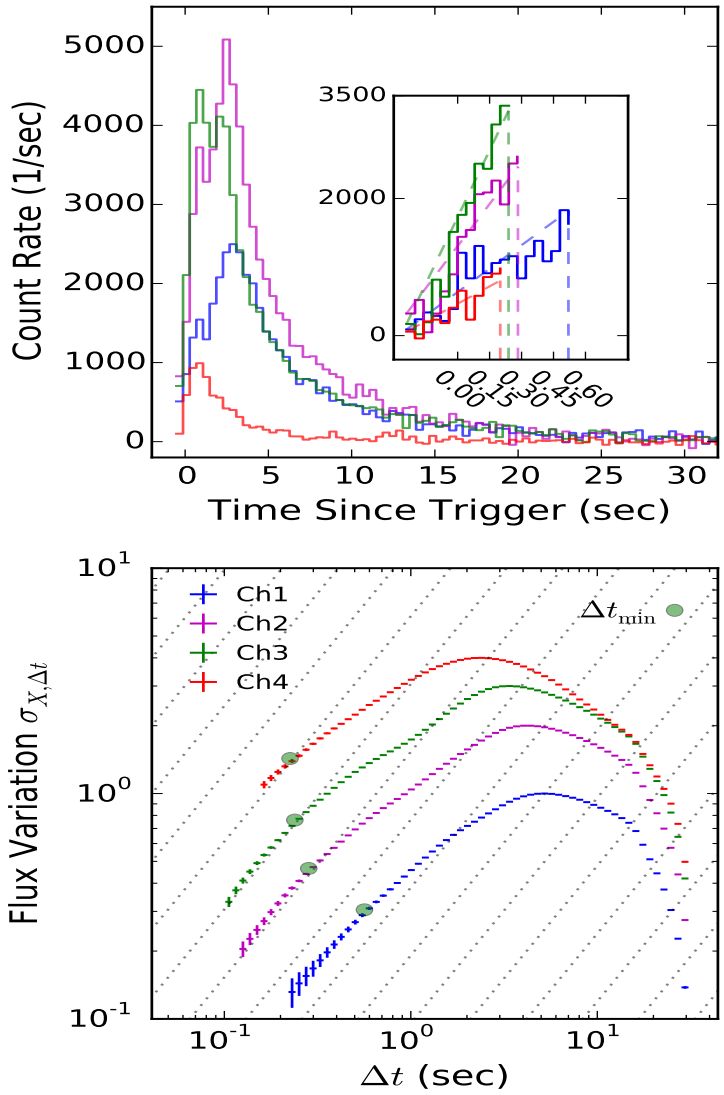

Figure 3.1: Top panel: *Fermi*/GBM light curves of the GRB 110721A split in 4 different energy bands. Bottom panel: The Haar wavelet scaleogram $\sigma_{X,\Delta t}$, rescaled for plotting purposes, corresponding to each channel versus timescale Δt for GRB 110721A. We derive minimum timescales (marked with green circles) – 0.56 ± 0.09 s, 0.28 ± 0.05 s, 0.24 ± 0.04 s, and 0.22 ± 0.04 s for the channels 1, 2, 3, and 4, respectively – which increase in lower energy bands. In the top panel, the inset displays the the pulse rise with finer time binning, with dashed lines dropped onto the x-axis to demark the derived $\Delta t_{\rm min}$ values for each channel.

We now focus on the softest energy band of GRB 110721A, denoting the light curve as $X(t)$. Although there is excess signal present on timescales as short as $\Delta t = 0.4$ s (Figure 3.1 - channel 1), these timescales correspond to a region of the plot where the first order SF rises linearly timescale, $\sigma_{X,\Delta t} \equiv \langle |X(t+\Delta t) - X(t)|^2 \rangle_t^{1/2} \propto \Delta t$. (Here, $\langle . \rangle_t$ denotes an average over time t.) We interpret this linear rise as an indication that the GRB exhibits temporally-smooth variations on these timescales (i.e., $X(t+\Delta t) \approx X(t) + X'(t)\Delta t$), while changing to exhibit temporally-unsmooth variations on longer timescales. The $\sigma_{X,\Delta t}$ points deviate significantly from the $\sigma_{X,\Delta t} \propto \Delta t$ curve at $\Delta t_{\rm min} = 0.56 \pm 0.09$ s. This is the timescale of interest, describing the minimum variability time for uncorrelated variations in the GRB. This timescale is associated with the initial rise of the GRB in this channel, as can be seen from the Figure 3.1 inset.

The value for $\Delta t_{\rm min}$ is found by fitting a broken powerlaw to the $\sigma_{X,\Delta t}$ data points below the peak, assuming that $\sigma_{X,\Delta t}$ initially rises linearly with Δt (see also, Paper I) until flattening at $\Delta t_{\rm min}$. Uncertainties quoted here and below for $\Delta t_{\rm min}$ are determined by direct propagation of errors and correspond to 1σ confidence. If the lower-limit on $\Delta t_{\rm min}$ falls below the lowest measurable timescale (i.e., $\Delta t_{\rm S/N}$), we report only the 1σ upper limit for $\Delta t_{\rm min}$.

For this particular burst, $\Delta t_{\rm min}$ evolves from the hardest energy band to the softest energy band as one might expect: the softest energy band of a burst has longer minimum variability timescale compared to the hardest energy band of that burst. On timescales longer than $\Delta t_{\rm min}$, $\sigma_{X,\Delta t}$ is flatter than $\sigma_{X,\Delta t} \propto \Delta t$, indicating the presence of temporally-variable structure on these timescales. On a timescale of about 6 s, $\sigma_{X,\Delta t}$ begins turning over as we reach the timescales (tens of seconds) describing the overall emission envelope. We are not concerned here with those longer timescale structures, although we do note that $\sigma_{X,\Delta t}$ provides a rich, aggregate description of

this temporal activity.

In order to characterize and measure the average $\Delta t_{\rm min}$ for the *Fermi* sample as a function of spectral energy band, we utilize the Kaplan-Meier (KM; Kaplan & Meier 1958, see also Feigelson & Nelson 1985) survival analysis. This is necessary because many bursts only permit upper limit measurements of $\Delta t_{\rm min}$. Figure 3.2 summarizes how the minimum variability timescale varies with energy band. The KM cumulative plots – including the shaded 1σ error region – for each bandpass and the full (all channels combined) *Fermi*/GBM energy range are shown in the top panel. The sample $50^{\rm th}$ percentiles (i.e., medians) and the lowest $10^{\rm th}$ percentiles (shown with the dotted-lines in the top panel of Figure 3.2) are plotted in the bottom panel.

Table 3.1 summarizes the corresponding values. Since the KM cumulative estimation curve of channel 4 does not cross the 10% limit line, there is no value reported in Table 3.1 for this case.

Table 3.1: The Kaplan-Meier Median and $10^{\rm th}$ Percentile Timescales for Long-duration GRBs.

Band (keV)	$\Delta t_{\rm min}^{50\%}$ (msec)	$\Delta t_{\rm min}^{10\%}$ (msec)	Number Detected	Number Upper Limit
8–26	540 ± 67	25 ± 8	395	307
26–89	260 ± 26	4^{+4}_{-2}	431	319
89–299	150^{+23}_{-18}	2^{+2}_{-1}	413	335
299–1000	72^{+24}_{-21}	...	156	278
8–1000	130 ± 18	2^{+5}_{-1}	421	334

The reported values clearly show the tendency of increasing $\Delta t_{\rm min}$ with decreasing energy band. Because we tend to find a clear association between $\Delta t_{\rm min}$ and the rise time of the shortest GRB pulse (also, Paper I), this confirms that GRB pulse structures are narrower at higher energy and that understanding this effect is important

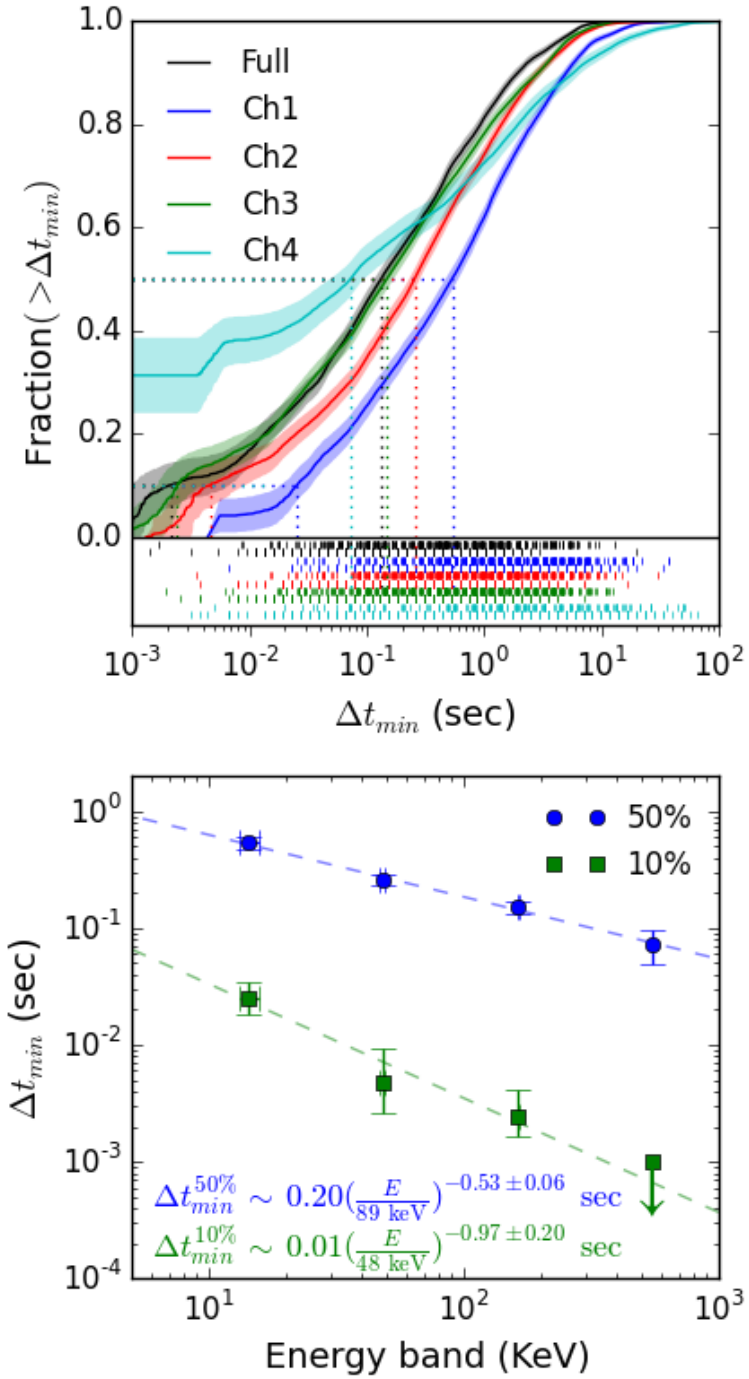

Figure 3.2: Top panel: The KM cumulative estimation curve of all long-duration GRBs in *Fermi* sample for each energy band including shaded 1σ region around each bandpass. The dotted lines show the 50^{th} percentile and the lowest 10^{th} percentile for each bandpass. The location of the of measured Δt_{min} values (top tics) and upper-limits (bottom tics of the same color) are shown in the sub-panel. Bottom panel: The KM median estimation of Δt_{min} versus energy band and the lowest 10^{th} percentile of Δt_{min} values versus energy band, including error bars. Note: since the KM cumulative estimation curve of channel 4 does not cross the 10% line, we plot an upper-limit.

for understanding any implications drawn from $\Delta t_{\rm min}$.

The KM median values of $\Delta t_{\rm min}$ versus energy band are well-fitted by a line $\Delta t_{min}^{50\%} = 0.20(E/89\,{\rm keV})^{-0.53\pm0.06}$ s (with reduced $\chi^2 = 0.64$). The derived power-law index here is in agreement with the power-law index of the relationship found for the average pulse width of peaks as a function of energy (Fenimore et al. 1995 and also from Norris et al. 1996). The KM estimation of the lowest 10% of $\Delta t_{\rm min}$ values versus the energy band can also be fitted by a power-law, with a steeper index, $\Delta t_{min}^{10\%} = 0.01(E/48\,{\rm keV})^{-0.97\pm0.20}$ s (with reduced $\chi^2 = 1.4$). The steeper index indicates that rare GRBs, which tend to be bright and spectrally hard GRBs, allow for tighter constraints on minimum timescales. This shifts the typical minimum timescales to smaller values as compared to those found for the bulk of the population. We explore the minimum timescale dependence on S/N and spectral hardness below for individual GRBs.

3.4.2 Consistency in the Joint Fermi/GBM and Swift/BAT Sample

In Paper I, we studied the robustness of our minimum timescales extracted for simulated bursts as the S/N is varied. It was demonstrated that the shapes of the $\sigma_{X,\Delta t}$ curves are highly stable as the S/N is strongly decreased (factor of ten), but the determination of the true $\Delta t_{\rm min}$ can be challenging. This is because GRBs tend to show evidence for temporally-smooth variation between timescales of non-smooth variability (e.g., pulse rise times) – which become harder to measure as S/N is decreased – and the longer timescales associated with non-smooth variability (e.g., the full duration of the pulse). The sample of bursts detected jointly by both *Swift*/BAT and *Fermi*/GBM provides a rich dataset to study this behavior. In addition to allowing us to verify consistency in the $\Delta t_{\rm min}$ estimates for bursts with similar S/N values, we can also directly observe (in many cases) the reliability of $\Delta t_{\rm min}$ for different S/N

values.

Figure 3.3 captures the variety of scaleograms produced for bursts detected by both the *Swift*/BAT and *Fermi*/GBM instruments. Here we utilize the 15–350 keV energy range for both *Swift*/BAT and *Fermi*/GBM, and we align the light curves and extract counts over the same time intervals for each burst. Although the instruments do not have identical effective area curves in these ranges, choosing the same energy range should minimize differences due to energy band (discussed in more detail in Section 3.4.4 below).

In the case of GRB 110213A (left panels), *Fermi*/GBM captured the higher sensitivity burst light curve. Oppositely in the case of GRB 080916A (middle panels), *Swift*/BAT captured a higher S/N light curve. The S/N level can be gauged from the light curves and taken directly from the $\Delta t_{\mathrm{S/N}}$ values, with high S/N translating directly to lower $\Delta t_{\mathrm{S/N}}$. There are many bursts (e.g., GRB 120119A, right panels) in the joint *Fermi*/GBM and *Swift*/BAT sample which correspond to closely similar S/N values and for which the resulting scaleograms are almost identical. We note that minimum timescales based simply on $\Delta t_{\mathrm{S/N}}$ (e.g., Walker et al. 2000) directly track the noise floor level. This is also the case for t_{β}, calculated according to the prescription of MacLachlan et al. (2013). In the most extreme examples (i.e., GRBs 090519A and 101011A), the $\Delta t_{\mathrm{S/N}}$ values differ by approximately an order of magnitude, the t_{β} values differ by approximately a factor of five, while the Δt_{min} values are consistent (Appendix B). Our method distinguishes between the *minimum detectable* timescale and the true minimum timescale in a more robust (although not-perfect, as we discuss more below) fashion.

Figure 3.4 displays a scatter plot of Δt_{min} determined for *Swift*/BAT versus *Fermi*/GBM. A line fit through the data points (blue curve with shaded gray 90% confidence region) is consistent with the dotted-line representing equality. The best-

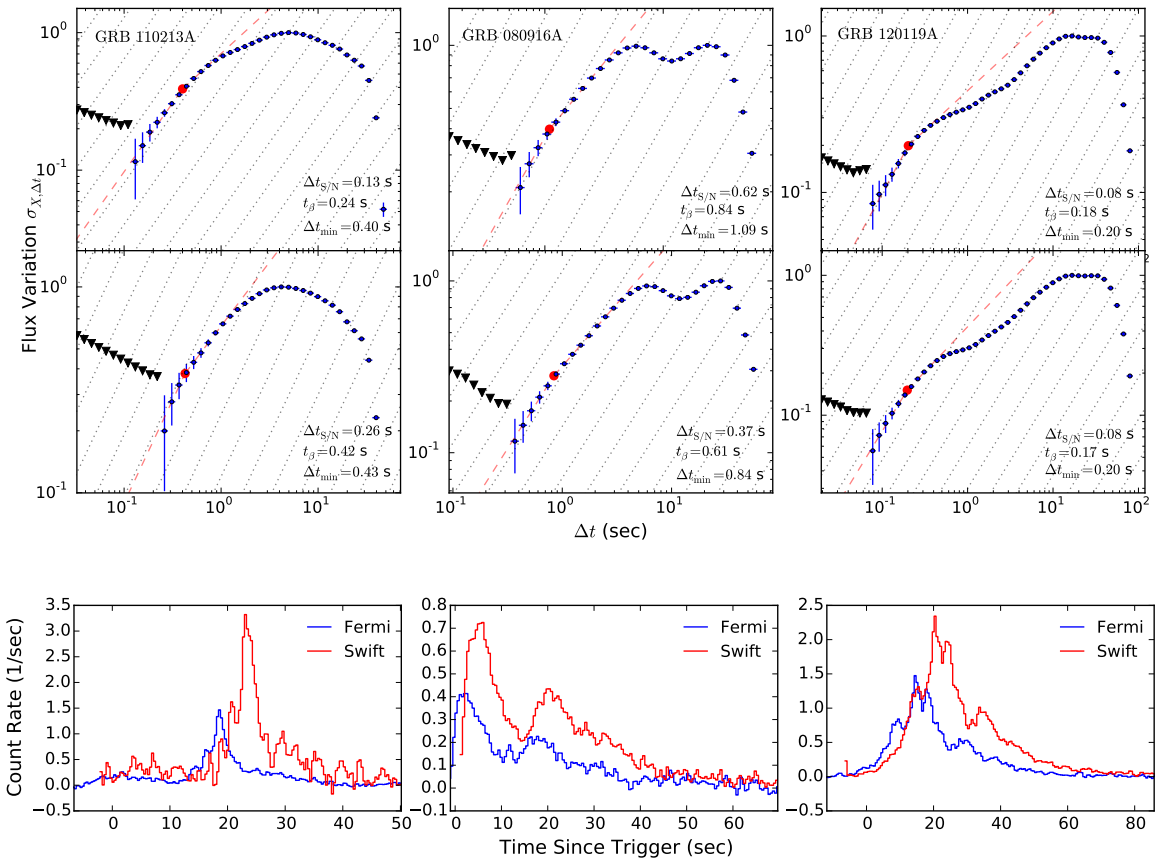

Figure 3.3: A gallery of Haar scaleograms, $\sigma_{X,\Delta t}$, representing a variety of possible structure functions calculated for *Fermi*/GBM and *Swift*/BAT (both: 15–350 keV) with different level of sensitivity for detection of various GRBs. The left, middle, and right panels correspond to GRB 110213A, GRB 080916A, and GRB 120119A, respectively. The first and second rows show the structure functions retrieved from the GRBs light curves detected by *Fermi*/GBM and *Swift*/BAT, respectively. The third row shows the light curves in the T_{100} duration region. In each of these, the red dashed-lines represent a passage from the temporally-smooth ($\sigma_{X,\Delta t} \propto \Delta t$) region to a flatter region and the red circle marks the extracted minimum variability timescale, $\Delta t_{\rm min}$, after which the light curves transition to a temporally-unsmooth behavior. Triangles denote 3σ upper limits.

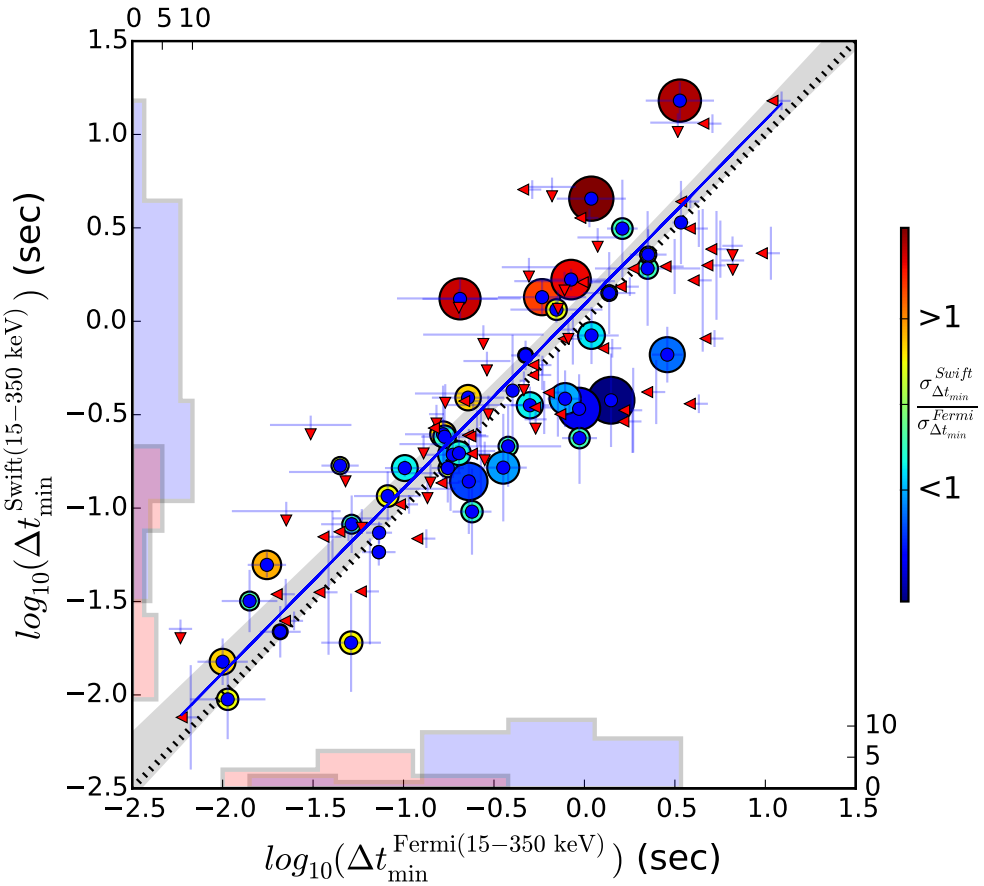

Figure 3.4: $\Delta t_{\rm min}$ for the sample of joint *Fermi*/GBM and *Swift*/BAT bursts. The red and blue histograms correspond to the short and long-duration GRBs, respectively. The arrows show the upper limit burst cases. The black dotted-line represents equality. The relative size of the circles is scaled with the absolute value of the log of the ratio of flux variation at the shortest observable variability timescale $\Delta t_{\rm S/N}$, providing a measure of whether each satellite samples the same (small circles) or very different (large circles) regions of the scaleogram at the inferred $\Delta t_{\rm min}$. The color bar can be used to identify which instrument generated the higher $\sigma_{X,\Delta t}$.

fit line has a normalization $= 1.13 \pm 0.13$ and a slope $= 0.99 \pm 0.02$. For this fit the reduced $\chi^2 = 2.86$ (for 42 degrees of freedom) and is dominated by a small number of outliers. The fraction of bursts not consistent with the fit, both below and above the line are: 12% and 15%, respectively. The close consistency of this line with the unit line demonstrates that our method is robust and that our error bars, calculated by direct error propagation, are likely to be accurate.

We do note, however, that the $\Delta t_{\rm min}$ values calculated for *Swift* versus *Fermi* do exhibit small, systematic differences. On average, bursts detected by *Swift* (in the same energy band) tend to have 13% longer $\Delta t_{\rm min}$ values as compared to *Fermi*. Histograms showing the spread in the overall populations are also drawn along the axes in Figure 3.4.

To study the origin of the outliers to the fit in Figure 3.4, we scale the relative size of the circles with the absolute value of the log of the ratio of flux variation at the shortest observable variability timescale $\Delta t_{\rm S/N}$. This is intended to provide an indication of whether each satellite sampled the same (small circles) or very different (large circles) regions of the scaleogram at the inferred $\Delta t_{\rm min}$. The color bar can be used to identify which instrument generated the higher $\sigma_{X,\Delta t}$.

In general, we find that once the $\log(\Delta t_{\rm S/N})$ ratios exceed 0.5 dex (corresponding to 0.5 dex in log(S/N) or roughly a factor 10 in flux) the more sensitive satellite tends to yield a lower measurement of $\Delta t_{\rm min}$. This is consistent with our findings from Paper I. Given that such variation is not known a-priori in this case (because the light curves are not based on a simulation), the tendency to detect lower $\Delta t_{\rm min}$ when possible suggests a fractal nature of the phenomenon. Care must be taken in interpreting GRB minimum timescales, because the phenomenology suggests these could always be limits on the true minimum timescales. However, we do note the important feature of the scaleograms: hidden (i.e., low S/N) minimum timescales will always correspond to smaller variations in the fractional flux levels. In this sense, a perfect accounting of the minimum timescales may not be necessary, because very short minimum timescales tend to represent fractionally tiny (or alternatively very rare) episodes in the GRB emission.

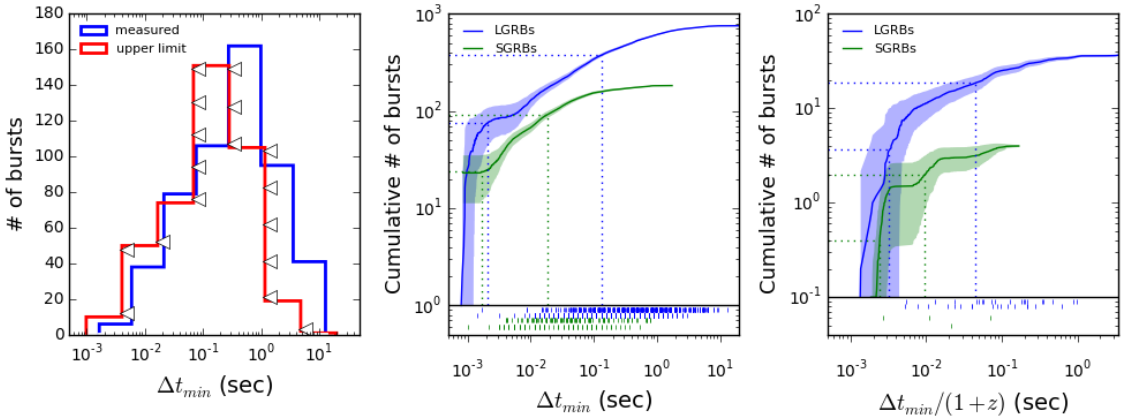

Figure 3.5: Left panel: the histograms of $\Delta t_{\rm min}$ with measurements (blue) and for GRBs allowing for upper limits only (red). Middle and right panels: the cumulative histograms of bursts in the observer and source frames, respectively. The KM estimation curve with 1σ error region around the curve is shown in these panels. The dotted lines correspond to the minimum timescale of the lowest 10% and 50% of bursts, shown for the short and long-duration GRBs, separately. Sub-panels show the locations of detections and upper-limits, as in Figure 3.2. For long-duration (short-duration) GRBs, we have 421 (107) measurements and 334 (76) upper limits in the observer frame and 24 (3) measurements and 18 (1) upper limits in the source frame.

3.4.3 Distribution of $\Delta t_{\rm min}$ Values for Fermi/GBM

Figure 3.5 (left) shows histograms for the *Fermi* GRBs permitting measurement of and also upper limits on $\Delta t_{\rm min}$. The two distributions have consistent mean values. The middle and right panels of Figure 3.5 show the KM cumulative histograms in the observer and source frames, respectively. The dotted-lines correspond to the minimum timescale of the lowest 10% and 50% (median) of short and long-duration bursts.

We find a median minimum timescale for long-duration (short-duration) GRBs in the observer frame of 134 ms (18 ms). In the source frame, we find a median minimum timescale for long-duration (short-duration) GRBs of 45 ms (10 ms). It is interesting that these numbers are a factor of 3–10 smaller than those we found for *Swift* in Paper I. The largest differences, in the case of short-duration GRBs, are

attributable to the increased number of well-detected short-duration GRBs by *Fermi*. As we discuss below (Section 3.4.4), $\Delta t_{\rm min}$ also appears to vary by a factor of ≈ 3 depending on the burst hardness. The *Fermi* sample is studied using the full energy range, and the sample appears to be spectrally harder than the *Swift* sample, overall.

We also report $\Delta t_{\rm min}$ of the most exotic GRBs in *Fermi* sample – the lowest $10^{\rm th}$ percentile of bursts with the shortest $\Delta t_{\rm min}$. The $10^{\rm th}$ percentile $\Delta t_{\rm min}$ values for long-duration (short-duration) GRBs in the observer frame found to be 2.2 ms (1.9 ms). In the source frame, we find 2.9 ms (2.4 ms). These numbers are consistent with the findings in Paper I that millisecond variability appears to be rare in GRBs.

From Figure 3.5, we find that the $\Delta t_{\rm min}$ distribution of long-duration GRBs is displaced from that of short-duration GRBs (16σ, t-test 17σ, log-rank test (Mantel, 1966)). The log-rank test includes the upper limits, unlike the t-test. This finding is consistent with the presented results in Paper I for *Swift*. This discrepancy is still present in the source frame (2.3σ, t-test and 3.4σ, log-rank test) unlike in Paper I where the distribution centers appeared to be consistent. The *Swift* small sample of short-duration GRBs with known-z is likely the main reason for the observed degeneracy. The significant observer frame discrepancy is likely driven by the fact that short-duration GRBs tend to be detected only at low-redshift, unlike long-duration GRBs which span a broad range of redshifts. Examining the dispersion in $\log(\Delta t_{\rm min})$ values, we see no strong evidence for dissimilar values for the long and short-duration samples ($< 1.3\sigma$, F-test). This finding is also fully consistent with the presented results in Paper I, where it was also found (using a sample of *Swift* GRBs) that the two histograms are quite broad and very similar in dispersion.

Figure 3.6 displays our minimum variability timescale, $\Delta t_{\rm min}$, versus the GRB duration, T_{90}. The short and long-duration GRBs are shown with diamond and circle symbols, respectively. In this plot the relative size of symbols is proportional to the

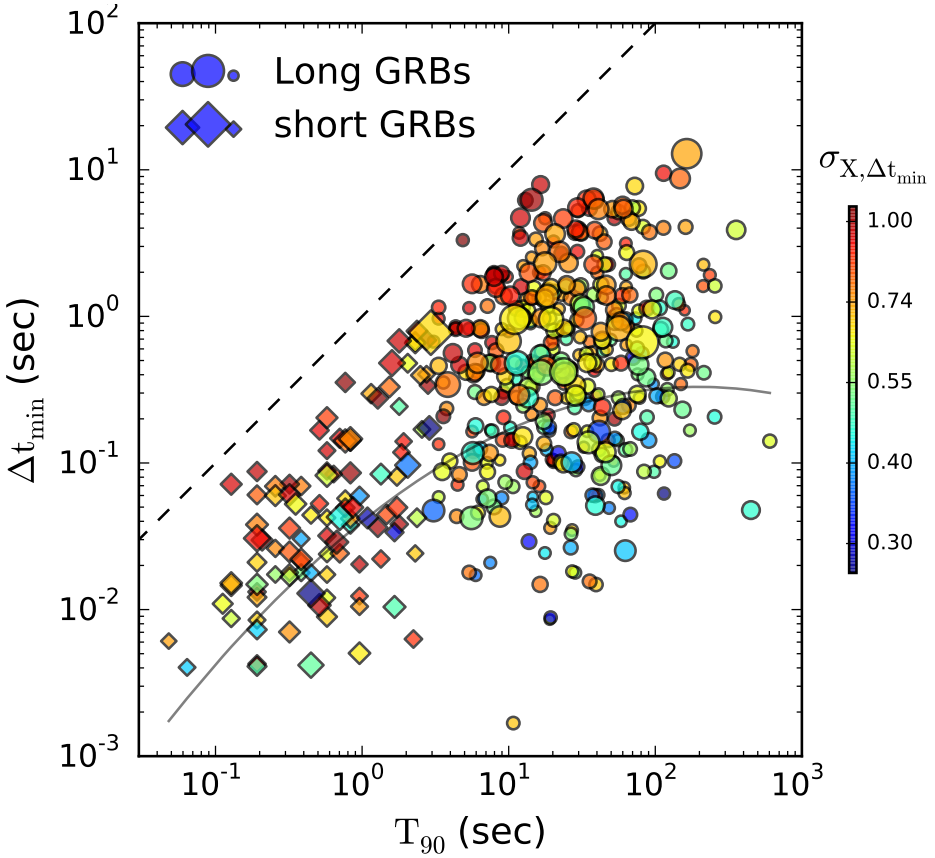

Figure 3.6: The GRB minimum timescale, $\Delta t_{\rm min}$, plotted versus the GRB T_{90} duration. Circles (diamonds) represent long-duration (short-duration) GRBs. The point colors represent the flux variation level ($\sigma_{X,\Delta t_{\rm min}}$) at $\Delta t_{\rm min}$. Also plotted as a curved line is the typical minimum observable timescale, $\Delta t_{\rm S/N}$, as a function of T_{90}. The symbol sizes are proportional to the ratio of $\Delta t_{\rm min}/\Delta t_{\rm S/N}$ for each GRB. The dashed line shows the equality line.

ratio between minimum variability and S/N timescale ($\Delta t_{\rm min}/\Delta t_{\rm S/N}$). As described above, $\Delta t_{\rm S/N}$ represents the first statistically significant timescale in the Haar wavelet scaleogram. The color of the points in Figure 3.6 corresponds to the flux variation level, $\sigma_{X,\Delta t}$, at $\Delta t_{\rm min}$. A curved black line is also plotted to show a typical value for the minimum observable time ($\Delta t_{\rm S/N}$) versus T_{90}. Values for T_{90} are taken from Table 7 of von Kienlin et al. (2014).

We first note from the colors in Figure 3.6 that GRBs with $\Delta t_{\rm min}$ close to T_{90} tend to have flux variations of order unity. These are bursts with simple, single-pulse

time profiles. As can be seen from the range of point sizes in Figure 3.6, most are not simply low S/N events where fine time structure cannot be observed. Also, we see that there are GRBs with both high and low S/N which have complex time-series ($\Delta t_{\rm min} \ll T_{90}$). Based on the point sizes, the short-timescale variation have higher ratio of $\Delta t_{\rm min}/\Delta t_{\rm S/N}$ for the short-duration GRBs of the similar $\Delta t_{\rm min}$ in comparison with that of the long-duration GRBs. Short-duration GRBs tend to have a higher $\sigma_{X,\Delta t}$ for the similar value of $\Delta t_{\rm min}$ compared with the long-duration GRBs.
These findings are all consistent with the similar results explained in Paper I; although we have a better ratio of short-duration GRBs to long-duration GRBs, here.

From a Kendall's τ-test (Kendall, 1938), we find only marginal evidence that $\Delta t_{\rm min}$ and T_{90} are correlated ($\tau_k = 0.33$, 11σ above zero). The $\Delta t_{\rm min}$ values in Figure 3.6 are bound from above by T_{90}, and they do not strongly correlate with T_{90} within the allowed region of the plot. In Paper I, we studied this relation for the entire sample of *Swift* GRBs and found only a marginal evidence that $\Delta t_{\rm min}$ and T_{90} are correlated ($\tau_k = 0.38$, 1.5σ). Even when we utilized the robust duration estimate $T_{\rm R45}$ (Reichart et al., 2001) in place of T_{90} no significant correlation was found ($\tau_k = 0.6$, 2.4σ). If we perform a truncated Kendall's τ test which only compares GRBs above one-another's threshold (Lloyd-Ronning & Petrosian, 2002), the correlation strength drops precipitously ($\tau_k = 0.06$, 1.4σ). We, therefore, believe there is no strong evidence supporting a real correlation between $\Delta t_{\rm min}$ and T_{90}.

3.4.4 The Dependence of $\Delta t_{\rm min}$ on Spectral Hardness

We investigate here how a burst's spectral hardness impacts its minimum variability timescale. We define the hardness ratio (HR) as the total counts in the hard composite channel (89–1000 keV, our combined channels 3 and 4) divided by the total counts in the soft composite channel (8–89 keV, our channels 1 and 2). We plot in

Figure 3.7 (top panel) the ratio of $\Delta t_{\rm min}$ for these two composite channels against the *HR* of the two corresponding bandpasses. GRBs with harder spectra tend to have a lower $\Delta t_{\rm min}$ ratio, by as much as a factor ≈ 3, for both short and long-duration GRBs. This relationship can be captured using a best-fitted linear model through all the bursts, shown in Figure 3.7 (top panel), with slope $= -0.34 \pm 0.04$.

The change in minimum timescale with hardness can be understood from the effects of relativistic beaming on emission instantaneously emitted in the rest frame by a moving shell (e.g., Fenimore et al., 1996; Ryde & Petrosian, 2002; Kocevski et al., 2003). If the material on the line-of-site has a Doppler factor $\Gamma(1-\beta)$, propagating with a speed $v = \beta c$ and Lorentz factor Γ, material above or below the line of site at angle θ will have a Doppler factor $\Gamma(1-\beta cos(\theta)) \approx (1+(\Gamma\theta)^2)/2\Gamma$, larger by a factor $1+(\Gamma\theta)^2$. The off-axis emission will also arrive later, at a time $t-t_e = R/c(1-\cos(\theta))$, where R is the emission radius, after the start of the emission at t_e. If we assume $R = 2\Gamma^2 ct_e$, then the Doppler factor increases in time, in the observer frame, as t/t_e. As a result, the photon flux observed at fixed energy E will decrease as higher and higher rest-frame-energy photons reach the bandpass, as $(t/t_e)^{\alpha-2}$. Here, α is the photon index and the power of 2 arises from relativistic beaming.

Thus, we expect that impulsive releases of energy in the rest frame will be smoothed over – in a fashion that is stronger at low energy ($\alpha \approx -1$) as compared to high energy (above $E_{\rm peak}$, $\alpha \lesssim -2$) – as viewed in the observer frame. The degree of smoothing expected above $E_{\rm peak}$ is a factor 2–3 less than the smoothing expected at observer frame energies below $E_{\rm peak}$. This effect naturally explains the decreasing minimum timescale we observe with increasing spectral bandpass, and it suggests that the tightest constraints on minimum timescale should be obtained from the highest available instrument bandpass. It should also be sufficient to confirm that $E_{\rm pk}$ is below, or perhaps within, a given bandpass.

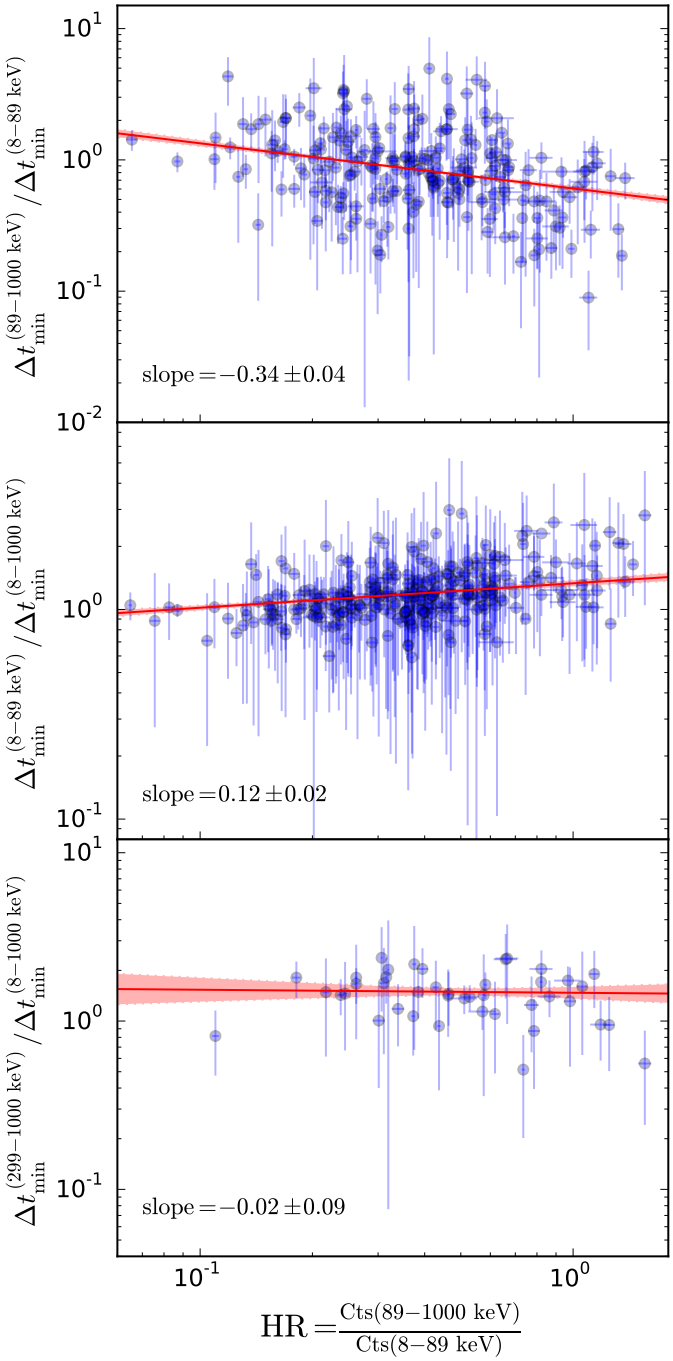

Figure 3.7: Top panel: The ratio of minimum variability timescale for channels $3+4$ and channels $1+2$, plotted against hardness ratio for the corresponding composite channels. Middle and bottom panels: The ratio of $\Delta t_{\rm min}$ for channels $1+2$ and channel 4 over full energy band, separately plotted against hardness ratio. The best fitted linear model through the bursts including shaded 1σ error region is also shown in each panel.

Figure 3.7 (middle panel) shows the ratio of $\Delta t_{\rm min}$ for the soft composite channel over the full energy band against the *HR*. This plot shows how $\Delta t_{\rm min}$ is approximately the same in each bandpass until the hardness ratio goes beyond roughly its median value. The bursts in this plot well-fitted by a line with slope $= 0.12 \pm 0.02$.

The ratio of $\Delta t_{\rm min}$ for the hardest channel (#4) over the full energy band against the *HR* is shown in Figure 3.7 (bottom panel). Here, the best-fit line (slope $= -0.02 \pm 0.09$) is consistent with being flat: the minimum timescales appear to be independent of this hardness ratio for all but perhaps the hardest handful of *Fermi* GRBs. We conclude that utilizing the full *Fermi*/GBM bandpass – which yields $\Delta t_{\rm min}$ constraints consistent with those derived from the soft energy channel for soft GRBs and also $\Delta t_{\rm min}$ constraints consistent with those derived from the hard energy channel for hard GRBs – is an acceptable procedure for determining the tightest constraints on $\Delta t_{\rm min}$.

3.4.5 Constraints on the Size of the Central Engine

The minimum timescale provides an upper limit on the size of the GRB emission region, in turn providing hints on the nature of the GRB progenitor and potentially shedding light on the nature of emission mechanism. In Paper I, we summarized how an association of a minimum timescale with a physical size is not unique, because the observed timescales depend strongly also on the emitting surface velocity.

The minimum Lorentz factor Γ can be estimated from the compactness argument (Lithwick & Sari, 2001). If we assume a spectrum with photon index $\alpha = -2$ (see Ackermann et al. 2013, Figure 25) – typical for GRB spectra above the pair-production limit and also appropriate for the range of energies which dominate the luminosity

(near the νF_ν spectral peak) – we find

$$\Gamma \gtrsim 110 \left(\frac{L}{10^{51}\,\mathrm{erg/s}} \frac{1+z}{\Delta t_{\mathrm{min}}/0.1\,\mathrm{sec}} \right)^{1/5}, \tag{3.1}$$

where L is the gamma-ray luminosity. If we regard Δt_{min} as corresponding to the bolometric emission, it is most natural to use the full *Fermi*/GBM bandpass for its estimation rather than a fixed rest frame bandpass. It could be argued that corrections should also be made to account for spectral hardness, based perhaps on the assumption that GRBs have a single, fixed rest frame hardness – an unlikely possibility – modulated only by Lorentz factor. However, based on the analysis in Section 3.4.4 above, any corrections would be small.

Utilizing our Δt_{min} estimates and limits for the full *Fermi*/GBM bandpass, we find that 50% of *Fermi* GRBs must have $\Gamma > 190$. In the case of the most energetic events, 10% of *Fermi* GRBs require $\Gamma > 410$. To calculate these fractions for short-duration bursts without measured redshift, we follow D'Avanzo et al. (2014) in assigning an average $z = 0.85$. For long-duration GRBs lacking redshift, we assign the average $z = 2.18$.

Similarly, for some maximally allowed Γ_{max}, compactness limits the emission radius to be greater than

$$R_{\mathrm{min}} \simeq 2.8{\times}10^{10} \frac{L}{10^{51}\,\mathrm{erg/s}} \left(\frac{\Gamma_{\mathrm{max}}}{1200} \right)^{-3} \mathrm{cm}. \tag{3.2}$$

This minimum bound on the radius can be compared to the maximum bound on the radius established by the temporal variability:

$$\begin{aligned} R_{\mathrm{max}} &= c \frac{\Delta t_{\mathrm{min}}}{1+z} \Gamma_{\mathrm{max}}^2, \\ &\simeq 4.4{\times}10^{15} \frac{\Delta t_{\mathrm{min}}/0.1\,\mathrm{sec}}{1+z} \left(\frac{\Gamma_{\mathrm{max}}}{1200} \right)^2 \mathrm{cm}. \end{aligned} \tag{3.3}$$

Here, we conservatively take $\Gamma_{\mathrm{max}} \sim 1200$ from Racusin et al. (2011).

If emission were to occur at the minimum allowable radius, $R_{\rm min}$, it would correspond to variability timescales as short as $\Delta t = R_{\rm min}/(2c\Gamma^2_{\rm max}) \lessapprox 1\mu$s. Because such timescales are not observed, a more realistic bound on the minimum emission radius is $R_c = 2c\Gamma^2_{\rm min}\Delta t_{\rm min}/(1+z)$, or

$$R_c \simeq 7.3{\times}10^{13} \left(\frac{L}{10^{51}\,{\rm erg/s}}\right)^{2/5} \left(\frac{\Delta t_{\rm min}/0.1\,{\rm sec}}{1+z}\right)^{3/5} {\rm cm}. \quad (3.4)$$

Figure 3.8 shows the emission radius, R_c, for all the bursts with measured $\Delta t_{\rm min}$ in *Fermi*/GBM sample versus rest-frame T_{90}. The shaded region shows the interval between the $R_{\rm min}$ and $R_{\rm max}$. The interpretation of R_c as a characteristic minimum radius for the emission is motivated further in Section 3.5.

The short-duration GRBs have a KM mean $R_c = 3.3 \times 10^{13}$ cm. This is about four times smaller than the KM mean $R_c = 1.3 \times 10^{14}$ cm for long-duration GRBs. While this represents a statistically significant separation (18σ, t-test), it is substantially less than the factor of approximately twenty separation between the mean T_{90} durations (Figure 3.8, also Kouveliotou et al., 1993). In contrast to the findings of Barnacka & Loeb (2014) – where the emission radius was argued to simply scale with the T_{90} duration – we find a broader overlap in the populations.

3.4.6 Evolution of $\Delta t_{\rm min}$ with z

Because GRBs are present over a very broad redshift range, the signature of time-dilation – and perhaps of any evolution in GRB time-structure with redshift – should be present in GRB time-series. Finding the signature of time-dilation in GRBs has remained elusive (Norris et al. 1994; Kocevski & Petrosian 2013, but see, e.g., Zhang et al. 2013). In our previous attempt described in Paper I, we utilized *Swift* GRBs and demonstrated a correlation between $\Delta t_{\rm min}$ and redshift, marginally stronger than expected simply from time-dilation. We discussed how this excess correlation strength

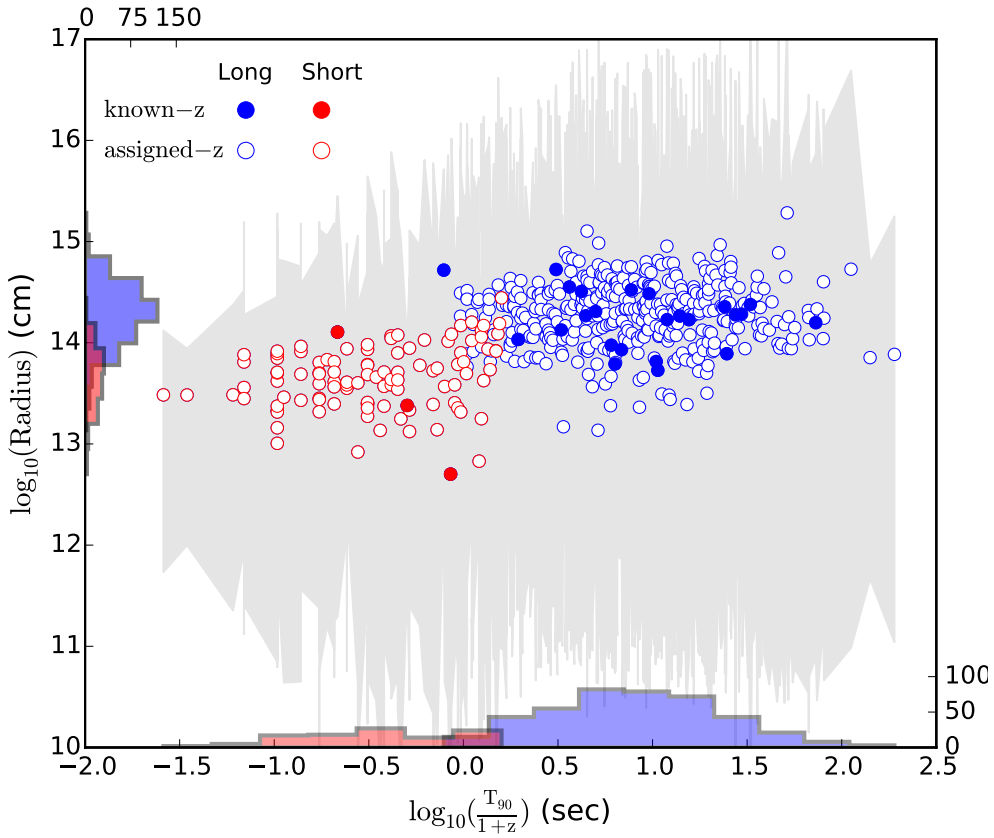

Figure 3.8: The characteristic emission radii R_c (Equation 3.4) plotted versus rest frame T_{90} for the *Fermi*/GBM bursts. The shaded region shows the interval between the minimum and maximum emission radii allowed. The bursts with known-z and assigned-z are denoted with filled and unfilled circles, respectively. The short and long-duration GRBs are denoted with red and blue colors, respectively.

was possibly due to the utilization of a fixed observer frame bandpass instead of a fixed rest frame bandpass in the analysis. For *Fermi*/GBM, the broad instrument energy range permits analysis in a fixed rest frame bandpass.

We identify 46 *Fermi* GRBs, including 4 short-duration GRBs, with measured redshifts. Light curves are extracted in the rest frame 89–299 keV band and analyzed. In Figure 3.9 we plot $\Delta t_{\rm min}/(1+z)$ versus $1+z$ for the long-duration GRBs. Redshift values are taken from Butler et al. (2007, 2010, and references therein), Butler (2013),

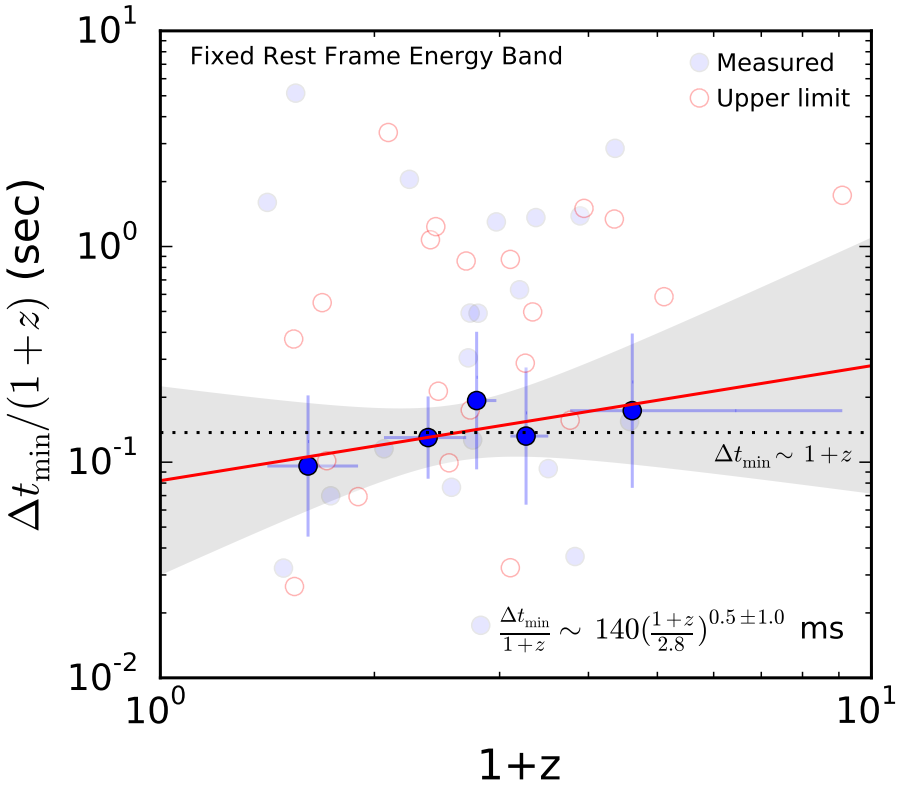

Figure 3.9: Minimum variability timescale in the rest frame 89–299 keV energy band versus redshift, z. The blue circles show the KM mean values of $\Delta t_{\rm min}$ for groups of 7–10 bursts of similar redshift. The shaded region represents the 1σ confidence interval for the fitted red line. The dotted black line shows the expected evolution due to simple cosmological time dilation, namely $\Delta t_{\rm min} \sim 1+z$. The faint blue circles show all GRBs with measured $\Delta t_{\rm min}$ and known-z and the unfilled circles show GRBs with upper limit values for $\Delta t_{\rm min}$.

and this webpage[3]. The blue circles in Figure 3.9 correspond to the KM mean values of $\Delta t_{\rm min}$ for sets of between 7 and 10 bursts, grouped by redshift intervals. The unbinned data are plotted in the background for the entire sample and for those with measured $\Delta t_{\rm min}$ using unfilled and filled circles, respectively. We find that the binned data can be well-fitted by a line $\Delta t_{\rm min}/(1+z) \sim 140((1+z)/2.8)^{0.5\pm1.0}$ ms, suggesting possibly increase in timescale with z but also consistent the prediction of simple time-dilation (dotted line).

[3] `http://www.mpe.mpg.de/~jcg/grbgen.html`

3.5 Conclusions

Using a technique based on Haar wavelets, previously developed in Paper I, we studied the temporal properties of a large sample of GRB gamma-ray prompt-emission light curves captured by the GBM instrument onboard *Fermi* prior to July 11, 2012. We analyzed the time histories in four energy bands. While the derived values for $\Delta t_{\rm min}$ are highly-dependent upon bandpass, we find that the use of the full energy band allows for the tightest constraints on the size of the emission region. In principle, the highest-energy bandpass should yield the tightest constraint (Section 3.4.4). However, S/N in the highest-energy channels is often low; the full energy bandpass allows for increased S/N while maintaining a consistent $\Delta t_{\rm min}$ estimate.

Applying our technique to the joint *Fermi*/GBM and *Swift*/BAT sample, we find close consistency in the minimum timescales derived for each instrument. However, as suggested by simulations in Paper I – and observed for a handful of bursts of widely varying S/N in Section 3.4.2 – $\Delta t_{\rm min}$ values below the measurement limit ($\Delta t_{\rm S/N}$) can be present. It is thus important to consider our $\Delta t_{\rm min}$ values as defined given the observed data, with the possibility of improved limits given better data. We urge caution, in particular, in interpreting minimum timescales determined using hard X-ray data (e.g., *Swift*/BAT). Minimum timescale estimates using the full *Fermi*/GBM bandpass are a factor 2–3 times more constraining than those determined from *Fermi*/GBM data in a *Swift*/BAT bandpass.

Considering measurements and limits, we find a median minimum variability timescale in the observer frame of 134 ms (long-duration; 18 ms for short-duration GRBs). In the source frame, for a smaller sample of 33 GRBs, we find a median timescale of 45 ms (long-duration; 10 ms for short-duration GRBs). This finding validates our previous results in Paper I, confirming that millisecond variability appears

to be rare in GRBs. In the most extreme examples, 10% of the long-duration GRB sample yields evidence for 2.2 ms variability (1.9 ms for short-duration GRBs). In the source frame, we find similar numbers, 2.9 ms for long-duration GRBs and 2.4 ms for short-duration GRBs. Even if we restrict to the 67 GRBs within minimum detectable timescales $t_{\rm S/N} < 10$ ms, only 10% of the brightest and/or most impulsive GRBs show evidence for variability on timescales below 4.2 ms in the observer frame.

3.5.1 Constraints on the Fireball Model

In the "external shock" model (e.g., Rees & Meszaros, 1992), gamma-rays are produced as the GRB sweeps up and excites clouds in the external medium. The extracted $\Delta t_{\rm min}$ can circumscribe the size scale of the impacted cloud along the line of sight. For a thin shell (e.g., Mészáros, 2006), the gamma-ray radiation will start when the relativistic shell hits the inner boundary of the cloud with the peak flux produced as the shell reaches the densest region or center of the cloud. The size scale of the impacted cloud is limited by $2\Gamma^2 c\,\Delta t_{\rm min}$ since the shock is moving near light speed (Fenimore et al., 1996). For the smallest $\Delta t_{\rm min}$ found $\sim$1 ms, and assuming $\Gamma < 1000$, the cloud size must be smaller than 4 AU.

If the angular size of an impacted cloud as viewed from the GRB central engine is Θ, the minimum variability timescales is constrained to be $\delta\Theta\,\Gamma < \Delta t_{\rm min}/2\,T_{\rm rise}$ (Paper I). Here, $T_{\rm rise}$ denotes the overall time to reach the maximum gamma-ray flux. The fraction of the emitting shell that becomes active is expected to be of order $0.1\Delta t_{\rm min}/2\,T_{\rm rise}$ (Fenimore et al., 1999). For the bursts in the *Fermi* sample with typical minimum variability timescale $\Delta t_{\rm min} \sim T_{\rm rise}$, there is no need to consider a highly-clumped external medium and the external shock scenario is viable.

However, there are many bursts (e.g., Figure 3.6) which do exhibit $\Delta t_{\rm min}/T_{\rm rise} \ll 1$. If this variability results from a clumped external medium, then a significant fraction

of the energy from the GRB must escape without interacting and producing gamma-rays. Early X-ray afterglow observations (e.g., Nousek et al., 2006), on the other hand, demonstrate the need for a high (order unity) efficiency in tapping the kinetic energy of the flow to produce gamma-rays. Thus, external shocks likely cannot explain the finest-time-scale variability.

In the "internal shock" scenario (e.g., Rees & Meszaros, 1994), the relativistic expanding outflow released from a central engine is assumed to be variable, consisting of multiple shells of different Γ. The dispersion in Γ is related to the observed variability of the light curve, as $\Delta\Gamma/\Gamma \approx 1/2\,(\Delta t_{\rm min}/T_{\rm rise})$ (Paper I), with many of the *Fermi* light curves requiring $\Delta\Gamma \approx \Gamma$. Efficient production of gamma-rays also requires $\Delta\Gamma \approx \Gamma$ (Piran, 1999; Kobayashi & Sari, 2001). It is, therefore, natural to assume that some of the gamma-ray emission is released with the minimum possible Lorentz factor $\Gamma_{\rm min} \approx 200$ (Section 3.4.5) allowed from compactness considerations. As a result, considering variability at the few millisecond level, some GRBs must emit at radii of order $R_c \approx 2\Gamma_{\rm min}^2 c\,\Delta t_{\rm min} \approx 10^{13}$ cm (Equation 3.4, Figure 3.8). This is also the extent to which minimum variability timescales can limit the size of the progenitor.

We find that long-duration GRBs appear to have typical emission radii $R_c \approx 1.3{\times}10^{14}$ cm, while short-duration GRBs have four times smaller typical emission radii, $R_c \approx 3.3{\times}10^{13}$ cm. There is large scatter in the inferred radii of each population, and the distributions appear to strongly overlap. It is unclear whether the dichotomy in short and long-duration GRB T_{90} durations maps cleanly to a similar dichotomy in the size of the emission regions.

Finally, we note that our minimum timescales appear to correlate with redshift in fashion consistent with cosmological time-dilation. Correcting for this, we find no significant evidence that $\Delta t_{\rm min}/(1+z)$ evolves with redshift. This may be partly

because the number of *Fermi* GRBs with measured redshifts is low (e.g., as compared to *Swift*; Paper I). Future increases in the sample size will surely allow for tighter constraints on minimum emission radii, Lorentz factors, and progenitor dimensions as well as allowing us to better understand whether any of these quantities vary with cosmic time.

Chapter 4

SEARCH FOR SUPERNOVAE IN EXTREME STAR-FORMING GALAXIES USING THE PALOMAR TRANSIENT FACTORY

4.1 Abstract

Extreme star-forming galaxies are expected to have very high supernova rates, yet direct observational evidence has remained elusive. The most extreme star-forming galaxies in the local universe are luminous infrared galaxies (LIRGs). We present the results of a 5-year comprehensive SN search study by the Palomar Transient Factory (PTF) aimed to measure the SN rates in the LIRGs. The PTF survey presents a wealth of cadence coverage for 121 LIRGs in the Great Observatories All-sky LIRG Survey (GOALS; Armus et al., 2009). Using GOLAS far-ultraviolet (FUV) measurements to estimate the optically visible, unobscured star formation in these systems, we are able to predict, assuming an IMF, the expected number of SNe visible to PTF.

Difference imaging and the visual search are used to search for optical transients in the (U)LIRGs consistent with SNe. We find 5 SNe, of which 3 came out as the result of a visual search and 2 using the implemented image subtraction algorithm. We use Monte Carlo simulations to calculate the detection efficiency in our analyses. We found the expected average of SN rate for the LIRGs in our sample, $0.05 \pm 0.02\,yr^{-1}$/galaxy, which is consistent with the mean value of SN rate estimated using FUV light, $0.060 \pm 0.002\,yr^{-1}$/galaxy.

A version of this chapter will be submitted to *The Astrophysical Journal*.

4.2 Introduction

The rate of supernovae (SNe) is a fundamental observable for astrophysical studies. Measurements of the SN rate and its evolution over cosmic time provides valuable information on the chemical evolution of galaxies, the kinematics and composition of the interstellar medium, and the production of cosmic rays. They shed light on our understanding of the initial mass function (IMF) models, and provide constraints for stellar evolution theories. In a given stellar population, the rate of core-collapse SNe (CCSNe; types II and Ib/c) is a direct measure of the ongoing star formation rate (SFR), because of their short-lived progenitors. Therefore, the evolution of CCSN rates as a function of redshifts can be used to track the cosmic star-formation history. While the CCSN rates in normal galaxies such as the Milky Way is low, $\sim$0.01–0.02 yr^{-1}, it is expected to be much higher – $\sim$ several orders of magnitude – in the most extreme starburst galaxies.

Many surveys with various scientific goals have been conducted in order to estimate the rate of SNe in starburst galaxies. In the optical bands, attempts to search for SNe in such galaxies did not confirm finding high SN rates (e.g. Richmond et al., 1998; Navasardyan et al., 2001). In the infrared bands, SNe searches reported higher SN rates, $\sim$1 order of magnitude in the starburst galaxies (e.g. Maiolino et al., 2002; Mannucci et al., 2003). The dusty nature of many starburst galaxies and the extreme extinction in their nuclear regions ($A_V > 25$ mag) diminishes the light drastically, up to $\sim$70–90%, and makes the probing task quite challenging (Dahlen et al. 2012, and reference therein, see also Miluzio et al. 2013).

The observed discrepancy between CCSN rates and SFRs at various redshifts has remained an open question. The visual searches of SNe have been summarized by van den Bergh & McClure (1994). A series of papers by Cappellaro et al. (1993a,b,

1997) laid out the SN rate calculations, in detail. CCSN rates have been estimated both for the local universe (Li et al., 2011) and at high redshifts (Dahlen et al., 2004; Cappellaro et al., 2005; Botticella et al., 2008; Bazin et al., 2009; Melinder et al., 2012; Dahlen et al., 2012). Leaman et al. (2011) and Li et al. (2011) showed measurements of the observed rates of SNe in the local universe using the Lick Observatory Supernova Search (LOSS). Miluzio et al. (2013) explored a relation between the star formation and the SN rates in the extreme environment of starburst galaxies. Despite all these efforts, published estimates of the SN rates still bring large uncertainties.

We present in this chapter, for the first time, the results of a 5-year comprehensive SN search study by the PTF aimed to measure the SN rates in the LIRGs. The PTF survey presents a wealth of cadence coverage for 121 (U)LIRGs in the GOALS. Difference imaging and the visual search are used to search for optical transients in the (U)LIRGs consistent with SNe. Using GOLAS far-ultraviolet (FUV) measurements to estimate the optically visible, unobscured star formation in these systems, we are able to predict, assuming an IMF, the expected number of SNe visible to PTF and hence calculate SNe rate. The FUV observations, uncorrected for reddening, provides a clear lower limit on the predicted SNe rate, since the optical is, by definition, less affected by extinction. These results then are compared with observed SNe rate of the same targets.

The chapter is organized as follows. Section 2 describes the galaxies in our sample. In Section 3, we present the implemented SNe search method. Section 4 provides observationally calculated SN rates and computationally calculated SN rates, and the comparison between the results of these two different methods. Section 5 discusses likely uncertainties and biases in the SN rate calculations. Our conclusions are summarized in Section 6.

We adopt a cosmology of $\Omega_\Lambda = 0.72$, $\Omega_m = 0.28$, with $H_0 = 70$ km s^{-1} Mpc^{-1}

throughout this chapter. All magnitudes in this chapter are in the AB system.

4.3 Data

4.3.1 The Galaxy Sample: Local (U)LIRGs

A starburst galaxy is a galaxy undergoing an exceptionally high rate of star formation, ∼10–100 $M_{\odot} yr^{-1}$, as compared to typical star-forming galaxies in the local universe, a few $M_{\odot}\ yr^{-1}$. At these high levels of star formation, the supply of gas and dust within the galaxy would be exhausted quickly, in a few million years, indicating a fairly new intense episodes of star formation. The most extreme starbursts in the local universe are "luminous infrared galaxies" i.e. LIRGs with $11 < log_{10}(L_{ir}/L_{\odot}) < 12$ and "ultra luminous infrared galaxies" i.e. ULIRGs with $log_{10}(L_{ir}/L_{\odot}) > 12$. For a complete review of the properties of (U)LIRGs, we refer our readers to Sanders & Mirabel (1996). LIRGs form a morphologically diverse group of galaxies, unlike ULIRGs which are nearly always involved in the final stages of a violent and spectacular merger. By their very nature, LIRGs are dusty galaxies, wherein a large fraction (over 90% for the most luminous systems) of the UV light emitted by stars and/or AGN is absorbed by grains and reradiated in the far-infrared. Extreme star-forming galaxies are expected to have much higher SN rates compared to normal galaxies because they generate their enormous power through intense starbursts and the fueling of Active Galactic Nuclei (AGN).

The GOALS [1] is a 60 μm flux limited IRAS sample in which has characterized a sample of over 200 of the most luminous infrared-selected galaxies in the local universe ($z < 0.088$) across the electromagnetic spectrum. In a comprehensive study, GOALS combines imaging and spectroscopic data from NASA's Spitzer, Hubble,

[1] see `goals.ipac.caltech.edu`

Chandra and GALEX space-borne observatories. Specifically GALEX provides the UV properties of a large number of LIRGs through imaging in both the FUV and the NUV wavelengths. The GOALS sample consists of 181 LIRGs, as well as over 20 ULIRGs. These objects are a complete subset of the IRAS Revised Bright Galaxy Sample (RBGS; Sanders et al., 2003), which comprises 629 extragalactic objects with 60 μm flux densities $S_{60} > 5.24$ Jy – the brightest 60 μm sources in the extragalactic sky – and Galactic latitude above five degrees. The LIRGs and ULIRGs targeted in GOALS span the full range of nuclear spectral types (type-1 and type-2 AGN, LINERs, and starbursts) and interaction stages (major mergers, minor mergers, and isolated galaxies). They provide an unbiased picture of the processes responsible for enhanced infrared emission in the local Universe, and may be analogs for comparisons with infrared and sub-millimeter selected galaxies at high-redshift.

The fact that some of (U)LIRGs in GOALS (e.g., Mrk 171, Mrk 266, Mrk 231, Mrk 273, Mrk 617, and Mrk 848) were first identified as starburst galaxies and AGN by Markarian survey in UV (Armus et al., 2009) shows many LIRGs often have measurable UV fluxes (see, e.g., Mazzarella & Balzano, 1986). This is due to variations in the spiral distribution dust of these galaxies. Of the 202 LIRGs in GOALS, 145 have been observed with the GALEX telescope in the NUV and FUV filters. Surace et al. (1998) examined the warm ULIRGs sample ($f_{25}/f_{60} > 0.2$) [2] of Sanders et al. (1988) using HST /WFPC2 and found a population of compact, powerful star-forming knots (compact emission regions not identified as nuclei) in all of those objects. Using the same sample, Surace & Sanders (1999) showed significant extra-nuclear optically detected star-formation that may contribute as much as 25% of the bolometric luminosity.

[2]The quantities f_{25} and f_{60} represent the *IRAS* flux densities in Jy at 25 μm and 60 μm respectively.

4.3.2 Observations: the Palomar Transient Factory

The PTF is a fully-automated, wide-field survey aimed at a systematic exploration of the optical transient sky (Rau et al., 2009; Law et al., 2009). PTF utilizes a 7.1 $\deg^2$ camera on the Palomar 48-inch Oschin Schmidt telescope to survey the sky primarily at a single wavelength (R-band) at a rate of 1000–3000 $\deg^2$ per night. PTF, in the course of mapping the sky, has also imaged all of the northern hemisphere GOALS objects many tens of times over the course of a five-year plan (2009 – 2014). There are more than 3 million R-band images available in the PTF archive (Surace et al., 2015). The data are used to detect and study transient and moving objects such as gamma ray bursts, SNe, quasars, galactic stars, and asteroids. As a search engine for finding SNe, the PTF saw first light in December 2008 and found its first SN in March 2009. Under typical seeing conditions the camera achieves a full width at half-maximum intensity (FWHM) $\sim 2.0''$, and 5σ limiting magnitudes of $R \approx 21.0$, $g' \approx 21.6$ and H$\alpha \approx 18$ mag can be reached in a 60 s exposure.

The PTF archive provides a wealth of cadence coverage for these galaxies and the GOALS provides the FUV flux measurements for the majority of the LIRGs in the sample. Combining the data from the PTF survey and the GOALS assembles the largest sample of SN rate studies in the U(LIRGs). The observationally determined SN rates are compared with that expected from the amount of the FUV flux measurements of the same targets using the stellar population synthesis models. The ultraviolet stellar continuum (912–3000 Å) of galaxies is a tracer of the recent SFR. Within the UV range, the far-UV radiation (FUV; 1500 Å) is a better SFR indicator than the near-UV radiation (NUV; 2500 Å), because the NUV is contaminated by evolved stars, while the FUV is dominated by the radiation from new, massive, short-lived stars (see e.g., Madau et al. 1998). We utilize *SB99*, a stellar evolution

model, and the FUV flux measurements of galaxies to estimate the SN rates.

4.4 The SN Searches

Out of 203 galaxies in the GOALS sample, only 133 of them have images with more than one epoch observed in the R-band, a result of seeing only the northern sky. The distribution of these 133 galaxies in the sky is shown in Figure 4.1 with blue and red color circles representing the LIRGs and ULIRGs, respectively. FUV flux measurement values are available only for 91 out of the 133 galaxies. These 91 galaxies construct our sample. In order to distinguish these galaxies from the rest, they are highlight with darker colors in Figure 4.1. We show the results of LIRGs and ULIRGs separately throughout this chapter just for historical reasons; however, they are not actually different in terms of selection.

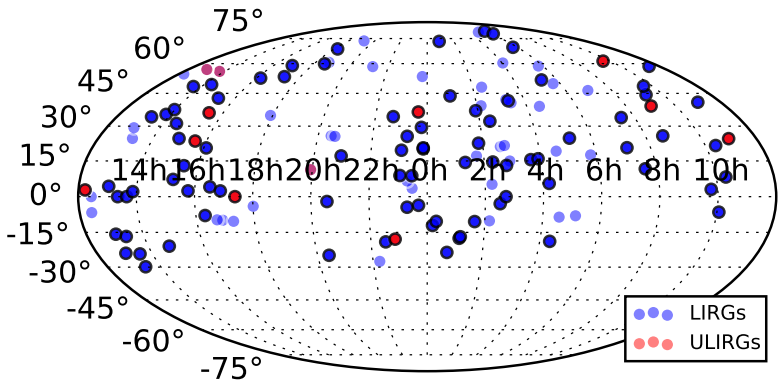

Figure 4.1: Distribution of (U)LIRGs in our sample observed by the PTF in the sky. These galaxies (133) are a subset of the GOALS objects with more than 1 epoch observed in the R-band and available in the PTF archive. LIRGs and ULIRGs are specified with the blue and red colors, respectively. The final sample (91 out of 133) is selected from the objects with available FUV flux measurements. The galaxies in our sample are highlighted with darker colors.

The list of galaxy sample is reported in Appendix C (Table C.1). Along with the galaxy name, correspondent IRAS name, and equatorial coordinates (Cols. 1 - 4), we report the infrared luminosity (Col. 5; $\log_{10}(L_{ir}/L)$) and the luminosity distance, D_L,

(Col. 6). Further descriptions on Table C.1 will be discussed in the following section. The sample is made of 82 LIRGs and 9 ULIRGs with the cumulative histogram of number of galaxies versus $\log_{10}(L_{ir}/L_{\odot})$ as shown in Figure 4.2.

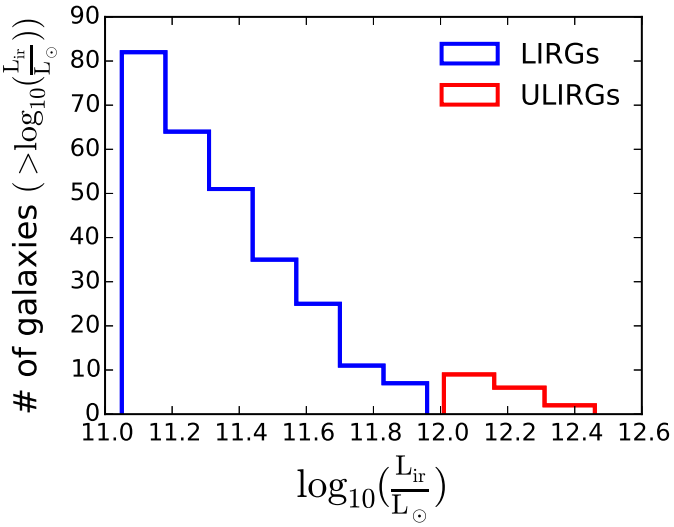

Figure 4.2: Cumulative number of galaxies versus $\log_{10}(L_{ir}/L_{\odot})$ for LIRGs (blue) and ULIRGs (red) in the sample, separately.

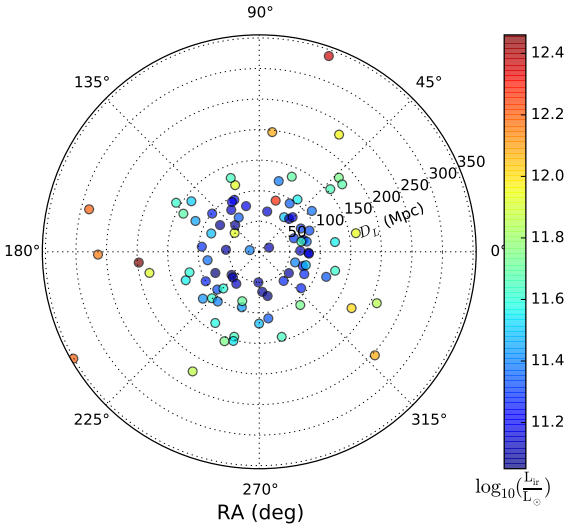

Figure 4.3: The volumetric distribution of galaxies in our sample as a function of the *RA* (deg) and the D_L (Mpc). The color-bar shows IR-luminosity of each galaxy in the sample.

For each of the galaxies in our sample, we downloaded from the PTF archive [3] all the available *FITS* files in the R-band. The volumetric distribution of galaxies in our sample is displayed in the Figure 4.3, as a function of the RA (deg) and the D_L (Mpc). The color-bar shows IR-luminosity of each galaxy in the sample. The median values of D_L for the LIRGs and ULIRGs are 92.65 Mpc and 254.0 Mpc, respectively.

In the PTF archive, the cadence information and epoch numbers vary from one observed galaxy to another galaxy in our sample; an uneven cadence. Figure 4.4 shows a histogram of the number of epochs for galaxies in the sample. The average values of the counted epochs for LIRGs and ULIRGs in our sample are 60 and 50, respectively.

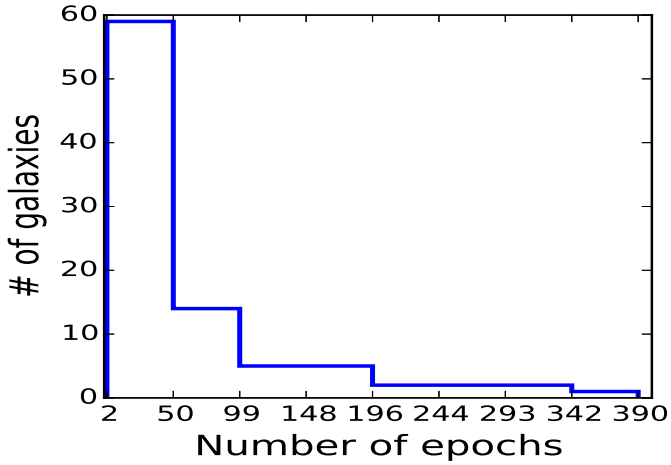

Figure 4.4: Histogram of the number of epochs for galaxies in the sample.

The distribution of PTF cadence for each galaxy in the sample, specified with its $\log_{10}(L_{ir}/L_{\odot})$ value, is shown in Figure 4.5. The LIRGs and ULIRGs in the sample are separated in the bottom and top panels to help with the space between cadences. The x-axis shows the distribution of epochs in days since the first observation of a galaxy in the sample. The observed uneven cadences here is a primary characteristic

[3] `http://irsa.ipac.caltech.edu/applications/ptf/`

of an un-targeted SNe survey. This originates from two sources: (1) a 6-month alias occurs since many targets are only visible from the ground seasonally, and (2) PTF uses a non-uniform sky sampling strategy.

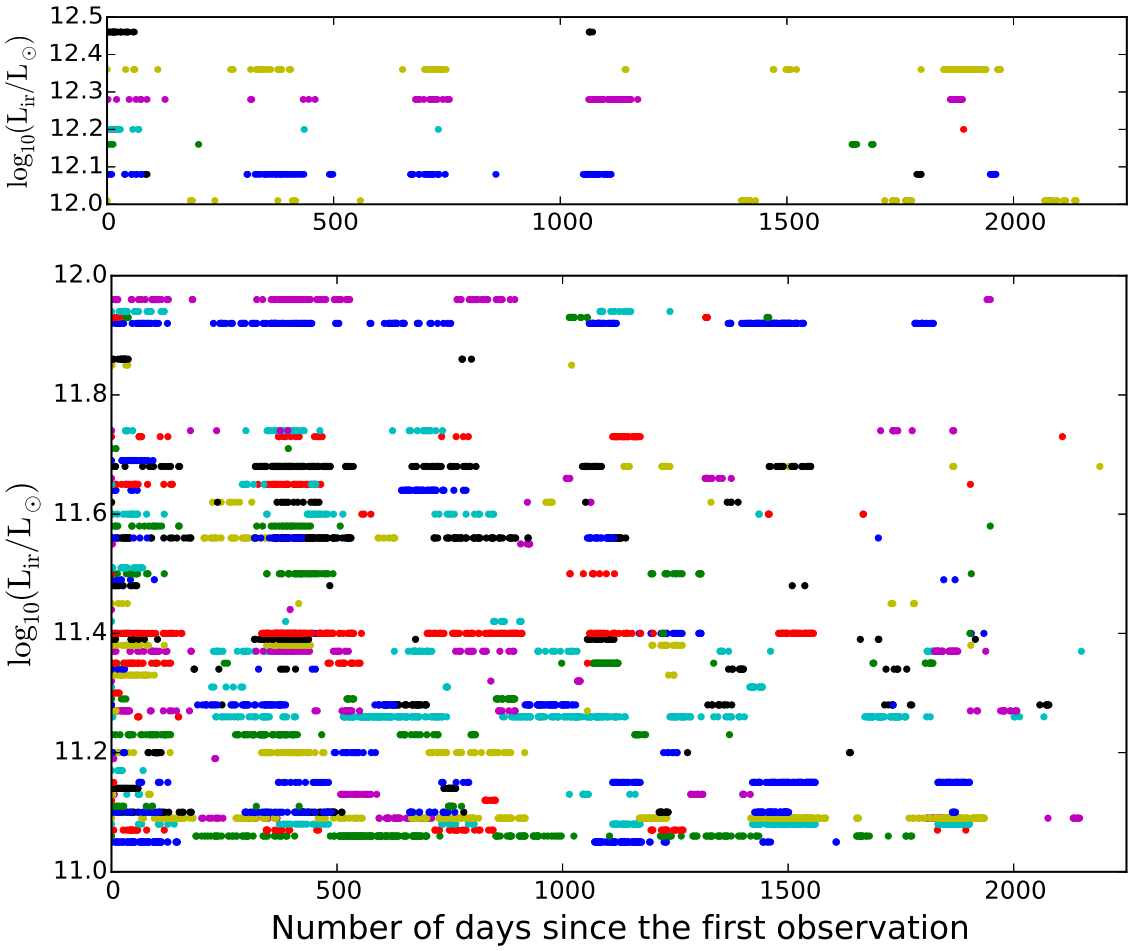

Figure 4.5: The PTF cadence of each galaxy in the sample. The cadence for a galaxy is shown with small circles where they are placed at the $\log_{10}(L_{ir}/L_{\odot})$ value of that galaxy using a different color. The LIRGs and ULIRGs in the sample are separated in the bottom and top panels to help with the space between cadences. The x-axis shows the distribution of epochs in days since the first observation of a galaxy in the sample. Color is only for clarity and has no specific meaning.

4.4.1 Counting the SNe

Transient phenomena discovery such as SN explosions is a primary goal of the PTF project. After taking images using the PTF, data are transferred to NERSC Edison where running a real-time reduction pipeline. The PTF automated pipeline matches images taken at different epochs under different observing conditions and implements an image subtraction algorithm to search for transients. The extracted sources labeled as transient candidates pass through a machine-learning classifier where prioritizes real transients over artifacts, e.g., *bad* subtractions. The final results are then displayed through a web portal named "the followup Marshal" for visual inspection by the human. The PTF automated pipeline achieves the goal of identifying optical transients within minutes of images being taken (Law et al., 2009). Given the relatively small size of our sample, we decided to initiate a visually inspected SN search first. Image subtraction methods make it easy to extract transients; however, their high false alarm rates (FARs) due to production of a large number of spurious "candidate" objects and machine-learned vetting algorithms would never remove the human element in the inspection process (Bloom et al., 2012). To accomplish this task, we downloaded all the available R-band *FITS* files in the PTF archive for each galaxy in our sample. Stamps of *FITS* files are made with the size of 5 arcmin radius centered at a galaxy center. For each galaxy, the stamps are stacked in the chronological order to construct a *cubeset FITS* file. Caution needs to be taken in order to adjust galaxy coordinates of the stamps and to homogenize galaxy flux levels by subtracting their zero point levels. It would be easy then to go quickly through all the images and search for any bright transients such as supernova visually. We should note that a visual search could not guarantee a supernova detection in a galaxy nuclear region due to limited spatial resolution. We can expect, at best, to find the supernovae which

occur in the circumnuclear regions. Dust does obscure the majority of star-forming regions in galaxy nucleus regions; however, the circumnuclear regions may remain unobscured. The unobscured parts can have well-characterized star-forming characteristics and can reach ∼10% of the total galaxy brightness which is not a negligible amount.

We inspected carefully each of 91 *cubeset FITS* files using the DS9 software [4] . Given the highly complex shape and morphology of the galaxies in the sample, we used the very high-resolution *Hubble Space Telescope* (HST) optical images (Haan et al., 2011). The HST images were used as a guide to identify transients actually associated with the galaxy, as opposed to nearby coincidental background objects. At the end of the visual search we were able to identify 3 SNe in the whole sample. We also have run the image subtraction module of the RATIR LIGO followup pipeline (Golkhou et al., 2017b) to detect any hidden SN events especially in the nuclear regions of the galaxies in our sample. This enabled us to add 2 more SNe into the list. Therefore, we detected 5 SNe in total. Figure 4.6 presents the finding charts for these SNe.

In case an SN found visually, the images on the left show science frames and the images on the right show reference frames. If an SN found using the image subtraction code, the subtracted image is also shown on the far right. The location of an SN is marked with the red cross on the frames. Our investigation shows that none of the newfound SNe are a new discovery.

The PTF pipeline had missed most of these detected SNe. We should note that it is not unexpected to witness failures in the SN detections by a fully automated transient search such as the PTF pipeline. The main reason is that not all the frames labeled as transients by the PTF pipeline – which could be as $\sim 10^6$ transients per

[4] `http://ds9.si.edu/site/Home.html`

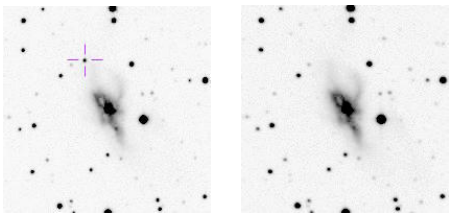

(a) SN 2010gp (sci) (b) SN 2010gp (ref)

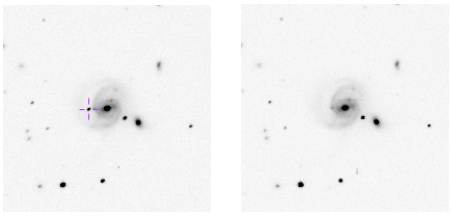

(c) SN 2011hb (sci) (d) SN 2011hb (ref)

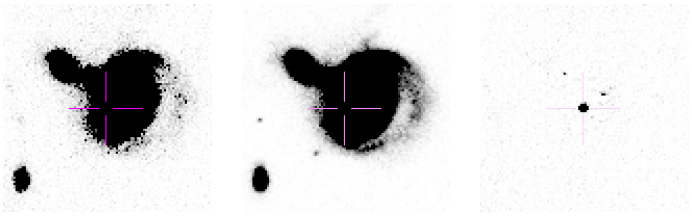

(e) SN 2011ee (sci) (f) SN 2011ee (ref) (g) SN 2011ee (sub)

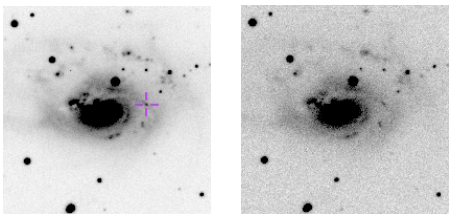

(h) SN 2013cc (sci) (i) SN 2013cc

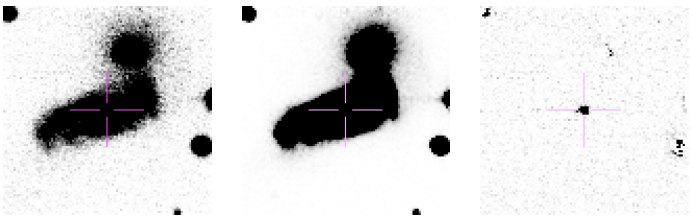

(j) SN 2014dj (sci) (k) SN 2014dj (ref) (l) SN 2014dj (sub)

Figure 4.6: The SNe finding charts. The images on the left show science frames and the images on the right (the middle in case an SN found using the image subtraction code; right: the subtracted images) show reference frames. The location of an SN is marked with the red cross. The sizes of all the postage-stamps are: 5×5 arcmin^2. All images are displayed with north at the top and east to the left.

night with different real-bogus scores [5] – receive the human inspection and the level of care which is the focus of this work. Brink et al. (2013) noted that the vast majority of transient candidate objects found by PTF on a given difference image are spurious: in a typical field, only about 1 in 1000 extracted candidate objects (considered to be at least as significant as a 5σ detection) are what regarded as having an astrophysical origin.

Investigating data available on the IAU ATel's website [6] reveals the reports of 57 SN occurrences – 1961L SN in NGC 3221 is the first one – in the same regions as our interested search domains. Out of this number, 16 SNe occurred after 2009. We found two main reasons why the PTF survey only could detect 5 SNe and failed to detect the rest, 9 SNe: (1) they discovered in the *NIR*-bands and the PTF is an optical survey and (2) they happened during the time when the PTF was shut down or was surveying other regions of the sky. Table 4.1 lists the information of these 16 SNe including SN names, their types, optical or *NIR* band of discovery, the SN R-magnitude values, their corresponding galaxy names and D_L values, and a short description of the main reason why we are not able to recover them in our SN search.

This shows that a detailed modeling of the PTF cadence is required to calculate the SN rate (see Section 4.5). Therefore, the calculations and analyses in this chapter restrict to the SNe with available cadence information in the PTF archive.

4.5 SN Rate Calculations

In this section, we discuss the observed SN rate and also computationally calculated SN rate using stellar population synthetic models such as *Starburst99* (Leitherer et al., 1999), and *BC03* (Bruzual & Charlot, 2003). Such models can estimate an SN

[5] a score which determines our confidence level to the origin of a candidate event; 1: real/astrophysical and 0: bogus/non-astrophysical (Bloom et al., 2012).

[6] `http://www.cbat.eps.harvard.edu/lists/Supernovae.html`

Table 4.1: The List of Detected SN Information.

Galaxy	IRAS name	SN name	type	discovered band	R-mag	$D_{\rm L}$ (Mpc)	comment
NGC 6240	F16504+0228	2010gp	Ia	unfiltered	17.5	116	VD
NGC 7674	F23254+0830	2011ee	Ic	optical	18.6	125	IMS
NGC 7674	F23254+0830	2011hb	Ia	optical	18.8	125	VD
NGC 1961	F05365+6921	2013cc	II	optical	17	59	VD
NGC 0317B	F00548+4331	2014dj	Ic	optical	17	77.8	IMS
NGC 3690	F11257+5850	2010O	Ib	optical	15.6	50.7	NP
NGC 3690	F11257+5850	2010P	IIb	NIR	18.3	50.7	NP
UGC 8387	F13182+3424	2010cu	II	K-band	17.7	110	NR
ESO 602-G025	F22287-1917	2010gg	II	unfiltered	17.7	110	NR
NGC 6621	F18131+6820	2010hi		unfiltered	18	94.3	NP
ARP 256	F00163-1039	2010hp	II	K-band	17.1	117.5	NR
UGC 8387	F13182+3424	2011hi	II	NIR (J,H,K)	17.9	110	NR
ARP 302N	F14547+2449	2012M	Ia	unfiltered	17	157	NP
ARP 086	F23444+2911	2013Q	Ia	unfiltered	17.5	73.6	NP
NGC 6240	F16504+0228	2013dc	IIP		18.7	116	NP
NGC 5936	F15276+1309	2013dh	Ia	unfiltered	18	67.1	NP

VD: the SN event detected via the visual search.

IMS: the SN event detected using an image subtraction algorithm.

NP: the PTF was not operational during the SN event.

NR: the SN occurred in the nucleus region.

rate based on the amount of FUV light produced in a particular galaxy. For galaxies in our sample, the values of FUV fluxes are obtained from Howell et al. (2010, Table 1). Counting the frequency of SN provides the observed rate of SN events. We employ a large sample of LIRGs to calculate the SN rates using these two completely different approaches. Finally, it is possible to assess any discrepancy between the two methods and account for biases causing the inconsistencies. The PTF cadence infor-

mation and the number of detected SNe could help to determine the observationally calculated SN rates. However, SN rate calculations based on FUV light reservoirs – e.g. starburst regions – using models can provide a lower limit estimates for the SN rates.

It should be note that FUV flux is being used as a proxy SFR indicator of optically visible star formation. This works because optical star formation is less extinguished than the FUV. Also, it is known from optical studies of LIRG star clusters (Surace et al., 1998; Surace & Sanders, 1999) that extra-nuclear star clusters are lightly obscured.

4.5.1 The SN Rate from Observation

In order to determine the frequency of the SN occurrences in a given survey, we need to know the total counts of all SN events and also the notion of "control-time" concept. Control-time for a galaxy is defined as the time interval during which an SN is visible or its brightness is above the limiting magnitude of the used observing instrument (Leaman et al., 2011). The control-time depends on the photometric evolution of an SN of a given type, and the distance of the galaxy under control. For further description on this concept, we refer our readers to Zwicky (1942), van den Bergh (1991), and Cappellaro et al. (1993a, 1997). Given the cadence of a particular galaxy in a survey, we can define the control-time of a specific type of SN as the following:

$$\text{"control} - \text{time"} = \Pr\big((\text{SN} \geq 1)\big|\text{C}\big) \times \text{T}^{\text{C}} \tag{4.1}$$

where, $\Pr\big((\text{SN} \geq 1)\big|\text{C}\big)$ represents the probability of observing a specific type of SN given the cadence, C, and T^{C} depicts the cadence coverage for that galaxy. In other words, the control-time is defined as the product of the total time duration of the survey for a given galaxy and the efficiency of finding one SN or more based on the

cadence information. The efficiency can be defined as the probability of finding one SN or more given a cadence and a template light curve of the SN type of interest.

The definition of control-time here is very similar to the conventional control-time, but different in terms of the implemented mathematical approach to calculate the SN rate (more details in Appendix D). In conclusion: if we discover N SN in a galaxy, $N_{\rm SN}$, while being controlled for a certain time, here is how we calculate the SN rate:

$$\mathrm{r_{SN}} = \frac{\mathrm{N_{SN}}}{\text{“control} - \text{time”}} \tag{4.2}$$

4.5.2 The Expected Value of the SN Rate

The search to detect the SN events in the unobscured regions of the galaxies in our sample resulted in 5 objects. A simple interpretation here could be a zero-count SN event in most galaxies in the sample, hence, a zero SN rate value for those galaxies. Surely, this is not a meaningful statement.

Assuming a Poisson distribution for the SN occurrences can lead us to the concept of the expected SN rate calculation for all the galaxies in our sample. We discuss this further in Appendix E and provide the mathematical framework of the expected SN rate calculation, in detail. In particular, Equation E.3 is the foundation of the expected SN rate calculation based on observations and is reproduced here:

$$\langle \mathrm{r_{SN}} \rangle \;=\; \frac{\sum_{i=1}^{N} k_i}{\sum_{i=1}^{N} \tau_i} \pm \frac{\sqrt{\sum_{i=1}^{N} k_i}}{\sum_{i=1}^{N} \tau_i} \tag{4.3}$$

where $\sum_{i=1}^{N} k_i$ and $\sum_{i=1}^{N} \tau_i$ are the total SN counts and the total control-time for all the N galaxies in the sample, respectively. $\langle . \rangle$ represents the expected value symbol.

4.5.2.1 The CCSN Light Curves

The control-time depends on the SN luminosity and the light curve evolution which make it vary from one SN type to others. Creating CCSN template light curves is a crucial step here but surely outside the scope of this research. Therefore, we decided to use CCSN template light curves in the R-band constructed by (Melinder et al., 2011, and references therein) and (Li et al., 2011). The SN spectra and absolute magnitude light curves are used to construct SN template light curves [7]. The used spectra extend from 1000 Å to 25000 Å and cover epochs from day ∼1-2 to ∼100 after an explosion. The extinction phenomenon and K-correction concept are implemented in the course of constructing the template light curves.

Since the $D_{\rm L}$ values are available for the galaxies in the sample (column 5 - Table C.1), the NED Cosmology Calculator [8] (Wright, 2006) is used to calculate the redshifts ($z_{mean} \sim 0.04$). The redshift values are then used to correct the SN template light curves.

4.5.2.2 Monte Carlo Simulations: the Detection Efficiency

It is possible to discover an SN if it occurs during a survey with an ideal cadence, e.g., the minimum observation interval of one day, and using an instrument with a limiting magnitude below the typical pick magnitude of that SN. However, in a real survey study like ours, the observation intervals are much longer than one day, and the cadence is often sparse, moreover sporadic, especially during a blind survey with no specific targets planned.

We perform Monte Carlo (MC) simulations to incorporate the effects of observation intervals and also uneven cadences in the SN rate calculation (see also; Li et al.,

[7] `https://c3.lbl.gov/nugent/nugent_templates.html`

[8] `http://www.astro.ucla.edu/~wright/CosmoCalc.html`

2011). For every galaxy in the sample with a cadence period of $T_{\rm C}$-day, we run $\#T_{\rm C}$ MC simulations for each particular type of CCSNe. For example, if we consider the survey period of 5 years for a galaxy, then the number of MC simulations with a specific light curve profile is $5 \times 365 \times 7(\text{CCSNe type}) = 12775$. Now if we play with the limiting magnitude of the survey and general properties of the SN light curve profiles, such as the peak magnitude and the visibility interval, we could end up running $\sim 10^8$ MC simulations for every galaxy in the sample. For simplicity, we adopt the R-band limiting magnitude of the PTF survey, 20.5 mag, in the MC simulations, here. We will discuss the effect of limiting-magnitude of the survey on the SN rate estimations later in the discussion section.

A schematic of the performed MC simulations is shown in the Figure 4.7.

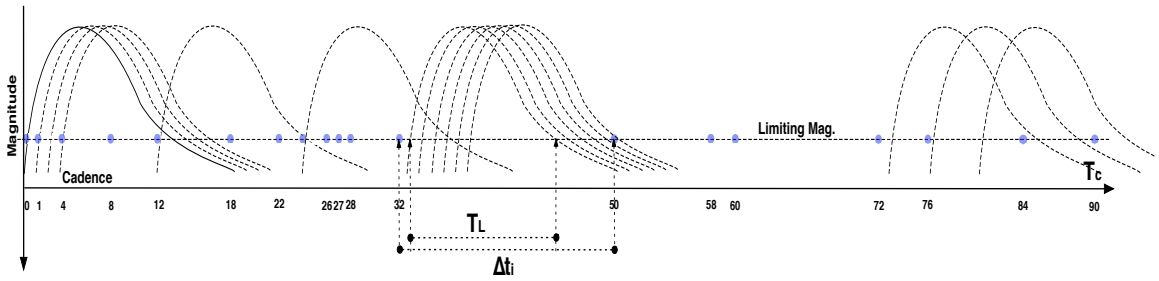

Figure 4.7: Schematic of the performed MC simulations. The small blue circles and corresponding numbers mark the locations of observing epochs (i.e. the cadence). The limiting magnitude of the survey is shown with the horizontal dashed line and $T_{\rm L}$ represents the number of days in which the SN is visible or it stays above the detection limit. $\Delta t_{\rm i}$ is the difference between two consecutive epochs and $T_{\rm C}$ is the cadence period.

We draw a typical CCSN template light curve which is translating along the horizontal axis (survey time) with the step size of one-day. To demonstrate the concept, we draw only some template light curves at different random epochs as illustrated in the Figure 4.7. The small blue circles and corresponding numbers mark the locations of observing epochs (i.e. the cadence) in the survey. The limiting magnitude of the survey is shown with the horizontal dashed line and the $T_{\rm L}$ represents

the number of days when the SN is visible or it stays above the detection limit. $\Delta t_{\rm i}$ depicts the difference between two consecutive epochs.

The SN detection efficiency given a cadence then can be calculated based on the MC simulations and as a probability formula described in Appendix D. As we mentioned earlier, a separate MC simulation is performed for each particular type of CCSNe. Finally, we combine the contributions of each SN type using the relevant fractions adopted from Smith et al. (2011) to calculate the total probability as the following:

$$\begin{aligned} \mathrm{Pr_{CCSN}} &= 0.482\,\mathrm{IIP} + 0.088\,\mathrm{IIn} + 0.064\,\mathrm{IIL} + 0.106\,\mathrm{IIb} \\ &\quad + 0.071\,\mathrm{Ib} + 0.149\,\mathrm{Ic} + 0.04\,\mathrm{Ibc_{pec}} \end{aligned} \tag{4.4}$$

This value and the total counts of SNe in a galaxy are used to calculate the SN rate expressed with Equation D.3. For every galaxy in the sample, the calculated probability values for *IIP, IIL, IIn, IIb+Ib/c* are provided in Table C.1 (Columns 7-10).

4.5.3 The SN Rates Based-on the Stellar Population Synthesis Models

Evolutionary stellar population synthesis (SPS) models provide tools to estimate galaxy properties i.e. colors, luminosity, mass-to-light ratio, and SN rate. The SPS codes produce model SEDs as a function of metallicity, star formation, IMF, age, and evolution of the simulated stellar populations. The *Starburst99* (SB99; Leitherer et al., 1999) and the *GALAXEV* (BC03; Bruzual & Charlot, 2003) are two of these standard SPS codes that have been used more widely among others in the literature (e.g., Zetterlund et al., 2015). We choose *SB99* [9] (Leitherer et al., 1999; Vázquez

[9] `http://www.stsci.edu/science/starburst99/`

& Leitherer, 2005) which is more suited for modeling very young ($\lesssim$ 30 Myr) stellar populations. This is mainly true because of adopting the stellar evolutionary tracks of the Geneva group (Schaller et al., 1992; Schaerer et al., 1993; Meynet et al., 1994) by *SB99* that are optimized for massive young stars, and also include, e.g., the Wolf-Rayet phase. We assume a stellar population with solar metallicity and adopt the default *SB99* IMF, i.e., a truncated Salpeter IMF with slope 1.3 in the range 0.1 - 0.5 $M_{\odot}$ and slope 2.3 in the range 0.5 - 120 $M_{\odot}$. For the star formation law, we require an instantaneous burst; wherein all the stars are created simultaneously. We adopt the *SB99* default for the rest of other parameters. The output of the model is the spectrum of a stellar population as a function of the duration of the star formation episode.

We decided to directly estimate the SN rates from measurable quantities, e.g., FUV fluxes as opposed to the conventional approach that measures SFRs first, and then convert them to SN rates. Spectral synthesis templates used in *SB99* contain newborn and young stars FUV continuum from the gas enshrouding the stellar populations. We note that a relation between the SFRs and the SN rates suffers from two main assumptions: (a) the kind of IMF we would employ in the model and (b) the range of masses for CCSN progenitors (Cappellaro, 2014). The model could be independent of IMF as long as we use the same IMF for SFR, and the needed conversion factor between luminosity and SFR; they cancel out each other. However, the choice of a mass range is very crucial in the model. It is also suggested that in the warm, dense, ISM conditions within a (U)LIRG, e.g., Arp 299-A (Pérez-Torres et al., 2009), M 82 (Doane & Mathews, 1993) and Arp 220 (Parra et al., 2007), the IMF should be top-heavy, in contrast with to the conventional Salpeter (Salpeter, 1955), or Kroupa (Kroupa, 2001) IMFs, where the production of massive stars ($M \gtrsim 8M_{\odot}$) that eventually produce CCSNe is low compared to the production of less massive

stars.

As discussed in Section 1, the luminosity at 1500 Å is a useful indicator of the SFR (Pettini et al., 1997) since the continuum at this wavelength comes from the late-O/early-B stars (Leitherer et al., 1999). We downloaded the time dependent monochromatic luminosity, L_{1500}, (erg s^{-1} $Å^{-1}$) and the SN rate (yr^{-1}) information for an instantaneous star-forming galaxy model of 10^6 $M_\odot$ with the solar metallicity, and a Salpeter IMF from the *SB99* website. Given the measurements of special FUV flux densities (erg s^{-1} cm^{-2} $Å^{-1}$) and the D_L, we calculate the amount of special FUV luminosities for every galaxy in the sample using $L_\nu = 4\pi D_L^2 f_\nu$ (erg s^{-1} $Å^{-1}$) formula. The luminosities are not corrected for dust. The L_ν/L_{1500} ratio enable us to estimate roughly how much massive a particular galaxy is in comparison with the model galaxy. This factor is used later to scale the amount of SN rate for that galaxy. The results of SN rate calculations for all the galaxies in the sample are provided in the last column of Table C.1. Figure 4.8 shows the distribution of the SN rates versus $\log_{10}(L_{ir}/L_\odot)$ for all the galaxies in the sample. Since ULIRGs have higher SRF compared to LIRGs, it is expected they also possess higher SN rates, in general. However, the measured FUV luminosities and hence predicted SN rates do not follow L_{ir} due to obstruction as it is shown in Figure 4.8.

4.5.4 The SN Rates Comparison

Finally, we want to compare the observationally determined values for the expected SN rates using the PTF survey and the computational estimations of the same quantities using the *SB99* model.

In order to characterize and measure the SN rates, we utilize the Kaplan-Meier (KM; Kaplan & Meier 1958, see also Feigelson & Nelson 1985) survival analysis. This is necessary because many galaxies only permit upper limit measurements of SN rates.

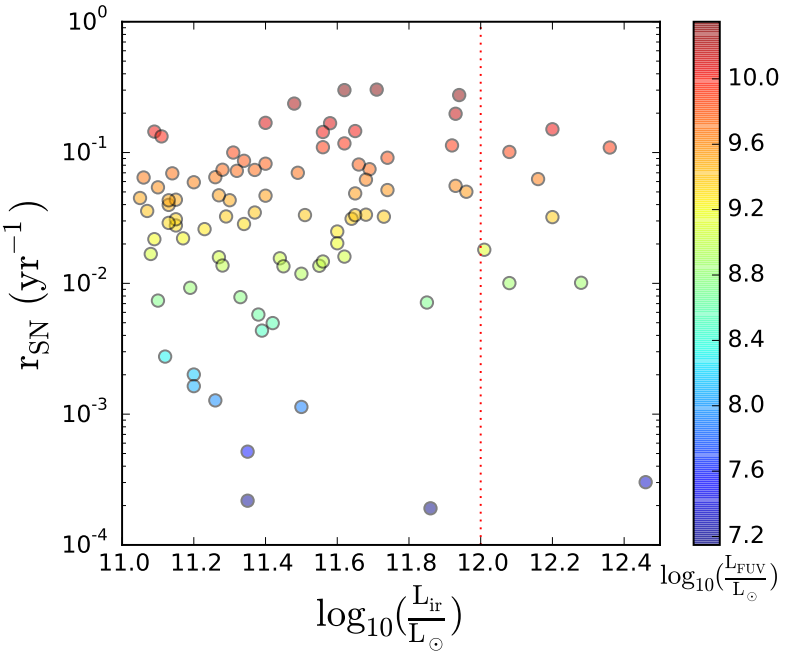

Figure 4.8: Distribution of the SN rates versus $\log_{10}(L_{ir}/L_\odot)$ for all the galaxies in the sample. The vertical red dotted-line separates the LIRGs and ULIRGs of the sample. Colorbar depicts the values of $\log_{10}(L_{FUV}/L_\odot)$.

Figure 4.9 illustrates the probability of the SN occurrence – including the shaded 1σ error region – as a function of control-time, τ (the blue solid line and the shaded region).

Using the same Poisson probability distribution assumption for the SN occurrences, we find the probability of finding one SN or more in our sample as $1 - exp\big(-(\sum_{i=1}^{N} k_i / \sum_{i=1}^{N} \tau_i)\,\tau\big)$. This expression is also shown in the Figure 4.9 with the dashed red line including the 1σ error region constrained between the dotted red lines. In order to compare these results with the SN rates estimations using the *SB99* model, we derive a similar formula as $1 - exp\big(-(\sum_{i=1}^{N} r_i)/N\,\tau\big)$ which is shown with the solid black line in the same Figure.

The plotted curves in the Figure 4.9 show that the results of observed SN rates could match with that of predicted SN rates at their higher margins. This consistency

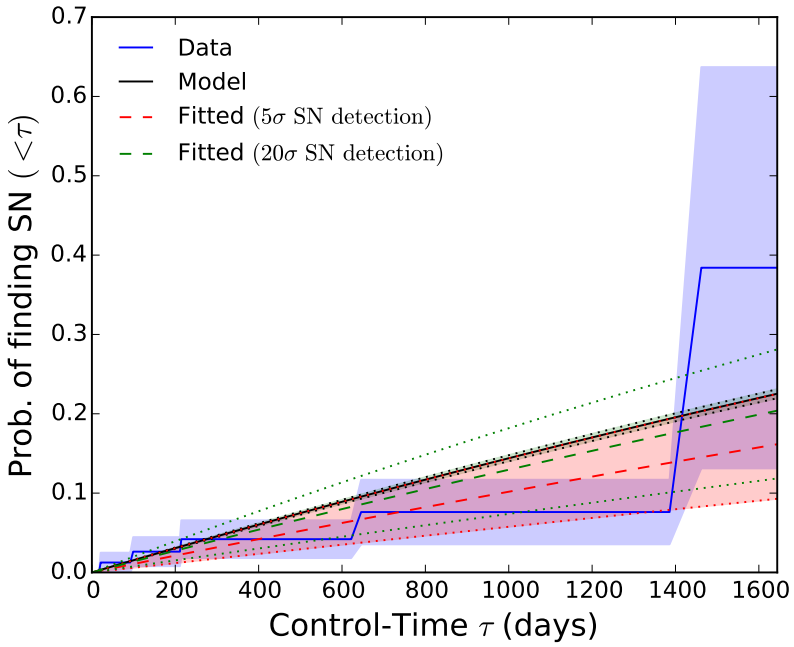

Figure 4.9: The KM cumulative estimation curve (the blue curve) of the SN rates for all galaxies in the sample including the shaded 1σ error region (the blue region) as a function of control-time, τ. The dashed red and green lines represent the $1-exp\big(-(\sum_{i=1}^{N} k_i/\sum_{i=1}^{N} \tau_i)\,\tau\big)$ formula, the probability of finding one SN or more in our sample, for 5σ and 20σ SN detections, respectively. The solid black curve represents the $1-exp\big(-(\sum_{i=1}^{N} r_i)/N\,\tau\big)$ formula, the same quantity estimation using the FUV flux measurements and the *SB99* model. The shaded 1σ error regions around the curves with edges marked with dots are also shown.

is optimistic if we adopt the nominal PTF limiting magnitude in the R-band, 20.5 (5σ), in the MC simulations. The limiting magnitude of the survey images is an important ingredient for the calculation of the control-time (Leaman et al., 2011) and hence the SN rate. We also implemented the MC simulations using the actual limiting magnitude measurements for the available epochs of the found SNe in the survey. However, we didn't find a significant difference in the results between fixing the limiting magnitude and the real available data. In order to determine the required confidence level for an SN detection, we modeled various point-spread function (PSF) models. We found that it is extremely difficult to distinguish an optical transient – visually or using an image-subtraction code – from the background noise with a 5σ

confidence level. It starts getting more distinct if we require 10σ confidence level or higher. If we adopt $m_o = 20.5$ and $F_x/F_o \sim 20\sigma/5\sigma$ and plug in the magnitude-flux relationship, $m_x - m_o = -2.5\, log_{10}(F_x/F_o)$, we obtain $m_x = 19$ mag. Implementing the MC simulations using a limiting magnitude of 19 mag instead of 20.5 mag would result in a better agreement between observations and predictions in our analyses. This is shown in the Figure 4.9 with a green curve. We need to emphasize that it is not our intention here to improve the agreement between observation and prediction. However, it is crucial in our study to verify the confidence level of an SN detection.

The expected average of the SN rate based on the PTF survey for the LIRGs in our sample is $0.05 \pm 0.02\, yr^{-1}$/galaxy. The mean value of SN rates for the same galaxies in the sample based on the FUV flux measurements is $0.060 \pm 0.002\, yr^{-1}$/galaxy. The results show consistent mean values of the SN rates between both of the implemented methods.

It should be noted that the presented results in this chapter are based on probing the surface brightness of galaxies in the sample. The direct detection of CCSNe in the extreme ambient densities of the (U)LIRG circumnuclear regions is extremely challenging, as the optical and IR emission of SNe is highly extinguished by the massive amounts of dust. Therefore using the optical PTF survey of the (U)LIRGs, we are able at best yield a lower limit to the actual CCSN rate.

4.6 Discussions

We review in this section the main reasons which might influence our results. These include uncertainties in the SN rate calculations, detection inefficiencies, and biases on the SN detections.

4.6.1 The SN Rates and Uncertainties

There will always be some fractions of the SN events which remain hidden in the nuclear regions due to very high dust extinction (Mannucci et al., 2007; Mattila et al., 2012). Therefore, what we calculate as the observed SN rates provides just a lower limit on the actual rates. SN searches are affected by uncertain extinction correction factors, which also influence galaxy luminosity measurements, in particular in the (rest frame) UV band (Cappellaro, 2014). Since none of these quantities are corrected for dust in this work, some effects may be expected.

Implementing the MC simulations enabled us to compensate for the detection inefficiencies in our analyses. However, we should note that an MC simulation could also be affected by the uncertainties in the SN template light curve constructions.

The shape of an IMF forms the backbone of every SPS models; it dictates the ratio between low (dwarf) and high (giant) stars in a galaxy model. Conventional IMFs such as Salpeter (1955), and Kroupa (2001) produce essentially much less massive stars which potentially produce CCSNe ($M > 8M_{\odot}$) compared to the low mass stars population. It can be shown easily that the SFR and the SN rate are highly sensitive to the lower bound of an IMF model. As a result, we argue that IMF conditions in (U)LIRGs may require some treatments, i.e. being considered top-heavy due to a higher Jeans mass (e.g., Klessen et al., 2007; Pérez-Torres et al., 2009).

4.6.2 Biases on the SN Detections

Searches for astrophysical transients e.g. SNe are characterized by various features in which each one may introduce some biases in the end results. These features include: (a) instrument characteristics e.g. field of view, pixel scale, (b) search strategies e.g. depth, survey cadence, and (c) vetting algorithms to distinguish real transient

objects from bogus ones. In a comprehensive SN rate study, it is vital to characterize the observational biases which target the total count of the SN detections and also the total control-time value. The efficiency of the SN searches in the nuclear regions of (U)LIRGs, with very high-extinction (Inami et al., 2010), reduces drastically due to incompetence in visual searches, and the low performance of the image subtraction algorithms in the high-surface-brightness regions (e.g., Holoien et al., 2017). In this study, observing a particular type of galaxies, (U)LIRGs, with large number statistics enabled us to reduce possible errors in the calculation of the mean SN rate.

4.7 Conclusions

We presented the results of a 5-year comprehensive SN search study aimed to measure the SN rates in the largest compiled sample of the (U)LIRGs, ∼90. This chapter described our survey strategy including the visual search of SN detections, the observationally determined values for the expected SN rates using the PTF survey, the computational estimations of the same quantities using the *SB99* model based on the FUV flux measurements, and finally the comparison between the results of these two different approaches.

The PTF survey provides a wealth of cadence coverage for 121 LIRGs and 12 ULIRGs. The GOALS provides the FUV flux measurements for 82 of the LIRGs and 9 of the ULIRGs. We found 5 SNe, of which 3 came out as the result of our visual search and 2 using the implemented image subtraction algorithm. Many SNe have been missed due to the cadence coverage, the survey detection threshold, or by other detection inefficiencies. We performed the MC simulations to calculate the control-time for each galaxy in the sample. We derived a formula to calculate the expected value of the SN rate for the entire LIRGs sample. The KM estimations are used to account for galaxies in the sample that only permit upper limit measurements

of SN rates. We used the results of the *SB99* model to estimate the SN rate for each galaxy in the sample based on the FUV flux measurement. We found the expected average of SN rate for the LIRGs in our sample, $0.05 \pm 0.02\, yr^{-1}$/galaxy, which is consistent with the mean value of SN rate estimated using FUV flux measurements, $0.060 \pm 0.002\, yr^{-1}$/galaxy.

Chapter 5

RATIR FOLLOW-UP OF LIGO/VIRGO GRAVITATIONAL WAVE EVENTS

V. Zach Golkhou, Nathaniel R. Butler, Robert Strausbaugh, Eleonora Troja, Alexander Kutyrev, William H. Lee, Carlos G. Román-Zúñiga, & Alan M. Watson

5.1 Abstract

Since the first detection of gravitational waves, GW 150914, by the advanced LIGO facility in September 2015, additional triggers have been reported. During the first observing run of LIGO, *O1*, the electromagnetic counterpart followup community received reports on two GW candidates, with the last one confirmed to be astrophysical. In addition to GW 150914, this added another confirmed GW detection to the list of LIGO discoveries during the *O1*. In this chapter, we report on the RATIR followup observations of the second trigger, G 194575, which is not of astrophysical interest. However, is of great interests to the robust design of a followup engine to explore large sky error region.

We discuss the development of an image-subtraction pipeline for the 6-color, optical/NIR imaging camera RATIR, that can reach $\sim 90\%$ followup efficiency with a very small ($\approx 1\%$) false alarm rate. Considering a two band (i and r) campaign in the Fall of 2015, we find that the requirement of simultaneous detection in both bands leads to a $\sim 60\%$ reduction in false alarm rate, which can be further reduced using additional bands. We also show that the performance of our proposed algorithm is robust to fluctuating observing conditions, maintaining a low false alarm rate with a modest decrease in system efficiency that can be overcome utilizing repeat visits.

A version of this chapter is submitted to *The Astronomical Journal*.

Expanding our pipeline to search for either optical or NIR detections (3 or more bands), considering separately the optical *riZ* and NIR *YJH* bands, should result in a false alarm rate $\approx 1\%$ and an efficiency $\approx 90\%$. RATIR's simultaneous optical/NIR observations are expected to yield about one candidate transient in the vast 100 deg^2 LIGO error region for prioritized followup with larger aperture telescopes.

5.2 Introduction

The first ever direct detection of the Gravitational Wave (GW) signal, GW 150914, was made by Advanced LIGO (Aasi et al., 2015) in September 2015 (Abbott et al., 2016a) from a binary blackhole merger (Abbott et al., 2016c). This discovery entered us into the GW era; however, complementary identification of electromagnetic (EM) counterparts to GW events is required to guide us to the next stage: the GW-EM multi-messenger astronomy era (Metzger & Berger, 2012).

A joint EM-GW detection would constrain the fundamental physical properties of compact binary coalescence (CBC) events such as the luminosity, energy scale, and host galaxy environment. However, identifying a counterpart is remarkably challenging due to the LIGO inherently weak localization of GW events ($\sim$ a few hundred deg^2). However, the scientific returns of such discovery justify any efforts taken, even a small step forward.

CBC events represent powerful engines for the production of gravitational (see e.g., Phinney, 1991; Belczynski et al., 2002; Abadie et al., 2010b), EM, and neutrino radiation. In the CBC model, a neutron star (NS) and compact companion in an otherwise stable orbit lose energy to gravitational waves (e.g., Ramirez-Ruiz & Fenimore, 2000; Nakar, 2007). Disruption of the NS(s) provides matter, which can be ejected in relativistic jets. The prompt gamma-ray emission is widely thought to be created by internal shocks, the interaction of outgoing matter shells at different velocities, while

the afterglow is thought to be created by external shocks – the interaction of the outflowing matter with the interstellar medium (e.g., Rees & Meszaros, 1992; Golkhou & Butler, 2014). Short-duration Gamma-ray Bursts (sGRBs) provide our best potential link to gravitational wave sources. If these events are due to collapse-object mergers (e.g., Nakar, 2007), copious gravitational waves are expected, and these can be detected by Advanced LIGO if the source is sufficiently nearby. Indeed, due to beaming, the LIGO rate should be significantly larger (factor 10; Chen & Holz 2013) than the observed sGRB rate.

Finding the potentially rapidly fading afterglow of a GW source requires the engagement of facilities world wide with fast response times. Many facilities have participated in the search for the EM counterparts of LIGO GW events – in the optical, X-ray, and radio bands – and have reported their followup strategies to the community (e.g., Connaughton et al., 2016; Evans et al., 2016; Kasliwal et al., 2016; Smartt et al., 2016; Soares-Santos et al., 2016; Díaz et al., 2016).

Here, we present the Reionization and Transients InfraRed (RATIR) observatory followup effort. RATIR is a simultaneous 6-channel imaging camera (r band through H band), mounted on a robotic 1.5 m telescope at San Pedro Mártir Observatory, Baja, CA, MX (Butler et al., 2012). The NIR capability of RATIR is highly desirable, with the recent clue that some sGRBs may be associated with very red "kilonova" events (Barnes & Kasen, 2013). The astrophysical relevance of a kilonova discovery goes far beyond the study of sGRBs with which they may be associated. It hands astronomers a powerful tool to identify the EM counterpart of future GW detections (Bloom et al., 2009; Metzger & Berger, 2012; Piran et al., 2013), and bears key implications for cosmic nucleosynthesis studies, as it suggests that NS mergers could be the prime sites for production of the heaviest (i.e. those with atomic mass number $A > 130$) r-process nuclei (e.g., Rosswog et al., 2014). The bulk of the energy is

emitted in the infrared band, and its emission peak is broad, lasting for $\sim 7-10$ days in the rest frame. A kilonova within 100 Mpc would likely be quite bright in the NIR and amenable to detection. At such distances the source in Tanvir et al. (2013) would have $H < 18.5$ mag (AB). RATIR reaches 10σ limiting AB magnitudes in 10 minutes of 22.0, 21.4, 20.2, 19.7, 19.6, 18.9 in the *riZYJH* bands, respectively.

In this chapter, we focus our analyses on the trigger G194575 (Singer et al., GCN 18442), which we were able to promptly observe in Fall 2015 (Butler et al., GCN 18455). Despite the fact that this trigger found to be unrelated to any astrophysical object later (LIGO Scientific Collaboration, GCN 18626), the rather larger error region $\sim$1000 deg^2 provided us a highly challenging exercise for the design of a robust exploratory pipeline. Similar to other triggers received from the LIGO collaboration team, the EM counterpart followup community responded quickly to the trigger and was actively followed until its non-astrophysical origin became apparent. During that time, ground-based observatories reported two sources of potential interest regarding the trigger, LSQ15bjb detected by the La Silla-QUEST (Rabinowitz et al., GCN 18473) and iPTF15dld detected by the iPTF (Singer et al., GCN 18497). RATIR observed the La Silla - QUEST candidate and reported a clear detection of the source in the i, r, and z bands (Golkhou et al., GCN 18500).

In section 2, we describe the survey strategy, data reduction, and analysis of the designed EM counterparts discovery pipeline. Field targeting and scheduling and also identifying and ignoring bad subtractions are presented in section 3. In section 4, we discuss our results, the expected false alarm and success rate, and address the community benefits from the RATIR pipeline. All magnitudes in the chapter are in the AB system.

5.3 Survey Strategy, Data Reduction, and Analysis

A search over the entire LIGO detector error region (several hundred square degree) using a narrow field of view (five to ten arcminute) instrument like RATIR is unfeasible due to observing time constraints. It is simply not possible to complete the survey sufficiently rapidly (within a few days) in two or more epochs to allow for a comprehensive search for variable, new objects. Instead, we target only portions of the LIGO error regions most likely to contain sGRBs.

In our strategy (Section 5.3.1), we search a much smaller portion of the LIGO error region by crossmatching GW galaxy catalog (White et al., 2011) sources and including only very bright luminous galaxies (Gehrels et al., 2016). The candidate galaxies selected based on a population-half-light criteria using the absolute B-band magnitudes, and are scheduled for visits twice per field. Return visits for image subtraction purposes are conducted on a subsequent nights.

With two or more frames captured for each target galaxy field, we performed digital image subtraction with the High Order Transform of PSF ANd Template Subtraction (HOTPANTS; Becker, 2015). HOTPANTS is an implementation of the Alard & Lupton (1998) algorithm, based on a spatially-variable kernel method that matches the PSFs of two astronomical images. Prior to running, the images are bias, dark, and sky-subtracted, flat-fielded, and astrometrically co-aligned using SWARP (Bertin et al., 2002). We use the Source Extractor (Bertin & Arnouts, 1996) software to identify sources for alignment and to estimate the image FWHM values. The quadrature difference between FWHM values is used to define the starting Gaussian sigma values for the HOTPANTS convolution. Custom point-spread-function (PSF) fitting software is used to estimate the image PSF and to obtain photometry for the difference frames. In our final photometric detections, we require $\geq 10\sigma$ detections.

While our image subtractions are typically very clean (e.g., Figure 5.2), residual flux can often be detected near bright sources or new image boundaries. These false sources are flagged and ignored (see Figure 5.3) by identifying a bright cataloged source within 10 arcsec, by comparing the (typically small) FWHM of the source relative to the median FWHM of the image, or by discarding sources near the image boundaries. Bad subtractions can also be obtained, typically yielding a large number (> 10) of detections. We have developed an automated filtering approach to minimize these cases using image quality metrics present prior to subtraction (Section 5.4.1).

5.3.1 Galaxy Strategy

A typical LIGO sky map error region is much larger than the field of view of optical or X-ray telescopes. Due to the time constraints of rapid followup, covering a few hundred or even a few tens of the sky square degrees is not a practical approach by a small FoV telescope. Therefore, finding an optimal strategy which determines the ideal domain of investigations should be at the core of any pipeline designs of LIGO GW followup sources (e.g., Hanna et al., 2014; Bartos et al., 2015). A catalog of galaxies which has already satisfied some critical criteria relevant to our search is required. These criteria are adequate sky coverage, sufficient depth, and galaxy brightness (high blue luminosity). The latter condition is important because blue luminosity is a tracer of recent star formation and sources produced by stars ought to track the light.

The Gravitational Wave Galaxy Catalog (GWGC; White et al., 2011) is an attempt to offer such a galaxy catalog and has been used by many followup groups e.g. DLT40, Swift-XRT, UL50, Kanata, OAO-WFC, and RATIR. We used GWGC as our main catalog during *O1* while also following a similar galaxy strategy as Gehrels et al. (2016) which considers only brighter galaxies that produce $\sim$50% of the light.

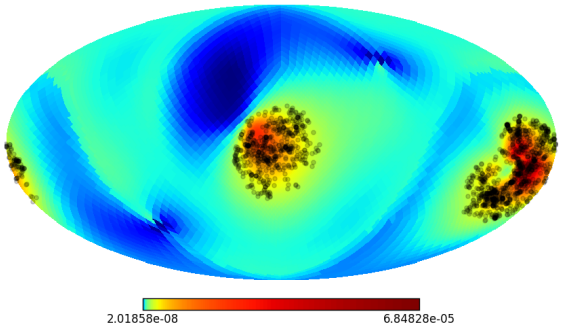

(a)

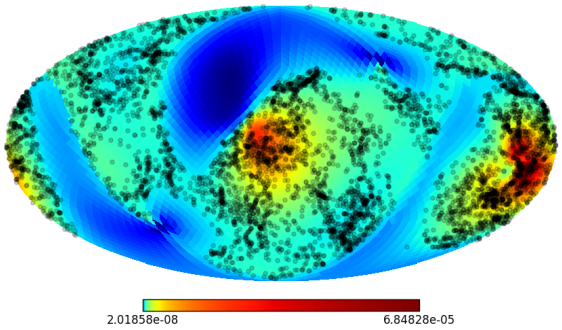

(b)

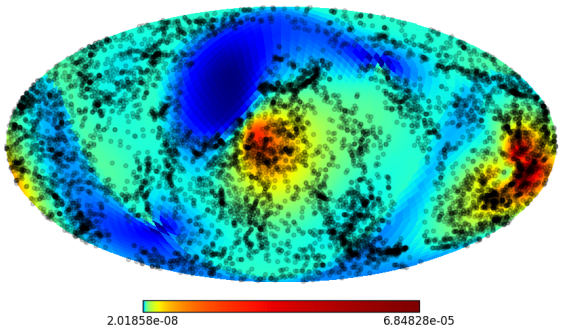

(c)

Figure 5.1: The BAYESTAR GW probability skymap in *log* for trigger G194575 over-plotted with the list of galaxies in the GWGC with black dots for 1σ (fig. 1a), 2σ (fig. 1b), and 3σ (fig. 1c).

This constrains the absolute blue magnitude of galaxies to less than -20.025 mag; eliminating ∼80% of galaxies in the GWGC.

The modified GWGC is complete ∼100% out to about 60 Mpc which is consistent with the LIGO estimate of sensitivity coverage during *O1* run. The estimate of completeness is defined based on B-band magnitude which is expected to follow sGRB rate (Fong et al., 2013). At distances ∼100 Mpc, the GWGC completeness reduces to about 85% for the selected bright galaxies (see the figure 3 of Gehrels et al. 2016). Caution will be necessary during the LIGO *O2* and later runs since we expect to detect GW events due to the binary NS at distances exceeding 100 Mpc (Abbott et al., 2016d), beyond which the incompleteness of the GWGC increases. New catalogs more suitable for the next LIGO runs are under construction (e.g. CLU, Gehrels et al. 2016, and GLADE [1], Dalya et al. 2016).

5.4 Field Targeting and Scheduling

Upon a trigger, our pipeline automatically receives the probability skymap error region from the LIGO collaboration. The sky localization is provided at low-latency by the "BAYESTAR" and "CWB" pipelines, and later with "LALInference". The skymap error region is projected onto the modified GWGC, as described in the previous section, and a list of candidate galaxies is made. Figure 5.1 shows the BAYESTAR GW probability skymap for trigger G194575 (Singer et al., GCN 18442). Regions with the darker red color represent higher probability GW source localization and regions with the darker blue color are associated with the lowest probability GW source locations. The color bar shows the corresponding probability values. The GWGC contains 53,312 galaxies and our bright galaxy criterion ($x_{1/2} > 0.626$, see Gehrels et al. (2016) for details) typically passes only ∼20% in a given sky area. Projecting

[1] `http://aquarius.elte.hu/glade/`

the G19475 skymap within 1σ error region onto our galaxy catalog results in 1539 candidate galaxies which are shown with black circles in Figure 1a. This number for 2σ (fig. 1b) and 3σ (fig. 1c) is 6057 and 8217, respectively.

Given that not all these galaxies will be visible at SPM, we expect to followup about half of the galaxies in the list. This is still a large number even for the 1σ error region. The RATIR scheduler selects and queues targets automatically to be imaged at the first available time. Nominally, we also rank the list of candidate galaxies based on the B-band luminosity value. It is also possible to prioritize based on distance estimates provided in the LIGO/Virgo GCN notices. An estimate of the LIGO GW source distance was not available during the *O1* run.

Given the available observing time, we observed 26 nearby galaxies ($D < 10$ Mpc) within the GWGC catalog and contained with the 1σ LIGO/Virgo error region for trigger G194575 (Singer et al., GCN 18442). Between RA 23.1 hours and RA 1.5 hours (J2000) with RATIR on the night of 2015/10/23, we obtained a total exposure of $\sim$8 minutes on each of the 26 fields (see Appendix D, Table D.1), reaching typical depths of r and $i = 21$ mag (AB, 10σ). These magnitudes are not corrected for Galactic extinction. Each field, centered upon one GWGC galaxy, has a size of approximately 5×5 arcmin^2. We observed these fields on two more consecutive nights (10/24 and 10/25; Table D.1). We had a typical seeing of 1.8 arcsec each night. To reach comparable limiting magnitudes on the third and final night, a 50% increase in exposure time was required to overcome highly non-photometric observing conditions. On the first two nights, the i-band zero points were stable (to within 10%) while the zero point varied by nearly a factor of unity on the third night. The NIR RATIR channels (*ZYJH*) were not available at this time.

Figure 5.2 shows a gallery of image subtraction frames for targets #14, #16, and #23 in the i and r bands. The images on the left, middle, and right columns show

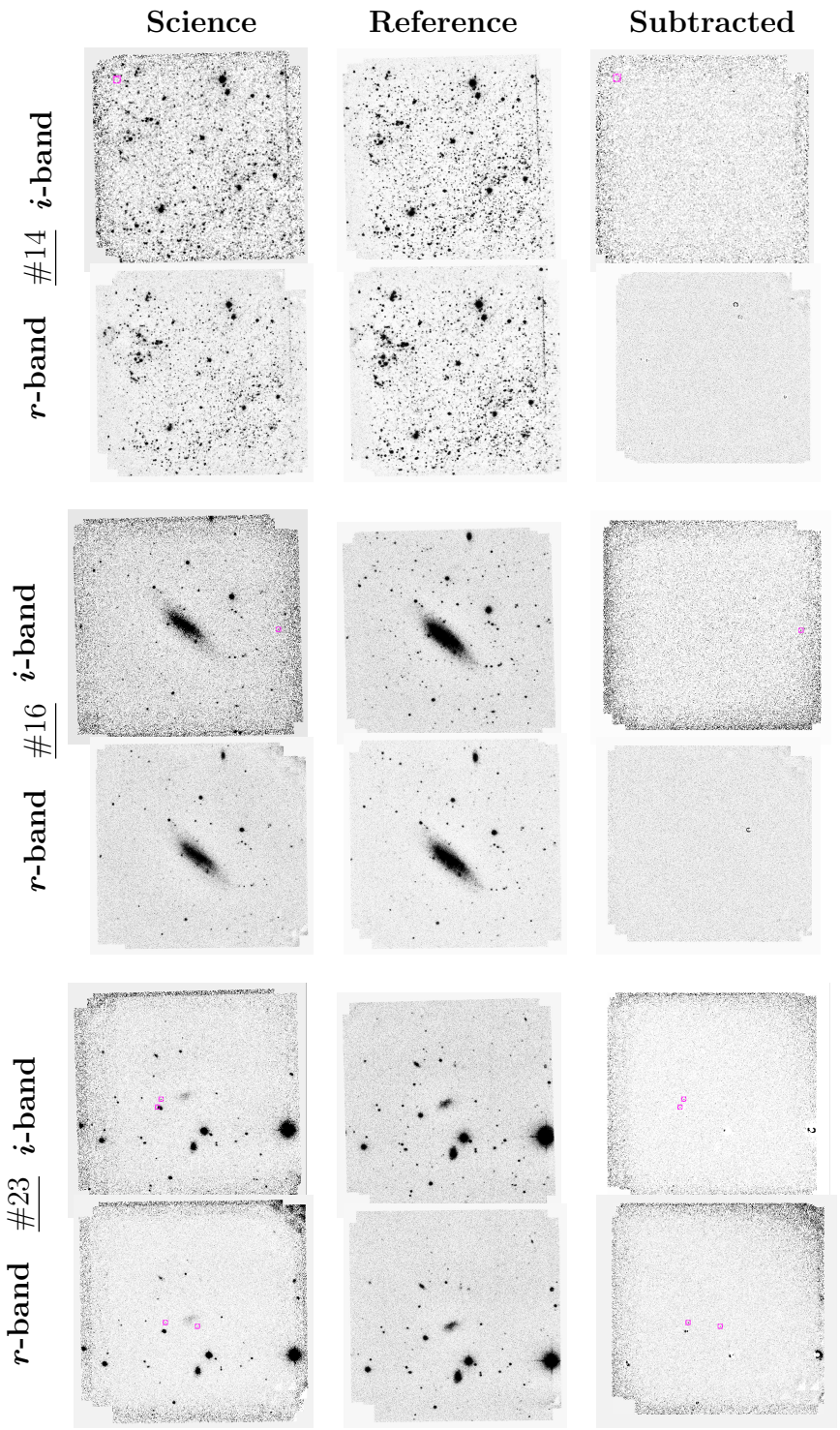

Figure 5.2: A gallery of image subtraction frames for targets #14 (1st & 2nd rows), #16 (3rd & 4th rows), and #23 (5th & 6th rows) in the i and r bands. The images on the left, middle, and right show science (10/24), reference (10/23), and the subtracted frames, respectively. Detected sources marked with red squares in the science and subtracted frames. The sizes of all the postage-stamps are: 5×5 arcmin^2.

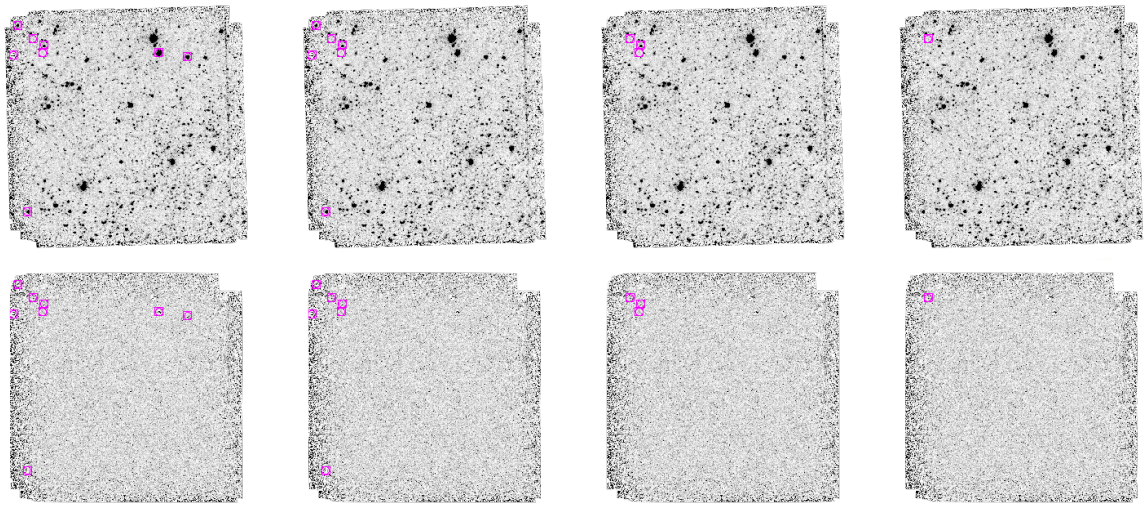

Figure 5.3: Various steps of removing false detected sources marked with red squares of target #14 in the source frame i-band (top row) and the subtracted frame (bottom row). All the raw detected sources are shown in the first column (no filter). The initial step of filtering rejects multiple detections around same stars (second column). The subsequent step of filtering removes false detections on the edge of a frame ('distance to edge' < 62 pixel). The last step of filtering rejects extra clustered detections around a source ('cluster radius' < 14 arcsec). The sizes of all the postage-stamps are: 5×5 arcmin^2.

science, reference, and the subtracted frames, respectively. We note that the image subtraction is typically extremely clean. Each of the selected targets shown in the Figure 5.2 represents a different type of target field. Target #14 is a very crowded field with many stars in the foreground and thus not very deep. Target #16 is a deep image with the targeted galaxy in the center and adequate sources for the alignment task, ideal for our purpose. Target #23 is a semi-crowded field with manageable number of sources for image-subtraction. Detected sources are marked with red squares in the science and subtracted frames. Fields #14 and #16 contain only one false detection in the i band. In field #23, each of the i and r bands comprises two false detections; however, only one of them appears in the same position on the two frames.

5.4.1 *Identifying and Ignoring Bad Subtractions*

We now implement our modified image-subtraction routine (Section 5.3) to detect any possible transients (see Figure 5.3). The top row in Figure 5.3 shows target #13 (science frame from 10/24) and the bottom row shows the subtracted frame (the 10/23 frame was used as the reference frame). Each column shows various steps of removing false detections. No filter is implemented for the first column. The initial step of filtering rejects multiple detections around same stars (second column). The subsequent step of filtering removes false detections on the edge of a frame ('distance to edge' < 62 pixel). The last step of filtering rejects extra clustered detections around a source ('cluster radius' < 14 arcsec).

In principle, having observed 26 galaxy targets in 2 optical bands for 3 consecutive nights, we can carry-out $26 \times 3 \times (2) \times 2 = 312$ different image subtractions. The extra factor of 2 takes into account the two possible way of subtracting two images. In practice, we would like to only conduct one subtraction per field in a way that yields the highest quality subtraction. We now use all possible subtractions to explore how to find the best possible subtraction.

Figure 5.4 shows a histogram of the number of detections in all frames. The number of false detections is zero for about half of the frames. For 90% of the rest is less than 10 detections, and we take < 10 detections to define a good subtraction. A well-posed subtraction will always have a deeper reference frame with better seeing as compared to the science frame. However, because our (time-limited) observation strategy typically leads to similar depths for both *science* and *reference* frames, it is often not possible (e.g. due to changing sky transmission) to know a-priori how to do the subtraction. Nevertheless, image statistics determined pre-subtraction can help us to address this problem.

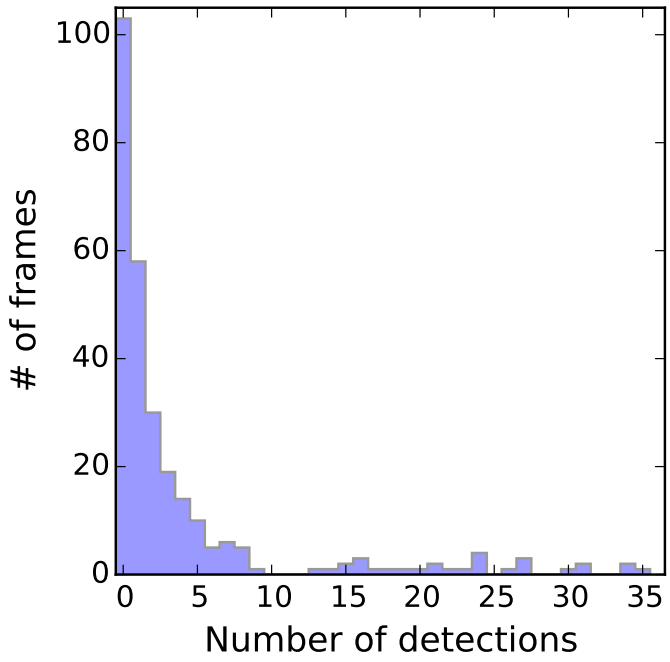

Figure 5.4: Histogram of number of detections in all frames.

We exploit the following image-quality statistics and seek to understand how these can be used to avoid bad subtractions: (1) the ratio of the PSF sigma in the science frame over the PSF sigma in the template, (2) the ratio of number of stars in science and template frames, and (3) the median of the RMS-fraction between science and template frames. Hereafter, we refer to these parameters as Par_1, Par_2, and Par_3, respectively. We now seek to define a sequential filtering on these parameters – to be coded into an image subtraction wrapper – that yields the most compact K%-Confidence Interval (C.I.; Eq. 5.1), e.g. 90%, dumping outliers).

$$\text{C.I.} = P(a_k \leq \text{Par}_\text{k} \leq b_k) \tag{5.1}$$

Here subscript $k = [1, 2, 3]$ and the a and b values specify the parameter lower and upper bounds that contain C.I. percent of that parameter space.

Figure 5.5 shows scatter plots of the Par_1, Par_2, and Par_3 values of all subtracted

images versus their number of detected sources, separately. It also presents the three stages of filtering implementing consecutively on their parameter spaces, in the same order. The Par_1 data within $[a_1, b_1]$ range feeds to the second filter which implements on the Par_2 space, and so forth, the Par_2 data within $[a_2, b_2]$ range feeds to the third filter which implements on the Par_3 space. To reach the 90%-C.I. at the end of filtering task, the image subtraction wrapper figures out how to set the same value of K between the filtering stages. Cuts in the parameter space are shown with dashed lines in the Figure 5.5.

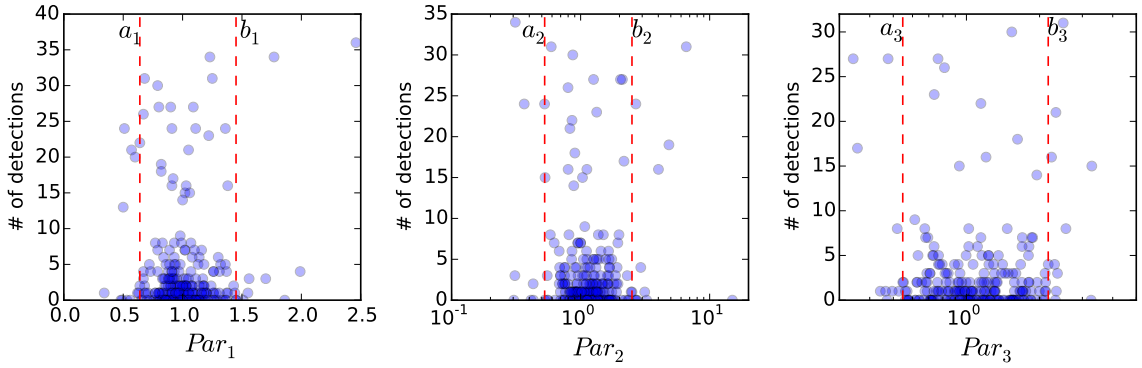

Figure 5.5: Three stages of filtering implementing consecutively on the Par_1 ($\sigma_{\rm sci}/\sigma_{\rm tmp}$), Par_2 ($N^{\star}_{\rm sci}/N^{\star}_{\rm tmp}$), and Par_3 ($RMS_{\rm sci}/RMS_{\rm tmp}$) parameter spaces, in order. Cuts in the parameter space keep data within the most compact 90%-confidence interval and are shown with dashed lines.

The expected performance of the image subtraction wrapper as the C.I. is varied can be visualized (Figure 5.6) by plotting the *Bad* subtraction rate versus image retention rate. We define in Equation 5.2 the image retention rate, $r_{\rm rtn}$, of a filter as the ratio of number of accepted *Good* subtracted frames, G_i, over the total number of input frames. Similarly, the *Bad* subtraction rate, $r_{\rm sb}$, is defined as the ratio of the number of accepted *Bad* frames, B_i, over the total number accepted frames, $B_i + G_i$ (Eq. 5.3). Subscripts i and o represent data inside and outside of the $[a_k, b_k]$ interval, respectively.

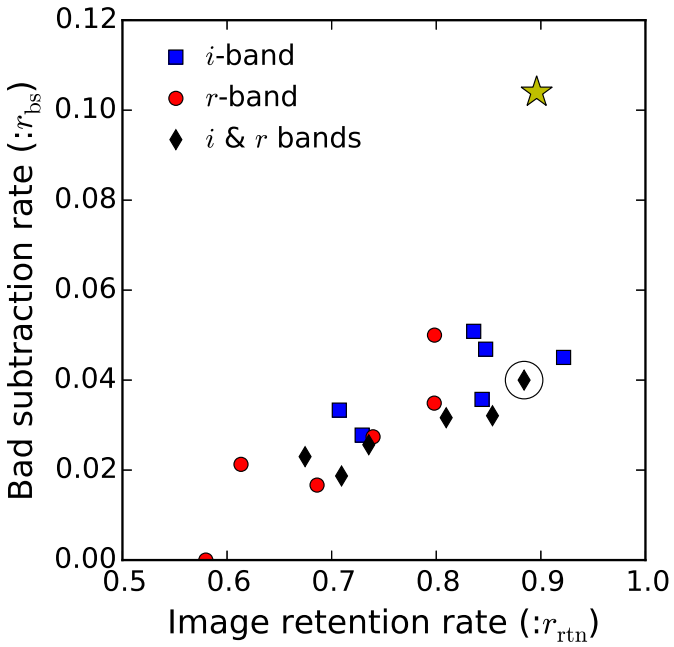

Figure 5.6: Yellow star: the performance of the system before filtering process (raw data). Blue squares: the wrapper performance estimations based on the i-band data as test set, while the r-band data was used as the training set (a 2-fold cross validation). Red circles: the wrapper performance estimations estimated based on the r-band data as test set, while the i-band data was used as the training set. Black diamonds: the wrapper performance estimations estimated based on both i and r bands. The circled black diamond specifies our desired system efficiency. *The wrapper delivers a robust performance independent of the input.*

$$i \in [a_k, b_k] \qquad o \notin [a_k, b_k]$$

$$\text{Image retention rate} : r_{\rm rtn} = \left(\frac{G_i}{\sum frames}\right) \tag{5.2}$$

$$\textit{Bad} \text{ subtraction rate} : r_{\rm sb} = \left(\frac{B_i}{B_i + G_i}\right) \tag{5.3}$$

Blue squares in Figure 5.6 represent the data points based on the i-band data as the test set and red circles show the data points based on the r-band data as the test set. Black diamonds correspond to use of both r and i bands. The tight clustering of these three curves in Figure 5.6 illustrates that the filtering system is quite robust with respect to which data are used to train and test and can achieve high image

retention rates ($\sim$ 90%) with low bad subtraction rates ($\sim$ 4%). For comparison purposes, the efficiency of the system prior to the filtering process, raw data, is also displayed on the Figure 5.6 with a yellow star. We adopt the circled black diamond in Figure 5.6 as our final bad subtraction filter. To reach this performance, the wrapper sets the following constraints for each of the Par_1, Par_2, and Par_3 values as [0.64, 1.45], [0.53, 2.5], and [0.55, 2.17], respectively.

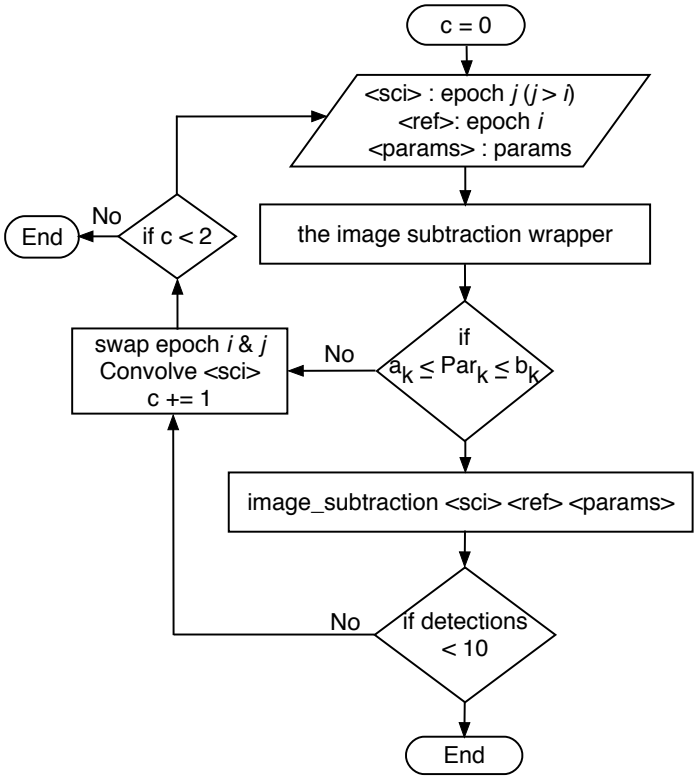

Figure 5.7: *Flowchart*. The procedure to determine how best to subtract two images to yield a reliable result (detections < 10).

For each of the imaged fields on two different epochs in our data set, we may now identify the optimal subtraction approach prior to performing the subtraction. This procedure is described using a *flowchart* presented in the Figure 5.7. The detailed steps in the *flowchart* are performed for each of the imaged fields in the i and r bands, separately. We note that, as the last step, a visual inspection is conducted to

to remove frames with spurious features like satellite trails.

5.5 Results & Discussion

RATIR performed rapid-response followup to the second GW trigger released to the EM partners by the LIGO team during the *O1* operating run. The observing time constraints allowed us to image 26 galaxies ($D < 10$ Mpc; Table D.1). The candidate fields were followed for two more consecutive nights. We imaged each of the 26 fields in both the i and r bands and performed our modified image subtraction routine to search for any possible transients.

For the 25 imaged fields on 10/23 and 10/24 nights, we found only two fields (out of 20) yielded more than zero detections at the same sky position in the both i and r bands. From this, we can estimate a false-alarm-rate (FAR) of $2/20 = 0.1$ and an efficiency of $20/25 = 0.8$. This is an "AND" rule for comparing the r and i bands to find detections. We can also consider an "OR" rule, either i or r band detections. We find FAR and efficiency values of 0.64 and 0.92, respectively, in this case. These results and those including the 10/25 night are shown in the Figure 5.8. The advantage of multi-bands imaging is clear.

Inspections of all the imaged fields on 10/25 epoch demonstrate a higher level of background noise – compared to the two previous epochs – due to the non-photometric conditions. This effect impacts primarily the detection efficiency as shown in the Figure 5.8.

Since the G19475 trigger was not of astrophysical origin, we did not expect to ascertain a real transient associated with the event. Therefore, we are not able to determine a true sensitivity. To validate the sensitivity of our approach, we analyze a set of supernova images captured with RATIR (PI, Ori Fox). The SNe images were taken using both RATIR's optical and Infra-red bands. Studying 5 SNe fields

in the *irZYJH* bands for two different epochs, we verified that all difference frames containing a 10σ flux excess are indeed recovered via our methodology.

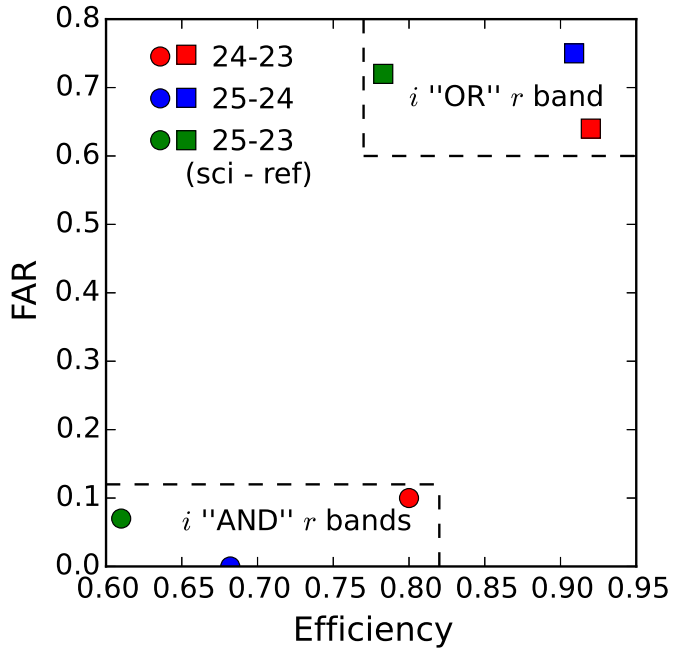

Figure 5.8: FAR and efficiency of the designed EM counterparts to GW events pipeline. Candidate galaxies are imaged on three subsequent epochs, 2015/10/23, 10/24, and 10/25. Algorithm throughput represents with circles if we require both i "AND" r bands and with squares if we require either i "OR" r band. The combination of multiple frames drives the *FAR* down as $\lesssim 0.1^{N_f-1}$ (N_f depicts the number of available filters).

5.5.1 End-to-End Sensitivity and False Alarm Rate

Given RATIR's simultaneous optical/NIR observing capability, an optimal strategy – which reduces *FAR* as much as possible while keeping sensitivity high – would be searching for either optical or NIR detections (3 or more bands), considering separately *riZ* and *YJH*. This can be viewed as a sGRB strategy with optimal depth (using the *riZ* filters), combined with a simultaneous NIR (*YJH* band) survey to find potential kilonovae. Extrapolating our results from optical bands (i and r), we expect a 3-band survey to exhibit a $FAR \approx 1\%$ and an image-retention efficiency $\approx 90\%$, provided that multiple nights are allocated to re-observe targets missed initially. We note

that a simultaneous multicolor approach is typically employed to increase the probability of detection (see e.g. Szalay et al., 1999); however, our approach is somewhat different in that we utilize the multiple bands to maintain (10σ) detection capability while greatly minimizing false alarms. This is a crucial aspect of the RATIR followup engine as it will add the most confidence to justify additional observing requests with larger aperture facilities. We have rigorously tested the tradeoff between false alarm rate and sensitivity in the design of our implemented methodology.

In order to estimate the total system throughput for potential EM gravitational wave counterparts detected by RATIR, we adopt a similar LIGO (and Virgo) error region fraction value as Gehrels et al. (2016) for *O2* (2017) $\sim 100\,\mathrm{deg}^2$. If we utilize the GWGC nearby galaxy catalog and select the brightest galaxies representing half of the population light (1 galaxy per deg^2, White et al. 2011), we can concentrate observations on about 100 galaxies in the LIGO (and Virgo) 3σ error region. Given that not all the candidate galaxies in our list will be visible at the RATIR observatory site, we expect the candidates list to be reduced by about half. As mentioned in the Section 1, RATIR reaches its design 10σ limiting magnitude in about 10 minutes, and the candidate sources are expected to be brighter than our limiting magnitudes. Allowing for a conservative overhead of 20% for slew between galaxy positions, we expect to be able to survey all the galaxies in about 10 hrs. In this case of narrower regions, we are able to integrate more deeply and also to check for same variability same night. Our nominal strategy is then to re-observe the field the next night (or the night after in the case of poor weather) to check for variability.

The brighter galaxy selection of the GWGC maintains a galaxy completeness near 100% to a distance of $\sim$90 Mpc and drops to 85% at the distance of $\sim$100 Mpc as the upper bound region. The error region source fraction resulting from the wrapped image subtraction approach reduces the search space region to about 90% as the im-

age retention rate. Our automated pipeline flags ∼1% of the candidate imaged fields as potential targets for the additional followup. Combining the galaxy completeness ($\approx 50\%$) with the RATIR survey completeness ($\approx 45\%$), limited primarily by observability, we estimate a final success rate of $\approx 20\%$. This is an excitingly large number, given the great scientific impact of an identified EM counterpart to a gravitational wave event. The possibility of multiple followup campaigns of separate triggers only increases our chances. In 2016/2017, RATIR observed the fields of two more LIGO triggers, and analyses are underway.

As LIGO/Virgo sensitivity increases, we will require a galaxy catalog which covers distances up to ∼450 Mpc (Bartos et al., 2013) with greater completeness than is currently available. There are some attempts to combine other galaxy catalogs e.g., the 2MASS Photometric Redshift Catalog (2MPZ; Bilicki et al., 2014) with the GWGC, as a short-term plan (see also Gehrels et al., 2016; Dalya et al., 2016). We plan to adopt a more complete galaxy catalog in our pipeline as it becomes available. We have been actively following LIGO triggers during the *O2* run as well as candidate counterparts reported by other EM followup groups. The results of our observations reported in LVC/GCN circulars (e.g., Golkhou et al., GCN 20485).

As a narrow field instrument ($\lesssim 10$ arcmin), RATIR should focus on nearby galaxies within the large LIGO error circles. These nearby events are, in turn, the most likely to yield decisive CBC associations. As a six-channel, multi-color instrument, RATIR's simultaneous observations of candidates greatly reduces the number of false alarms, while also providing spectral information and additional time-sampling (see e.g., Golkhou & Butler, 2014; Littlejohns et al., 2014; Golkhou et al., 2015c), important for afterglow studies. Moreover, with the recent clue that some sGRBs may be associated with very red "kilonova" events (Barnes & Kasen, 2013), NIR observations may be essential to afterglow detection.

Chapter 6

CONCLUSIONS AND FUTURE DIRECTIONS

6.1 Conclusions

Exploring time-domain astrophysics through observation, modeling and data analysis, this thesis combines careful statistical data analysis with astrophysical observations to reveal some aspects of underlying high-energy astronomical phenomena i.e., GRBs and SNe. Here, I summarize the key conclusions.

Temporal constraints on the size of GRB Progenitors:

★ We developed a novel methodology (see Chapter 2) which ties together wavelet and structure-function analyses to measure, for the first time, the actual minimum variability timescale ($\Delta t_{\rm min}$) of GRB light curves.

★ We distinguished that there is a fundamental flaw in referencing minimum timescale measurements to the noise floor: a burst can be (and typically is) smoothly varying on timescales well below timescales where impulsive variability occurs (see Chapter 2). For example, consider the exponential tail of a GRB pulse. Statistically significant differences in flux can be measured on arbitrarily short timescales, provided the burst has a very high SNR. In a way, minimum variability timescales referenced to the noise floor are just very fancy measures of SNR (see e.g., Walker et al. 2000, Bhat 2013, McLachlan et al. 2013).

★ We demonstrated that instead of identifying the shortest observable timescale as the true minimum timescale, it is additionally necessary to confirm that the source is actually varying (in a non-smooth sense) on these timescales. The

signature of this "true" form of variability is a structure function flatter than $\Delta t^{(1)}$. The justification for this is well-laid-out in Kocevski et al. (2007) and further clarified in (Golkhou & Butler, 2014) based on the first order structure functions.

★ We showed that apart from variability that is below the noise floor (hence unmeasurable), $\Delta t_{\rm min}$ does not appear to depend strongly on SNR (see Figure 2.5).

★ We demonstrated the evolution of $\Delta t_{\rm min}$ with bandpass, decreasing from the softest to the hardest energy band (see Figure 3.1).

★ Implementing our technique to the largest sample of GRBs collected by *Swift* and *Fermi* instruments, revealed that only less than 10% of GRBs exhibit evidence for variability on timescales below 2 ms (Golkhou et al., 2016a). We concluded that millisecond variability may be quite rare.

★ Our derivations for the minimum Lorentz factor, $\Gamma_{\rm min}$, and the minimum emission radius, $R = 2\,c\,\Gamma^2_{\rm min}\Delta t_{\rm min}/(1+z)$, find $\Gamma \gtrsim 400$ which imply typical emission radii $R \approx 3 \times 10^{13}$ cm for sGRBs and $R \approx 1 \times 10^{14}$ cm for lGRBs (see Figure 3.8).

★ We presented in Chapter 3 (see Figure 3.8) a novel sGRB selection methodology, a direct measure of the emission region size, to optimize LIGO followup with ground-based telescopes (Golkhou et al., 2017a).

★ We developed statistical methodologies in Chapters 2 and 3 – uncovering physically meaningful timescales – which may have broad use in other astrophysical areas such as exoplanets and pulsars (Golkhou et al., 2016b).

Extracting the signature of time evolution:

★ We utilized *Swift* GRBs and demonstrated a correlation between $\Delta t_{\rm min}$ and redshift, marginally stronger than expected simply from time dilation (see Section 2).

★ We extended our analyses to *Fermi*/GBM in which the broad instrument energy range permits analysis in a fixed rest-frame bandpass (see Section 3). We demonstrated that the minimum timescales appear to correlate with redshift in a fashion consistent with cosmological time dilation. Correcting for this, we found no significant evidence that $\Delta t_{\rm min}/(1+z)$ evolves with redshift (see Figure 3.9). This may be partly because the number of *Fermi* GRBs with measured redshifts is low (e.g., as compared to *Swift*).

Exploring SN rates in Extreme Star-forming Galaxies (LIRGs):

★ We presented the results of a 5-year comprehensive SN search study by the PTF aimed to measure the SN rates in the LIRGs. The PTF survey presents a wealth of cadence coverage for 121 LIRGs and the GOALS provides the FUV flux measurements for 82 of the LIRGs in the sample. Combining the data from these two surveys, we have compiled the largest sample, $\sim$90, of SN rate studies in the (U)LIRGs (see Appendix C, Table C.1).

★ Difference imaging is used to search for optical transients in the LIRGs consistent with SNe. The SN rates are compared with that expected from the amount of the FUV flux measurements of the same targets using the *SB99* model. We found 5 SNe, of which 3 came out as the result of a visual search and 2 using the implemented image subtraction algorithm (see Table 4.1).

★ We calculated the expected average of SN rate for the LIRGs in our sample, $0.05 \pm 0.02\, yr^{-1}$/galaxy, which is consistent with the mean value of SN rate estimated using FUV flux measurements, $0.060 \pm 0.002\, yr^{-1}$/galaxy (see Figure 4.9).

RATIR LIGO Followup:

★ We reported on the RATIR followup observations of the trigger, G 194575, which is not of astrophysical interest. However, is of great interests to the robust design of a followup engine to explore large sky error region ($\sim$ several hundred deg^2).

★ We discussed the development of an image-subtraction pipeline for the 6-color, optical/NIR imaging camera RATIR, that can reach $\sim 90\%$ followup efficiency with a very small ($\approx 1\%$) false alarm rate (Golkhou et al., 2017a).

★ Considering a two band (i and r) campaign in the Fall of 2015, we found that the requirement of simultaneous detection in both bands leads to a factor $\sim$10 reduction in false alarm rate, which can be further reduced using additional bands.

★ We also showed that the performance of our proposed algorithm is robust to fluctuating observing conditions, maintaining a low false alarm rate with a modest decrease in system efficiency that can be overcome utilizing repeat visits (see Figure 5.8).

★ We found that expanding our pipeline to search for either optical or NIR detections (3 or more bands), considering separately the optical *riZ* and NIR *YJH* bands, should result in a false alarm rate $\approx 1\%$ and an efficiency $\approx 90\%$ (see

Chapter 5).

Therefore, RATIR's simultaneous optical/NIR observations are expected to yield about one candidate transient in the vast 100 deg^2 LIGO error region for prioritized followup with larger aperture telescopes.

6.2 Future Directions

The field of time-domain astrophysics has been rich with discovery in the past two decades, thanks to the ongoing ground-based survey and space telescopes (e.g., *Swift*, *Fermi*, RATIR, PTF, LIGO). I identify the following key areas of research in which it will be especially important to explore.

6.2.1 Uncovering the LAT Emission Mechanism

In terms of temporal characteristics of GRB light curves, the next obvious immediate step would be extending the GBM analysis (Golkhou et al. 2015) to the Large Area Telescope (LAT; 20 MeV–300 GeV) on *Fermi*. We observed that the GBM minimum timescales appear to be longer in low-energy bands and shorter in high-energy bands, with the shortest timescales corresponding to counts in the 300 keV–1 MeV band. This was interpreted as being due to the fact that this band typically lies beyond the GRB spectral peak energy, $E_{\rm pk}$, leading to faster time variation due to the curvature and/or cooling effects. We need to examine whether this shortening of timescales persists into the LAT energy bands, indicating a similar emission mechanism. Also, we should test for the time evolution of the minimum timescale (as in Kocevski & Butler, 2007): a minimum timescale which increases with time would indicate an external shock origin (e.g., Ramirez-Ruiz & Fenimore, 2000) unlike the internal shock origin likely to explain the GBM emission.

6.2.2 *GRBs as Probes of the Early Universe*

There are few direct probes (Lyman-Break Galaxies and Lyman-Alpha Emitters) into cosmic star formation and the nature of the IGM following the dark ages at the epoch of reionization. GRBs are bright enough to be seen to very great distances and their afterglows can provide redshifts and positions for their host galaxies, and in some cases details of the ISM and the IGM close to the burst, irrespective of the host magnitude itself. Thus GRBs offer a unique tracer of early star formation and the galaxy populations in the era of reionization. A high signal to noise spectrum of a GRB afterglow of even one such event will finally provide the keys to understand the nature of Pop. III stars, and their assembly conditions. As a member of the RATIR group (Golkhou et al., 2015d, 2016d,c,e,g,f; Troja et al., 2016; Watson et al., 2016; Golkhou et al., 2016i,h), I am leading a campaign for rapid spectroscopic followup of candidate high-z GRBs. We have been already awarded ToOs for 10 consecutive semesters on Magellan/FIRE observatory in Chile and we plan to continue this effort. With the continued operation of *Swift* and future experiments like SVOM expected to come online, ground-based followup with systems like RATIR to identify JWST targets will be essential. I plan to continue my GRB work as well as to pursue tying in the next generation of large ground-based telescopes (e.g., LSST, TMT, and GMT).

6.2.3 *Optimizing Ground-based Followup of Explosive Transients*

Next generation transient factories will pose unprecedented demands upon ground-based followup resources. It would be necessary to develop novel strategies for enabling and optimizing observations of explosive transients. GRB triggers, and rapid high-z identification with experiments like RATIR, can generate JWST targets. We showed how a novel selection methodology – based on high-energy, sGRB properties

– can be used to optimize *Fermi* and LIGO/Virgo followup with RATIR and other facilities e.g. the Zwicky Transient Facility (ZTF). It would be crucial to investigate implementation of this and similar prioritization strategies for other instruments, exploiting multi-wavelength data and optimizing followup to achieve low false-alarm-rates. These observations can help identify GRB afterglows and aid in the search for the EM counterparts to gravitational wave triggers utilizing large ground-based telescopes.

6.2.4 Real-time Data Mining of Massive Data Streams from Synoptic Sky Surveys

The era of large-scale time-domain astronomical surveys has arrived with projects such as the PTF, CRTS, and Pan-STARRS and will rise exponentially with the ZTF, SKA, and Large Synoptic Survey Telescope (LSST; Abell et al., 2009).

The LSST – the most data-intensive project in the history of optical astronomy – will break the existing paradigms for analysis under the data stream and transform the way we seek insights into the physical phenomena underlying such complex data. As we explore the observable parameter space, there is a real possibility of discovery of new types of objects and phenomena. Outstanding detections trigger further automated data gathering or generating actions, building up a body of related information that needs to be collated, managed and, ultimately, appraised and analyzed to determine the optimal response. The techniques and methodologies underpinning these activities belong to a new mode of scientific discovery which recognizes data as the primary focus: experiments exist to generate data which is then searched for scientifically significant patterns rather than to support or test particular hypotheses (Graham et al., 2012). This change of emphasis demands astrophysicists to embrace new mining techniques of massive high dimensional data streams and machine learning algorithms and deploy their applications. Deep learning and automated feature

extraction technologies (see Chapter 5) are among these new techniques which can be exploited for photometric redshift estimations and astronomical classifications. Developing modular, parallel, and scalable scientific codes – which can be shared with other users – and data management are also crucial to enable analyses to scale to large datasets.

6.2.5 A New Era of Multi-messenger Astrophysics

Discovery of optical counterparts of gravitational wave events with LSST requires real-time data mining of sparse, incomplete, irregularly sampled, heterogeneous, noisy, and massive data streams; a big challenge which needs to be tackled. LSST is uniquely suited to find optical counterparts of gravitational waves. Gravitational waves have been detected at high significance by LIGO. Observation of optical counterparts of gravitational wave events, including mergers of black holes and neutron stars as well as other phenomena will provide a more precise measurement on the direction, redshift and other properties of the event, necessary for its full characterization. This is essential for testing cosmology, general relativity and probing the properties of matter at supranuclear densities in neutron stars.

In the context of current and upcoming facilities, it is an extremely exciting time for time-domain astrophysics. The field has been ripe with discovery, and will no doubt continue to satisfy and surprise us for decades to come.

REFERENCES

Aasi, J., Abadie, J., Abbott, B. P., et al. 2015, Classical and Quantum Gravity, 32, 115012

Abadie, J., Abbott, B. P., Abbott, R., et al. 2010a, Nuclear Instruments and Methods in Physics Research A, 624, 223

—. 2010b, Classical and Quantum Gravity, 27, 173001

Abbott, B. P., Abbott, R., Abbott, T. D., et al. 2016a, Physical Review Letters, 116, 131103

—. 2016b, Physical Review Letters, 116, 061102

—. 2016c, Physical Review Letters, 116, 241102

—. 2016d, Living Reviews in Relativity, 19, 1

Abdo, A. A., Ackermann, M., Ajello, M., et al. 2009a, ApJL, 706, L138

Abdo, A. A., Ackermann, M., Arimoto, M., et al. 2009b, Science, 323, 1688

Abdo, A. A., Ackermann, M., Ajello, M., et al. 2010, ApJ, 722, 520

Abell, P. A., Allison, J., Anderson, S. F., et al. 2009, arXiv preprint arXiv:0912.0201

Ackermann, M., Asano, K., Atwood, W. B., et al. 2010, ApJ, 716, 1178

Ackermann, M., Ajello, M., Asano, K., et al. 2011, ApJ, 729, 114

—. 2013, ApJS, 209, 11

Aharonian, F., Akhperjanian, A. G., Barres de Almeida, U., et al. 2009, A&A, 495, 505

Akerlof, C., Balsano, R., Barthelmy, S., et al. 1999, Nature, 398, 400

Alard, C., & Lupton, R. H. 1998, ApJ, 503, 325

Allan, D. W. 1966, Proceedings of the IEEE, 54, 221

Aretxaga, I., Cid Fernandes, R., & Terlevich, R. J. 1997, MNRAS, 286, 271

Armus, L., Mazzarella, J. M., Evans, A. S., et al. 2009, PASP, 121, 559

Atwood, W. B., Abdo, A. A., Ackermann, M., et al. 2009, ApJ, 697, 1071

Band, D., Matteson, J., Ford, L., et al. 1993, ApJ, 413, 281

Barnacka, A., & Loeb, A. 2014, ApJL, 794, L8

Barnes, J., & Kasen, D. 2013, ApJ, 775, 18

Barthelmy, S. D., Chincarini, G., Burrows, D. N., et al. 2005a, NewAt, 438, 994

Barthelmy, S. D., Barbier, L. M., Cummings, J. R., et al. 2005b, SSRv, 120, 143

Bartos, I., Brady, P., & Márka, S. 2013, Classical and Quantum Gravity, 30, 123001

Bartos, I., Crotts, A. P. S., & Márka, S. 2015, ApJL, 801, L1

Bazin, G., Palanque-Delabrouille, N., Rich, J., et al. 2009, A&A, 499, 653

Becker, A. 2015, HOTPANTS: High Order Transform of PSF ANd Template Subtraction, Astrophysics Source Code Library, ascl:1504.004

Belczynski, K., Kalogera, V., & Bulik, T. 2002, ApJ, 572, 407

Bellm, E. 2014, in The Third Hot-wiring the Transient Universe Workshop, ed. P. R. Wozniak, M. J. Graham, A. A. Mahabal, & R. Seaman, 27–33

Bellm, E. C. 2011, PhD thesis, University of California, Berkeley

Bellm, E. C., Hurley, K., Pal'shin, V., et al. 2008, ApJ, 688, 491

Beloborodov, A. M., Stern, B. E., & Svensson, R. 2000, ApJ, 535, 158

Berger, E., Price, P. A., Cenko, S. B., et al. 2005, Nature, 438, 988

Bertin, E., & Arnouts, S. 1996, A&AS, 117, 393

Bertin, E., Mellier, Y., Radovich, M., et al. 2002, in Astronomical Society of the Pacific Conference Series, Vol. 281, Astronomical Data Analysis Software and Systems XI, ed. D. A. Bohlender, D. Durand, & T. H. Handley, 228

Bhat, P. N. 2013, ArXiv e-prints, arXiv:1307.7618

Bhat, P. N., Fishman, G. J., Meegan, C. A., et al. 1992, Nature, 359, 217

Bhat, P. N., Briggs, M. S., Connaughton, V., et al. 2012, ApJ, 744, 141

Bilicki, M., Jarrett, T. H., Peacock, J. A., Cluver, M. E., & Steward, L. 2014, ApJS, 210, 9

Blake, C. H., Bloom, J. S., Starr, D. L., et al. 2005, Nature, 435, 181

Blandford, R. D., & McKee, C. F. 1976, Physics of Fluids, 19, 1130

Bloom, J. S. 2011, What are gamma-ray bursts? (Princeton University Press)

Bloom, J. S., Frail, D. A., & Kulkarni, S. R. 2003, ApJ, 594, 674

Bloom, J. S., Frail, D. A., & Sari, R. 2001, AJ, 121, 2879

Bloom, J. S., Kulkarni, S. R., Djorgovski, S. G., et al. 1999, Nature, 401, 453

Bloom, J. S., Prochaska, J. X., Pooley, D., et al. 2006, ApJ, 638, 354

Bloom, J. S., Perley, D. A., Li, W., et al. 2009, ApJ, 691, 723

Bloom, J. S., Richards, J. W., Nugent, P. E., et al. 2012, PASP, 124, 1175

Boella, G., Butler, R. C., Perola, G. C., et al. 1997, A&AS, 122, doi:10.1051/aas:1997136

Borgonovo, L. 2004, A&A, 418, 487

Botticella, M. T., Riello, M., Cappellaro, E., et al. 2008, A&A, 479, 49

Brink, H., Richards, J. W., Poznanski, D., et al. 2013, MNRAS, 435, 1047

Bromberg, O., Nakar, E., Piran, T., & Sari, R. 2012, ApJ, 749, 110

Bruzual, G., & Charlot, S. 2003, MNRAS, 344, 1000

Burrows, D. N., Hill, J. E., Nousek, J. A., et al. 2005, SSRv, 120, 165

Burrows, D. N., Grupe, D., Capalbi, M., et al. 2006, ApJ, 653, 468

Butler, N. 2013, The Astronomical Review, 8, 103

Butler, N., Gehrels, N., Golkhou, V. Z., et al. 2015, Gamma Ray Coordinates Network Circular, 18455

Butler, N., Klein, C., Fox, O., et al. 2012, Proc. SPIE, Vol. 8446, Ground-based and Airborne Instrumentation for Astronomy IV, 844610

Butler, N. R., Bloom, J. S., & Poznanski, D. 2010, ApJ, 711, 495

Butler, N. R., & Kocevski, D. 2007, ApJ, 663, 407

Butler, N. R., Kocevski, D., Bloom, J. S., & Curtis, J. L. 2007, ApJ, 671, 656

Butler, N. R., Li, W., Perley, D., et al. 2006, ApJ, 652, 1390

Campana, S., Mangano, V., Blustin, A. J., et al. 2006, Nature, 442, 1008

Cappellaro, E. 2014, in IAU Symposium, Vol. 296, Supernova Environmental Impacts, ed. A. Ray & R. A. McCray, 37–44

Cappellaro, E., Turatto, M., Benetti, S., et al. 1993a, A&A, 273, 383

—. 1993b, A&A, 268, 472

Cappellaro, E., Turatto, M., Tsvetkov, D. Y., et al. 1997, A&A, 322, 431

Cappellaro, E., Riello, M., Altavilla, G., et al. 2005, A&A, 430, 83

Cavallo, G., & Rees, M. J. 1978, MNRAS, 183, 359

Cenko, S. B., Frail, D. A., Harrison, F. A., et al. 2010, ApJ, 711, 641

Chandra, P., Cenko, S. B., Frail, D. A., et al. 2008, ApJ, 683, 924

Chang, H.-Y. 2001, ApJL, 557, L85

Chatfield, C. 2003, The analysis of time series: an introduction (CRC press)

Chatterjee, R., Bailyn, C. D., Bonning, E. W., et al. 2012, ApJ, 749, 191

Chen, H.-Y., & Holz, D. E. 2013, Physical Review Letters, 111, 181101

Cohen, E., Piran, T., & Sari, R. 1998, ApJ, 509, 717

Connaughton, V., Burns, E., Goldstein, A., et al. 2016, ApJL, 826, L6

Costa, E., Frontera, F., Heise, J., et al. 1997, Nature, 387, 783

Cristiani, S., Trentini, S., La Franca, F., et al. 1996, A&A, 306, 395

Cucchiara, A., Levan, A. J., Fox, D. B., et al. 2011, ApJ, 736, 7

Dahlen, T., Strolger, L.-G., Riess, A. G., et al. 2012, ApJ, 757, 70

—. 2004, ApJ, 613, 189

Daigne, F., Bošnjak, Ž., & Dubus, G. 2011, A&A, 526, A110

Dalya, G., Frei, Z., Galgoczi, G., Raffai, P., & de Souza, R. S. 2016, VizieR Online Data Catalog, 7275

Daubechies, I., ed. 1992, Ten lectures on wavelets

D'Avanzo, P., Salvaterra, R., Bernardini, M. G., et al. 2014, MNRAS, 442, 2342

Deng, M., & Schaefer, B. E. 1997, ApJ, 491, 720

Dessart, L., Burrows, A., Livne, E., & Ott, C. D. 2008, ApJL, 673, L43

Díaz, M. C., Beroiz, M., Peñuela, T., et al. 2016, ApJL, 828, L16

Dichiara, S., Guidorzi, C., Amati, L., & Frontera, F. 2013, MNRAS, 431, 3608

Doane, J. S., & Mathews, W. G. 1993, ApJ, 419, 573

Eichler, D., Livio, M., Piran, T., & Schramm, D. N. 1989, Nature, 340, 126

Esin, A. A., & Blandford, R. 2000, ApJL, 534, L151

Evans, P. A., Kennea, J. A., Barthelmy, S. D., et al. 2016, MNRAS, 460, L40

Feigelson, E. D., & Nelson, P. I. 1985, ApJ, 293, 192

Fenimore, E. E., Cooper, C., Ramirez-Ruiz, E., et al. 1999, ApJ, 512, 683

Fenimore, E. E., in 't Zand, J. J. M., Norris, J. P., Bonnell, J. T., & Nemiroff, R. J. 1995, ApJL, 448, L101

Fenimore, E. E., Madras, C. D., & Nayakshin, S. 1996, ApJ, 473, 998

Fishman, G., et al. 1989, in NASA Conference Publication, Vol. 2

Fong, W., & Berger, E. 2013, ApJ, 776, 18

Fong, W., Berger, E., & Fox, D. B. 2010, ApJ, 708, 9

Fong, W., Berger, E., Margutti, R., et al. 2012, ApJ, 756, 189

Fong, W., Berger, E., Chornock, R., et al. 2013, ApJ, 769, 56

Fox, D. B., Frail, D. A., Price, P. A., et al. 2005, Nature, 437, 845

Frail, D. A., Kulkarni, S. R., Nicastro, L., Feroci, M., & Taylor, G. B. 1997, Nature, 389, 261

Frail, D. A., Kulkarni, S. R., Sari, R., et al. 2001, ApJL, 562, L55

Fryer, C. L., Woosley, S. E., & Heger, A. 2001, ApJ, 550, 372

Galama, T. J., Vreeswijk, P. M., van Paradijs, J., et al. 1998, Nature, 395, 670

Gehrels, N., Cannizzo, J. K., Kanner, J., et al. 2016, ApJ, 820, 136

Gehrels, N., & Razzaque, S. 2013, Frontiers of Physics, 8, 661

Gehrels, N., Chincarini, G., Giommi, P., et al. 2004, ApJ, 611, 1005

Gehrels, N., Sarazin, C. L., O'Brien, P. T., et al. 2005, Nature, 437, 851

Gehrels, N., Norris, J. P., Barthelmy, S. D., et al. 2006, Nature, 444, 1044

Ghirlanda, G., Celotti, A., & Ghisellini, G. 2002, A&A, 393, 409

Ghisellini, G., Celotti, A., & Lazzati, D. 2000, MNRAS, 313, L1

Golkhou, V. Z., Butler, N., Gehrels, N., et al. 2015a, Gamma Ray Coordinates Network Circular, 18500

—. 2015b, Gamma Ray Coordinates Network Circular, 20485

Golkhou, V. Z., Butler, N., & Littlejohns, O. 2017a, in American Astronomical Society Meeting Abstracts, Vol. 229, American Astronomical Society Meeting Abstracts, 407.01

Golkhou, V. Z., & Butler, N. R. 2014, ApJ, 787, 90

Golkhou, V. Z., Butler, N. R., & Littlejohns, O. M. 2015c, ApJ, 811, 93

Golkhou, V. Z., Butler, N. R., & Littlejohns, O. M. 2016a, in LPI Contributions, Vol. 1962, Eighth Huntsville Gamma-Ray Burst Symposium, 4104

—. 2016b, VizieR Online Data Catalog, 181

Golkhou, V. Z., Butler, N. R., Strausbaugh, R., et al. 2017b, ArXiv e-prints, arXiv:1706.03898

Golkhou, V. Z., Butler, N., Watson, A. M., et al. 2015d, GRB Coordinates Network, 18386

—. 2016c, GRB Coordinates Network, 19202

—. 2016d, GRB Coordinates Network, 19007

—. 2016e, GRB Coordinates Network, 19203

—. 2016f, GRB Coordinates Network, 19243

—. 2016g, GRB Coordinates Network, 19236

—. 2016h, GRB Coordinates Network, 20066

—. 2016i, GRB Coordinates Network, 20052

González, M. M., Dingus, B. L., Kaneko, Y., et al. 2003, Nature, 424, 749

Graham, M. J., Djorgovski, S. G., Mahabal, A., et al. 2012, Distributed and Parallel Databases, 30, 371

Gruber, D., Krühler, T., Foley, S., et al. 2011, A&A, 528, A15

Guidorzi, C., Margutti, R., Amati, L., et al. 2012, MNRAS, 422, 1785

Haan, S., Surace, J. A., Armus, L., et al. 2011, AJ, 141, 100

Hanna, C., Mandel, I., & Vousden, W. 2014, ApJ, 784, 8

Harrison, F. A., Bloom, J. S., Frail, D. A., et al. 1999, ApJL, 523, L121

Hawkins, M. R. S. 2002, MNRAS, 329, 76

Hjorth, J., Sollerman, J., Møller, P., et al. 2003, Nature, 423, 847

Hjorth, J., Watson, D., Fynbo, J. P. U., et al. 2005, Nature, 437, 859

Holoien, T. W.-S., Stanek, K. Z., Kochanek, C. S., et al. 2017, MNRAS, 464, 2672

Hook, I. M., McMahon, R. G., Boyle, B. J., & Irwin, M. J. 1994, MNRAS, 268, 305

Horváth, I. 2002, A&A, 392, 791

Howell, J. H., Armus, L., Mazzarella, J. M., et al. 2010, ApJ, 715, 572

Hughes, P. A., Aller, H. D., & Aller, M. F. 1992, ApJ, 396, 469

Hulse, R. A., & Taylor, J. H. 1975, ApJL, 195, L51

Hurley, K., Dingus, B. L., Mukherjee, R., et al. 1994, Nature, 372, 652

in 't Zand, J. J. M., & Fenimore, E. E. 1996, ApJ, 464, 622

Inami, H., Armus, L., Surace, J. A., et al. 2010, AJ, 140, 63

Jakobsson, P., Hjorth, J., Malesani, D., et al. 2012, ApJ, 752, 62

Jarvis, A., Ong, R. A., Williams, D. A., et al. 2010, ApJ, 722, 862

Kaneko, Y., Magdalena González, M., Preece, R. D., Dingus, B. L., & Briggs, M. S. 2008, ApJ, 677, 1168

Kaplan, E. L., & Meier, P. 1958, Journal of the American Statistical Association, 53, 457

Kasliwal, M. M., Cenko, S. B., Singer, L. P., et al. 2016, ApJL, 824, L24

Katz, J. I. 1994, ApJL, 432, L107

Kendall, M. G. 1938, Biometrika

Kiuchi, K., Shibata, M., Montero, P. J., & Font, J. A. 2011, Physical Review Letters, 106, 251102

Klebesadel, R. W., Strong, I. B., & Olson, R. A. 1973, ApJL, 182, L85

Klessen, R. S., Spaans, M., & Jappsen, A.-K. 2007, MNRAS, 374, L29

Kobayashi, S., & Sari, R. 2001, ApJ, 551, 934

Kocevski, D., & Butler, N. 2008, ApJ, 680, 531

Kocevski, D., Butler, N., & Bloom, J. S. 2007, ApJ, 667, 1024

Kocevski, D., & Petrosian, V. 2013, ApJ, 765, 116

Kocevski, D., Ryde, F., & Liang, E. 2003, ApJ, 596, 389

Kochanek, C. S., & Piran, T. 1993, ApJL, 417, L17

Kolaczyk, E. D. 1997, ApJ, 483, 340

Kouveliotou, C., Meegan, C. A., Fishman, G. J., et al. 1993, ApJL, 413, L101

Krimm, H. A., Granot, J., Marshall, F. E., et al. 2007, ApJ, 665, 554

Kroupa, P. 2001, MNRAS, 322, 231

Kulkarni, S. R., Frail, D. A., Wieringa, M. H., et al. 1998, Nature, 395, 663

Kulkarni, S. R., Djorgovski, S. G., Odewahn, S. C., et al. 1999, Nature, 398, 389

Kumar, P. 1999, ApJL, 523, L113

Law, N. M., Kulkarni, S. R., Dekany, R. G., et al. 2009, PASP, 121, 1395

Lazzati, D., Rossi, E., Covino, S., Ghisellini, G., & Malesani, D. 2002, A&A, 396, L5

Leaman, J., Li, W., Chornock, R., & Filippenko, A. V. 2011, MNRAS, 412, 1419

Lee, W. H., & Ramirez-Ruiz, E. 2007, New Journal of Physics, 9, 17

Leibler, C. N., & Berger, E. 2010, ApJ, 725, 1202

Leitherer, C., Schaerer, D., Goldader, J. D., et al. 1999, ApJS, 123, 3

Li, W., Leaman, J., Chornock, R., et al. 2011, MNRAS, 412, 1441

Liang, E.-W., Racusin, J. L., Zhang, B., Zhang, B.-B., & Burrows, D. N. 2008, ApJ, 675, 528

LIGO Scientific Collaboration. 2015, Gamma Ray Coordinates Network Circular, 18626

LIGO Scientific Collaboration, Aasi, J., Abbott, B. P., et al. 2015, Classical and Quantum Gravity, 32, 074001

Link, B., Epstein, R. I., & Priedhorsky, W. C. 1993, ApJL, 408, L81

Lithwick, Y., & Sari, R. 2001, ApJ, 555, 540

Littlejohns, O. M., & Butler, N. R. 2014, MNRAS, 444, 3948

Littlejohns, O. M., Butler, N. R., Cucchiara, A., et al. 2014, AJ, 148, 2

Lloyd, N. M., & Petrosian, V. 2000, ApJ, 543, 722

Lloyd-Ronning, N. M., & Petrosian, V. 2002, ApJ, 565, 182

MacFadyen, A. I., & Woosley, S. E. 1999, ApJ, 524, 262

MacFadyen, A. I., Woosley, S. E., & Heger, A. 2001, ApJ, 550, 410

MacLachlan, G. A., Shenoy, A., Sonbas, E., et al. 2013, MNRAS, 432, 857

Madau, P., della Valle, M., & Panagia, N. 1998, MNRAS, 297, L17

Maiolino, R., Vanzi, L., Mannucci, F., et al. 2002, A&A, 389, 84

Malesani, D., Tagliaferri, G., Chincarini, G., et al. 2004, ApJL, 609, L5

Mannucci, F., Della Valle, M., & Panagia, N. 2007, MNRAS, 377, 1229

Mannucci, F., Maiolino, R., Cresci, G., et al. 2003, A&A, 401, 519

Mantel, N. 1966, Cancer chemotherapy reports. Part 1, 50, 163

Mattila, S., Dahlen, T., Efstathiou, A., et al. 2012, ApJ, 756, 111

Mazzarella, J. M., & Balzano, V. A. 1986, ApJS, 62, 751

Meegan, C., Lichti, G., Bhat, P. N., et al. 2009, ApJ, 702, 791

Meegan, C. A., Fishman, G. J., Wilson, R. B., et al. 1992, Nature, 355, 143

Melinder, J., Dahlen, T., Mencía-Trinchant, L., et al. 2011, A&A, 532, A29

Melinder, J., Dahlen, T., Mencía Trinchant, L., et al. 2012, A&A, 545, A96

Mészáros, P. 2006, Reports on Progress in Physics, 69, 2259

Mészáros, P., & Rees, M. J. 1997, ApJ, 476, 232

Meszaros, P., Rees, M. J., & Papathanassiou, H. 1994, ApJ, 432, 181

Mészáros, P., Rees, M. J., & Wijers, R. A. M. J. 1998, ApJ, 499, 301

Metzger, B. D., & Berger, E. 2012, ApJ, 746, 48

Metzger, B. D., Quataert, E., & Thompson, T. A. 2008, MNRAS, 385, 1455

Metzger, M. R., Djorgovski, S. G., Kulkarni, S. R., et al. 1997, Nature, 387, 878

Meynet, G., Maeder, A., Schaller, G., Schaerer, D., & Charbonnel, C. 1994, A&AS, 103

Miluzio, M., Cappellaro, E., Botticella, M. T., et al. 2013, A&A, 554, A127

Mitrofanov, I. G. 1989, Ap&SS, 155, 141

Nakar, E. 2007, PhR, 442, 166

Nakar, E., & Piran, T. 2002, MNRAS, 330, 920

Nakar, E., Piran, T., & Granot, J. 2003, NewA, 8, 495

Navasardyan, H., Petrosian, A. R., Turatto, M., Cappellaro, E., & Boulesteix, J. 2001, MNRAS, 328, 1181

Norris, J. P., & Bonnell, J. T. 2006, ApJ, 643, 266

Norris, J. P., Nemiroff, R. J., Bonnell, J. T., et al. 1996, ApJ, 459, 393

Norris, J. P., Nemiroff, R. J., Scargle, J. D., et al. 1994, ApJ, 424, 540

Nousek, J. A., Kouveliotou, C., Grupe, D., et al. 2006, ApJ, 642, 389

Oates, S. R., Page, M. J., Schady, P., et al. 2009, MNRAS, 395, 490

Ott, C. D., Reisswig, C., Schnetter, E., et al. 2011, Physical Review Letters, 106, 161103

Paczynski, B. 1986, ApJL, 308, L43

—. 1991, AcA, 41, 257

Page, K. L., Willingale, R., Osborne, J. P., et al. 2007, ApJ, 663, 1125

Paltani, S. 1999, in Astronomical Society of the Pacific Conference Series, Vol. 159, BL Lac Phenomenon, ed. L. O. Takalo & A. Sillanpää, 293

Parra, R., Conway, J. E., Diamond, P. J., et al. 2007, ApJ, 659, 314

Percival, D. B., & Walden, A. T. 2006, Wavelet methods for time series analysis, Vol. 4 (Cambridge University Press)

Pérez-Torres, M. A., Romero-Cañizales, C., Alberdi, A., & Polatidis, A. 2009, A&A, 507, L17

Perley, D. A., Cenko, S. B., Bloom, J. S., et al. 2009, AJ, 138, 1690

Pettini, M., Steidel, C. C., Dickinson, M., et al. 1997, in American Institute of Physics Conference Series, Vol. 408, American Institute of Physics Conference Series, ed. W. H. Waller, 279–283

Phinney, E. S. 1991, ApJL, 380, L17

Piran, T. 1999, PhR, 314, 575

Piran, T. 2003, Nature, 422, 268

Piran, T. 2004, Reviews of Modern Physics, 76, 1143

Piran, T., Nakar, E., & Rosswog, S. 2013, MNRAS, 430, 2121

Predoi, V., Clark, J., Creighton, T., et al. 2010, Classical and Quantum Gravity, 27, 084018

Preece, R. D., Briggs, M. S., Mallozzi, R. S., et al. 1998, ApJL, 506, L23

Quilligan, F., McBreen, B., Hanlon, L., et al. 2002, A&A, 385, 377

Rabinowitz, D., Baltay, C., Ellman, N., Woodward, E., & Nugent, P. 2015, Gamma Ray Coordinates Network Circular, 18473

Racusin, J. L., Karpov, S. V., Sokolowski, M., et al. 2008, Nature, 455, 183

Racusin, J. L., Oates, S. R., Schady, P., et al. 2011, ApJ, 738, 138

Ramirez-Ruiz, E., & Fenimore, E. E. 2000, ApJ, 539, 712

Rau, A., Kulkarni, S. R., Law, N. M., et al. 2009, PASP, 121, 1334

Rees, M. J., & Meszaros, P. 1992, MNRAS, 258, 41P

—. 1994, ApJL, 430, L93

Rees, M. J., & Mészáros, P. 1998, ApJL, 496, L1

Reichart, D. E., Lamb, D. Q., Fenimore, E. E., et al. 2001, ApJ, 552, 57

Rhoads, J. E. 1997, ApJL, 487, L1

Richmond, M. W., Filippenko, A. V., & Galisky, J. 1998, PASP, 110, 553

Romano, P., Campana, S., Chincarini, G., et al. 2006, A&A, 456, 917

Roming, P. W. A., Kennedy, T. E., Mason, K. O., et al. 2005, SSRv, 120, 95

Roming, P. W. A., Koch, T. S., Oates, S. R., et al. 2009, ApJ, 690, 163

Rosswog, S., Korobkin, O., Arcones, A., Thielemann, F.-K., & Piran, T. 2014, MNRAS, 439, 744

Ruffert, M., & Janka, H.-T. 1999, A&A, 344, 573

Ryde, F., & Petrosian, V. 2002, ApJ, 578, 290

Sakamoto, T., Lamb, D. Q., Kawai, N., et al. 2005, ApJ, 629, 311

Salpeter, E. E. 1955, ApJ, 121, 161

Salvaterra, R., Della Valle, M., Campana, S., et al. 2009, Nature, 461, 1258

Sanders, D. B., Mazzarella, J. M., Kim, D.-C., Surace, J. A., & Soifer, B. T. 2003, AJ, 126, 1607

Sanders, D. B., & Mirabel, I. F. 1996, ARA&A, 34, 749

Sanders, D. B., Soifer, B. T., Elias, J. H., et al. 1988, ApJ, 325, 74

Sari, R., & Piran, T. 1997, ApJ, 485, 270

—. 1999, ApJ, 520, 641

Sari, R., Piran, T., & Halpern, J. P. 1999, ApJL, 519, L17

Sari, R., Piran, T., & Narayan, R. 1998, ApJL, 497, L17

Scargle, J. D., Norris, J. P., Jackson, B., & Chiang, J. 2013, ApJ, 764, 167

Schaefer, B. E., Cohen, J., Teegarden, B. J., et al. 1993, ApJ, 404, 673

Schaerer, D., Meynet, G., Maeder, A., & Schaller, G. 1993, A&AS, 98, 523

Schaller, G., Schaerer, D., Meynet, G., & Maeder, A. 1992, A&AS, 96, 269

Simonetti, J. H., Cordes, J. M., & Heeschen, D. S. 1985, ApJ, 296, 46

Singer, L., Shawhan, P., Palliyaguru, N., et al. 2015a, Gamma Ray Coordinates Network Circular, 18442

Singer, L. P., Kasliwal, M. M., Ferretti, R., et al. 2015b, Gamma Ray Coordinates Network Circular, 18497

Smartt, S. J., Chambers, K. C., Smith, K. W., et al. 2016, MNRAS, 462, 4094

Smith, M. W. E., Fox, D. B., Cowen, D. F., et al. 2013, Astroparticle Physics, 45, 56

Smith, N., Li, W., Filippenko, A. V., & Chornock, R. 2011, MNRAS, 412, 1522

Soares-Santos, M., Kessler, R., Berger, E., et al. 2016, ApJL, 823, L33

Soderberg, A. M., Kulkarni, S. R., Nakar, E., et al. 2006, Nature, 442, 1014

Sonbas, E., MacLachlan, G. A., Dhuga, K. S., et al. 2015, ApJ, 805, 86

Stanek, K. Z., Matheson, T., Garnavich, P. M., et al. 2003, ApJL, 591, L17

Starling, R. L. C., Wiersema, K., Levan, A. J., et al. 2011, MNRAS, 411, 2792

Surace, J., Laher, R., Masci, F., Grillmair, C., & Helou, G. 2015, in Astronomical Society of the Pacific Conference Series, Vol. 495, Astronomical Data Analysis Software an Systems XXIV (ADASS XXIV), ed. A. R. Taylor & E. Rosolowsky, 197

Surace, J. A., & Sanders, D. B. 1999, ApJ, 512, 162

Surace, J. A., Sanders, D. B., Vacca, W. D., Veilleux, S., & Mazzarella, J. M. 1998, ApJ, 492, 116

Szalay, A. S., Connolly, A. J., & Szokoly, G. P. 1999, AJ, 117, 68

Tanvir, N. R., Levan, A. J., Fruchter, A. S., et al. 2013, Nature, 500, 547

Tanvir, N. R., Fox, D. B., Levan, A. J., et al. 2009, Nature, 461, 1254

Taylor, G. B., Frail, D. A., Berger, E., & Kulkarni, S. R. 2004, ApJL, 609, L1

Taylor, J. H., & Weisberg, J. M. 1982, ApJ, 253, 908

Taylor, P. A., Miller, J. C., & Podsiadlowski, P. 2011, MNRAS, 410, 2385

Trevese, D., Kron, R. G., Majewski, S. R., Bershady, M. A., & Koo, D. C. 1994, ApJ, 433, 494

Troja, E., Butler, N., Watson, A. M., et al. 2016, GRB Coordinates Network, 19588

Usov, V. V. 1992, Nature, 357, 472

van den Bergh, S. 1991, PhR, 204, 385

van den Bergh, S., & McClure, R. D. 1994, ApJ, 425, 205

van Eerten, H., Zhang, W., & MacFadyen, A. 2010, ApJ, 722, 235

van Eerten, H. J., Meliani, Z., Wijers, R. A. M. J., & Keppens, R. 2011, MNRAS, 410, 2016

van Paradijs, J., Groot, P. J., Galama, T., et al. 1997, Nature, 386, 686

Vázquez, G. A., & Leitherer, C. 2005, ApJ, 621, 695

Vestrand, W. T., Wozniak, P. R., Wren, J. A., et al. 2005, Nature, 435, 178

Villasenor, J. S., Lamb, D. Q., Ricker, G. R., et al. 2005, Nature, 437, 855

Virgili, F. J., Qin, Y., Zhang, B., & Liang, E. 2012, MNRAS, 424, 2821

von Kienlin, A., Meegan, C. A., Paciesas, W. S., et al. 2014, ApJS, 211, 13

Walker, K. C., Schaefer, B. E., & Fenimore, E. E. 2000, ApJ, 537, 264

Watson, A. M., Troja, E., Butler, N., et al. 2016, GRB Coordinates Network, 19602

Waxman, E., & Draine, B. T. 2000, ApJ, 537, 796

White, D. J., Daw, E. J., & Dhillon, V. S. 2011, Classical and Quantum Gravity, 28, 085016

Woosley, S. E. 1993, ApJ, 405, 273

Woosley, S. E., & Bloom, J. S. 2006, ARA&A, 44, 507

Woosley, S. E., & Heger, A. 2006, ApJ, 637, 914

Wright, E. L. 2006, PASP, 118, 1711

Wyithe, J. S. B., & Turner, E. L. 2001, MNRAS, 320, 21

Zetterlund, E., Levesque, E. M., Leitherer, C., & Danforth, C. W. 2015, ApJ, 805, 151

Zhang, B., & Mészáros, P. 2002, ApJ, 571, 876

Zhang, B., Zhang, B.-B., Virgili, F. J., et al. 2009, ApJ, 703, 1696

Zhang, F.-W., Fan, Y.-Z., Shao, L., & Wei, D.-M. 2013, ApJL, 778, L11

Zwicky, F. 1942, ApJ, 96, 28

APPENDIX A

SWIFT GRB MINIMUM TIMESCALES

Table A.1: *Swift* GRB Minimum Timescales

GRB	$\Delta t_{\rm min}$ (s)	$\Delta t_{\rm snr}$ (s)	T_{90} (s)	$\sigma_{X,t_{\rm min}}$	$\sigma_{X,t_{\rm snr}}$	χ^2/ν	S/N	z
041220	1.78 ± 0.30	0.64 ± 0.11	3.52 ± 0.13	0.468	0.249	0.0005	23.5	...
041223	0.32 ± 0.05	0.12 ± 0.02	108.00 ± 0.52	0.255	0.118	1.119	177.1	...
041224	2.51 ± 0.43	1.00 ± 0.48	141.48 ± 1.89	0.253	0.134	1.099	54.9	...
041228	9.90 ± 1.68	3.54 ± 0.60	55.50 ± 3.39	0.302	0.155	0.478	42.2	...
050117	...	0.31 ± 0.22	168.96 ± 0.86	...	0.179	9.758	78.4	...
050124	0.64 ± 0.11	0.23 ± 0.14	3.36 ± 0.13	0.359	0.190	2.067	36.9	...
050128	...	0.18 ± 0.09	24.48 ± 3.63	...	0.297	3.583	41.6	...
050215A	...	5.58 ± 2.64	66.50 ± 0.99	...	0.621	3.452	10.2	...
050219A	3.54 ± 0.60	1.31 ± 0.78	25.00 ± 1.04	0.358	0.141	0.063	50.8	...
050219B	...	0.18 ± 0.09	20.93 ± 0.92	...	0.179	2.794	71.9	...
050306	3.54 ± 0.60	1.31 ± 0.78	112.66 ± 1.37	0.404	0.226	2.353	26.5	...
050315	...	0.79 ± 0.26	94.60 ± 1.66	...	0.214	13.989	43.7	1.949
050318	0.64 ± 0.11	0.23 ± 0.14	30.96 ± 0.09	0.383	0.176	0.345	49	1.44
050319	4.99 ± 0.85	1.73 ± 1.20	153.55 ± 2.20	0.727	0.355	1.734	18.2	3.24
050326	0.23 ± 0.04	0.12 ± 0.02	30.24 ± 0.44	0.210	0.122	0.457	132.7	...
050401	2.51 ± 0.43	0.79 ± 0.26	34.41 ± 0.34	0.534	0.210	0.056	39.3	2.9
050410	...	19.66 ± 3.34	45.08 ± 2.94	...	0.221	8.085	36.2	...
050416A	1.26 ± 0.21	0.64 ± 0.11	2.91 ± 0.18	0.851	0.653	2.398	17.5	0.6535
050416B	1.78 ± 0.30	0.64 ± 0.11	3.32 ± 0.19	0.561	0.338	0.089	19.9	...
050418	2.51 ± 0.43	0.79 ± 0.26	82.77 ± 0.56	0.375	0.130	0.174	46.1	...
050422	13.95 ± 2.37	5.58 ± 2.64	59.52 ± 0.74	0.604	0.422	1.812	14	...
050502B	2.51 ± 0.43	0.64 ± 0.11	17.44 ± 0.26	0.663	0.239	0.755	25.3	...
050505	...	3.54 ± 0.60	60.20 ± 1.35	...	0.378	5.948	21.8	4.27
050509A	4.99 ± 0.85	1.73 ± 1.20	11.76 ± 0.90	0.429	0.232	0.759	23.3	...
050525	0.12 ± 0.02	0.03 ± 0.02	9.10 ± 0.04	0.130	0.045	0.021	339.9	0.606
050603	0.23 ± 0.04	0.12 ± 0.02	9.80 ± 0.39	0.531	0.319	0.827	42	2.821
050607	3.54 ± 0.60	1.31 ± 0.78	17.29 ± 0.47	0.607	0.313	0.305	14.7	...
050701	1.26 ± 0.21	0.64 ± 0.11	32.24 ± 1.39	0.477	0.292	0.614	40.8	...
050713A	...	0.79 ± 0.26	124.65 ± 13.10	...	0.110	2.944	72.8	...
050713B	39.04 ± 6.63	9.63 ± 6.69	132.94 ± 5.84	1.159	0.345	0.047	14.3	...
050715	...	1.31 ± 0.78	185.35 ± 5.64	...	0.321	2.985	28.7	...
050716	9.90 ± 1.68	3.54 ± 0.60	64.24 ± 0.91	0.399	0.182	0.028	20.7	...
050717	...	0.12 ± 0.02	79.38 ± 2.23	...	0.197	5.133	80.7	...
050721	9.90 ± 1.68	4.39 ± 1.45	39.56 ± 1.97	0.802	0.468	2.448	16.4	...
050724	0.23 ± 0.04	0.12 ± 0.02	2.50 ± 0.04	0.858	0.555	1.12	20.8	0.258
050726	...	30.99 ± 14.67	191.49 ± 2.27	...	0.528	17.183	14.3	...
050730	...	19.66 ± 3.34	60.48 ± 2.26	...	0.288	4.281	13.2	3.969
050801	1.78 ± 0.30	0.79 ± 0.26	5.88 ± 0.20	0.796	0.443	0.388	18.2	1.56
050803	...	3.54 ± 0.60	88.20 ± 1.35	...	0.346	7.235	19.9	0.422
050820A	...	1.00 ± 0.48	239.68 ± 0.37	...	0.158	6.907	41.4	2.6147
050820B	0.45 ± 0.08	0.18 ± 0.09	12.69 ± 0.21	0.176	0.100	1.988	80.7	...
050822	2.51 ± 0.43	0.79 ± 0.26	104.88 ± 2.63	0.432	0.228	0.326	31.7	1.434
050827	...	0.79 ± 0.26	50.16 ± 2.19	...	0.200	18.603	35.8	...
050904	...	9.63 ± 6.69	197.20 ± 2.26	...	0.114	3.09	38.4	6.29
050911	3.54 ± 0.60	1.31 ± 0.78	16.29 ± 0.13	0.884	0.658	0.033	10.4	...
050915A	...	1.31 ± 0.78	21.39 ± 0.59	...	0.474	8.993	12.6	2.5273
050915B	...	1.00 ± 0.48	41.20 ± 1.21	...	0.145	10.202	60.6	...
050922B	...	19.66 ± 3.34	251.72 ± 22.34	...	0.670	4.557	14.6	...
050922C	...	0.12 ± 0.02	4.56 ± 0.12	...	0.158	3.384	60	2.198
051001	...	19.66 ± 3.34	55.90 ± 1.63	...	0.259	3.014	21.1	2.4296
051006	...	0.64 ± 0.11	26.46 ± 0.53	...	0.610	2.796	17.3	1.059

Continued on Next Page...

Table A.1 – Continued

GRB	$\Delta t_{\rm min}$ (s)	$\Delta t_{\rm snr}$ (s)	T_{90} (s)	$\sigma_{X,t_{\rm min}}$	$\sigma_{X,t_{\rm snr}}$	χ^2/ν	S/N	z
051008	...	0.64 ± 0.11	45.10 ± 1.02	...	0.207	7.985	62.1	...
051021B	9.90 ± 1.68	4.39 ± 1.45	33.54 ± 1.37	0.667	0.338	0.151	18.8	...
051111	...	0.64 ± 0.11	50.96 ± 2.45	...	0.145	5.237	62.6	1.55
051113	...	1.00 ± 0.48	96.75 ± 0.80	...	0.394	9.862	19.4	...
051117A	27.70 ± 4.70	9.63 ± 6.69	238.14 ± 13.14	0.297	0.110	0.091	53.8	...
051221A	0.01 ± 0.001	0.005 ± 0.001	1.24 ± 0.03	0.383	0.219	0.196	65.6	0.5459
051227	...	1.00 ± 0.48	4.30 ± 0.19	...	0.482	2.809	12.5	0.714
060102	...	0.06 ± 0.04	3.76 ± 0.36	...	0.876	10.871	8.6	...
060105	...	0.14 ± 0.05	55.20 ± 0.34	...	0.126	5.052	134.4	...
060108	7.03 ± 1.19	3.54 ± 0.60	15.28 ± 1.10	0.581	0.429	0.248	20.5	2.03
060110	...	0.79 ± 0.26	24.00 ± 1.19	...	0.114	2.915	51.7	...
060111A	...	1.00 ± 0.48	15.26 ± 0.89	...	0.118	2.841	49.2	...
060111B	...	1.73 ± 1.20	61.38 ± 1.22	...	0.386	3.821	19.8	...
060115	...	3.54 ± 0.60	109.89 ± 1.14	...	0.319	3.464	27.4	3.53
060117	0.12 ± 0.02	0.03 ± 0.02	17.29 ± 0.11	0.224	0.071	0.165	186.7	...
060202	...	19.66 ± 3.34	205.92 ± 2.52	...	0.415	11.538	15.1	0.783
060204B	...	1.31 ± 0.78	40.68 ± 1.40	...	0.155	6.533	43.2	...
060206	1.26 ± 0.21	0.64 ± 0.11	6.06 ± 0.16	0.385	0.212	0.104	45.1	4.045
060210	1.26 ± 0.21	0.64 ± 0.11	369.94 ± 20.65	0.336	0.292	1.471	42.8	3.91
060211B	...	3.54 ± 0.60	11.13 ± 0.57	...	0.723	8.384	11.9	...
060223A	4.99 ± 0.85	1.73 ± 1.20	8.40 ± 0.28	0.351	0.200	0.004	18	4.41
060223B	...	0.18 ± 0.09	10.60 ± 0.28	...	0.197	5.135	52.2	...
060306	...	0.14 ± 0.05	60.96 ± 0.80	...	0.249	3.321	42.5	3.5
060312	2.51 ± 0.43	1.00 ± 0.48	45.25 ± 0.86	0.239	0.152	2.277	42.9	...
060313	...	0.02 ± 0.002	0.78 ± 0.01	...	0.346	8.479	48.4	...
060319	...	0.79 ± 0.26	5.28 ± 0.28	...	0.471	5.361	13.2	...
060322	...	0.79 ± 0.26	210.40 ± 1.04	...	0.141	5.938	51.1	...
060403	7.03 ± 1.19	3.54 ± 0.60	26.40 ± 0.57	0.608	0.329	0.16	22.2	...
060413	7.03 ± 1.19	3.54 ± 0.60	120.84 ± 3.89	0.197	0.114	0.006	58.4	...
060418	...	0.14 ± 0.05	103.24 ± 10.33	...	0.200	7.018	80.6	1.489
060421	...	0.64 ± 0.11	11.11 ± 0.46	...	0.176	3.918	42.1	...
060424	...	0.64 ± 0.11	37.86 ± 0.50	...	0.706	5.333	14.9	...
060428A	2.51 ± 0.43	0.79 ± 0.26	52.60 ± 3.38	0.454	0.164	0.011	37.9	...
060501	2.51 ± 0.43	1.00 ± 0.48	12.18 ± 0.42	0.525	0.326	2.67	22.3	...
060502A	13.95 ± 2.37	3.54 ± 0.60	30.24 ± 4.18	0.481	0.158	0.021	45.7	1.51
060502B	0.08 ± 0.01	0.03 ± 0.01	0.16 ± 0.02	0.933	0.607	0.274	13	0.287
060507	...	3.54 ± 0.60	52.08 ± 1.43	...	0.402	8.001	15.7	...
060510A	2.51 ± 0.43	1.00 ± 0.48	21.85 ± 0.77	0.541	0.295	1.864	27.8	...
060510B	...	1.99 ± 0.94	229.89 ± 2.77	...	0.315	50.089	22.3	4.9
060515	...	19.66 ± 3.34	59.85 ± 3.67	...	0.488	4.495	17.3	...
060526	1.78 ± 0.30	0.79 ± 0.26	295.55 ± 4.01	0.421	0.348	2.173	23.5	3.221
060607A	7.03 ± 1.19	1.31 ± 0.78	102.55 ± 3.35	0.496	0.118	0.198	50.7	3.082
060607B	...	3.54 ± 0.60	31.03 ± 1.54	...	0.319	7.49	25.8	...
060614	...	0.12 ± 0.02	108.80 ± 0.86	...	0.100	2.946	191.9	0.125
060707	13.95 ± 2.37	5.58 ± 2.64	75.14 ± 2.46	0.539	0.310	1.413	20.1	3.425
060708	...	0.64 ± 0.11	7.50 ± 0.45	...	0.342	6.693	30.1	1.92
060714	...	1.00 ± 0.48	118.72 ± 1.87	...	0.212	7.126	44	2.711
060719	1.78 ± 0.30	0.79 ± 0.26	57.00 ± 0.84	0.219	0.138	2.216	47.2	1.532
060729	4.99 ± 0.85	1.73 ± 1.20	119.14 ± 1.40	0.356	0.161	0.182	44.9	0.54
060813	...	0.14 ± 0.05	15.84 ± 0.74	...	0.105	7.665	101.9	...
060814	0.90 ± 0.15	0.31 ± 0.22	159.16 ± 4.08	0.152	0.063	0.641	173.9	0.84
060825	1.26 ± 0.21	0.64 ± 0.11	8.55 ± 0.23	0.355	0.243	1.355	47.3	...

Continued on Next Page...

Table A.1 – Continued

GRB	$\Delta t_{\rm min}$ (s)	$\Delta t_{\rm snr}$ (s)	T_{90} (s)	$\sigma_{X,t_{\rm min}}$	$\sigma_{X,t_{\rm snr}}$	χ^2/ν	S/N	z
060904A	0.23 ± 0.04	0.12 ± 0.02	75.21 ± 0.57	0.176	0.114	0.704	127.1	...
060904B	...	1.00 ± 0.48	171.04 ± 2.29	...	0.158	3.506	34.2	0.703
060906	2.51 ± 0.43	1.00 ± 0.48	72.96 ± 9.41	0.362	0.274	0.613	30.5	3.686
060908	...	0.64 ± 0.11	18.48 ± 0.17	...	0.192	6.975	47.4	1.8836
060912A	0.64 ± 0.11	0.23 ± 0.14	5.92 ± 0.35	0.407	0.138	0.0005	43.5	0.937
060919	2.51 ± 0.43	1.00 ± 0.48	4.70 ± 0.17	0.546	0.344	0.0005	17.2	...
060923A	...	5.58 ± 2.64	56.98 ± 2.49	...	0.655	23.112	10.6	...
060926	3.54 ± 0.60	1.31 ± 0.78	7.05 ± 0.39	0.456	0.303	1.435	17	3.2
060927	1.26 ± 0.21	0.31 ± 0.22	23.03 ± 0.26	0.502	0.155	0.091	43.1	5.6
060929	...	19.66 ± 3.34	550.44 ± 2.05	...	1.075	5.722	11	...
061004	1.26 ± 0.21	0.31 ± 0.22	6.54 ± 0.23	0.574	0.145	0.097	37.5	...
061006	0.08 ± 0.01	0.03 ± 0.02	1.54 ± 0.09	0.409	0.219	1.802	42.6	...
061007	0.16 ± 0.03	0.06 ± 0.04	74.90 ± 0.51	0.118	0.045	0.005	330.4	1.261
061021	0.64 ± 0.11	0.23 ± 0.14	12.06 ± 0.32	0.298	0.118	0.304	50.9	0.3463
061110A	19.66 ± 3.34	7.26 ± 4.32	47.04 ± 1.80	0.383	0.187	0.008	24.1	0.757
061121	0.12 ± 0.02	0.04 ± 0.03	83.00 ± 12.50	0.130	0.055	0.52	273.8	1.314
061126	0.23 ± 0.04	0.12 ± 0.02	26.78 ± 0.46	0.176	0.134	1.349	85.7	1.159
061201	...	0.12 ± 0.02	0.86 ± 0.03	...	0.456	3.274	21.4	...
061202	1.26 ± 0.21	0.64 ± 0.11	125.35 ± 17.30	0.184	0.110	0.401	85.5	...
061210	...	0.01 ± 0.01	0.10 ± 0.01	...	0.375	7.051	22.5	0.41
061222A	0.12 ± 0.02	0.04 ± 0.03	81.65 ± 4.24	0.200	0.089	0.489	139.9	2.088
061222B	...	5.58 ± 2.64	42.00 ± 2.15	...	0.297	24.964	22.6	3.355
070103	...	0.64 ± 0.11	10.92 ± 0.14	...	0.773	7.521	9.1	2.6208
070107	...	1.31 ± 0.78	357.50 ± 9.40	...	0.145	9.529	48.2	...
070110	...	5.58 ± 2.64	47.70 ± 1.54	...	0.210	6.48	25.9	2.352
070129	...	4.39 ± 1.45	92.15 ± 2.24	...	0.348	5.09	22.2	2.3384
070220	0.45 ± 0.08	0.18 ± 0.09	150.67 ± 7.75	0.197	0.105	0.944	114.6	...
070223	9.90 ± 1.68	4.39 ± 1.45	76.32 ± 1.66	0.510	0.329	0.919	14.6	...
070306	1.26 ± 0.21	0.64 ± 0.11	261.36 ± 6.65	0.232	0.141	2.017	85.4	1.497
070318	4.99 ± 0.85	1.00 ± 0.48	51.00 ± 2.32	0.391	0.114	1.27	48.1	0.836
070328	0.90 ± 0.15	0.31 ± 0.22	49.60 ± 1.11	0.182	0.089	1.232	110.4	...
070411	...	1.31 ± 0.78	108.56 ± 3.62	...	0.228	24.981	30.4	2.954
070419B	4.99 ± 0.85	1.73 ± 1.20	133.75 ± 2.85	0.251	0.095	0.247	84.6	...
070420	...	1.00 ± 0.48	95.91 ± 1.64	...	0.148	5.253	63.7	...
070427	...	0.79 ± 0.26	12.24 ± 0.44	...	0.190	7.941	40	...
070508	0.08 ± 0.01	0.03 ± 0.01	21.20 ± 0.25	0.161	0.063	0.142	262.1	0.82
070517	2.51 ± 0.43	1.00 ± 0.48	6.16 ± 0.27	0.893	0.636	1.603	8.7	...
070521	0.23 ± 0.04	0.12 ± 0.02	561.20 ± 6.66	0.268	0.161	0.474	118.6	...
070529	19.66 ± 3.34	5.58 ± 2.64	112.21 ± 2.94	0.819	0.434	2.329	13.5	2.4996
070531	13.95 ± 2.37	5.58 ± 2.64	37.20 ± 3.01	0.608	0.407	0.87	14.4	...
070612A	27.70 ± 4.70	9.63 ± 6.69	254.74 ± 3.63	0.514	0.179	1.147	24.9	0.617
070612B	4.99 ± 0.85	1.73 ± 1.20	15.52 ± 1.09	0.577	0.245	0.482	24.2	...
070616	1.26 ± 0.21	0.64 ± 0.11	443.52 ± 9.13	0.170	0.114	0.863	149.2	...
070621	...	0.79 ± 0.26	36.12 ± 0.81	...	0.200	3.027	48.8	...
070628	2.51 ± 0.43	1.00 ± 0.48	13.26 ± 0.39	0.268	0.118	0.104	50.5	...
070704	1.26 ± 0.21	0.64 ± 0.11	384.78 ± 4.64	0.230	0.134	0.005	74.2	...
070714A	1.26 ± 0.21	0.64 ± 0.11	2.56 ± 0.24	0.582	0.500	2.673	21.5	...
070714B	0.12 ± 0.02	0.04 ± 0.03	64.18 ± 1.60	0.679	0.339	0.662	35.8	0.92
070721B	...	0.79 ± 0.26	330.66 ± 6.28	...	0.293	5.287	26.8	3.626
070808	3.54 ± 0.60	1.00 ± 0.48	57.20 ± 4.87	0.753	0.247	0.249	24.3	...
070810A	...	1.73 ± 1.20	7.68 ± 0.41	...	0.228	4.068	24.6	2.17
070911	0.45 ± 0.08	0.18 ± 0.09	177.00 ± 2.69	0.214	0.105	0.588	148.6	...

Continued on Next Page...

Table A.1 – Continued

GRB	$\Delta t_{\rm min}$ (s)	$\Delta t_{\rm snr}$ (s)	T_{90} (s)	$\sigma_{X,t_{\rm min}}$	$\sigma_{X,t_{\rm snr}}$	χ^2/ν	S/N	z
070917	0.64 ± 0.11	0.14 ± 0.05	7.44 ± 0.39	0.263	0.089	2.213	82	...
070920A	27.70 ± 4.70	10.23 ± 6.09	57.00 ± 1.50	0.831	0.529	2.149	12.9	...
070920B	9.90 ± 1.68	3.54 ± 0.60	21.63 ± 0.59	0.451	0.200	0.0005	31.3	...
071001	7.03 ± 1.19	3.54 ± 0.60	66.30 ± 1.87	0.647	0.468	2.499	20.1	...
071003	...	0.18 ± 0.09	148.32 ± 0.68	...	0.148	4.527	79.7	1.605
071010B	0.90 ± 0.15	0.31 ± 0.22	34.68 ± 1.02	0.155	0.055	0.624	136.3	0.947
071011	3.54 ± 0.60	1.31 ± 0.78	87.04 ± 5.23	0.643	0.297	0.02	28.7	...
071020	...	0.04 ± 0.03	4.40 ± 0.27	...	0.126	5.084	100.3	2.145
071021	13.95 ± 2.37	5.58 ± 2.64	204.96 ± 17.95	0.567	0.333	0.197	17.7	2.452
071025	2.51 ± 0.43	1.00 ± 0.48	161.17 ± 5.40	0.202	0.114	1.575	86	...
071031	19.66 ± 3.34	5.58 ± 2.64	187.18 ± 7.12	0.911	0.470	1.221	15.9	2.692
071117	0.64 ± 0.11	0.18 ± 0.09	6.48 ± 0.76	0.315	0.095	0.071	76.4	1.331
071129	27.70 ± 4.70	9.63 ± 6.69	206.08 ± 6.98	0.717	0.270	2.21	23.9	...
080205	9.90 ± 1.68	3.54 ± 0.60	113.27 ± 2.65	0.526	0.266	0.209	33.6	...
080207	...	1.31 ± 0.78	310.98 ± 9.34	...	0.217	9.354	61.9	2.0858
080210	...	3.54 ± 0.60	43.89 ± 4.36	...	0.274	13.123	36.6	2.641
080212	...	5.58 ± 2.64	132.24 ± 2.55	...	0.279	4.293	24.7	...
080229A	0.23 ± 0.04	0.12 ± 0.02	50.18 ± 1.47	0.205	0.122	0.322	111.6	...
080303	4.99 ± 0.85	1.31 ± 0.78	44.68 ± 2.41	0.944	0.371	0.002	17.5	...
080307	...	24.36 ± 8.04	97.82 ± 5.26	...	0.464	5.109	16.9	...
080310	19.66 ± 3.34	5.58 ± 2.64	361.92 ± 3.75	0.559	0.192	0.005	27.5	2.4266
080319A	...	5.58 ± 2.64	45.63 ± 1.62	...	0.308	6.849	23.9	...
080319B	0.04 ± 0.01	0.02 ± 0.002	147.32 ± 2.50	0.063	0.032	0.212	725.4	0.937
080319C	1.78 ± 0.30	0.79 ± 0.26	32.88 ± 3.27	0.277	0.155	0.038	60.5	1.95
080320	9.90 ± 1.68	3.54 ± 0.60	21.42 ± 2.10	0.685	0.598	0.495	13.6	...
080325	109.21 ± 18.55	40.33 ± 24.01	183.92 ± 5.98	0.757	0.421	0.026	18.1	...
080328	0.45 ± 0.08	0.18 ± 0.09	91.00 ± 0.30	0.173	0.114	2.235	83.7	...
080330	...	9.63 ± 6.69	66.10 ± 0.98	...	0.531	7.587	13.4	1.51
080409	1.26 ± 0.21	0.64 ± 0.11	9.94 ± 0.12	0.631	0.457	1.804	24.7	...
080411	0.16 ± 0.03	0.04 ± 0.03	58.29 ± 0.46	0.114	0.032	1.085	379.3	1.03
080413A	0.64 ± 0.11	0.23 ± 0.14	46.62 ± 0.13	0.210	0.089	0.147	74.8	2.433
080413B	0.45 ± 0.08	0.18 ± 0.09	7.04 ± 0.43	0.326	0.130	1.271	64.4	1.1
080426	0.32 ± 0.05	0.12 ± 0.02	1.72 ± 0.10	0.695	0.279	0.064	28.1	...
080430	2.51 ± 0.43	0.64 ± 0.11	16.20 ± 0.78	0.484	0.145	1.89	52.7	0.767
080503	...	1.73 ± 1.20	178.92 ± 19.16	...	0.261	5.171	34.5	...
080515	9.90 ± 1.68	3.54 ± 0.60	22.05 ± 1.34	0.675	0.401	0.644	18.8	...
080516	...	0.64 ± 0.11	6.84 ± 0.17	...	0.851	11.739	11.9	...
080520	...	0.23 ± 0.14	2.97 ± 0.24	...	1.171	4.533	8.3	1.545
080523	19.66 ± 3.34	7.26 ± 4.32	55.38 ± 3.25	0.571	0.305	0.041	21.6	...
080602	...	0.31 ± 0.22	85.12 ± 2.65	...	0.214	3.884	39.5	...
080603B	0.23 ± 0.04	0.12 ± 0.02	59.50 ± 0.51	0.195	0.164	1.087	70	2.69
080605	...	0.12 ± 0.02	19.57 ± 0.32	...	0.138	8.338	157.5	1.6398
080607	0.32 ± 0.05	0.14 ± 0.05	83.66 ± 0.83	0.247	0.145	0.796	123	3.036
080613B	0.23 ± 0.04	0.12 ± 0.02	83.21 ± 5.07	0.313	0.217	0.783	94.4	...
080623	...	1.31 ± 0.78	16.10 ± 1.11	...	0.316	7.376	21.5	...
080701	3.54 ± 0.60	1.00 ± 0.48	9.35 ± 0.49	0.574	0.190	0.137	26.7	...
080707	...	3.54 ± 0.60	30.25 ± 0.43	...	0.546	15.939	17.2	1.23
080714	1.78 ± 0.30	0.64 ± 0.11	34.20 ± 2.29	0.406	0.184	0.085	44.9	...
080721	1.26 ± 0.21	0.64 ± 0.11	29.92 ± 2.29	0.467	0.295	1.324	37.2	2.602
080723A	...	1.73 ± 1.20	24.89 ± 2.81	...	0.509	3.905	14	...
080725	4.99 ± 0.85	1.73 ± 1.20	129.64 ± 4.42	0.324	0.130	0.046	46.1	...
080727B	...	0.12 ± 0.02	18.30 ± 10.97	...	0.192	20.44	81.4	...

Continued on Next Page...

Table A.1 – Continued

GRB	$\Delta t_{\rm min}$ (s)	$\Delta t_{\rm snr}$ (s)	T_{90} (s)	$\sigma_{X,t_{\rm min}}$	$\sigma_{X,t_{\rm snr}}$	χ^2/ν	S/N	z
080727C	1.78 ± 0.30	0.79 ± 0.26	99.84 ± 5.99	0.247	0.134	1.115	76.2	...
080802	...	19.66 ± 3.34	173.60 ± 9.01	...	0.580	4.468	18	...
080804	...	4.39 ± 1.45	61.74 ± 8.81	...	0.200	7.444	31.1	2.2
080805	13.95 ± 2.37	3.54 ± 0.60	111.84 ± 9.11	0.483	0.141	1.828	49.7	1.505
080810	...	0.64 ± 0.11	453.15 ± 5.09	...	0.265	7.042	57.9	3.35
080903	...	1.73 ± 1.20	69.30 ± 3.38	...	0.200	15.485	37.5	...
080905A	0.45 ± 0.08	0.18 ± 0.09	1.04 ± 0.03	0.671	0.685	2.466	11.4	0.1218
080905B	4.99 ± 0.85	1.73 ± 1.20	103.97 ± 4.68	0.543	0.310	2.201	22.8	2.374
080906	...	7.26 ± 4.32	159.28 ± 6.95	...	0.145	8.826	47.2	...
080915B	0.45 ± 0.08	0.18 ± 0.09	3.64 ± 0.24	0.322	0.141	1.021	53.3	...
080916A	...	0.64 ± 0.11	62.53 ± 3.24	...	0.100	3.07	89.3	0.689
080928	...	0.64 ± 0.11	284.90 ± 12.16	...	0.374	3.327	39.8	1.692
081007	3.54 ± 0.60	1.31 ± 0.78	5.55 ± 0.26	0.422	0.339	1.64	19.6	0.5295
081008	...	0.79 ± 0.26	199.32 ± 11.52	...	0.173	4.481	50.7	1.9685
081012	...	4.39 ± 1.45	32.00 ± 2.32	...	0.552	5.651	16.3	...
081022	...	19.66 ± 3.34	149.60 ± 8.46	...	0.361	5.614	28.3	...
081024A	...	0.18 ± 0.09	1.86 ± 0.05	...	0.537	3.939	14.5	...
081028	55.00 ± 9.34	19.66 ± 3.34	275.59 ± 9.68	0.485	0.224	0.139	42	3.038
081102	7.03 ± 1.19	3.54 ± 0.60	63.00 ± 4.72	0.559	0.319	0.096	25.4	...
081104	27.70 ± 4.70	9.63 ± 6.69	41.36 ± 1.21	0.327	0.251	0.964	22.4	...
081109A	9.90 ± 1.68	3.54 ± 0.60	70.14 ± 1.89	0.342	0.122	0.097	58.7	...
081118	39.04 ± 6.63	15.61 ± 7.39	66.55 ± 5.08	0.481	0.270	0.141	19.8	2.58
081126	...	0.64 ± 0.11	59.60 ± 1.40	...	0.219	13.958	52.9	...
081128	...	0.79 ± 0.26	108.48 ± 3.63	...	0.297	45.3	36.2	...
081203A	...	0.31 ± 0.22	254.28 ± 26.94	...	0.173	6.359	80.3	2.1
081210	...	0.23 ± 0.14	150.97 ± 1.85	...	0.221	10.995	35.9	...
081221	0.64 ± 0.11	0.18 ± 0.09	34.23 ± 0.64	0.126	0.032	1.137	278.7	2.26
081222	0.45 ± 0.08	0.14 ± 0.05	33.48 ± 1.44	0.158	0.063	0.026	147.6	2.77
081230	...	5.15 ± 3.07	55.10 ± 1.25	...	0.283	4.571	22.2	...
090102	...	0.79 ± 0.26	30.69 ± 1.21	...	0.277	4.99	35.5	1.547
090113	0.64 ± 0.11	0.23 ± 0.14	8.80 ± 0.13	0.545	0.257	0.393	32.3	1.7493
090123	13.95 ± 2.37	4.39 ± 1.45	141.96 ± 5.23	0.646	0.285	1.702	24.6	...
090129	2.51 ± 0.43	0.79 ± 0.26	18.20 ± 0.91	0.341	0.110	0.064	68.7	...
090201	...	0.64 ± 0.11	89.44 ± 1.72	...	0.148	4.291	88.6	...
090301	0.23 ± 0.04	0.12 ± 0.02	42.64 ± 1.25	0.158	0.089	0.015	179.8	...
090313	...	3.54 ± 0.60	90.24 ± 6.75	...	1.616	14.27	12.4	3.375
090401A	0.45 ± 0.08	0.14 ± 0.05	117.36 ± 5.68	0.310	0.114	0.117	109.6	...
090401B	0.06 ± 0.01	0.03 ± 0.01	227.52 ± 17.09	0.192	0.105	0.602	156.5	...
090404	1.78 ± 0.30	0.64 ± 0.11	85.84 ± 4.14	0.274	0.155	0.715	61.7	...
090407	...	9.63 ± 6.69	147.52 ± 1.02	...	0.514	25.54	13.5	1.4485
090410	...	0.64 ± 0.11	167.00 ± 1.43	...	0.197	13.446	67.4	...
090418	...	0.64 ± 0.11	57.97 ± 0.85	...	0.261	7.604	52.4	1.608
090419	...	0.90 ± 0.15	433.32 ± 5.21	...	1.346	207.759	14.3	...
090422	1.26 ± 0.21	0.23 ± 0.14	55.82 ± 9.32	0.881	0.405	2.266	16.1	...
090423	1.78 ± 0.30	0.79 ± 0.26	12.36 ± 0.59	0.495	0.308	1.211	31.3	8.1
090424	0.12 ± 0.02	0.04 ± 0.03	50.28 ± 0.53	0.202	0.095	0.767	131.7	0.544
090429B	...	0.79 ± 0.26	5.80 ± 0.29	...	0.319	8.201	22.1	9.4
090509	...	5.58 ± 2.64	293.28 ± 2.76	...	0.338	5.731	17.1	...
090510	0.23 ± 0.04	0.12 ± 0.02	0.54 ± 0.08	0.762	0.616	0.31	14.9	0.903
090515	0.04 ± 0.01	0.02 ± 0.002	0.07 ± 0.02	1.105	0.992	1.285	11.1	...
090516	...	4.39 ± 1.45	228.48 ± 9.45	...	0.504	8.23	24	4.109
090518	1.78 ± 0.30	0.64 ± 0.11	45.80 ± 6.71	0.606	0.378	0.861	24.1	...

Continued on Next Page...

Table A.1 – Continued

GRB	$\Delta t_{\rm min}$ (s)	$\Delta t_{\rm snr}$ (s)	T_{90} (s)	$\sigma_{X,t_{\rm min}}$	$\sigma_{X,t_{\rm snr}}$	χ^2/ν	S/N	z
090519	39.04 ± 6.63	19.66 ± 3.34	81.77 ± 6.00	0.483	0.494	1.263	15.2	3.85
090530	1.26 ± 0.21	0.64 ± 0.11	40.76 ± 1.15	0.554	0.349	0.008	23.7	...
090531A	...	1.73 ± 1.20	45.90 ± 4.91	...	0.217	3.284	32.8	...
090531B	1.78 ± 0.30	0.79 ± 0.26	55.52 ± 0.37	0.756	0.493	0.442	20.1	...
090618	0.45 ± 0.08	0.14 ± 0.05	115.20 ± 0.43	0.071	0.032	0.032	719.8	0.54
090621A	1.26 ± 0.21	0.64 ± 0.11	265.37 ± 1.47	0.170	0.118	0.783	67.2	...
090621B	0.08 ± 0.01	0.03 ± 0.02	0.20 ± 0.03	0.992	0.675	1.333	13.1	...
090628	7.03 ± 1.19	1.73 ± 1.20	27.70 ± 1.61	0.849	0.313	0.618	18.2	...
090709A	0.32 ± 0.05	0.14 ± 0.05	344.85 ± 64.00	0.118	0.063	0.115	251.6	...
090709B	7.03 ± 1.19	1.73 ± 1.20	31.20 ± 1.81	0.933	0.375	0.64	17.7	...
090712	39.04 ± 6.63	19.66 ± 3.34	169.26 ± 10.06	0.686	0.369	0.0005	29.9	...
090715B	...	0.64 ± 0.11	267.54 ± 4.54	...	0.134	8.104	84.9	3
090726	...	5.58 ± 2.64	51.03 ± 0.97	...	0.390	9.288	17.2	2.71
090727	55.00 ± 9.34	24.36 ± 8.04	300.60 ± 3.90	0.857	0.604	0.994	12.3	...
090728	...	7.26 ± 4.32	32.76 ± 3.34	...	0.469	3.981	15	...
090807	...	7.26 ± 4.32	151.59 ± 3.76	...	0.415	6.657	21.3	...
090809	39.04 ± 6.63	19.66 ± 3.34	192.92 ± 5.24	0.893	0.939	0.611	11.8	2.737
090812	0.90 ± 0.15	0.31 ± 0.22	99.76 ± 15.30	0.290	0.145	1.34	78.5	2.452
090813	0.32 ± 0.05	0.12 ± 0.02	7.92 ± 0.24	0.463	0.324	0.293	28	...
090904A	7.03 ± 1.19	3.54 ± 0.60	162.48 ± 5.26	0.424	0.176	2.643	50.1	...
090904B	7.03 ± 1.19	3.54 ± 0.60	58.20 ± 2.40	0.230	0.195	1.999	42.6	...
090912	27.70 ± 4.70	5.58 ± 2.64	151.13 ± 8.03	0.653	0.200	0.815	33.3	...
090916	2.21 ± 0.73	0.79 ± 0.26	53.20 ± 2.08	1.212	1.138	2.693	10.1	...
090926B	...	3.54 ± 0.60	126.36 ± 5.21	...	0.235	4.024	63.3	1.24
090927	...	0.64 ± 0.11	18.36 ± 1.33	...	0.800	5.846	14.3	1.37
090929B	...	0.12 ± 0.02	371.28 ± 2.42	...	0.279	2.927	52.1	...
091018	0.45 ± 0.08	0.18 ± 0.09	4.44 ± 0.15	0.245	0.095	2.267	83.3	0.971
091020	1.78 ± 0.30	0.64 ± 0.11	39.00 ± 1.07	0.247	0.130	1.488	55.8	1.71
091024	...	3.54 ± 0.60	114.73 ± 4.95	...	0.255	8.486	45.2	1.092
091026	7.03 ± 1.19	1.31 ± 0.78	77.42 ± 6.88	0.785	0.192	0.399	30	...
091029	2.51 ± 0.43	1.00 ± 0.48	39.96 ± 1.28	0.195	0.105	2.099	68.4	2.752
091102	...	0.64 ± 0.11	7.07 ± 0.14	...	0.417	3.454	23.3	...
091112	9.90 ± 1.68	3.54 ± 0.60	27.44 ± 2.09	0.581	0.249	0.019	24.1	...
091127	0.23 ± 0.04	0.12 ± 0.02	9.57 ± 0.56	0.332	0.228	0.756	50.7	0.49
091130	9.90 ± 1.68	3.54 ± 0.60	388.96 ± 7.62	0.747	0.277	0.21	27.5	...
091208A	...	1.31 ± 0.78	80.80 ± 4.87	...	0.210	3.732	32.8	...
091208B	0.90 ± 0.15	0.23 ± 0.14	15.21 ± 1.31	0.766	0.247	0.291	29.5	1.063
091221	...	0.64 ± 0.11	68.97 ± 2.02	...	0.134	5.837	85.1	...
100111A	2.51 ± 0.43	0.79 ± 0.26	15.12 ± 0.96	0.766	0.295	0.003	22.9	...
100117A	...	0.64 ± 0.11	638.58 ± 11.62	...	1.525	17.319	11.1	...
100212A	0.64 ± 0.11	0.23 ± 0.14	168.70 ± 3.60	0.693	0.338	1.574	16.3	...
100213A	0.45 ± 0.08	0.18 ± 0.09	2.37 ± 0.11	0.508	0.366	1.972	19.4	...
100305A	...	7.26 ± 4.32	169.99 ± 13.62	...	0.669	23.24	13.9	...
100413A	...	3.54 ± 0.60	197.40 ± 2.34	...	0.184	4.429	47.7	...
100423A	...	0.06 ± 0.04	115.32 ± 9.82	...	0.192	8.861	83	...
100424A	55.00 ± 9.34	19.66 ± 3.34	110.25 ± 5.30	0.514	0.283	0.02	24.3	2.465
100425A	...	4.39 ± 1.45	43.56 ± 1.03	...	0.680	19.417	14.8	1.755
100504A	4.99 ± 0.85	1.73 ± 1.20	98.07 ± 2.27	0.195	0.130	0.176	45.6	...
100513A	39.04 ± 6.63	19.66 ± 3.34	65.10 ± 4.39	0.286	0.265	0.085	23.3	4.772
100522A	...	0.12 ± 0.02	35.22 ± 0.32	...	0.214	12.353	60.8	...
100606A	...	1.00 ± 0.48	191.73 ± 32.09	...	0.276	4.892	41.9	...
100614A	...	40.33 ± 24.01	179.52 ± 12.80	...	0.305	6.963	21	...

Continued on Next Page...

Table A.1 – Continued

GRB	$\Delta t_{\rm min}$ (s)	$\Delta t_{\rm snr}$ (s)	T_{90} (s)	$\sigma_{X,t_{\rm min}}$	$\sigma_{X,t_{\rm snr}}$	χ^2/ν	S/N	z
100615A	...	0.23 ± 0.14	43.46 ± 1.30	...	0.084	4.412	107.3	1.398
100619A	0.90 ± 0.15	0.31 ± 0.22	97.90 ± 0.33	0.202	0.077	0.19	82.7	...
100621A	1.26 ± 0.21	0.31 ± 0.22	66.33 ± 1.27	0.164	0.032	1.806	295.2	0.542
100625A	...	0.03 ± 0.02	0.40 ± 0.06	...	0.265	6.59	28.3	...
100702A	0.16 ± 0.03	0.06 ± 0.04	0.52 ± 0.03	0.796	0.374	0.891	19	...
100704A	...	0.64 ± 0.11	194.56 ± 4.13	...	0.158	4.05	78.1	...
100725A	...	7.26 ± 4.32	151.89 ± 8.15	...	0.187	5.831	30.1	...
100725B	...	0.64 ± 0.11	209.92 ± 7.42	...	0.179	21.013	94.3	...
100727A	4.99 ± 0.85	1.73 ± 1.20	92.75 ± 4.21	0.545	0.192	1.518	31.8	...
100728A	0.23 ± 0.04	0.12 ± 0.02	222.00 ± 6.89	0.118	0.089	2.153	296.9	1.567
100728B	4.99 ± 0.85	1.73 ± 1.20	11.52 ± 0.78	0.617	0.268	0.213	20.6	2.106
100802A	9.90 ± 1.68	3.54 ± 0.60	564.20 ± 14.25	0.709	0.270	0.204	30.6	...
100807A	...	1.00 ± 0.48	8.30 ± 0.45	...	0.533	3.168	14.3	...
100814A	...	0.79 ± 0.26	176.96 ± 3.61	...	0.089	3.591	98	1.44
100816A	0.23 ± 0.04	0.12 ± 0.02	2.50 ± 0.22	0.179	0.148	1.399	58	0.8049
100823A	7.03 ± 1.19	3.54 ± 0.60	18.64 ± 0.93	0.752	0.581	2.434	18.4	...
100901A	39.04 ± 6.63	19.66 ± 3.34	459.19 ± 10.66	0.722	0.548	0.404	17.8	1.408
100902A	13.95 ± 2.37	4.39 ± 1.45	442.68 ± 4.49	0.414	0.192	0.494	33.6	...
100904A	7.03 ± 1.19	3.54 ± 0.60	27.60 ± 2.14	0.512	0.473	1.126	19.6	...
100906A	0.64 ± 0.11	0.23 ± 0.14	116.85 ± 0.69	0.148	0.071	0.699	135.6	1.727
100924A	...	0.64 ± 0.11	75.84 ± 2.06	...	0.245	8.779	67	...
101008A	...	0.79 ± 0.26	9.50 ± 0.18	...	0.422	3.079	20	...
101011A	...	1.00 ± 0.48	38.22 ± 1.88	...	0.293	3.636	24.7	...
101017A	...	0.06 ± 0.04	78.44 ± 1.85	...	0.141	7.878	160.8	...
101023A	0.32 ± 0.05	0.12 ± 0.02	81.64 ± 0.65	0.110	0.045	0.009	277	...
101024A	0.23 ± 0.04	0.12 ± 0.02	19.11 ± 0.17	0.310	0.200	1.507	44.9	...
101030A	9.90 ± 1.68	3.54 ± 0.60	108.64 ± 3.39	0.438	0.164	1.175	43.3	...
101117B	0.32 ± 0.05	0.14 ± 0.05	5.44 ± 0.53	0.423	0.259	1.231	37	...
101213A	...	4.39 ± 1.45	175.68 ± 15.30	...	0.214	7.832	40.8	0.414
101219A	...	0.12 ± 0.02	0.86 ± 0.06	...	0.395	7.509	33.7	0.718
110102A	0.45 ± 0.08	0.18 ± 0.09	271.18 ± 2.13	0.138	0.077	2.427	144	...
110106B	...	1.31 ± 0.78	26.68 ± 1.04	...	0.308	10.004	29.7	...
110119A	0.90 ± 0.15	0.31 ± 0.22	209.07 ± 1.38	0.310	0.152	0.686	84	...
110201A	7.03 ± 1.19	3.54 ± 0.60	13.60 ± 0.66	0.491	0.383	0.886	27.8	...
110205A	0.64 ± 0.11	0.23 ± 0.14	277.02 ± 4.67	0.219	0.118	1.547	150.4	2.22
110207A	...	0.23 ± 0.14	94.80 ± 4.75	...	0.344	3.023	27	...
110212A	...	1.00 ± 0.48	4.65 ± 0.35	...	0.313	2.931	18.2	...
110213A	1.78 ± 0.30	0.79 ± 0.26	43.12 ± 3.47	0.502	0.276	0.771	31	1.46
110223A	...	19.66 ± 3.34	85.20 ± 4.86	...	1.633	6.669	8.5	...
110223B	...	4.39 ± 1.45	64.17 ± 2.55	...	0.866	7.41	13.7	...
110315A	...	1.00 ± 0.48	95.13 ± 2.24	...	0.239	5.195	42.4	...
110318A	...	0.23 ± 0.14	16.80 ± 0.65	...	0.138	25.792	63.2	...
110319A	2.51 ± 0.43	0.79 ± 0.26	20.90 ± 0.71	0.366	0.134	0.07	65.6	...
110402A	...	0.18 ± 0.09	108.42 ± 9.73	...	0.829	2.735	17.4	...
110407A	39.04 ± 6.63	19.66 ± 3.34	156.04 ± 4.84	0.603	0.452	2.396	22.7	...
110411A	9.90 ± 1.68	3.54 ± 0.60	82.77 ± 1.06	0.321	0.130	0.062	52.6	...
110412A	9.90 ± 1.68	4.39 ± 1.45	24.45 ± 1.07	0.567	0.310	0.471	20	...
110414A	...	5.58 ± 2.64	159.87 ± 4.14	...	0.277	2.79	21.9	...
110420A	1.78 ± 0.30	0.64 ± 0.11	15.30 ± 0.95	0.391	0.141	0.191	65	...
110422A	0.23 ± 0.04	0.12 ± 0.02	26.73 ± 0.29	0.118	0.077	0.626	210.1	1.77
110503A	0.64 ± 0.11	0.18 ± 0.09	9.31 ± 0.64	0.341	0.130	1.417	62.7	1.613
110519A	4.99 ± 0.85	1.00 ± 0.48	27.74 ± 0.99	0.445	0.071	0.424	73.2	...

Continued on Next Page...

Table A.1 – Continued

GRB	$\Delta t_{\rm min}$ (s)	$\Delta t_{\rm snr}$ (s)	T_{90} (s)	$\sigma_{X,t_{\rm min}}$	$\sigma_{X,t_{\rm snr}}$	χ^2/ν	S/N	z
110520A	9.90 ± 1.68	3.54 ± 0.60	20.06 ± 0.89	0.462	0.253	0.051	25.9	...
110530A	...	9.63 ± 6.69	46.42 ± 2.26	...	0.533	3.249	12.7	...
110610A	0.90 ± 0.15	0.31 ± 0.22	54.06 ± 2.17	0.265	0.114	0.423	74.8	...
110625A	0.90 ± 0.15	0.18 ± 0.09	64.50 ± 4.25	0.506	0.126	0.241	82	...
110709A	0.23 ± 0.04	0.12 ± 0.02	47.04 ± 1.10	0.164	0.110	0.562	149.2	...
110709B	...	0.64 ± 0.11	57.64 ± 1.08	...	0.164	8.727	108.1	...
110709B	0.64 ± 0.11	0.23 ± 0.14	267.12 ± 2.24	0.212	0.110	0.639	118	...
110715A	0.16 ± 0.03	0.04 ± 0.03	13.15 ± 1.40	0.145	0.045	0.107	202.3	0.82
110731A	...	0.12 ± 0.02	46.56 ± 7.14	...	0.155	4.02	130.3	2.83
110801A	...	1.73 ± 1.20	400.40 ± 1.99	...	0.261	7.97	35.6	1.858
110818A	...	4.39 ± 1.45	77.28 ± 5.61	...	0.295	8.552	30	3.36
110820A	...	4.39 ± 1.45	267.92 ± 2.79	...	0.648	10.202	16.3	...
110915A	...	0.18 ± 0.09	80.86 ± 0.72	...	0.145	7.191	63.3	...
110921A	9.90 ± 1.68	4.39 ± 1.45	33.25 ± 2.00	0.674	0.454	1.653	16.5	...
111008A	...	1.00 ± 0.48	75.66 ± 2.25	...	0.217	5.976	39.2	4.9898
111016A	19.66 ± 3.34	5.58 ± 2.64	554.58 ± 5.16	0.454	0.187	0.705	35.7	...
111022A	...	1.73 ± 1.20	25.60 ± 0.89	...	0.122	4.448	40.4	...
111029A	...	1.31 ± 0.78	8.28 ± 0.25	...	0.245	28.086	25	...
111103A	1.26 ± 0.21	0.64 ± 0.11	11.83 ± 0.13	0.369	0.307	0.714	28.6	...
111103B	...	0.14 ± 0.05	155.74 ± 6.88	...	0.100	3.237	119.6	...
111107A	...	1.73 ± 1.20	31.59 ± 2.44	...	0.290	5.256	23.1	2.893
111121A	0.08 ± 0.01	0.03 ± 0.02	113.16 ± 6.18	0.385	0.224	0.555	37.9	...
111123A	...	3.54 ± 0.60	235.20 ± 6.58	...	0.152	10.182	67	3.1516
111225A	13.95 ± 2.37	5.58 ± 2.64	75.60 ± 2.41	0.511	0.277	0.113	21.7	...
111228A	0.32 ± 0.05	0.12 ± 0.02	101.40 ± 1.31	0.305	0.114	0.346	94.9	0.714
120102A	0.32 ± 0.05	0.14 ± 0.05	41.52 ± 18.21	0.219	0.110	0.295	97	...
120106A	...	0.79 ± 0.26	66.12 ± 1.26	...	0.330	3.676	25.5	...
120116A	1.26 ± 0.21	0.64 ± 0.11	36.08 ± 1.12	0.190	0.114	0.103	82.1	...
120118B	...	1.31 ± 0.78	30.78 ± 2.85	...	0.235	5.851	30.7	2.943
120119A	0.32 ± 0.05	0.14 ± 0.05	70.40 ± 4.32	0.114	0.063	0.366	221.5	1.728
120213A	2.51 ± 0.43	1.00 ± 0.48	38.88 ± 1.53	0.179	0.110	2.292	62.4	...
120218A	...	1.31 ± 0.78	33.60 ± 1.03	...	0.609	3.189	16.4	...
120305A	...	0.006 ± 0.003	0.76 ± 0.26	...	0.290	5.753	31.9	...
120308A	...	19.66 ± 3.34	56.71 ± 3.94	...	0.390	13.445	25.1	...
120311A	0.90 ± 0.15	0.23 ± 0.14	3.68 ± 0.28	0.825	0.261	1.043	25.9	...
120311B	...	1.73 ± 1.20	32.40 ± 1.76	...	0.322	2.803	24.3	...
120324A	0.32 ± 0.05	0.14 ± 0.05	198.72 ± 22.97	0.272	0.138	0.28	124.4	...
120326A	...	0.64 ± 0.11	72.72 ± 3.08	...	0.126	3.532	87.2	1.798
120327A	1.26 ± 0.21	0.64 ± 0.11	71.20 ± 2.33	0.327	0.182	0.159	63.2	2.813
120328A	...	1.73 ± 1.20	30.24 ± 2.75	...	0.490	20.18	17	...
120404A	19.66 ± 3.34	7.26 ± 4.32	40.50 ± 1.49	0.556	0.279	0.125	23.2	2.876
120514A	...	1.00 ± 0.48	167.05 ± 1.21	...	0.228	5.409	28.8	...
120521B	...	19.66 ± 3.34	78.88 ± 6.86	...	0.482	3.636	17.3	...
120521C	3.54 ± 0.60	1.31 ± 0.78	33.18 ± 2.38	0.485	0.182	0.66	31.2	...
120612A	55.00 ± 9.34	24.36 ± 8.04	129.80 ± 13.33	0.609	0.437	0.627	16.1	...
120624B	0.32 ± 0.05	0.14 ± 0.05	174.72 ± 0.28	0.164	0.105	2.071	212.6	...
120703A	0.45 ± 0.08	0.14 ± 0.05	52.83 ± 4.07	0.341	0.114	0.032	67.4	...
120712A	...	0.64 ± 0.11	18.46 ± 1.07	...	0.316	20.141	40.7	4.1745
120714A	...	4.39 ± 1.45	20.40 ± 1.33	...	0.427	2.862	18.1	...
120729A	1.26 ± 0.21	0.64 ± 0.11	78.65 ± 6.50	0.207	0.138	0.302	54	0.8
120802A	1.78 ± 0.30	0.64 ± 0.11	50.16 ± 1.52	0.458	0.210	0.39	46	3.796
120803B	...	3.54 ± 0.60	46.20 ± 3.07	...	0.253	3.317	36.9	...

Continued on Next Page...

Table A.1 – Continued

GRB	$\Delta t_{\rm min}$ (s)	$\Delta t_{\rm snr}$ (s)	T_{90} (s)	$\sigma_{X,t_{\rm min}}$	$\sigma_{X,t_{\rm snr}}$	χ^2/ν	S/N	z
120804A	0.16 ± 0.03	0.06 ± 0.04	1.78 ± 0.32	0.423	0.228	0.894	35.1	...
120811C	1.78 ± 0.30	0.64 ± 0.11	25.20 ± 1.26	0.245	0.100	0.056	83	2.671
120815A	...	1.00 ± 0.48	9.68 ± 1.21	...	0.479	3.449	14.3	2.358
120907A	2.51 ± 0.43	1.00 ± 0.48	6.27 ± 0.28	0.720	0.455	0.872	15.6	0.97
120909A	...	1.31 ± 0.78	617.70 ± 30.95	...	0.217	8.982	49.9	3.93
120911A	...	1.00 ± 0.48	22.14 ± 1.44	...	0.249	4.206	23.4	...
120913A	2.51 ± 0.43	0.79 ± 0.26	32.20 ± 1.68	0.628	0.245	0.851	28	...
120913B	1.78 ± 0.30	0.79 ± 0.26	129.95 ± 1.85	0.210	0.114	0.882	96.3	...
120922A	...	0.79 ± 0.26	179.54 ± 6.27	...	0.173	5.161	43.2	3.1
120927A	...	3.54 ± 0.60	44.10 ± 3.52	...	0.190	5.714	42.8	...
121001A	77.50 ± 13.16	30.99 ± 14.67	148.75 ± 5.79	0.257	0.263	2.197	20.3	...
121011A	19.66 ± 3.34	7.26 ± 4.32	130.98 ± 14.87	0.783	0.335	0.0005	18.6	...
121014A	1.78 ± 0.30	0.79 ± 0.26	58.56 ± 0.43	0.632	0.385	0.078	22.3	...
121024A	7.03 ± 1.19	3.54 ± 0.60	12.46 ± 0.39	0.356	0.349	1.49	19.5	2.298
121027A	9.90 ± 1.68	3.54 ± 0.60	69.30 ± 1.90	0.604	0.232	0.077	38	1.77
121031A	1.26 ± 0.21	0.64 ± 0.11	118.82 ± 3.72	0.187	0.158	2.041	64.1	...
121102A	1.78 ± 0.30	0.79 ± 0.26	33.60 ± 2.67	0.230	0.152	1.93	56.1	...
121108A	...	1.00 ± 0.48	46.17 ± 23.31	...	0.300	11.583	23.8	...
121117A	9.90 ± 1.68	3.54 ± 0.60	32.62 ± 2.47	0.640	0.283	1.611	30.3	...
121123A	3.54 ± 0.60	1.00 ± 0.48	330.88 ± 4.12	0.190	0.071	0.021	130.8	...
121125A	...	0.64 ± 0.11	59.16 ± 4.60	...	0.288	21.644	69.4	...
121128A	...	0.12 ± 0.02	25.65 ± 5.47	...	0.155	2.83	122.3	2.2
121201A	...	1.31 ± 0.78	39.04 ± 2.93	...	0.484	17.138	19.7	3.385
121209A	...	0.23 ± 0.14	43.70 ± 0.46	...	0.239	3.628	39.7	...
121211A	3.54 ± 0.60	1.31 ± 0.78	184.14 ± 2.31	0.537	0.327	0.322	22.3	1.023
121217A	1.78 ± 0.30	0.79 ± 0.26	847.50 ± 12.05	0.221	0.148	2.344	47.8	...
130131A	...	4.39 ± 1.45	51.90 ± 0.40	...	0.818	8.121	13.7	...
130206A	...	5.58 ± 2.64	115.60 ± 17.20	...	0.338	3.412	21.4	...
130215A	...	19.66 ± 3.34	89.05 ± 8.39	...	0.561	4.956	19.4	0.597
130216A	...	0.12 ± 0.02	7.12 ± 0.29	...	0.232	19.947	77.1	...
130306A	3.54 ± 0.60	1.00 ± 0.48	356.15 ± 11.23	0.134	0.045	0.26	156.4	...
130315A	19.66 ± 3.34	7.26 ± 4.32	235.77 ± 3.86	0.498	0.173	2.249	37.1	...
130420A	3.54 ± 0.60	1.00 ± 0.48	114.84 ± 4.84	0.200	0.071	0.255	100.7	1.297
130420B	...	0.79 ± 0.26	10.36 ± 0.70	...	0.237	4.679	29.2	...
130427A	0.06 ± 0.01	0.02 ± 0.002	324.70 ± 2.50	0.063	0.032	0.187	635.6	0.3399
130427B	4.99 ± 0.85	1.31 ± 0.78	7.04 ± 0.26	0.387	0.241	0.862	23.2	2.78
130502A	0.90 ± 0.15	0.31 ± 0.22	3.09 ± 0.14	0.748	0.414	0.968	16.2	...
130504A	9.90 ± 1.68	4.39 ± 1.45	140.94 ± 9.45	0.730	0.504	2.598	18	...
130505A	4.99 ± 0.85	1.31 ± 0.78	292.81 ± 33.84	0.663	0.302	1.397	26	2.27
130511A	...	0.31 ± 0.22	4.95 ± 0.82	...	0.657	7.214	11	1.3033
130514A	1.78 ± 0.30	0.79 ± 0.26	220.32 ± 5.60	0.197	0.141	1.507	79.1	3.6
130521A	2.51 ± 0.43	1.00 ± 0.48	12.00 ± 0.67	0.669	0.302	0.416	20.1	...
130527A	0.64 ± 0.11	0.23 ± 0.14	73.92 ± 6.86	0.355	0.202	2.247	48.1	...
130528A	...	0.64 ± 0.11	652.24 ± 16.89	...	0.164	14.596	86.7	...
130529A	...	24.36 ± 8.04	98.58 ± 4.02	...	0.324	3.621	19.5	...
130603A	39.04 ± 6.63	9.63 ± 6.69	64.90 ± 2.87	0.367	0.161	0.203	31.9	...
130603B	0.01 ± 0.002	0.005 ± 0.001	0.22 ± 0.01	0.396	0.195	0.995	46.9	0.3564
130604A	27.70 ± 4.70	9.63 ± 6.69	78.07 ± 9.81	0.493	0.224	0.162	26.1	1.06
130605A	7.03 ± 1.19	3.54 ± 0.60	12.32 ± 0.60	0.466	0.492	1.008	16	...
130606A	0.90 ± 0.15	0.31 ± 0.22	278.52 ± 3.54	0.414	0.219	0.414	41.7	5.913
130609A	4.99 ± 0.85	1.73 ± 1.20	7.20 ± 0.29	0.277	0.200	0.523	27.3	...
130609B	0.90 ± 0.15	0.31 ± 0.22	254.80 ± 6.66	0.195	0.084	0.534	108.9	...

Continued on Next Page...

Table A.1 – Continued

GRB	$\Delta t_{\rm min}$ (s)	$\Delta t_{\rm snr}$ (s)	T_{90} (s)	$\sigma_{X,t_{\rm min}}$	$\sigma_{X,t_{\rm snr}}$	χ^2/ν	S/N	z
130610A	7.03 ± 1.19	3.54 ± 0.60	48.45 ± 2.35	0.482	0.221	1.129	46.8	2.092
130615A	153.89 ± 26.13	53.49 ± 37.17	343.10 ± 6.64	0.601	0.257	0.357	19.2	...
130625A	13.95 ± 2.37	3.54 ± 0.60	40.64 ± 1.98	0.536	0.228	1.749	30.4	...
130627B	13.95 ± 2.37	5.58 ± 2.64	30.40 ± 1.90	0.673	0.397	0.03	18.2	...
130701A	...	0.14 ± 0.05	4.62 ± 0.09	...	0.134	5.736	71.1	1.155
130722A	1.78 ± 0.30	0.64 ± 0.11	89.40 ± 1.26	0.241	0.095	0.336	154.3	...
130727A	0.45 ± 0.08	0.18 ± 0.09	13.86 ± 0.32	0.292	0.134	0.197	88.2	...
130806A	1.78 ± 0.30	0.79 ± 0.26	6.27 ± 0.18	0.616	0.425	1.524	18.9	...
130807A	...	1.00 ± 0.48	302.25 ± 8.64	...	0.422	4.636	21.6	...
130812A	1.26 ± 0.21	0.64 ± 0.11	8.28 ± 0.24	0.438	0.355	1.282	33.5	...
130831A	0.64 ± 0.11	0.23 ± 0.14	34.65 ± 0.53	0.200	0.071	0.777	92.3	...
130907A	0.06 ± 0.01	0.03 ± 0.01	357.23 ± 2.03	0.071	0.045	2.184	801.4	...
130919A	...	19.66 ± 3.34	86.52 ± 4.00	...	0.469	16.655	19.9	...
131002B	13.95 ± 2.37	5.58 ± 2.64	54.72 ± 4.12	0.631	0.261	2.564	24.7	...

APPENDIX B

FERMI GRB MINIMUM TIMESCALES

Table B.1: *Fermi* GRB Minimum Timescales

Trigger ID	GRB Name	$\Delta t_{\rm min}$ (s)	$\Delta t_{\rm S/N}$ (s)	T_{90} (s)	$T_{100}^{\rm start}$ (s)	$T_{100}^{\rm stop}$ (s)	$\sigma_{X,t_{\rm min}}$	$\sigma_{X,t_{\rm S/N}}$	z
080714086	080714B	0.821 ± 0.223	0.522 ± 0.045	5.376 ± 2.360	-3.437	7.283	0.90	0.57	...
080714425	080714C	1.984 ± 1.040	1.241 ± 0.108	40.192 ± 1.145	-22.987	55.766	0.64	0.40	...
080714745	080714A	1.384 ± 0.143	0.620 ± 0.054	59.649 ± 11.276	-29.747	88.936	0.74	0.33	...
080715950	080715A	< 0.101	0.011 ± 0.001	7.872 ± 0.272	-2.203	11.867	0.90	0.20	...
080717543	080717A	0.568 ± 0.194	0.369 ± 0.032	36.609 ± 2.985	-23.414	49.420	0.53	0.34	...
080719529	080719A	1.990 ± 0.830	1.241 ± 0.108	16.128 ± 17.887	-12.339	19.739	0.64	0.40	...
080723557	080723B	0.040 ± 0.017	0.027 ± 0.002	58.369 ± 1.985	-0.180	89.694	0.22	0.15	...
080723913	080723C	0.013 ± 0.004	0.008 ± 0.001	0.192 ± 0.345	-0.160	0.224	0.96	0.58	...
080723985	080723D	< 0.309	0.065 ± 0.006	42.817 ± 0.659	-4.995	66.909	0.29	0.13	...
080724401	080724A	< 0.129	0.016 ± 0.001	379.397 ± 2.202	-10.638	390.213	0.50	0.13	...
080725435	080725A	< 1.700	0.439 ± 0.038	25.920 ± 1.208	-14.091	35.934	0.28	0.15	...
080725541	080725B	< 0.266	0.065 ± 0.006	0.960 ± 1.292	-0.603	1.230	0.90	0.35	...
080727964	080727C	< 0.883	0.369 ± 0.032	89.089 ± 6.476	-31.416	90.623	0.27	0.20	...
080730520	080730A	< 0.794	0.184 ± 0.016	17.408 ± 6.229	-9.197	25.429	0.28	0.12	...
080730786	080730B	< 0.297	0.046 ± 0.004	13.312 ± 4.222	-7.171	19.295	0.57	0.11	...
080802386	080802A	0.017 ± 0.006	0.011 ± 0.001	0.576 ± 0.091	-0.352	0.796	0.69	0.45	...
080803772	080803A	1.326 ± 0.295	0.738 ± 0.064	26.240 ± 1.691	-13.245	38.973	0.60	0.33	...
080804456	080804B	< 1.538	0.522 ± 0.045	501.830 ± 6.476	-27.198	493.126	0.34	0.32	...
080804972	080804A	0.702 ± 0.338	0.439 ± 0.038	24.704 ± 1.460	-11.880	37.273	0.26	0.16	2.2
080805496	080805B	1.551 ± 0.340	0.620 ± 0.054	29.440 ± 3.566	-6.944	42.221	0.59	0.24	...
080805584	080805C	4.656 ± 1.341	2.087 ± 0.181	65.665 ± 14.676	-25.892	93.609	0.60	0.27	...
080806584	080806A	0.659 ± 0.290	0.310 ± 0.027	2.304 ± 0.453	-3.254	1.138	0.66	0.31	...
080806896	080806B	< 0.538	0.130 ± 0.011	75.777 ± 4.185	-35.328	64.275	0.33	0.14	...
080807993	080807A	0.009 ± 0.003	0.007 ± 0.001	19.072 ± 0.181	-9.447	27.148	0.39	0.30	...
080808451	080808A	0.853 ± 0.267	0.522 ± 0.045	4.352 ± 0.832	-3.696	4.376	0.85	0.52	...
080808565	080808B	2.298 ± 0.106	0.522 ± 0.045	17.728 ± 1.489	-6.343	28.211	0.55	0.12	...
080808772	080808C	1.610 ± 0.709	1.043 ± 0.090	211.970 ± 6.557	-170.562	146.090	0.68	0.44	...
080809808	080809A	< 4.629	1.043 ± 0.090	28.160 ± 2.896	-21.022	32.482	0.61	0.25	...
080810549	080810A	0.102 ± 0.040	0.065 ± 0.006	107.457 ± 15.413	-28.134	114.761	0.43	0.28	3.35
080812889	080812A	0.486 ± 0.311	0.310 ± 0.027	15.040 ± 0.462	-9.237	18.738	0.61	0.39	...
080815917	080815A	< 0.258	0.110 ± 0.010	0.832 ± 0.320	-0.730	0.927	0.62	0.52	...
080816503	080816A	< 0.152	0.033 ± 0.003	64.769 ± 1.810	-1.421	84.710	0.45	0.18	...
080816989	080816B	0.083 ± 0.019	0.039 ± 0.003	4.608 ± 0.453	-0.141	6.805	0.59	0.27	...
080817161	080817A	0.243 ± 0.070	0.110 ± 0.010	60.289 ± 0.466	-23.013	89.108	0.15	0.07	...
080817720	080817B	0.043 ± 0.018	0.023 ± 0.002	4.416 ± 0.363	-2.274	6.526	0.59	0.31	...
080818579	080818A	0.229 ± 0.070	0.078 ± 0.007	59.329 ± 8.749	-28.682	85.806	0.50	0.17	...
080818945	080818B	< 0.493	0.155 ± 0.013	13.376 ± 0.410	-7.141	19.445	0.45	0.30	...
080821332	080821A	0.305 ± 0.118	0.155 ± 0.013	5.888 ± 0.264	-4.199	7.503	0.29	0.15	...
080823363	080823A	0.675 ± 0.207	0.310 ± 0.027	43.457 ± 1.717	-5.181	63.888	0.34	0.15	...
080824909	080824A	0.117 ± 0.019	0.046 ± 0.004	7.424 ± 2.005	-5.754	7.825	0.57	0.22	...
080825593	080825C	< 0.248	0.023 ± 0.002	20.992 ± 0.231	-1.418	32.569	0.50	0.07	...
080828189	080828B	< 0.135	0.078 ± 0.007	3.008 ± 3.329	-1.621	4.379	0.66	0.80	...
080829790	080829A	< 1.534	0.310 ± 0.027	7.680 ± 0.377	-4.122	11.162	0.52	0.19	...
080830368	080830A	0.294 ± 0.220	0.184 ± 0.016	40.896 ± 5.069	-21.972	59.788	0.38	0.24	...
080831053	080831A	< 0.017	0.004 ± 0.001	0.576 ± 1.168	-0.576	0.572	0.88	0.53	...
080831921	080831B	0.797 ± 0.349	0.522 ± 0.045	74.497 ± 1.243	-32.933	106.344	0.41	0.27	...
080904886	080904A	0.193 ± 0.041	0.078 ± 0.007	17.344 ± 1.385	-9.587	23.359	0.31	0.13	...
080905499	080905A	0.012 ± 0.003	0.008 ± 0.001	0.960 ± 0.345	-0.539	1.371	0.87	0.56	0.1218
080905570	080905C	0.447 ± 0.245	0.310 ± 0.027	26.624 ± 2.896	-19.918	32.523	0.36	0.25	...
080905705	080905B	< 3.071	0.738 ± 0.064	105.984 ± 6.802	-23.660	123.652	0.78	0.34	2.374
080906212	080906B	0.173 ± 0.024	0.065 ± 0.006	2.875 ± 0.767	-1.426	4.294	0.27	0.10	...

Continued on Next Page...

Table B.1 – Continued

Trigger ID	GRB Name	$\Delta t_{\rm min}$ (s)	$\Delta t_{\rm S/N}$ (s)	T_{90} (s)	$T_{100}^{\rm start}$ (s)	$T_{100}^{\rm stop}$ (s)	$\sigma_{X,t_{\rm min}}$	$\sigma_{X,t_{\rm S/N}}$	z
080912360	080912A	< 4.072	0.620 ± 0.054	16.384 ± 2.896	-11.184	21.412	0.77	0.17	...
080913735	080913B	0.124 ± 0.090	0.065 ± 0.006	41.217 ± 7.281	-20.617	61.371	0.52	0.28	...
080916009	080916C	< 0.160	0.039 ± 0.003	62.977 ± 0.810	-14.295	87.070	0.24	0.11	...
080916406	080916A	1.639 ± 0.197	0.522 ± 0.045	46.337 ± 7.173	-22.503	69.674	0.56	0.18	0.689
080919790	080919B	0.011 ± 0.001	0.004 ± 0.001	0.512 ± 0.405	-0.382	0.637	0.98	0.40	...
080920268	080920A	9.473 ± 1.615	4.174 ± 0.362	113.921 ± 3.125	-33.216	163.865	0.82	0.36	...
080924766	080924A	0.467 ± 0.064	0.219 ± 0.019	39.937 ± 4.222	-27.818	48.429	0.55	0.26	...
080925775	080925A	< 0.350	0.078 ± 0.007	31.744 ± 3.167	-16.746	46.099	0.24	0.08	...
080927480	080927A	2.257 ± 0.790	1.043 ± 0.090	45.313 ± 3.083	-22.579	67.568	0.42	0.20	...
080928628	080928A	< 0.344	0.110 ± 0.010	14.336 ± 4.007	-8.896	19.600	0.75	0.41	1.692
081003644	081003C	< 0.546	0.155 ± 0.013	50.177 ± 3.692	-21.521	65.256	0.69	0.46	...
081006604	081006A	< 0.620	0.219 ± 0.019	6.400 ± 0.923	-3.424	9.312	0.69	0.58	...
081006872	081006B	0.134 ± 0.067	0.092 ± 0.008	3.328 ± 1.305	-2.163	4.477	0.75	0.52	...
081008832	081008A	< 1.260	0.261 ± 0.023	150.015 ± 12.892	-29.594	201.406	0.30	0.20	1.9685
081009140	081009A	0.163 ± 0.013	0.039 ± 0.003	41.345 ± 0.264	-3.900	61.004	0.14	0.03	...
081009690	081009B	< 0.601	0.219 ± 0.019	176.191 ± 2.127	-25.547	194.678	0.21	0.18	...
081012045	081012B	< 0.023	0.005 ± 0.001	1.216 ± 1.748	-1.174	1.238	0.93	0.61	...
081012549	081012A	< 2.163	0.522 ± 0.045	30.721 ± 5.615	-20.507	40.626	0.52	0.28	...
081017474	081017B	< 1.446	0.219 ± 0.019	28.416 ± 2.757	-27.044	29.472	0.77	0.38	...
081021398	081021A	< 2.008	0.620 ± 0.054	26.112 ± 3.974	-3.499	29.125	0.43	0.29	...
081022364	081022A	1.982 ± 0.290	0.877 ± 0.076	17.152 ± 3.727	-11.056	23.052	0.74	0.33	...
081024245	081024A	0.086 ± 0.009	0.039 ± 0.003	0.832 ± 1.282	-1.242	0.415	1.02	0.46	...
081024851	081024C	5.151 ± 0.941	2.482 ± 0.215	56.065 ± 2.064	-8.117	82.139	0.32	0.16	...
081024891	081024B	< 0.056	0.016 ± 0.001	0.640 ± 0.264	-0.381	0.893	0.81	0.54	...
081025349	081025A	< 0.196	0.065 ± 0.006	22.528 ± 0.724	-11.667	24.815	0.37	0.32	...
081028538	081028B	< 0.350	0.078 ± 0.007	13.312 ± 1.280	-14.531	11.935	0.41	0.23	...
081101167	081101C	< 4.574	1.043 ± 0.090	9.984 ± 9.051	-8.389	6.980	1.05	0.72	...
081101491	081101A	0.072 ± 0.010	0.033 ± 0.003	0.128 ± 0.091	-0.128	0.128	0.95	0.43	...
081101532	081101B	< 0.158	0.055 ± 0.005	8.256 ± 0.889	-2.456	12.047	0.27	0.25	...
081102365	081102B	0.081 ± 0.015	0.046 ± 0.004	1.728 ± 0.231	-0.923	2.517	0.70	0.40	...
081102739	081102A	< 7.327	0.620 ± 0.054	34.817 ± 2.415	-9.686	51.562	1.36	0.22	...
081105614	081105B	0.036 ± 0.005	0.019 ± 0.002	1.280 ± 1.368	-0.698	1.850	1.01	0.54	...
081107321	081107A	0.034 ± 0.012	0.019 ± 0.002	1.664 ± 0.234	-0.935	2.302	0.30	0.17	...
081109293	081109A	< 5.608	1.476 ± 0.128	58.369 ± 5.221	-25.721	80.494	0.46	0.18	...
081110601	081110A	0.291 ± 0.011	0.078 ± 0.007	11.776 ± 2.573	-5.581	17.821	0.63	0.17	...
081113230	081113A	0.012 ± 0.005	0.008 ± 0.001	0.576 ± 1.350	-0.288	0.860	0.63	0.42	...
081115891	081115A	< 0.158	0.046 ± 0.004	0.320 ± 0.653	-0.350	0.286	0.77	0.52	...
081118876	081118B	< 0.962	0.155 ± 0.013	20.736 ± 1.379	-2.143	31.216	0.31	0.10	...
081119184	081119A	< 0.333	0.078 ± 0.007	0.320 ± 0.680	-0.478	0.158	1.12	0.64	...
081120618	081120A	< 0.467	0.184 ± 0.016	25.344 ± 0.923	-13.827	36.599	0.23	0.22	...
081121858	081121A	0.203 ± 0.030	0.092 ± 0.008	41.985 ± 8.510	-5.898	62.110	0.57	0.26	2.512
081122520	081122A	< 0.102	0.023 ± 0.002	23.296 ± 2.111	-11.796	34.532	0.43	0.18	...
081122614	081122B	0.012 ± 0.002	0.007 ± 0.001	0.192 ± 0.091	-0.160	0.224	0.73	0.40	...
081124060	081124A	0.955 ± 0.040	0.184 ± 0.016	19.456 ± 1.086	-9.127	29.559	0.43	0.08	...
081125496	081125A	< 0.326	0.078 ± 0.007	9.280 ± 0.607	-4.082	14.386	0.19	0.10	...
081126899	081126A	< 0.635	0.110 ± 0.010	54.145 ± 0.923	-29.069	62.968	0.47	0.15	...
081129161	081129A	0.123 ± 0.093	0.065 ± 0.006	62.657 ± 7.318	-28.029	93.493	0.27	0.14	...
081130212	081130A	0.006 ± 0.002	0.004 ± 0.001	2.240 ± 1.002	-1.173	3.285	0.88	0.53	...
081130629	081130B	< 0.685	0.184 ± 0.016	45.569 ± 3.908	-38.657	19.081	0.49	0.20	...
081204004	081204C	< 0.434	0.110 ± 0.010	7.424 ± 1.846	-9.309	5.457	0.57	0.26	...
081204517	081204B	< 0.037	0.008 ± 0.001	0.192 ± 0.286	-0.160	0.224	0.95	0.36	...
081206275	081206A	< 10.133	1.043 ± 0.090	24.576 ± 5.724	-23.623	25.497	0.84	0.21	...

Continued on Next Page...

Table B.1 – Continued

Trigger ID	GRB Name	$\Delta t_{\rm min}$ (s)	$\Delta t_{\rm S/N}$ (s)	T_{90} (s)	$T_{100}^{\rm start}$ (s)	$T_{100}^{\rm stop}$ (s)	$\sigma_{X,t_{\rm min}}$	$\sigma_{X,t_{\rm S/N}}$	z
081206604	081206B	1.859 ± 0.239	0.620 ± 0.054	7.936 ± 4.382	-5.984	9.856	0.88	0.29	...
081206987	081206C	< 7.263	1.476 ± 0.128	22.528 ± 2.919	-17.043	27.771	0.99	0.31	...
081207680	081207A	0.346 ± 0.150	0.261 ± 0.023	97.282 ± 2.347	-26.296	131.297	0.17	0.12	...
081209981	081209A	< 0.007	0.004 ± 0.001	0.192 ± 0.143	-0.160	0.224	0.45	0.47	...
081213173	081213A	< 0.020	0.004 ± 0.001	0.256 ± 0.286	-0.384	0.128	0.87	0.52	...
081215784	081215A	0.042 ± 0.004	0.010 ± 0.001	5.568 ± 0.143	-1.544	9.520	0.30	0.07	...
081215880	081215B	0.481 ± 0.082	0.184 ± 0.016	7.680 ± 2.064	-4.058	11.226	0.94	0.36	...
081216531	081216A	< 0.028	0.008 ± 0.001	0.768 ± 0.429	-0.377	1.151	0.39	0.20	...
081217983	081217A	< 0.268	0.065 ± 0.006	29.696 ± 12.892	-12.112	29.737	0.26	0.16	...
081221681	081221A	< 0.600	0.130 ± 0.011	29.697 ± 0.410	-2.773	47.683	0.20	0.06	2.26
081222204	081222A	0.176 ± 0.088	0.092 ± 0.008	18.880 ± 2.318	-8.962	28.043	0.14	0.07	2.77
081223419	081223A	0.082 ± 0.010	0.033 ± 0.003	0.576 ± 0.143	-0.352	0.796	0.61	0.24	...
081224887	081224A	0.544 ± 0.052	0.155 ± 0.013	16.448 ± 1.159	-0.341	25.306	0.25	0.07	...
081225257	081225A	< 0.497	0.155 ± 0.013	41.217 ± 5.667	-31.733	42.839	0.41	0.37	...
081226044	081226A	0.143 ± 0.024	0.065 ± 0.006	0.832 ± 1.032	-0.602	1.055	0.87	0.40	...
081226156	081226C	< 0.829	0.261 ± 0.023	65.793 ± 1.619	-55.553	24.607	0.63	0.31	...
081226509	081226B	0.061 ± 0.015	0.033 ± 0.003	0.192 ± 0.143	-0.160	0.224	0.82	0.44	...
081229187	081229A	0.141 ± 0.026	0.055 ± 0.005	0.768 ± 0.724	-0.633	0.895	0.80	0.31	...
081230871	081230B	< 0.620	0.261 ± 0.023	0.512 ± 0.272	-0.382	0.637	0.69	0.99	...
081231140	081231A	0.089 ± 0.057	0.055 ± 0.005	28.736 ± 2.611	-11.869	41.550	0.31	0.19	...
090101758	090101A	0.815 ± 0.278	0.369 ± 0.032	108.802 ± 1.619	-20.076	128.980	0.25	0.11	...
090102122	090102A	0.033 ± 0.013	0.019 ± 0.002	26.624 ± 0.810	-11.645	41.329	0.31	0.18	1.547
090107681	090107B	< 1.404	0.522 ± 0.045	18.432 ± 2.896	-11.178	25.478	0.65	0.59	...
090108020	090108A	0.043 ± 0.008	0.014 ± 0.001	0.704 ± 0.143	-0.414	0.985	0.45	0.14	...
090108322	090108B	0.038 ± 0.006	0.016 ± 0.001	0.192 ± 0.143	-0.160	0.202	0.78	0.33	...
090109332	090109A	< 0.266	0.130 ± 0.011	1.728 ± 0.820	-1.115	2.325	0.91	0.95	...
090112332	090112A	0.480 ± 0.053	0.219 ± 0.019	58.369 ± 4.783	-31.537	72.344	0.76	0.35	...
090112729	090112B	0.101 ± 0.059	0.055 ± 0.005	14.080 ± 5.126	-7.738	20.141	0.18	0.10	...
090113778	090113A	0.136 ± 0.062	0.065 ± 0.006	17.408 ± 3.238	-10.669	23.957	0.53	0.25	1.7493
090117335	090117B	< 0.892	0.130 ± 0.011	27.264 ± 1.286	-13.895	40.352	0.97	0.27	...
090117632	090117C	0.402 ± 0.258	0.261 ± 0.023	75.777 ± 3.238	-50.177	35.008	0.30	0.20	...
090117640	090117A	< 0.138	0.039 ± 0.003	15.552 ± 4.580	-12.020	17.972	0.36	0.19	...
090120627	090120A	0.118 ± 0.027	0.078 ± 0.007	1.856 ± 0.181	-1.439	2.260	0.91	0.60	...
090126227	090126B	1.668 ± 0.140	0.522 ± 0.045	5.632 ± 0.810	-4.586	6.654	0.76	0.24	...
090126245	090126C	0.020 ± 0.009	0.014 ± 0.001	0.960 ± 0.231	-0.859	1.051	0.97	0.65	...
090129880	090129A	0.973 ± 0.054	0.310 ± 0.027	16.640 ± 3.328	-4.998	24.621	0.58	0.19	...
090131090	090131A	0.138 ± 0.005	0.033 ± 0.003	35.073 ± 1.056	-2.175	55.674	0.38	0.09	...
090202347	090202A	< 0.902	0.130 ± 0.011	12.608 ± 0.345	-2.147	19.021	0.69	0.18	...
090206620	090206A	0.017 ± 0.004	0.010 ± 0.001	0.320 ± 0.143	-0.222	0.414	0.58	0.33	...
090207777	090207A	1.651 ± 0.286	0.620 ± 0.054	24.832 ± 3.899	-12.810	35.589	0.55	0.21	...
090213236	090213A	3.244 ± 1.884	2.087 ± 0.181	20.224 ± 6.192	-14.109	26.129	0.80	0.51	...
090217206	090217A	< 0.108	0.019 ± 0.002	33.280 ± 0.724	-15.762	40.481	0.33	0.11	...
090219074	090219A	< 0.282	0.055 ± 0.005	0.448 ± 0.272	-0.233	0.608	1.08	0.64	...
090222179	090222A	< 0.979	0.184 ± 0.016	17.408 ± 3.238	-10.669	23.957	0.70	0.24	...
090225009	090225A	< 0.697	0.184 ± 0.016	2.176 ± 2.833	-2.749	1.355	0.95	0.80	...
090227310	090227A	0.069 ± 0.018	0.046 ± 0.004	16.189 ± 0.831	-8.015	24.183	0.70	0.47	...
090227772	090227B	< 0.005	0.001 ± 0.001	1.280 ± 1.026	-0.698	1.837	0.22	0.20	...
090228204	090228A	0.004 ± 0.001	0.001 ± 0.001	0.448 ± 0.143	-0.221	0.672	0.51	0.17	...
090228976	090228B	< 2.017	0.522 ± 0.045	7.936 ± 1.379	-3.936	11.904	0.68	0.35	...
090301315	090301B	0.425 ± 0.180	0.184 ± 0.016	23.296 ± 2.064	-28.491	17.138	0.40	0.17	...
090304216	090304A	< 0.700	0.310 ± 0.027	2.816 ± 0.923	-1.658	3.942	0.82	0.74	...
090305052	090305B	< 0.029	0.008 ± 0.001	1.856 ± 0.580	-0.991	2.708	0.41	0.39	...

Continued on Next Page...

Table B.1 – Continued

Trigger ID	GRB Name	$\Delta t_{\rm min}$ (s)	$\Delta t_{\rm S/N}$ (s)	T_{90} (s)	$T_{100}^{\rm start}$ (s)	$T_{100}^{\rm stop}$ (s)	$\sigma_{X,t_{\rm min}}$	$\sigma_{X,t_{\rm S/N}}$	z
090306245	090306C	< 2.198	0.877 ± 0.076	27.904 ± 14.857	-7.727	38.866	0.59	0.45	...
090307167	090307B	< 5.470	1.476 ± 0.128	29.440 ± 1.810	-8.042	38.768	0.87	0.54	...
090308734	090308B	0.010 ± 0.004	0.004 ± 0.001	1.664 ± 0.286	-1.146	2.174	0.49	0.21	...
090309767	090309B	1.183 ± 0.313	0.620 ± 0.054	56.513 ± 5.146	-2.549	83.896	0.41	0.22	...
090310189	090310A	0.502 ± 0.108	0.219 ± 0.019	116.930 ± 1.056	-11.521	143.982	0.57	0.25	...
090316311	090316A	< 0.099	0.019 ± 0.002	10.240 ± 1.557	-14.797	5.581	0.76	0.50	...
090319622	090319A	< 0.884	0.219 ± 0.019	54.785 ± 2.202	-25.649	69.121	0.59	0.32	...
090320045	090320C	0.794 ± 0.204	0.369 ± 0.032	2.368 ± 0.272	-3.288	1.432	0.86	0.40	...
090320418	090320A	1.924 ± 0.269	0.877 ± 0.076	7.936 ± 1.296	-5.600	10.240	0.94	0.43	...
090320801	090320B	< 0.755	0.155 ± 0.013	29.184 ± 4.536	-14.960	43.108	0.71	0.29	...
090323002	090323A	0.103 ± 0.070	0.055 ± 0.005	135.170 ± 1.448	-6.138	161.460	0.14	0.07	3.57*
090326633	090326A	< 0.313	0.092 ± 0.008	16.128 ± 3.208	-17.203	14.875	0.55	0.36	...
090327404	090327A	0.892 ± 0.612	0.620 ± 0.054	14.080 ± 1.379	-3.014	22.330	0.24	0.16	...
090328401	090328A	< 0.040	0.014 ± 0.001	61.697 ± 1.810	-26.139	91.670	0.20	0.15	0.736*
090328713	090328B	0.004 ± 0.001	0.002 ± 0.001	0.192 ± 1.032	-0.160	0.224	0.49	0.27	...
090330279	090330A	< 0.442	0.155 ± 0.013	73.473 ± 1.717	-51.969	38.580	0.17	0.15	...
090331681	090331A	0.042 ± 0.014	0.023 ± 0.002	0.832 ± 0.143	-0.474	1.183	0.75	0.42	...
090403314	090403A	1.350 ± 0.665	0.738 ± 0.064	14.848 ± 1.846	-9.658	19.874	0.50	0.27	...
090405663	090405A	0.044 ± 0.022	0.027 ± 0.002	0.448 ± 1.498	-0.285	0.608	0.66	0.41	...
090409288	090409A	4.008 ± 1.319	2.482 ± 0.215	30.337 ± 2.796	-24.130	10.131	0.80	0.49	...
090411838	090411A	< 0.154	0.033 ± 0.003	21.501 ± 3.237	-4.835	32.144	0.54	0.37	...
090411991	090411B	0.214 ± 0.041	0.130 ± 0.011	14.336 ± 1.086	-4.904	22.160	0.59	0.36	...
090412061	090412A	< 0.741	0.369 ± 0.032	0.896 ± 0.264	-1.275	0.512	0.82	0.98	...
090413122	090413A	0.128 ± 0.070	0.092 ± 0.008	32.513 ± 4.360	-27.634	26.316	0.52	0.38	...
090418816	090418C	0.061 ± 0.009	0.027 ± 0.002	0.320 ± 0.405	-0.222	0.414	0.95	0.43	...
090419997	090419B	0.885 ± 0.705	0.522 ± 0.045	166.915 ± 11.723	-65.793	183.828	0.24	0.14	...
090422150	090422A	0.304 ± 0.114	0.184 ± 0.016	9.216 ± 0.362	-5.082	13.226	0.78	0.47	...
090423330	090423A	1.177 ± 0.592	0.620 ± 0.054	7.168 ± 2.415	-9.440	4.808	0.63	0.33	8.1
090424592	090424A	< 0.036	0.008 ± 0.001	14.144 ± 0.264	-4.512	21.506	0.21	0.06	0.544
090425377	090425A	0.294 ± 0.040	0.110 ± 0.010	75.393 ± 2.450	-3.087	100.937	0.41	0.15	...
090426066	090426B	0.407 ± 0.175	0.261 ± 0.023	16.128 ± 5.152	-9.779	22.299	0.70	0.45	...
090426690	090426C	0.169 ± 0.086	0.130 ± 0.011	7.488 ± 2.496	-4.713	10.023	0.24	0.19	...
090427644	090427B	< 1.669	0.522 ± 0.045	1.024 ± 0.362	-2.301	-0.261	0.75	1.00	...
090427688	090427C	< 1.316	0.261 ± 0.023	12.288 ± 1.280	-7.111	17.327	0.60	0.37	...
090428441	090428A	0.103 ± 0.056	0.046 ± 0.004	3.968 ± 1.506	-2.160	5.760	0.43	0.19	...
090428552	090428B	1.166 ± 0.181	0.439 ± 0.038	31.489 ± 11.846	-24.161	38.484	0.42	0.16	...
090429530	090429C	1.343 ± 0.336	0.620 ± 0.054	14.336 ± 4.007	-9.664	18.832	0.65	0.30	...
090429753	090429D	< 0.077	0.023 ± 0.002	0.640 ± 0.466	-0.509	0.765	0.48	0.34	...
090502777	090502A	0.247 ± 0.065	0.130 ± 0.011	66.048 ± 1.619	-12.712	74.461	0.59	0.31	...
090509215	090509A	< 0.555	0.184 ± 0.016	283.844 ± 2.463	-26.945	296.632	0.67	0.57	...
090510016	090510A	0.005 ± 0.001	0.002 ± 0.001	0.960 ± 0.138	-0.523	1.387	0.66	0.29	0.903
090510325	090510B	< 2.938	0.877 ± 0.076	7.424 ± 1.717	-4.701	10.065	0.91	0.50	...
090511684	090511A	< 0.596	0.219 ± 0.019	7.616 ± 1.605	-5.250	9.950	0.52	0.39	...
090513916	090513A	< 3.891	1.043 ± 0.090	25.280 ± 7.146	-13.438	36.869	0.43	0.32	...
090513941	090513B	3.709 ± 1.682	2.482 ± 0.215	11.776 ± 2.064	-9.677	13.725	0.70	0.47	...
090514006	090514A	0.689 ± 0.131	0.261 ± 0.023	43.521 ± 1.739	-21.364	65.240	0.47	0.18	...
090514726	090514B	< 0.190	0.055 ± 0.005	2.240 ± 0.286	-1.749	2.709	0.45	0.21	...
090514734	090514C	1.021 ± 0.189	0.522 ± 0.045	54.401 ± 4.077	-29.469	68.451	0.37	0.19	...
090516137	090516B	0.683 ± 0.300	0.369 ± 0.032	118.018 ± 4.028	-30.772	141.508	0.28	0.15	...
090516353	090516A	0.415 ± 0.185	0.261 ± 0.023	123.074 ± 2.896	-36.097	123.449	0.41	0.26	4.109
090516853	090516C	0.331 ± 0.099	0.155 ± 0.013	14.464 ± 3.093	-7.258	21.518	0.46	0.22	...
090518080	090518A	0.479 ± 0.158	0.261 ± 0.023	2.048 ± 0.410	-1.658	2.422	0.64	0.35	...

Continued on Next Page...

Table B.1 – Continued

Trigger ID	GRB Name	$\Delta t_{\rm min}$ (s)	$\Delta t_{\rm S/N}$ (s)	T_{90} (s)	$T_{100}^{\rm start}$ (s)	$T_{100}^{\rm stop}$ (s)	$\sigma_{X,t_{\rm min}}$	$\sigma_{X,t_{\rm S/N}}$	z
090518244	090518B	0.279 ± 0.064	0.130 ± 0.011	6.784 ± 1.000	-3.744	9.748	0.56	0.26	...
090519462	090519B	< 0.652	0.155 ± 0.013	91.329 ± 3.692	-27.530	117.668	0.73	0.39	...
090519881	090519A	< 0.934	0.369 ± 0.032	74.177 ± 5.177	-21.539	109.724	0.63	0.57	3.85
090520832	090520B	0.354 ± 0.062	0.184 ± 0.016	0.768 ± 0.834	-0.825	0.703	1.03	0.54	...
090520850	090520C	< 0.171	0.039 ± 0.003	3.776 ± 0.923	-2.261	5.259	0.59	0.27	...
090520876	090520D	1.219 ± 0.181	0.369 ± 0.032	30.657 ± 0.859	-22.112	15.269	0.35	0.11	...
090522344	090522A	0.104 ± 0.046	0.065 ± 0.006	20.288 ± 6.262	-14.911	25.447	0.56	0.35	...
090524346	090524A	< 0.383	0.092 ± 0.008	54.337 ± 0.870	-13.415	77.299	0.24	0.10	...
090528173	090528A	< 0.994	0.439 ± 0.038	35.905 ± 2.187	-24.522	46.919	0.17	0.18	...
090528516	090528B	0.163 ± 0.047	0.065 ± 0.006	79.041 ± 1.088	-25.734	116.538	0.22	0.09	...
090529310	090529B	< 0.762	0.219 ± 0.019	3.072 ± 0.362	-2.039	4.081	0.80	0.37	...
090529564	090529C	< 0.049	0.014 ± 0.001	9.853 ± 0.179	-4.389	13.126	0.29	0.13	...
090530760	090530B	< 3.443	0.620 ± 0.054	127.554 ± 1.319	-2.343	159.632	0.45	0.09	...
090531775	090531B	0.049 ± 0.012	0.027 ± 0.002	0.768 ± 0.231	-0.377	1.151	0.94	0.52	...
090602564	090602A	< 0.994	0.261 ± 0.023	20.736 ± 7.209	-11.808	29.010	0.51	0.44	...
090606471	090606A	< 7.550	1.755 ± 0.152	8.064 ± 1.262	-5.274	10.766	0.93	0.79	...
090608052	090608A	< 2.164	0.439 ± 0.038	21.504 ± 2.290	-27.072	15.712	0.70	0.36	...
090610648	090610A	0.422 ± 0.150	0.219 ± 0.019	6.144 ± 8.136	-7.139	5.079	0.53	0.27	...
090610723	090610B	1.210 ± 0.545	0.738 ± 0.064	144.896 ± 3.367	-5.092	213.677	0.61	0.37	...
090610883	090610C	< 2.689	0.620 ± 0.054	7.424 ± 1.639	-6.493	8.273	0.81	0.46	...
090612619	090612A	0.785 ± 0.100	0.261 ± 0.023	42.433 ± 2.888	-36.096	10.313	0.55	0.18	...
090616157	090616A	0.297 ± 0.084	0.155 ± 0.013	1.152 ± 1.168	-0.757	1.534	0.73	0.38	...
090617208	090617A	0.015 ± 0.003	0.007 ± 0.001	0.192 ± 0.143	-0.160	0.224	0.54	0.24	...
090618353	090618A	0.284 ± 0.205	0.155 ± 0.013	112.386 ± 1.086	-2.620	146.845	0.09	0.05	0.54
090620400	090620A	0.279 ± 0.034	0.078 ± 0.007	13.568 ± 0.724	-6.208	20.776	0.23	0.06	...
090620901	090620B	< 0.529	0.155 ± 0.013	0.960 ± 0.272	-1.051	0.859	0.80	0.55	...
090621185	090621A	1.144 ± 0.486	0.522 ± 0.045	106.754 ± 14.373	-15.613	157.306	0.23	0.11	...
090621417	090621C	< 0.311	0.078 ± 0.007	27.008 ± 6.136	-17.122	36.608	0.65	0.32	...
090621447	090621D	< 0.344	0.184 ± 0.016	26.112 ± 5.655	-13.187	38.751	0.48	0.52	...
090621922	090621B	0.022 ± 0.004	0.010 ± 0.001	0.384 ± 1.032	-0.316	0.447	0.85	0.37	...
090623107	090623A	< 0.061	0.014 ± 0.001	47.105 ± 2.573	-11.502	69.509	0.54	0.32	...
090623913	090623B	< 0.717	0.130 ± 0.011	7.168 ± 3.114	-3.450	10.440	0.70	0.22	...
090625234	090625A	2.531 ± 1.209	1.755 ± 0.152	14.336 ± 0.923	-10.688	17.808	0.55	0.38	...
090625560	090625B	< 4.831	0.620 ± 0.054	11.776 ± 2.673	-7.373	16.029	1.22	0.23	...
090626189	090626A	< 0.117	0.014 ± 0.001	48.897 ± 2.828	-14.397	74.564	0.44	0.11	...
090629543	090629A	< 1.271	0.522 ± 0.045	20.480 ± 4.762	-19.656	21.099	0.81	0.72	...
090630311	090630A	< 0.415	0.110 ± 0.010	2.880 ± 0.320	-2.066	3.666	0.49	0.21	...
090701225	090701A	0.562 ± 0.079	0.184 ± 0.016	4.160 ± 0.692	-5.579	2.699	0.90	0.30	...
090703329	090703A	0.819 ± 0.473	0.522 ± 0.045	8.960 ± 1.864	-6.739	11.091	0.48	0.31	...
090704242	090704A	5.503 ± 2.061	2.482 ± 0.215	69.889 ± 5.724	-27.225	90.872	0.36	0.16	...
090704783	090704B	1.582 ± 0.496	0.620 ± 0.054	19.456 ± 2.064	-11.431	27.255	0.50	0.19	...
090706283	090706A	0.405 ± 0.164	0.261 ± 0.023	119.810 ± 5.030	-35.841	86.191	0.61	0.39	...
090708152	090708A	< 2.938	0.738 ± 0.064	21.248 ± 3.167	-9.901	27.906	0.60	0.30	...
090709630	090709B	< 1.214	0.310 ± 0.027	22.272 ± 9.230	-1.837	33.779	0.41	0.19	...
090711850	090711A	0.103 ± 0.038	0.078 ± 0.007	51.969 ± 2.560	-26.687	76.714	0.55	0.42	...
090712160	090712A	< 8.746	1.755 ± 0.152	87.041 ± 7.799	-65.537	53.241	0.42	0.23	...
090713020	090713A	2.019 ± 0.648	1.043 ± 0.090	82.817 ± 2.318	-21.558	124.998	0.30	0.16	...
090717034	090717A	< 0.098	0.039 ± 0.003	65.537 ± 1.557	-1.218	98.373	0.12	0.10	...
090717111	090717B	< 0.315	0.092 ± 0.008	0.384 ± 0.181	-0.316	0.383	1.04	0.67	...
090718720	090718A	< 2.821	0.877 ± 0.076	76.481 ± 3.416	-27.975	101.277	0.60	0.47	...
090718762	090718B	0.418 ± 0.028	0.065 ± 0.006	23.744 ± 0.802	-8.363	38.879	0.34	0.05	...
090719063	090719A	0.479 ± 0.037	0.092 ± 0.008	11.392 ± 0.466	-4.749	17.897	0.22	0.04	...

Continued on Next Page...

Table B.1 – Continued

Trigger ID	GRB Name	$\Delta t_{\rm min}$ (s)	$\Delta t_{\rm S/N}$ (s)	T_{90} (s)	$T_{100}^{\rm start}$ (s)	$T_{100}^{\rm stop}$ (s)	$\sigma_{X,t_{\rm min}}$	$\sigma_{X,t_{\rm S/N}}$	z
090720276	090720A	< 1.190	0.130 ± 0.011	3.712 ± 0.724	-2.931	4.468	0.82	0.13	...
090720710	090720B	0.002 ± 0.001	0.001 ± 0.001	10.752 ± 1.056	-5.692	15.788	0.50	0.29	...
090725838	090725A	1.985 ± 0.358	0.620 ± 0.054	13.760 ± 1.229	-10.139	17.243	0.68	0.21	...
090726218	090726B	0.165 ± 0.038	0.092 ± 0.008	7.680 ± 0.724	-1.446	9.536	0.25	0.14	...
090730608	090730A	0.143 ± 0.027	0.078 ± 0.007	9.088 ± 1.680	-6.167	11.903	0.71	0.39	...
090802235	090802A	0.015 ± 0.002	0.007 ± 0.001	0.128 ± 0.091	-0.128	0.128	0.72	0.32	...
090802666	090802B	< 1.929	0.877 ± 0.076	27.520 ± 6.192	-14.390	40.374	0.38	0.28	...
090804940	090804A	< 0.406	0.065 ± 0.006	5.568 ± 0.362	-0.619	8.944	0.33	0.07	...
090805622	090805A	0.595 ± 0.235	0.369 ± 0.032	46.592 ± 2.318	-23.769	68.925	0.50	0.31	...
090807832	090807B	0.058 ± 0.021	0.033 ± 0.003	17.920 ± 2.757	-10.150	25.510	0.41	0.23	...
090809978	090809B	0.954 ± 0.016	0.130 ± 0.011	11.008 ± 0.320	-4.365	17.525	0.45	0.06	...
090810659	090810A	2.044 ± 0.777	0.877 ± 0.076	123.458 ± 1.747	-26.686	146.130	0.29	0.12	...
090810781	090810B	1.946 ± 1.098	1.241 ± 0.108	62.977 ± 11.865	-2.990	94.598	0.26	0.17	...
090811696	090811A	< 0.355	0.078 ± 0.007	14.848 ± 1.145	-7.610	21.922	1.10	0.50	...
090813174	090813A	< 0.053	0.011 ± 0.001	7.552 ± 0.362	-3.360	11.644	0.48	0.19	...
090814368	090814C	< 0.010	0.005 ± 0.001	0.192 ± 0.143	-0.160	0.224	0.48	0.54	...
090814950	090814D	< 0.454	0.092 ± 0.008	108.610 ± 8.816	-21.960	111.618	0.56	0.29	...
090815300	090815A	0.049 ± 0.021	0.033 ± 0.003	48.385 ± 1.086	-8.847	70.980	0.16	0.10	...
090815438	090815B	0.829 ± 0.049	0.155 ± 0.013	56.321 ± 18.461	-36.865	47.544	0.53	0.10	...
090815946	090815D	2.252 ± 0.663	1.476 ± 0.128	212.992 ± 1.950	-21.832	257.171	0.51	0.34	...
090817036	090817A	1.108 ± 0.162	0.439 ± 0.038	52.417 ± 10.657	-27.050	65.174	0.60	0.24	...
090819607	090819A	0.004 ± 0.002	0.003 ± 0.001	0.192 ± 0.202	-0.224	0.160	0.90	0.55	...
090820027	090820A	< 0.365	0.065 ± 0.006	12.416 ± 0.181	28.363	49.691	0.15	0.03	...
090820509	090820B	0.047 ± 0.027	0.033 ± 0.003	15.296 ± 4.610	-2.054	22.700	0.34	0.24	...
090823133	090823B	0.639 ± 0.273	0.439 ± 0.038	63.361 ± 4.545	-53.249	36.723	0.55	0.38	...
090824918	090824A	5.731 ± 0.883	2.087 ± 0.181	59.905 ± 10.014	-30.634	84.973	0.65	0.24	...
090826068	090826A	0.105 ± 0.048	0.078 ± 0.007	8.704 ± 2.862	-5.334	11.978	0.45	0.34	...
090828099	090828A	< 0.450	0.092 ± 0.008	68.417 ± 3.167	-30.773	86.191	0.25	0.10	...
090829672	090829A	0.044 ± 0.017	0.023 ± 0.002	67.585 ± 2.896	-5.623	97.098	0.12	0.06	...
090829702	090829B	1.405 ± 0.501	0.738 ± 0.064	101.633 ± 2.290	-16.818	153.903	0.30	0.16	...
090831317	090831A	0.015 ± 0.004	0.008 ± 0.001	39.424 ± 0.572	-0.301	58.829	0.49	0.26	...
090902401	090902A	< 0.420	0.078 ± 0.007	3.200 ± 1.797	-3.888	2.128	0.84	0.29	...
090902462	090902B	0.009 ± 0.003	0.005 ± 0.001	19.328 ± 0.286	-0.573	31.691	0.11	0.07	1.822*
090904058	090904B	0.278 ± 0.127	0.155 ± 0.013	56.065 ± 1.846	-21.726	65.727	0.35	0.19	...
090904581	090904C	0.428 ± 0.174	0.261 ± 0.023	38.401 ± 3.093	-21.379	55.037	0.83	0.51	...
090907017	090907A	0.289 ± 0.159	0.219 ± 0.019	39.489 ± 4.443	-32.220	46.345	0.76	0.58	...
090907808	090907B	0.038 ± 0.011	0.023 ± 0.002	0.832 ± 0.320	-0.666	0.991	0.46	0.28	...
090908314	090908A	< 1.285	0.261 ± 0.023	67.329 ± 4.700	-59.137	36.253	0.69	0.34	...
090908341	090908B	< 1.369	0.219 ± 0.019	36.864 ± 0.923	-18.329	55.023	0.76	0.45	...
090909487	090909A	6.245 ± 0.444	1.476 ± 0.128	14.336 ± 2.896	-11.200	17.296	0.97	0.23	...
090909854	090909B	< 0.042	0.011 ± 0.001	1.152 ± 2.244	-1.333	0.525	0.62	0.53	...
090910812	090910A	< 0.333	0.110 ± 0.010	53.441 ± 13.334	-7.771	80.939	0.33	0.29	...
090912660	090912A	8.724 ± 0.682	2.482 ± 0.215	147.651 ± 9.718	-4.926	179.624	0.65	0.18	...
090915650	090915A	< 0.671	0.219 ± 0.019	76.609 ± 1.559	-28.987	113.489	0.41	0.29	...
090917661	090917A	0.438 ± 0.288	0.261 ± 0.023	26.624 ± 1.134	-13.373	39.601	0.52	0.31	...
090920035	090920A	< 1.316	0.261 ± 0.023	26.624 ± 1.056	-20.792	31.383	0.50	0.35	...
090922539	090922A	0.383 ± 0.044	0.130 ± 0.011	87.041 ± 0.810	-2.671	102.648	0.29	0.10	...
090922605	090922B	0.200 ± 0.042	0.110 ± 0.010	52.736 ± 1.810	-26.293	78.620	0.98	0.54	...
090924625	090924A	0.053 ± 0.015	0.023 ± 0.002	0.352 ± 0.101	-0.237	0.463	0.65	0.29	...
090925389	090925A	0.806 ± 0.447	0.522 ± 0.045	25.472 ± 3.525	-3.385	38.115	0.29	0.19	...
090926181	090926A	0.029 ± 0.004	0.014 ± 0.001	13.760 ± 0.286	-0.782	22.747	0.12	0.05	2.1062*
090926914	090926B	< 2.353	0.620 ± 0.054	55.553 ± 7.638	-15.799	84.173	0.24	0.13	1.24

Continued on Next Page...

Table B.1 – Continued

Trigger ID	GRB Name	$\Delta t_{\rm min}$ (s)	$\Delta t_{\rm S/N}$ (s)	T_{90} (s)	$T_{100}^{\rm start}$ (s)	$T_{100}^{\rm stop}$ (s)	$\sigma_{X,t_{\rm min}}$	$\sigma_{X,t_{\rm S/N}}$	z
090927422	090927A	0.167 ± 0.063	0.092 ± 0.008	0.512 ± 0.231	-0.446	0.573	0.93	0.52	1.37
090928646	090928A	< 1.026	0.219 ± 0.019	15.616 ± 2.611	-7.994	15.718	0.55	0.23	...
090929190	090929A	0.046 ± 0.021	0.023 ± 0.002	6.174 ± 1.298	-3.060	9.260	0.44	0.22	...
091002685	091002A	0.403 ± 0.109	0.261 ± 0.023	2.752 ± 3.089	-2.712	2.768	0.74	0.48	...
091003191	091003A	0.041 ± 0.011	0.023 ± 0.002	20.224 ± 0.362	-0.688	31.057	0.40	0.23	0.8969*
091005679	091005A	< 1.041	0.310 ± 0.027	6.976 ± 0.572	-8.133	5.787	0.69	0.47	...
091010113	091010A	0.017 ± 0.011	0.011 ± 0.001	5.952 ± 0.143	-1.220	9.056	0.15	0.10	...
091012783	091012A	< 0.019	0.005 ± 0.001	0.704 ± 2.499	-0.350	1.049	0.68	0.43	...
091015129	091015B	< 1.915	0.439 ± 0.038	3.840 ± 0.590	-4.205	3.437	1.12	0.42	...
091017861	091017A	< 1.783	0.219 ± 0.019	2.624 ± 0.462	-2.133	3.081	1.50	0.34	...
091017985	091017B	3.226 ± 0.642	1.476 ± 0.128	44.800 ± 3.367	-23.922	62.094	0.66	0.30	...
091018957	091018B	0.087 ± 0.018	0.046 ± 0.004	0.192 ± 0.286	-0.160	0.224	0.97	0.51	...
091019750	091019A	0.030 ± 0.003	0.014 ± 0.001	0.208 ± 0.172	-0.215	0.199	0.94	0.43	...
091020900	091020A	< 1.339	0.261 ± 0.023	24.256 ± 7.973	-15.599	32.639	0.37	0.12	1.71
091020977	091020B	< 0.029	0.010 ± 0.001	37.505 ± 0.905	-17.457	57.168	0.37	0.34	...
091023021	091023A	0.800 ± 0.085	0.369 ± 0.032	6.528 ± 1.857	-3.683	9.291	0.82	0.38	...
091024372	091024A	< 1.179	0.310 ± 0.027	93.954 ± 5.221	-19.493	137.387	0.41	0.27	1.092
091024380	091024A	< 2.404	0.738 ± 0.064	450.569 ± 2.360	-13.943	452.617	0.31	0.17	...
091026485	091026B	1.152 ± 0.240	0.620 ± 0.054	3.328 ± 0.779	-2.547	4.093	0.78	0.42	...
091026550	091026A	< 1.236	0.439 ± 0.038	8.960 ± 1.379	-9.555	8.275	0.81	0.63	...
091030613	091030B	0.036 ± 0.016	0.023 ± 0.002	19.200 ± 0.871	-8.928	29.280	0.56	0.36	...
091030828	091030A	0.087 ± 0.038	0.055 ± 0.005	98.050 ± 4.128	-30.675	120.306	0.26	0.16	...
091031500	091031A	< 0.034	0.011 ± 0.001	33.921 ± 0.462	-1.857	52.076	0.36	0.30	...
091101143	091101A	0.069 ± 0.024	0.039 ± 0.003	10.688 ± 0.842	-1.578	16.151	0.33	0.19	...
091102607	091102A	< 0.541	0.110 ± 0.010	6.656 ± 3.435	-4.071	9.209	0.74	0.51	...
091103912	091103A	0.329 ± 0.073	0.110 ± 0.010	13.568 ± 6.023	-8.768	18.216	0.36	0.12	...
091106762	091106A	0.059 ± 0.019	0.046 ± 0.004	14.592 ± 16.147	-8.509	20.651	0.19	0.15	...
091107635	091107A	0.485 ± 0.204	0.261 ± 0.023	11.008 ± 10.546	-8.269	13.621	0.48	0.26	...
091109895	091109C	< 0.253	0.039 ± 0.003	30.976 ± 4.580	-20.772	40.838	0.89	0.21	...
091112737	091112A	1.603 ± 0.854	0.738 ± 0.064	24.576 ± 0.923	-12.941	35.933	0.32	0.15	...
091112928	091112B	< 1.100	0.310 ± 0.027	21.184 ± 0.977	-11.256	30.892	0.36	0.27	...
091115177	091115A	< 0.826	0.219 ± 0.019	37.376 ± 2.360	-20.202	54.518	0.74	0.48	...
091117080	091117B	4.017 ± 1.245	2.087 ± 0.181	113.664 ± 2.360	-21.271	118.531	0.60	0.31	...
091120191	091120A	0.096 ± 0.018	0.027 ± 0.002	50.177 ± 2.111	-6.942	67.295	0.28	0.08	...
091122163	091122A	< 0.369	0.092 ± 0.008	1.984 ± 1.925	-2.456	1.504	1.00	0.45	...
091123081	091123B	< 0.851	0.184 ± 0.016	15.552 ± 1.866	-17.688	13.236	0.78	0.34	...
091123298	091123A	0.141 ± 0.038	0.078 ± 0.007	604.491 ± 11.676	-3.840	608.587	0.40	0.22	...
091126333	091126A	0.021 ± 0.006	0.011 ± 0.001	0.192 ± 0.091	-0.160	0.224	0.69	0.37	...
091127976	091127A	< 0.103	0.011 ± 0.001	8.701 ± 0.571	-4.304	13.008	0.42	0.07	0.49
091128285	091128A	0.205 ± 0.075	0.110 ± 0.010	87.810 ± 13.662	-25.749	86.635	0.26	0.14	...
091201089	091201A	6.200 ± 0.791	2.951 ± 0.256	12.992 ± 2.010	-14.181	11.649	0.96	0.46	...
091202072	091202B	< 0.898	0.184 ± 0.016	27.648 ± 3.566	-18.704	36.300	0.66	0.47	...
091202219	091202C	< 0.650	0.219 ± 0.019	111.106 ± 3.692	-38.913	116.994	0.42	0.39	...
091207333	091207A	0.035 ± 0.023	0.023 ± 0.002	27.073 ± 0.916	-0.616	40.786	0.49	0.32	...
091208410	091208B	0.151 ± 0.014	0.046 ± 0.004	12.480 ± 5.018	-6.306	18.530	0.46	0.14	1.063
091209001	091209A	< 1.863	0.620 ± 0.054	42.945 ± 8.035	-27.314	48.689	0.25	0.19	...
091215234	091215A	0.825 ± 0.575	0.522 ± 0.045	4.352 ± 0.362	-4.208	4.472	0.53	0.34	...
091219462	091219A	< 0.234	0.092 ± 0.008	8.128 ± 1.866	-4.219	11.939	0.41	0.36	...
091220442	091220A	1.378 ± 0.053	0.310 ± 0.027	18.368 ± 0.590	-2.103	27.824	0.56	0.13	...
091221870	091221A	< 0.437	0.078 ± 0.007	23.040 ± 5.177	-5.261	33.446	0.37	0.15	...
091223191	091223A	0.204 ± 0.034	0.092 ± 0.008	0.576 ± 0.181	-0.544	0.604	0.86	0.39	...
091223511	091223B	< 3.963	1.476 ± 0.128	49.725 ± 1.379	-7.269	74.272	0.32	0.22	...

Continued on Next Page...

Table B.1 – Continued

Trigger ID	GRB Name	$\Delta t_{\rm min}$ (s)	$\Delta t_{\rm S/N}$ (s)	T_{90} (s)	$T_{100}^{\rm start}$ (s)	$T_{100}^{\rm stop}$ (s)	$\sigma_{X,t_{\rm min}}$	$\sigma_{X,t_{\rm S/N}}$	z
091224373	091224A	0.057 ± 0.036	0.039 ± 0.003	0.768 ± 0.231	-0.569	0.959	0.68	0.46	...
091227294	091227A	< 0.387	0.078 ± 0.007	21.888 ± 0.889	-9.274	31.423	0.43	0.26	...
091230260	091230B	3.143 ± 1.630	2.087 ± 0.181	62.976 ± 3.874	-26.272	90.204	0.79	0.52	...
091230712	091230C	< 5.208	1.043 ± 0.090	35.137 ± 3.974	-18.021	49.059	0.86	0.29	...
091231206	091231A	1.646 ± 0.328	0.738 ± 0.064	42.561 ± 3.664	-13.320	66.267	0.42	0.19	...
091231540	091231B	< 6.337	1.043 ± 0.090	15.616 ± 2.757	-15.418	15.626	1.27	0.52	...
100101028	100101A	0.338 ± 0.099	0.219 ± 0.019	2.816 ± 0.320	-1.658	3.942	1.01	0.66	...
100101988	100101B	< 0.889	0.184 ± 0.016	1.984 ± 2.049	-1.572	1.952	1.06	0.43	...
100107074	100107A	0.032 ± 0.008	0.019 ± 0.002	0.576 ± 0.465	-0.336	0.812	0.94	0.57	...
100111176	100111A	0.664 ± 0.189	0.310 ± 0.027	19.520 ± 5.367	-20.416	18.428	0.70	0.33	...
100112418	100112A	1.405 ± 0.528	0.877 ± 0.076	23.040 ± 0.572	-15.757	30.093	0.53	0.33	...
100116897	100116A	0.287 ± 0.072	0.130 ± 0.011	102.530 ± 1.485	-11.035	123.266	0.18	0.08	...
100117879	100117A	0.069 ± 0.013	0.033 ± 0.003	0.256 ± 0.834	-0.192	0.320	0.79	0.37	...
100118100	100118A	0.205 ± 0.066	0.110 ± 0.010	9.216 ± 6.720	-5.770	11.434	0.78	0.42	...
100122616	100122A	< 0.171	0.046 ± 0.004	22.528 ± 2.769	-3.783	38.779	0.13	0.06	...
100126460	100126A	0.144 ± 0.062	0.092 ± 0.008	10.624 ± 12.673	-6.541	14.593	0.79	0.50	...
100130729	100130A	< 1.170	0.310 ± 0.027	99.074 ± 3.328	-30.885	105.817	0.32	0.14	...
100130777	100130B	< 1.626	0.310 ± 0.027	86.018 ± 6.988	-30.340	108.120	0.44	0.18	...
100131730	100131A	0.087 ± 0.009	0.033 ± 0.003	3.520 ± 0.453	-1.550	5.454	0.42	0.16	...
100201588	100201A	< 2.151	0.522 ± 0.045	122.114 ± 1.280	-20.185	147.091	0.29	0.15	...
100204024	100204A	1.292 ± 0.273	0.439 ± 0.038	136.195 ± 27.553	-95.234	58.843	0.24	0.08	...
100204566	100204B	< 0.406	0.261 ± 0.023	32.513 ± 2.862	-30.401	18.349	0.67	0.84	...
100204858	100204C	0.140 ± 0.051	0.092 ± 0.008	1.920 ± 2.375	-1.590	2.230	0.91	0.60	...
100205490	100205B	< 1.480	0.261 ± 0.023	14.848 ± 2.290	-8.378	21.154	0.75	0.31	...
100206563	100206A	< 0.017	0.005 ± 0.001	0.128 ± 0.091	-0.128	0.128	0.37	0.25	...
100207665	100207A	< 13.736	2.951 ± 0.256	15.360 ± 3.874	-10.419	20.147	1.11	0.48	...
100207721	100207B	4.675 ± 2.569	2.951 ± 0.256	17.728 ± 6.492	-17.995	17.267	0.72	0.45	...
100208386	100208A	< 0.156	0.092 ± 0.008	0.192 ± 0.264	-0.160	0.224	0.79	1.00	...
100210101	100210A	0.945 ± 0.271	0.522 ± 0.045	29.184 ± 5.655	-19.253	33.271	0.47	0.26	...
100211440	100211A	0.468 ± 0.256	0.219 ± 0.019	21.376 ± 0.923	-9.949	32.557	0.20	0.09	...
100212550	100212B	0.235 ± 0.066	0.130 ± 0.011	3.773 ± 0.270	-1.871	5.649	0.58	0.32	...
100212588	100212A	0.396 ± 0.109	0.219 ± 0.019	2.496 ± 0.202	-1.692	3.293	0.74	0.41	...
100216422	100216A	< 0.045	0.010 ± 0.001	0.192 ± 0.143	-0.160	0.224	0.78	0.57	...
100218194	100218A	3.673 ± 2.832	2.482 ± 0.215	29.185 ± 5.813	-17.989	38.912	0.46	0.31	...
100219026	100219B	< 2.169	0.877 ± 0.076	59.712 ± 4.955	-24.571	76.919	0.46	0.43	...
100221368	100221A	4.651 ± 0.557	1.476 ± 0.128	23.552 ± 1.032	-13.815	31.852	0.72	0.23	...
100223110	100223A	< 0.022	0.007 ± 0.001	0.256 ± 0.091	-0.192	0.320	0.45	0.29	...
100224112	100224B	0.125 ± 0.034	0.065 ± 0.006	67.329 ± 6.988	-30.345	88.812	0.34	0.18	...
100225115	100225A	< 0.277	0.046 ± 0.004	12.992 ± 1.925	-3.059	19.137	0.54	0.30	...
100225249	100225B	< 5.244	2.482 ± 0.215	32.000 ± 20.419	-14.232	47.208	0.75	0.78	...
100225580	100225C	0.125 ± 0.056	0.065 ± 0.006	6.400 ± 1.086	-3.680	9.056	0.19	0.10	...
100225703	100225D	0.071 ± 0.023	0.046 ± 0.004	4.480 ± 1.431	-3.370	5.546	0.74	0.48	...
100228544	100228A	1.399 ± 0.517	0.620 ± 0.054	67.072 ± 4.720	-21.926	98.112	0.65	0.29	...
100228873	100228B	< 1.757	0.439 ± 0.038	8.704 ± 2.318	-6.358	10.954	0.90	0.34	...
100301068	100301A	0.010 ± 0.006	0.007 ± 0.001	0.960 ± 1.002	-1.371	0.539	0.75	0.47	...
100301223	100301B	0.163 ± 0.049	0.092 ± 0.008	26.625 ± 1.431	-13.438	39.270	0.61	0.35	...
100304004	100304A	< 1.076	0.310 ± 0.027	181.507 ± 21.682	-30.590	247.104	0.65	0.49	...
100304534	100304B	0.971 ± 0.268	0.522 ± 0.045	19.008 ± 2.782	-18.971	19.029	0.47	0.25	...
100306199	100306A	< 4.089	0.738 ± 0.064	7.168 ± 2.064	-7.904	6.344	1.01	0.61	...
100307928	100307A	1.342 ± 0.669	0.738 ± 0.064	16.128 ± 2.187	-11.059	21.019	0.43	0.23	...
100311518	100311A	< 4.290	0.877 ± 0.076	9.024 ± 1.042	-1.568	11.240	1.11	0.40	...
100313288	100313A	< 1.788	0.184 ± 0.016	12.864 ± 2.099	-9.186	16.406	0.97	0.16	...

Continued on Next Page...

Table B.1 – Continued

Trigger ID	GRB Name	$\Delta t_{\rm min}$ (s)	$\Delta t_{\rm S/N}$ (s)	T_{90} (s)	$T_{100}^{\rm start}$ (s)	$T_{100}^{\rm stop}$ (s)	$\sigma_{X,t_{\rm min}}$	$\sigma_{X,t_{\rm S/N}}$	z
100313509	100313B	6.269 ± 0.384	2.087 ± 0.181	34.048 ± 2.996	-15.873	47.782	0.75	0.25	...
100315361	100315A	5.453 ± 1.239	2.482 ± 0.215	35.584 ± 2.290	-22.194	48.610	0.81	0.37	...
100318611	100318A	1.529 ± 0.303	0.877 ± 0.076	18.432 ± 0.923	-10.922	22.050	0.52	0.30	...
100322045	100322A	0.060 ± 0.021	0.033 ± 0.003	37.121 ± 0.231	-14.268	51.435	0.16	0.09	...
100323542	100323A	< 1.659	0.310 ± 0.027	60.673 ± 3.620	-21.511	70.692	0.69	0.25	...
100324172	100324B	< 0.213	0.027 ± 0.002	17.920 ± 2.064	-8.294	27.366	0.39	0.07	...
100325246	100325B	0.582 ± 0.123	0.261 ± 0.023	8.192 ± 1.086	-5.270	10.681	0.67	0.30	...
100325275	100325A	0.100 ± 0.064	0.065 ± 0.006	7.104 ± 1.619	-1.346	10.226	0.42	0.27	...
100326294	100326A	< 0.133	0.046 ± 0.004	5.632 ± 2.064	-8.170	3.070	0.87	0.69	...
100326402	100326B	< 0.451	0.184 ± 0.016	171.011 ± 29.126	-72.705	106.679	0.28	0.26	...
100328141	100328A	< 0.012	0.004 ± 0.001	0.384 ± 0.143	-0.252	0.511	0.80	0.51	...
100330309	100330A	< 0.202	0.078 ± 0.007	10.048 ± 0.318	-3.207	15.066	0.28	0.22	...
100330856	100330B	0.830 ± 0.165	0.310 ± 0.027	5.120 ± 0.453	-3.686	6.502	0.82	0.31	...
100401297	100401A	< 0.575	0.092 ± 0.008	92.416 ± 4.291	-28.449	102.759	0.84	0.29	...
100406758	100406A	0.589 ± 0.112	0.310 ± 0.027	5.888 ± 2.919	-4.199	7.503	0.84	0.44	...
100410356	100410A	1.862 ± 0.586	1.241 ± 0.108	9.728 ± 2.202	-10.707	8.635	0.78	0.52	...
100410740	100410B	< 0.274	0.046 ± 0.004	22.016 ± 4.700	-11.930	31.850	0.92	0.41	...
100411516	100411A	0.053 ± 0.019	0.033 ± 0.003	0.512 ± 0.231	-0.318	0.701	0.89	0.55	...
100413732	100413A	0.579 ± 0.169	0.369 ± 0.032	179.651 ± 2.817	-18.053	193.922	0.62	0.40	...
100414097	100414A	0.026 ± 0.007	0.014 ± 0.001	26.497 ± 2.073	-11.269	41.427	0.18	0.09	...
100417166	100417A	0.008 ± 0.004	0.005 ± 0.001	0.192 ± 0.091	-0.160	0.224	0.69	0.44	...
100417789	100417B	4.668 ± 0.775	2.482 ± 0.215	52.545 ± 1.856	-14.351	76.018	0.92	0.49	...
100420008	100420B	0.796 ± 0.222	0.369 ± 0.032	20.288 ± 0.405	-9.855	29.691	0.39	0.18	...
100421917	100421A	< 1.544	0.369 ± 0.032	47.489 ± 10.849	-30.454	30.321	0.55	0.28	...
100423244	100423B	< 0.310	0.046 ± 0.004	16.512 ± 2.226	-6.579	25.100	0.65	0.24	...
100424729	100424B	0.470 ± 0.127	0.261 ± 0.023	175.107 ± 1.493	-29.411	163.199	0.66	0.36	...
100424876	100424C	< 0.361	0.078 ± 0.007	169.987 ± 3.557	-15.379	208.994	0.50	0.21	...
100427356	100427A	< 0.500	0.130 ± 0.011	12.544 ± 7.389	-11.075	11.246	0.52	0.26	...
100429999	100429A	< 5.330	0.620 ± 0.054	25.024 ± 6.582	-25.154	24.635	0.90	0.16	...
100502356	100502A	< 0.255	0.078 ± 0.007	95.810 ± 2.382	-14.519	124.391	0.42	0.31	...
100503554	100503A	< 0.093	0.023 ± 0.002	129.602 ± 10.230	-14.648	169.384	0.36	0.26	...
100504806	100504A	7.929 ± 0.893	2.951 ± 0.256	16.512 ± 1.810	-6.963	25.871	0.90	0.34	...
100506653	100506A	< 2.295	0.522 ± 0.045	21.376 ± 1.891	-18.525	23.768	0.42	0.21	...
100507577	100507A	0.578 ± 0.222	0.369 ± 0.032	44.033 ± 5.221	-17.746	65.012	0.26	0.17	...
100510810	100510A	< 5.659	0.877 ± 0.076	31.169 ± 4.017	-18.725	43.284	0.86	0.19	...
100511035	100511A	0.082 ± 0.017	0.027 ± 0.002	42.433 ± 1.478	-19.539	64.452	0.34	0.12	...
100513879	100513B	0.376 ± 0.150	0.219 ± 0.019	11.136 ± 1.145	-6.288	15.840	0.23	0.14	...
100515467	100515A	< 0.193	0.055 ± 0.005	10.624 ± 1.431	-5.901	15.233	0.19	0.09	...
100516369	100516A	< 0.061	0.016 ± 0.001	2.112 ± 1.134	-2.971	1.228	0.94	0.69	...
100516396	100516B	0.084 ± 0.046	0.055 ± 0.005	0.640 ± 0.487	-0.893	0.381	0.86	0.56	...
100517072	100517B	0.069 ± 0.036	0.039 ± 0.003	55.808 ± 1.810	-4.270	81.104	0.22	0.12	...
100517132	100517C	0.693 ± 0.393	0.522 ± 0.045	19.840 ± 3.620	-10.333	29.149	0.52	0.39	...
100517154	100517D	< 0.186	0.039 ± 0.003	30.464 ± 0.810	-15.333	45.282	0.46	0.20	...
100517243	100517E	< 1.080	0.184 ± 0.016	29.632 ± 4.482	-28.161	30.782	0.85	0.24	...
100517639	100517F	< 0.219	0.039 ± 0.003	5.440 ± 0.604	-3.461	7.365	0.56	0.23	...
100519204	100519A	0.961 ± 0.465	0.522 ± 0.045	62.913 ± 3.929	-21.585	89.748	0.18	0.10	...
100522157	100522A	< 0.090	0.019 ± 0.002	35.326 ± 0.715	-2.547	52.905	0.58	0.22	...
100525744	100525A	0.045 ± 0.011	0.023 ± 0.002	1.472 ± 1.974	-1.119	1.816	0.85	0.44	...
100527795	100527A	< 0.230	0.065 ± 0.006	184.579 ± 3.238	-92.674	120.498	0.49	0.30	...
100528075	100528A	< 0.428	0.078 ± 0.007	22.464 ± 0.749	-11.378	33.318	0.19	0.07	...
100530737	100530A	0.965 ± 0.403	0.620 ± 0.054	3.328 ± 0.810	-2.675	3.965	0.81	0.52	...
100604287	100604A	0.416 ± 0.223	0.261 ± 0.023	13.440 ± 0.871	-8.957	17.654	0.29	0.18	...

Continued on Next Page...

Table B.1 – Continued

Trigger ID	GRB Name	$\Delta t_{\rm min}$ (s)	$\Delta t_{\rm S/N}$ (s)	T_{90} (s)	$T_{100}^{\rm start}$ (s)	$T_{100}^{\rm stop}$ (s)	$\sigma_{X,t_{\rm min}}$	$\sigma_{X,t_{\rm S/N}}$	z
100605774	100605A	1.562 ± 0.310	0.522 ± 0.045	8.192 ± 2.862	-5.085	11.193	0.78	0.26	...
100608382	100608A	0.545 ± 0.173	0.369 ± 0.032	30.208 ± 1.619	-22.606	35.982	0.51	0.34	...
100609783	100609A	< 2.015	0.522 ± 0.045	230.404 ± 8.689	-9.593	236.935	0.25	0.17	...
100612545	100612A	0.024 ± 0.007	0.016 ± 0.001	0.576 ± 0.181	-0.288	0.860	0.64	0.43	...
100612726	100612B	< 0.394	0.065 ± 0.006	8.576 ± 3.210	-3.549	13.485	0.20	0.05	...
100614498	100614B	0.167 ± 0.091	0.110 ± 0.010	172.291 ± 12.447	-149.763	22.975	0.33	0.22	...
100615083	100615A	0.487 ± 0.092	0.184 ± 0.016	37.377 ± 0.979	-2.627	51.172	0.38	0.14	1.398
100619015	100619A	< 0.473	0.130 ± 0.011	96.002 ± 1.319	-29.359	113.681	0.42	0.22	...
100620119	100620A	< 0.944	0.261 ± 0.023	51.841 ± 8.518	-20.497	75.407	0.55	0.36	...
100621452	100621B	< 1.532	0.310 ± 0.027	123.906 ± 5.515	-29.098	141.884	0.60	0.24	...
100621529	100621C	< 0.120	0.033 ± 0.003	1.024 ± 0.202	-0.957	1.083	1.02	0.66	...
100625773	100625A	0.031 ± 0.005	0.010 ± 0.001	0.192 ± 0.143	-0.160	0.224	0.92	0.29	...
100625891	100625B	1.123 ± 0.321	0.738 ± 0.064	29.184 ± 1.086	-16.459	36.065	0.54	0.36	...
100629801	100629A	0.146 ± 0.014	0.055 ± 0.005	0.832 ± 0.373	-0.538	1.119	0.76	0.29	...
100701490	100701B	< 0.004	0.001 ± 0.001	22.016 ± 5.568	-1.790	32.090	0.39	0.33	...
100704149	100704A	0.413 ± 0.105	0.219 ± 0.019	214.404 ± 5.917	-38.145	275.680	0.29	0.15	...
100706693	100706A	< 0.295	0.065 ± 0.006	0.128 ± 0.143	-0.192	0.064	0.76	0.99	...
100707032	100707A	0.665 ± 0.012	0.078 ± 0.007	81.793 ± 1.218	-2.742	113.386	0.44	0.05	...
100709602	100709A	< 1.297	0.261 ± 0.023	100.098 ± 1.527	-23.050	138.079	0.52	0.21	...
100713980	100713B	0.293 ± 0.080	0.130 ± 0.011	7.616 ± 0.529	-4.162	11.038	0.45	0.20	...
100714672	100714A	< 0.387	0.110 ± 0.010	35.584 ± 5.126	-17.988	52.816	1.06	0.75	...
100714686	100714B	0.101 ± 0.015	0.039 ± 0.003	5.632 ± 2.064	-6.122	5.118	0.68	0.26	...
100715477	100715A	1.559 ± 0.529	0.738 ± 0.064	14.848 ± 3.665	-8.378	21.154	0.42	0.20	...
100717372	100717A	< 0.053	0.016 ± 0.001	5.952 ± 1.507	-3.588	8.352	0.85	0.52	...
100717446	100717B	< 0.035	0.011 ± 0.001	2.432 ± 1.356	-1.338	3.502	0.71	0.71	...
100718160	100718B	< 0.093	0.033 ± 0.003	32.640 ± 1.864	-30.925	17.055	0.47	0.41	...
100718796	100718A	6.240 ± 0.521	2.087 ± 0.181	38.656 ± 8.002	-14.291	54.875	0.85	0.28	...
100719311	100719B	0.480 ± 0.069	0.155 ± 0.013	1.600 ± 0.854	-2.120	0.856	0.95	0.31	...
100719825	100719C	0.672 ± 0.303	0.439 ± 0.038	3.072 ± 3.114	-3.861	0.912	0.71	0.46	...
100719989	100719D	< 0.039	0.014 ± 0.001	21.824 ± 1.305	-8.396	34.153	0.12	0.10	...
100722096	100722A	0.057 ± 0.013	0.019 ± 0.002	7.165 ± 1.055	-3.546	10.702	0.30	0.10	...
100722291	100722B	< 0.159	0.092 ± 0.008	1.280 ± 0.905	-1.850	0.698	0.80	0.97	...
100724029	100724A	0.062 ± 0.029	0.039 ± 0.003	114.690 ± 3.238	-11.967	145.144	0.08	0.05	...
100725475	100725B	0.471 ± 0.123	0.261 ± 0.023	146.434 ± 4.971	-23.608	160.881	0.49	0.27	...
100727238	100727A	< 5.037	1.043 ± 0.090	23.808 ± 2.769	-13.678	28.924	0.99	0.36	...
100728095	100728A	< 0.090	0.027 ± 0.002	165.378 ± 2.896	-7.363	207.605	0.17	0.11	1.567
100728439	100728B	0.174 ± 0.105	0.110 ± 0.010	10.240 ± 1.846	-7.117	13.261	0.23	0.14	2.106
100730463	100730A	2.726 ± 0.989	1.241 ± 0.108	63.873 ± 8.776	-25.030	93.749	0.44	0.20	...
100802240	100802A	3.948 ± 0.414	1.476 ± 0.128	28.672 ± 3.167	-16.056	40.977	0.77	0.29	...
100804104	100804A	0.057 ± 0.031	0.039 ± 0.003	6.592 ± 0.771	-2.812	9.953	0.16	0.11	...
100805300	100805B	< 0.042	0.011 ± 0.001	0.064 ± 0.072	-0.128	-0.001	0.88	0.57	...
100805845	100805C	0.928 ± 0.076	0.310 ± 0.027	58.430 ± 6.426	-1.567	87.231	0.60	0.20	...
100810049	100810A	0.169 ± 0.069	0.110 ± 0.010	2.560 ± 1.741	-3.123	1.971	0.59	0.38	...
100811108	100811A	< 0.019	0.004 ± 0.001	0.384 ± 0.091	-0.252	0.511	0.53	0.27	...
100811781	100811B	0.278 ± 0.168	0.184 ± 0.016	78.080 ± 3.840	-91.642	63.738	0.49	0.33	...
100814160	100814A	< 3.299	0.522 ± 0.045	150.530 ± 1.619	-23.817	180.890	0.60	0.14	1.44
100814351	100814B	0.482 ± 0.072	0.184 ± 0.016	7.424 ± 0.923	-4.445	10.321	0.31	0.12	...
100816009	100816B	< 1.320	0.522 ± 0.045	62.401 ± 5.278	-22.266	71.334	0.17	0.16	...
100816026	100816A	< 0.333	0.039 ± 0.003	2.045 ± 0.229	-1.012	3.068	0.42	0.10	0.8049
100819498	100819A	< 3.737	0.738 ± 0.064	12.544 ± 1.810	-11.075	13.879	0.65	0.28	...
100820373	100820A	< 0.056	0.016 ± 0.001	8.960 ± 2.187	-5.203	12.627	0.28	0.17	...
100825287	100825A	0.460 ± 0.055	0.184 ± 0.016	3.328 ± 1.846	-2.931	3.709	0.51	0.20	...

Continued on Next Page...

Table B.1 – Continued

Trigger ID	GRB Name	$\Delta t_{\rm min}$ (s)	$\Delta t_{\rm S/N}$ (s)	T_{90} (s)	$T_{100}^{\rm start}$ (s)	$T_{100}^{\rm stop}$ (s)	$\sigma_{X,t_{\rm min}}$	$\sigma_{X,t_{\rm S/N}}$	z
100826957	100826A	< 0.106	0.027 ± 0.002	84.993 ± 0.724	-3.774	120.297	0.14	0.06	...
100827455	100827A	< 0.010	0.004 ± 0.001	0.576 ± 0.389	-0.416	0.732	0.41	0.37	...
100829374	100829B	1.116 ± 0.186	0.369 ± 0.032	94.977 ± 2.767	-11.729	116.467	0.41	0.14	...
100829876	100829A	0.043 ± 0.003	0.011 ± 0.001	8.704 ± 0.389	-4.214	13.098	0.51	0.14	...
100831651	100831A	< 2.380	1.476 ± 0.128	40.193 ± 11.986	-23.296	37.078	0.65	0.81	...
100902990	100902B	2.756 ± 0.302	0.738 ± 0.064	22.272 ± 3.338	-15.127	29.171	0.63	0.17	...
100905907	100905B	< 1.443	0.369 ± 0.032	11.520 ± 1.145	-10.310	11.578	0.49	0.23	...
100906576	100906A	< 0.303	0.065 ± 0.006	110.594 ± 2.828	-4.127	134.098	0.17	0.11	1.727
100907751	100907A	< 3.082	0.219 ± 0.019	5.376 ± 2.187	-4.205	6.515	1.84	0.29	...
100910818	100910A	< 0.064	0.011 ± 0.001	13.824 ± 0.724	-5.224	22.001	0.47	0.12	...
100911816	100911A	0.164 ± 0.060	0.110 ± 0.010	5.632 ± 1.999	-3.562	7.678	0.70	0.47	...
100915243	100915B	1.982 ± 0.354	1.043 ± 0.090	7.936 ± 3.367	-11.360	4.480	0.96	0.51	...
100916779	100916A	0.088 ± 0.008	0.039 ± 0.003	12.800 ± 2.111	-4.288	18.880	0.88	0.39	...
100918863	100918A	< 2.057	0.310 ± 0.027	86.017 ± 8.689	-4.822	134.498	0.34	0.08	...
100919884	100919A	0.692 ± 0.429	0.439 ± 0.038	49.601 ± 2.975	-38.401	21.044	0.27	0.17	...
100922625	100922A	0.817 ± 0.190	0.439 ± 0.038	4.352 ± 0.923	-3.184	5.496	0.91	0.49	...
100923844	100923A	< 1.057	0.155 ± 0.013	51.713 ± 5.838	-17.127	72.830	0.62	0.18	...
100924165	100924A	< 0.343	0.078 ± 0.007	9.024 ± 0.362	-5.109	12.841	0.52	0.17	...
100926595	100926A	< 0.582	0.155 ± 0.013	32.256 ± 0.572	-30.222	14.914	0.28	0.19	...
100926694	100926B	2.261 ± 0.423	0.738 ± 0.064	37.888 ± 2.611	-21.894	47.805	0.69	0.23	...
100929235	100929A	1.612 ± 0.282	0.738 ± 0.064	8.192 ± 2.360	-6.365	9.913	0.80	0.37	...
100929315	100929B	0.466 ± 0.084	0.184 ± 0.016	4.608 ± 1.305	-2.797	6.357	0.87	0.35	...
100929916	100929C	0.036 ± 0.006	0.016 ± 0.001	0.320 ± 0.143	-0.286	0.350	0.87	0.39	...
101002279	101002A	< 0.874	0.261 ± 0.023	7.168 ± 2.290	-7.904	6.344	0.82	0.56	...
101003244	101003A	< 0.453	0.092 ± 0.008	9.984 ± 1.448	-6.736	13.124	0.36	0.16	...
101004426	101004A	4.074 ± 1.692	2.087 ± 0.181	161.027 ± 7.836	-141.058	27.355	0.54	0.28	...
101008697	101008A	0.280 ± 0.048	0.130 ± 0.011	8.960 ± 1.846	-6.995	10.835	0.96	0.45	...
101010190	101010A	0.857 ± 0.410	0.522 ± 0.045	65.025 ± 6.165	-31.985	74.648	0.63	0.38	...
101011707	101011A	< 1.419	0.261 ± 0.023	36.352 ± 2.318	-19.047	53.269	1.15	0.64	...
101013412	101013A	< 0.084	0.016 ± 0.001	15.360 ± 0.572	-7.027	20.314	0.51	0.29	...
101014175	101014A	0.048 ± 0.003	0.016 ± 0.001	449.415 ± 1.410	-13.188	450.823	0.23	0.08	...
101015558	101015A	< 0.574	0.130 ± 0.011	500.552 ± 7.408	-18.252	498.504	0.42	0.23	...
101016243	101016A	0.343 ± 0.011	0.065 ± 0.006	3.840 ± 0.362	-1.786	4.205	0.62	0.12	...
101017619	101017B	2.264 ± 0.373	1.241 ± 0.108	47.872 ± 1.950	-24.945	70.775	0.86	0.47	...
101021009	101021A	0.318 ± 0.123	0.184 ± 0.016	120.770 ± 12.237	-51.457	89.321	0.32	0.18	...
101021063	101021B	< 0.108	0.046 ± 0.004	1.536 ± 2.360	-1.235	1.790	0.63	0.55	...
101023951	101023A	0.468 ± 0.025	0.130 ± 0.011	76.801 ± 8.256	-14.464	114.560	0.29	0.08	...
101024486	101024A	0.102 ± 0.040	0.065 ± 0.006	20.224 ± 2.828	-13.908	26.329	0.65	0.42	...
101025146	101025A	0.503 ± 0.184	0.369 ± 0.032	14.336 ± 1.846	-8.896	19.600	0.93	0.69	...
101026034	101026A	0.017 ± 0.010	0.011 ± 0.001	0.256 ± 0.091	-0.256	0.256	0.56	0.36	...
101027230	101027A	0.022 ± 0.007	0.014 ± 0.001	1.344 ± 1.802	-1.947	0.733	0.88	0.54	...
101030664	101030A	< 9.810	2.087 ± 0.181	95.746 ± 4.375	-69.633	54.959	0.79	0.25	...
101031625	101031A	< 0.014	0.007 ± 0.001	0.384 ± 0.462	-0.252	0.511	0.54	0.52	...
101101744	101101A	0.059 ± 0.021	0.039 ± 0.003	3.328 ± 2.862	-3.955	2.685	0.38	0.25	...
101101899	101101B	3.682 ± 1.935	1.755 ± 0.152	31.232 ± 1.619	-20.063	37.382	0.42	0.20	...
101102840	101102A	< 3.802	0.738 ± 0.064	43.520 ± 6.676	-23.251	63.354	0.55	0.33	...
101104810	101104A	< 0.148	0.055 ± 0.005	1.280 ± 0.572	-1.146	1.402	0.54	0.41	...
101107011	101107A	< 0.849	0.310 ± 0.027	375.814 ± 8.444	-31.567	378.118	0.38	0.36	...
101112924	101112A	0.390 ± 0.086	0.155 ± 0.013	9.472 ± 2.996	-8.691	8.243	0.47	0.19	...
101112984	101112B	< 5.121	1.476 ± 0.128	82.944 ± 1.717	-28.320	91.114	0.66	0.28	...
101113483	101113A	< 1.198	0.261 ± 0.023	12.288 ± 0.572	-4.501	18.095	0.66	0.22	...
101116481	101116A	0.088 ± 0.034	0.055 ± 0.005	0.576 ± 0.820	-0.416	0.732	0.97	0.60	...

Continued on Next Page...

Table B.1 – Continued

Trigger ID	GRB Name	$\Delta t_{\rm min}$ (s)	$\Delta t_{\rm S/N}$ (s)	T_{90} (s)	$T_{100}^{\rm start}$ (s)	$T_{100}^{\rm stop}$ (s)	$\sigma_{X,t_{\rm min}}$	$\sigma_{X,t_{\rm S/N}}$	z
101117496	101117C	0.470 ± 0.093	0.261 ± 0.023	50.177 ± 1.639	-5.184	73.065	0.45	0.25	...
101119685	101119A	< 0.404	0.078 ± 0.007	0.640 ± 0.607	-0.637	0.637	1.14	0.62	...
101123952	101123A	< 0.077	0.014 ± 0.001	103.938 ± 0.724	-4.124	163.187	0.22	0.07	...
101126198	101126A	< 0.177	0.039 ± 0.003	43.837 ± 1.747	-11.444	65.679	0.14	0.06	...
101127093	101127A	2.765 ± 1.240	1.476 ± 0.128	29.440 ± 4.471	-17.812	40.774	0.83	0.44	...
101127102	101127B	5.416 ± 0.520	1.755 ± 0.152	60.672 ± 7.322	-30.731	85.736	0.65	0.21	...
101128322	101128A	< 1.624	0.310 ± 0.027	8.192 ± 1.493	-6.877	9.401	0.61	0.28	...
101129652	101129A	0.018 ± 0.005	0.011 ± 0.001	0.384 ± 0.143	-0.252	0.511	0.53	0.34	...
101129726	101129B	< 0.024	0.005 ± 0.001	0.576 ± 0.143	-0.346	0.796	0.57	0.35	...
101130074	101130B	3.312 ± 0.561	2.087 ± 0.181	4.864 ± 2.769	-4.714	4.958	1.05	0.66	...
101201418	101201A	0.844 ± 0.329	0.261 ± 0.023	112.639 ± 7.455	-33.282	139.026	0.24	0.07	...
101202154	101202A	< 1.458	0.877 ± 0.076	18.432 ± 3.665	-9.130	27.526	0.83	0.95	...
101204343	101204B	0.015 ± 0.003	0.007 ± 0.001	0.128 ± 0.091	-0.128	0.128	0.71	0.32	...
101205309	101205A	< 3.249	0.738 ± 0.064	7.936 ± 5.938	-7.776	8.064	1.06	0.51	...
101206036	101206A	< 0.813	0.130 ± 0.011	34.813 ± 5.837	-17.091	52.161	0.66	0.22	...
101207536	101207A	0.068 ± 0.028	0.046 ± 0.004	61.441 ± 3.727	-6.013	94.134	0.50	0.34	...
101208498	101208B	0.097 ± 0.010	0.033 ± 0.003	2.048 ± 0.951	-1.658	2.422	0.37	0.13	...
101211485	101211A	1.092 ± 0.435	0.522 ± 0.045	13.568 ± 7.030	-9.536	17.448	0.42	0.20	...
101213451	101213A	< 5.901	0.877 ± 0.076	45.057 ± 1.950	-22.252	67.828	0.90	0.19	0.414
101213849	101213B	0.069 ± 0.022	0.046 ± 0.004	6.656 ± 1.145	-5.095	8.185	0.39	0.26	...
101214748	101214A	< 0.038	0.007 ± 0.001	2.240 ± 2.084	-2.517	1.941	0.92	0.58	...
101216721	101216A	< 0.105	0.027 ± 0.002	1.917 ± 0.551	-0.954	2.864	0.20	0.12	...
101219686	101219B	5.386 ± 0.868	2.087 ± 0.181	51.009 ± 1.775	-8.423	72.157	0.56	0.22	0.55
101220576	101220A	7.748 ± 0.937	2.951 ± 0.256	72.449 ± 4.048	-21.684	93.495	0.47	0.18	...
101223834	101223A	< 20.645	2.482 ± 0.215	56.065 ± 5.497	-41.217	42.437	1.44	0.28	...
101224227	101224A	0.050 ± 0.008	0.023 ± 0.002	1.728 ± 1.680	-0.923	2.517	0.88	0.41	...
101224578	101224B	< 0.145	0.039 ± 0.003	44.737 ± 0.889	-2.649	66.667	0.28	0.21	...
101224614	101224C	< 3.617	0.620 ± 0.054	25.601 ± 3.416	-15.233	35.711	0.62	0.19	...
101224998	101224D	0.212 ± 0.073	0.130 ± 0.011	18.688 ± 8.719	-19.044	18.130	0.90	0.55	...
101225377	101225B	0.557 ± 0.141	0.310 ± 0.027	81.217 ± 35.377	-7.910	125.258	0.18	0.10	...
101227195	101227A	< 0.535	0.092 ± 0.008	95.488 ± 1.639	-16.013	141.529	0.90	0.44	...
101227406	101227B	0.231 ± 0.109	0.092 ± 0.008	153.347 ± 2.573	-27.564	185.578	0.28	0.11	...
101227536	101227C	< 0.075	0.023 ± 0.002	28.865 ± 3.088	-14.500	42.931	0.61	0.32	...
101231067	101231A	0.098 ± 0.011	0.039 ± 0.003	23.614 ± 0.572	-6.265	27.955	0.46	0.18	...
110101202	110101A	0.208 ± 0.031	0.110 ± 0.010	3.584 ± 1.493	-4.080	3.044	1.02	0.54	...
110101506	110101B	1.915 ± 0.614	1.241 ± 0.108	235.523 ± 8.256	-103.425	141.832	0.72	0.47	...
110102788	110102A	0.206 ± 0.039	0.110 ± 0.010	253.956 ± 2.049	-119.426	184.990	0.22	0.12	...
110105877	110105A	0.276 ± 0.074	0.110 ± 0.010	123.394 ± 6.476	-17.725	127.863	0.37	0.15	...
110106893	110106B	0.671 ± 0.287	0.439 ± 0.038	35.521 ± 3.612	-23.837	33.350	0.63	0.41	...
110107886	110107A	< 0.330	0.078 ± 0.007	183.555 ± 24.406	-61.185	122.967	0.58	0.35	...
110108977	110108A	1.001 ± 0.542	0.738 ± 0.064	51.456 ± 6.955	-19.677	76.516	0.63	0.47	...
110112934	110112B	0.024 ± 0.012	0.016 ± 0.001	2.304 ± 2.538	-2.102	2.474	0.70	0.47	...
110117364	110117A	< 32.263	19.855 ± 1.720	72.448 ± 9.051	-28.161	89.192	0.89	0.91	...
110117626	110117B	< 0.441	0.110 ± 0.010	43.264 ± 1.639	-23.640	62.447	0.69	0.36	...
110118857	110118A	0.334 ± 0.063	0.155 ± 0.013	34.561 ± 2.360	-23.346	45.428	0.41	0.19	...
110119931	110119A	< 0.280	0.130 ± 0.011	205.828 ± 1.864	-26.362	298.834	0.39	0.39	...
110120666	110120A	0.018 ± 0.007	0.011 ± 0.001	28.417 ± 9.793	-13.821	42.695	0.31	0.19	...
110123804	110123A	< 0.358	0.092 ± 0.008	17.856 ± 0.810	-7.608	27.359	0.14	0.08	...
110124784	110124A	1.141 ± 0.401	0.738 ± 0.064	5.376 ± 2.202	-5.997	4.723	0.86	0.56	...
110125894	110125A	< 0.753	0.184 ± 0.016	4.800 ± 0.923	-2.520	6.264	0.56	0.22	...
110128073	110128A	1.594 ± 0.248	0.738 ± 0.064	12.160 ± 4.971	-11.843	12.355	0.88	0.41	2.339
110130230	110130A	< 1.525	0.620 ± 0.054	47.360 ± 2.187	-16.863	70.753	0.59	0.47	...

Continued on Next Page...

Table B.1 – Continued

Trigger ID	GRB Name	$\Delta t_{\rm min}$ (s)	$\Delta t_{\rm S/N}$ (s)	T_{90} (s)	$T_{100}^{\rm start}$ (s)	$T_{100}^{\rm stop}$ (s)	$\sigma_{X,t_{\rm min}}$	$\sigma_{X,t_{\rm S/N}}$	z
110131780	110131A	< 0.252	0.092 ± 0.008	0.384 ± 1.478	-0.380	0.383	0.87	0.79	...
110201399	110201A	< 1.426	0.522 ± 0.045	8.192 ± 0.870	-5.853	10.425	0.67	0.65	...
110204179	110204A	0.279 ± 0.177	0.184 ± 0.016	28.673 ± 6.720	-17.968	39.066	0.28	0.19	...
110205027	110205B	0.841 ± 0.132	0.522 ± 0.045	6.400 ± 3.238	-5.984	6.752	1.01	0.63	...
110205588	110205C	1.100 ± 0.469	0.877 ± 0.076	158.720 ± 2.290	-29.430	170.557	0.76	0.60	...
110206202	110206B	0.464 ± 0.166	0.310 ± 0.027	12.288 ± 1.639	-12.487	11.951	0.86	0.57	...
110207470	110207A	< 0.035	0.005 ± 0.001	37.888 ± 2.290	-19.642	45.133	0.87	0.42	...
110207959	110207B	0.662 ± 0.189	0.369 ± 0.032	7.680 ± 4.944	-4.570	10.714	0.87	0.48	...
110209165	110209A	< 1.042	0.310 ± 0.027	5.632 ± 0.916	-6.570	4.670	0.78	0.68	...
110212550	110212B	0.004 ± 0.001	0.003 ± 0.001	0.064 ± 0.036	-0.080	0.048	0.42	0.27	...
110213220	110213A	0.481 ± 0.046	0.155 ± 0.013	34.305 ± 1.639	-17.759	50.155	0.45	0.14	1.46
110213876	110213C	0.072 ± 0.013	0.039 ± 0.003	0.320 ± 0.810	-0.286	0.350	1.01	0.55	...
110217591	110217A	< 8.528	2.087 ± 0.181	60.672 ± 11.611	-17.766	87.176	0.89	0.44	...
110220761	110220A	0.968 ± 0.099	0.219 ± 0.019	33.024 ± 8.738	-18.091	47.619	0.67	0.15	...
110221244	110221A	< 2.216	0.439 ± 0.038	13.056 ± 1.846	-8.007	17.943	0.64	0.19	...
110226989	110226A	0.935 ± 0.213	0.522 ± 0.045	14.080 ± 0.923	-6.035	18.746	0.49	0.27	...
110227009	110227A	< 0.204	0.039 ± 0.003	1.728 ± 0.653	-1.051	2.389	0.80	0.54	...
110227229	110227B	1.162 ± 0.657	0.620 ± 0.054	18.432 ± 2.187	-10.154	26.502	0.38	0.20	...
110227420	110227C	0.834 ± 0.341	0.522 ± 0.045	25.600 ± 6.869	-23.936	27.008	0.36	0.23	...
110228011	110228A	< 2.126	0.439 ± 0.038	44.481 ± 2.834	-30.721	20.031	0.34	0.15	...
110228792	110228B	4.334 ± 0.930	1.476 ± 0.128	17.152 ± 2.360	-12.336	21.772	0.67	0.23	...
110301214	110301A	0.117 ± 0.007	0.027 ± 0.002	5.693 ± 0.362	-2.822	8.538	0.23	0.05	...
110302043	110302A	< 1.905	0.369 ± 0.032	38.336 ± 2.509	-25.192	46.083	0.70	0.18	...
110304071	110304A	< 0.791	0.184 ± 0.016	19.520 ± 1.498	-9.333	28.926	0.63	0.25	...
110307972	110307A	< 0.101	0.016 ± 0.001	2.304 ± 3.444	-2.888	1.642	1.09	0.41	...
110311812	110311A	1.653 ± 0.372	0.620 ± 0.054	6.400 ± 1.639	-4.960	7.776	0.61	0.23	...
110316139	110316A	< 0.075	0.019 ± 0.002	2.944 ± 2.199	-4.467	1.383	0.94	0.58	...
110318552	110318A	0.052 ± 0.024	0.033 ± 0.003	14.464 ± 1.094	-9.722	17.752	0.19	0.12	...
110319628	110319C	3.353 ± 1.320	1.755 ± 0.152	15.336 ± 1.446	-9.899	20.587	0.55	0.29	...
110319815	110319B	1.184 ± 0.382	0.738 ± 0.064	31.232 ± 5.049	-17.977	44.151	0.65	0.40	...
110321346	110321A	3.755 ± 0.563	1.476 ± 0.128	30.720 ± 10.764	-13.964	41.947	0.76	0.30	...
110322558	110322A	< 0.443	0.155 ± 0.013	36.097 ± 1.846	-21.973	49.827	0.57	0.49	...
110328520	110328B	< 1.131	0.219 ± 0.019	141.315 ± 29.767	-32.705	211.743	0.21	0.13	...
110331604	110331A	< 0.411	0.155 ± 0.013	3.200 ± 0.951	-1.648	4.720	0.52	0.38	...
110401920	110401A	0.042 ± 0.013	0.023 ± 0.002	2.368 ± 1.270	-1.840	2.904	0.59	0.32	...
110402009	110402A	0.016 ± 0.004	0.008 ± 0.001	35.649 ± 1.461	-16.437	54.487	0.63	0.33	...
110409179	110409A	0.009 ± 0.002	0.005 ± 0.001	0.128 ± 0.143	-0.192	0.064	0.61	0.38	...
110410133	110410A	< 1.210	0.184 ± 0.016	61.952 ± 1.379	-22.963	64.373	0.72	0.27	...
110410772	110410B	< 0.282	0.155 ± 0.013	8.064 ± 1.368	-8.730	7.310	0.50	0.55	...
110411629	110411B	< 4.331	0.439 ± 0.038	23.552 ± 1.950	-15.504	31.340	1.11	0.25	...
110412315	110412A	3.645 ± 0.307	1.043 ± 0.090	20.733 ± 4.636	-3.014	30.966	0.54	0.15	...
110413938	110413A	< 0.844	0.184 ± 0.016	54.272 ± 2.172	-24.129	70.283	1.02	0.76	...
110415541	110415A	0.426 ± 0.186	0.219 ± 0.019	166.146 ± 0.810	-81.989	248.629	0.44	0.23	...
110420946	110420B	< 0.012	0.003 ± 0.001	0.128 ± 0.516	-0.128	0.128	0.97	0.52	...
110421757	110421A	< 0.197	0.039 ± 0.003	40.449 ± 0.923	-16.443	47.857	0.25	0.17	...
110422029	110422B	0.025 ± 0.005	0.011 ± 0.001	0.320 ± 0.453	-0.267	0.286	0.83	0.38	...
110424758	110424A	0.029 ± 0.004	0.011 ± 0.001	0.672 ± 1.120	-0.356	0.944	1.01	0.40	...
110426629	110426A	3.890 ± 0.476	1.241 ± 0.108	356.357 ± 4.345	-5.933	370.949	0.38	0.12	...
110428338	110428B	< 0.207	0.065 ± 0.006	101.634 ± 2.919	-53.761	54.151	0.35	0.20	...
110430375	110430A	1.158 ± 0.154	0.310 ± 0.027	32.513 ± 1.717	-3.376	49.598	0.29	0.08	...
110503145	110503B	< 0.577	0.219 ± 0.019	7.936 ± 1.145	-4.192	11.648	0.26	0.20	...
110505203	110505A	< 0.209	0.078 ± 0.007	4.096 ± 0.545	-2.420	5.740	0.26	0.21	...

Continued on Next Page...

Table B.1 – Continued

Trigger ID	GRB Name	$\Delta t_{\rm min}$ (s)	$\Delta t_{\rm S/N}$ (s)	T_{90} (s)	$T_{100}^{\rm start}$ (s)	$T_{100}^{\rm stop}$ (s)	$\sigma_{X,t_{\rm min}}$	$\sigma_{X,t_{\rm S/N}}$	z
110509142	110509A	4.423 ± 0.997	1.755 ± 0.152	68.864 ± 2.757	-25.701	78.966	0.51	0.20	...
110509475	110509B	< 0.031	0.008 ± 0.001	0.640 ± 0.779	-0.637	0.637	0.87	0.45	...
110511616	110511A	< 0.665	0.369 ± 0.032	5.888 ± 1.639	-5.479	6.223	0.48	0.54	...
110517453	110517A	0.042 ± 0.021	0.027 ± 0.002	0.576 ± 1.810	-0.352	0.796	0.67	0.43	...
110517573	110517A	< 0.068	0.014 ± 0.001	23.040 ± 0.362	-11.661	34.189	0.34	0.21	...
110520302	110520B	1.089 ± 0.434	0.738 ± 0.064	12.288 ± 11.337	-16.583	7.855	0.64	0.43	...
110521478	110521B	0.482 ± 0.038	0.130 ± 0.011	6.141 ± 0.809	-3.037	9.181	0.60	0.16	...
110522256	110522A	< 4.687	1.476 ± 0.128	28.160 ± 2.673	-22.654	33.384	0.44	0.24	...
110522296	110522B	< 1.063	0.261 ± 0.023	27.136 ± 1.950	-18.502	35.467	0.85	0.41	...
110522633	110522C	< 0.365	0.078 ± 0.007	58.112 ± 2.828	-13.153	86.779	0.57	0.24	...
110523344	110523A	< 0.525	0.130 ± 0.011	44.544 ± 2.611	-23.437	65.197	0.51	0.24	...
110526715	110526A	0.018 ± 0.011	0.011 ± 0.001	0.448 ± 0.528	-0.349	0.544	0.41	0.26	...
110528624	110528A	< 0.739	0.261 ± 0.023	69.633 ± 5.526	-16.318	103.428	0.40	0.33	...
110529034	110529A	< 0.014	0.003 ± 0.001	0.512 ± 0.091	-0.382	0.637	0.45	0.20	...
110529262	110529B	0.118 ± 0.023	0.033 ± 0.003	45.825 ± 1.810	-22.591	53.012	0.41	0.11	...
110529811	110529C	< 4.650	1.043 ± 0.090	34.817 ± 4.636	-19.803	49.449	0.52	0.19	...
110531448	110531A	< 3.878	1.043 ± 0.090	38.656 ± 2.360	-15.335	53.058	0.54	0.20	...
110601681	110601A	< 0.162	0.033 ± 0.003	52.206 ± 13.350	-25.910	77.968	0.87	0.47	...
110605183	110605A	2.272 ± 0.075	0.369 ± 0.032	82.689 ± 3.083	-19.503	114.439	0.52	0.08	...
110605780	110605B	0.330 ± 0.072	0.155 ± 0.013	1.536 ± 1.056	-1.009	2.046	0.80	0.38	...
110609185	110609A	0.791 ± 0.375	0.522 ± 0.045	9.984 ± 4.471	-8.272	9.792	0.70	0.46	...
110609425	110609B	< 0.785	0.310 ± 0.027	33.024 ± 2.896	-23.015	28.166	0.49	0.44	...
110610640	110610A	< 0.136	0.055 ± 0.005	43.521 ± 2.862	-15.860	59.429	0.24	0.22	...
110613631	110613A	2.594 ± 1.358	1.755 ± 0.152	40.193 ± 3.874	-20.249	59.709	0.41	0.28	...
110616648	110616A	2.209 ± 0.932	1.476 ± 0.128	12.544 ± 2.611	-10.819	12.254	0.55	0.37	...
110618366	110618A	12.874 ± 0.363	1.755 ± 0.152	163.843 ± 11.406	-59.600	241.866	0.54	0.07	...
110622158	110622A	0.522 ± 0.600	0.261 ± 0.023	70.401 ± 0.773	-8.228	106.524	0.10	0.05	...
110624906	110624A	< 1.128	0.310 ± 0.027	3.520 ± 4.948	-3.022	3.982	0.87	0.56	...
110625579	110625B	< 4.195	0.620 ± 0.054	35.584 ± 1.846	-18.128	52.676	0.58	0.14	...
110625881	110625A	0.101 ± 0.012	0.027 ± 0.002	26.881 ± 0.572	-0.865	43.756	0.19	0.05	...
110626448	110626A	0.827 ± 0.111	0.310 ± 0.027	6.400 ± 1.145	-3.936	8.800	0.55	0.21	...
110629174	110629A	0.062 ± 0.034	0.039 ± 0.003	61.694 ± 18.690	-0.319	92.201	0.51	0.32	...
110702187	110702A	0.165 ± 0.064	0.110 ± 0.010	34.369 ± 5.736	-27.769	40.607	0.42	0.28	...
110703557	110703A	< 0.296	0.092 ± 0.008	6.720 ± 1.619	-7.550	5.822	0.41	0.20	...
110705151	110705A	0.007 ± 0.004	0.004 ± 0.001	0.192 ± 0.036	-0.112	0.272	0.43	0.22	...
110705364	110705B	< 0.233	0.055 ± 0.005	19.200 ± 0.923	-3.872	28.960	0.54	0.23	...
110706202	110706A	< 0.372	0.130 ± 0.011	12.032 ± 4.382	-7.498	16.422	0.40	0.33	...
110706477	110706B	0.968 ± 0.523	0.620 ± 0.054	73.217 ± 14.612	-27.027	106.197	0.21	0.13	...
110706728	110706C	< 0.104	0.046 ± 0.004	16.896 ± 6.339	-8.244	25.348	0.36	0.32	...
110706977	110706D	0.272 ± 0.171	0.184 ± 0.016	33.216 ± 4.007	-20.431	31.693	0.18	0.12	...
110709463	110709C	0.406 ± 0.023	0.092 ± 0.008	24.061 ± 0.722	-11.908	35.972	0.50	0.11	...
110709642	110709A	0.113 ± 0.043	0.055 ± 0.005	43.201 ± 0.405	-11.473	64.127	0.31	0.15	...
110709862	110709D	< 0.903	0.310 ± 0.027	5.376 ± 1.493	-4.461	6.259	0.48	0.30	...
110710954	110710A	0.101 ± 0.031	0.046 ± 0.004	22.720 ± 1.604	-11.265	24.405	0.41	0.18	...
110716018	110716A	0.087 ± 0.034	0.039 ± 0.003	7.168 ± 1.747	-6.624	7.624	0.43	0.19	...
110717180	110717A	0.011 ± 0.003	0.005 ± 0.001	0.112 ± 0.072	-0.071	0.151	0.64	0.32	...
110717319	110717B	0.143 ± 0.066	0.065 ± 0.006	90.369 ± 0.810	-19.022	112.904	0.17	0.08	...
110720177	110720A	< 1.198	0.261 ± 0.023	11.200 ± 0.602	-5.672	16.616	0.41	0.11	...
110721200	110721A	0.116 ± 0.065	0.055 ± 0.005	21.822 ± 0.572	-0.326	32.622	0.11	0.05	...
110722694	110722A	< 2.514	0.439 ± 0.038	73.473 ± 11.404	-21.936	109.558	0.31	0.10	...
110722710	110722B	< 1.041	0.310 ± 0.027	14.336 ± 2.721	-11.712	16.784	0.49	0.28	...
110725236	110725A	< 0.335	0.078 ± 0.007	20.224 ± 1.056	-11.037	29.201	0.52	0.28	...

Continued on Next Page...

Table B.1 – Continued

Trigger ID	GRB Name	$\Delta t_{\rm min}$ (s)	$\Delta t_{\rm S/N}$ (s)	T_{90} (s)	$T_{100}^{\rm start}$ (s)	$T_{100}^{\rm stop}$ (s)	$\sigma_{X,t_{\rm min}}$	$\sigma_{X,t_{\rm S/N}}$	z
110726211	110726B	0.297 ± 0.068	0.155 ± 0.013	29.952 ± 10.608	-16.674	40.811	0.47	0.24	...
110728056	110728A	< 0.047	0.033 ± 0.003	0.704 ± 0.231	-0.177	0.921	0.76	0.99	...
110729142	110729A	< 0.267	0.110 ± 0.010	408.582 ± 2.290	-69.423	410.662	0.19	0.17	...
110730008	110730A	3.726 ± 1.291	1.755 ± 0.152	28.416 ± 2.919	-22.074	34.442	0.61	0.29	...
110730660	110730B	0.557 ± 0.189	0.310 ± 0.027	33.856 ± 1.811	-23.117	37.457	0.39	0.22	...
110731465	110731A	0.021 ± 0.015	0.014 ± 0.001	7.485 ± 0.572	-3.705	11.181	0.16	0.10	2.83
110801335	110801B	0.070 ± 0.024	0.039 ± 0.003	0.384 ± 0.326	-0.316	0.447	0.79	0.44	...
110803783	110803A	< 2.303	0.522 ± 0.045	186.883 ± 2.986	-156.675	123.457	0.68	0.31	...
110806934	110806A	< 0.404	0.130 ± 0.011	28.416 ± 0.923	-5.014	42.698	0.24	0.16	...
110809461	110809A	0.245 ± 0.086	0.130 ± 0.011	12.544 ± 4.615	-10.563	14.391	0.32	0.17	...
110812899	110812B	0.280 ± 0.052	0.155 ± 0.013	11.264 ± 3.727	-7.882	14.526	0.57	0.32	...
110813237	110813A	0.497 ± 0.164	0.184 ± 0.016	22.784 ± 3.114	-13.001	32.331	0.30	0.11	...
110817191	110817A	0.179 ± 0.041	0.078 ± 0.007	5.949 ± 0.572	-1.580	8.874	0.22	0.10	...
110818860	110818A	< 2.791	0.522 ± 0.045	67.073 ± 3.916	-43.192	90.258	0.64	0.27	3.36
110819665	110819A	0.249 ± 0.063	0.130 ± 0.011	16.384 ± 6.149	-8.624	23.972	0.57	0.30	...
110820476	110820C	1.134 ± 0.172	0.522 ± 0.045	11.264 ± 7.331	-9.674	12.734	0.70	0.32	...
110824009	110824A	< 0.011	0.003 ± 0.001	76.607 ± 9.220	-2.685	114.513	0.26	0.18	...
110825102	110825A	0.025 ± 0.004	0.007 ± 0.001	62.465 ± 0.231	-0.447	91.993	0.19	0.05	...
110825265	110825B	< 3.304	0.877 ± 0.076	51.073 ± 3.389	-29.971	59.894	0.54	0.32	...
110831282	110831A	< 0.987	0.155 ± 0.013	98.881 ± 3.138	-28.680	127.551	0.94	0.26	...
110901230	110901A	0.384 ± 0.267	0.261 ± 0.023	22.528 ± 5.620	-13.205	25.979	0.42	0.29	...
110903009	110903B	0.288 ± 0.014	0.078 ± 0.007	28.672 ± 2.429	-15.223	41.811	0.41	0.11	...
110903111	110903A	< 0.210	0.055 ± 0.005	341.254 ± 2.288	-27.997	340.998	0.27	0.16	...
110904124	110904A	< 0.233	0.078 ± 0.007	83.905 ± 3.853	-24.368	123.296	0.28	0.22	...
110904163	110904B	< 0.327	0.110 ± 0.010	51.457 ± 4.128	-26.841	75.525	0.48	0.29	...
110904531	110904C	1.471 ± 0.708	0.738 ± 0.064	20.480 ± 5.479	-12.698	28.058	0.27	0.13	...
110906302	110906B	0.832 ± 0.155	0.310 ± 0.027	23.936 ± 2.550	-17.232	30.368	0.49	0.18	...
110909116	110909A	0.279 ± 0.067	0.130 ± 0.011	20.736 ± 1.639	-22.560	18.672	0.66	0.31	...
110911071	110911A	1.894 ± 0.458	1.241 ± 0.108	8.960 ± 4.352	-9.043	8.787	1.05	0.69	...
110916016	110916A	0.681 ± 0.123	0.261 ± 0.023	1.792 ± 1.993	-2.301	1.277	0.96	0.37	...
110919634	110919A	0.251 ± 0.072	0.130 ± 0.011	35.073 ± 3.974	-6.170	62.898	0.17	0.09	...
110920338	110920A	0.337 ± 0.188	0.184 ± 0.016	9.728 ± 0.810	-5.331	11.095	0.38	0.21	...
110920546	110920A	< 2.096	0.369 ± 0.032	160.771 ± 5.221	-2.659	191.860	0.14	0.04	...
110921444	110921C	0.345 ± 0.109	0.219 ± 0.019	149.507 ± 10.691	-68.609	86.150	0.64	0.41	...
110921577	110921A	< 1.497	0.877 ± 0.076	40.705 ± 1.810	-30.209	30.615	0.31	0.31	...
110921912	110921B	0.024 ± 0.010	0.016 ± 0.001	17.664 ± 0.345	-7.850	27.294	0.21	0.14	...
110923835	110923A	1.388 ± 0.170	0.439 ± 0.038	46.398 ± 11.279	-22.509	69.323	0.63	0.20	...
110926107	110926A	0.605 ± 0.253	0.310 ± 0.027	75.265 ± 1.280	-18.385	89.990	0.27	0.14	...
110928180	110928B	< 0.203	0.110 ± 0.010	148.226 ± 1.925	-192.673	91.909	0.20	0.23	...
110929187	110929A	0.416 ± 0.097	0.184 ± 0.016	5.120 ± 0.572	-3.046	7.142	0.47	0.21	...
110930564	110930A	6.368 ± 0.798	1.755 ± 0.152	37.889 ± 5.431	-25.519	49.862	0.71	0.20	...
111001804	111001A	0.021 ± 0.012	0.014 ± 0.001	0.384 ± 1.361	-0.444	0.319	0.85	0.55	...
111003465	111003A	0.415 ± 0.027	0.078 ± 0.007	16.640 ± 1.056	-7.725	25.389	0.31	0.06	...
111005398	111005B	0.721 ± 0.160	0.439 ± 0.038	30.720 ± 3.093	-15.718	34.662	0.51	0.31	...
111008992	111008B	< 12.204	2.087 ± 0.181	42.496 ± 4.128	-11.671	57.996	0.71	0.20	...
111009282	111009A	< 1.073	0.184 ± 0.016	20.736 ± 4.221	-1.826	24.281	0.31	0.07	...
111010237	111010A	4.084 ± 1.659	2.087 ± 0.181	82.433 ± 8.444	-29.758	119.422	0.40	0.21	...
111010660	111010B	0.466 ± 0.078	0.155 ± 0.013	8.704 ± 2.111	-5.334	11.978	0.72	0.24	...
111010709	111010C	0.918 ± 0.299	0.369 ± 0.032	52.993 ± 0.923	-12.740	75.736	0.34	0.14	...
111010899	111010D	< 0.789	0.439 ± 0.038	18.560 ± 2.988	-23.919	10.417	0.44	0.46	...
111011094	111011A	< 0.007	0.002 ± 0.001	1.472 ± 0.771	-0.799	2.136	0.67	0.43	...
111012456	111012A	0.463 ± 0.108	0.184 ± 0.016	20.736 ± 0.724	-9.248	31.984	0.31	0.13	...

Continued on Next Page...

Table B.1 – Continued

Trigger ID	GRB Name	$\Delta t_{\rm min}$ (s)	$\Delta t_{\rm S/N}$ (s)	T_{90} (s)	$T_{100}^{\rm start}$ (s)	$T_{100}^{\rm stop}$ (s)	$\sigma_{X,t_{\rm min}}$	$\sigma_{X,t_{\rm S/N}}$	z
111012811	111012B	0.050 ± 0.012	0.023 ± 0.002	7.936 ± 1.145	-4.448	11.392	0.29	0.13	...
111015427	111015A	< 0.550	0.110 ± 0.010	92.737 ± 3.319	-21.640	137.838	0.63	0.21	...
111017657	111017A	< 1.527	0.110 ± 0.010	11.072 ± 0.410	-5.231	16.779	0.68	0.06	...
111018595	111018B	< 1.584	0.439 ± 0.038	8.192 ± 1.864	-4.829	11.449	0.90	0.37	...
111018785	111018C	5.258 ± 1.211	2.951 ± 0.256	29.697 ± 1.810	-21.047	33.268	0.65	0.37	...
111022854	111022C	< 0.035	0.008 ± 0.001	0.192 ± 0.707	-0.224	0.160	0.79	0.42	...
111024722	111024B	< 0.250	0.039 ± 0.003	68.609 ± 2.896	-40.110	96.404	0.52	0.16	...
111024896	111024C	0.038 ± 0.010	0.023 ± 0.002	1.792 ± 1.846	-0.490	2.429	0.99	0.60	...
111025078	111025A	< 5.390	1.241 ± 0.108	51.712 ± 2.202	-20.322	76.874	0.76	0.39	...
111103441	111103A	0.138 ± 0.037	0.078 ± 0.007	11.968 ± 6.426	-6.056	17.744	0.44	0.25	...
111103948	111103C	0.018 ± 0.006	0.011 ± 0.001	0.320 ± 0.181	-0.222	0.414	0.71	0.45	...
111105457	111105A	0.241 ± 0.060	0.092 ± 0.008	43.520 ± 0.572	-19.655	35.180	0.78	0.30	...
111107035	111107A	3.425 ± 0.439	1.476 ± 0.128	12.032 ± 0.923	-7.498	16.422	0.89	0.38	2.893
111107076	111107B	1.089 ± 0.282	0.620 ± 0.054	77.185 ± 0.810	-29.068	93.648	0.43	0.24	...
111109453	111109B	< 0.981	0.310 ± 0.027	4.864 ± 2.757	-4.581	4.702	0.57	0.47	...
111109873	111109C	< 3.936	0.620 ± 0.054	9.664 ± 6.457	-9.394	9.830	1.09	0.28	...
111112908	111112A	< 0.023	0.005 ± 0.001	0.192 ± 0.091	-0.160	0.224	0.65	0.26	...
111113410	111113B	0.395 ± 0.093	0.155 ± 0.013	15.360 ± 1.639	-8.627	21.478	0.39	0.15	...
111114233	111114A	0.801 ± 0.398	0.522 ± 0.045	22.016 ± 2.673	-7.378	28.702	0.58	0.38	...
111117510	111117A	0.009 ± 0.003	0.004 ± 0.001	0.576 ± 0.143	-0.416	0.732	0.70	0.34	...
111117526	111117B	< 2.730	1.043 ± 0.090	23.808 ± 1.717	-13.069	34.293	0.49	0.34	...
111120556	111120A	< 2.860	0.369 ± 0.032	98.626 ± 2.970	-27.729	84.697	0.50	0.14	...
111124308	111124A	1.964 ± 0.185	0.877 ± 0.076	8.960 ± 3.114	-5.203	12.538	0.89	0.40	...
111127810	111127A	0.166 ± 0.130	0.110 ± 0.010	19.008 ± 2.548	-10.181	27.249	0.15	0.10	...
111201599	111201A	2.912 ± 0.897	1.476 ± 0.128	16.896 ± 3.974	-6.956	23.428	0.59	0.30	...
111203054	111203A	0.143 ± 0.060	0.092 ± 0.008	55.553 ± 5.684	-44.545	16.940	0.28	0.18	...
111203609	111203B	1.124 ± 0.622	0.738 ± 0.064	22.016 ± 6.734	-13.722	30.058	0.51	0.34	...
111208353	111208A	5.394 ± 0.408	1.476 ± 0.128	40.961 ± 4.345	-24.415	53.819	0.60	0.16	...
111216389	111216A	0.087 ± 0.027	0.046 ± 0.004	83.777 ± 0.500	-18.851	105.951	0.37	0.19	...
111220486	111220A	0.051 ± 0.008	0.016 ± 0.001	39.041 ± 5.101	-6.318	49.900	0.23	0.07	...
111221739	111221A	0.018 ± 0.006	0.011 ± 0.001	27.136 ± 7.186	-13.952	40.016	0.42	0.27	...
111222619	111222A	0.007 ± 0.001	0.003 ± 0.001	0.320 ± 0.143	-0.222	0.414	0.76	0.34	...
111226795	111226A	< 4.661	0.877 ± 0.076	74.753 ± 8.749	-25.023	93.066	0.33	0.10	...
111228453	111228B	0.775 ± 0.011	0.092 ± 0.008	2.944 ± 0.979	-1.363	4.487	0.68	0.08	...
111228657	111228A	< 0.085	0.033 ± 0.003	99.842 ± 2.111	-49.409	78.603	0.18	0.12	0.714
111230683	111230A	< 0.246	0.065 ± 0.006	28.160 ± 1.557	-26.692	29.347	0.52	0.41	...
111230819	111230B	< 0.108	0.033 ± 0.003	12.736 ± 1.145	-6.952	18.360	0.56	0.32	...
120101354	120101A	< 0.103	0.016 ± 0.001	0.128 ± 0.072	-0.160	0.096	1.44	0.45	...
120102095	120102A	0.338 ± 0.023	0.092 ± 0.008	28.417 ± 8.204	-25.674	29.990	0.47	0.13	...
120102416	120102B	0.597 ± 0.272	0.369 ± 0.032	20.224 ± 2.769	-20.335	19.903	0.40	0.25	...
120105584	120105A	< 1.909	0.439 ± 0.038	22.528 ± 2.202	-19.408	25.407	0.53	0.24	...
120107384	120107A	< 0.060	0.027 ± 0.002	23.040 ± 0.143	-11.341	34.509	0.25	0.24	...
120109824	120109A	3.875 ± 1.183	1.476 ± 0.128	38.656 ± 3.114	-21.079	55.815	0.69	0.26	...
120111051	120111A	5.451 ± 2.729	2.482 ± 0.215	76.801 ± 5.515	-26.410	104.150	0.45	0.20	...
120114433	120114B	0.688 ± 0.159	0.369 ± 0.032	2.752 ± 1.569	-0.263	3.984	1.06	0.57	...
120114681	120114A	1.346 ± 1.016	0.877 ± 0.076	43.264 ± 5.804	-29.369	56.718	0.37	0.24	...
120118709	120118B	1.410 ± 0.482	0.738 ± 0.064	37.825 ± 12.586	-22.152	53.109	0.33	0.17	2.943
120118898	120118C	< 0.168	0.027 ± 0.002	17.152 ± 2.111	-9.180	25.100	0.58	0.17	...
120119170	120119A	< 0.463	0.078 ± 0.007	55.297 ± 6.229	-15.904	85.811	0.33	0.09	1.728
120119229	120119B	0.083 ± 0.030	0.055 ± 0.005	41.728 ± 1.557	-20.692	62.330	0.44	0.29	...
120119354	120119C	0.464 ± 0.057	0.219 ± 0.019	16.384 ± 1.493	-16.048	16.548	0.61	0.29	...
120120432	120120A	< 8.745	1.241 ± 0.108	32.256 ± 6.481	-15.893	48.265	1.09	0.28	...

Continued on Next Page...

Table B.1 – Continued

Trigger ID	GRB Name	$\Delta t_{\rm min}$ (s)	$\Delta t_{\rm S/N}$ (s)	T_{90} (s)	$T_{100}^{\rm start}$ (s)	$T_{100}^{\rm stop}$ (s)	$\sigma_{X,t_{\rm min}}$	$\sigma_{X,t_{\rm S/N}}$	z
120121101	120121B	< 1.305	0.439 ± 0.038	18.432 ± 3.727	-12.458	24.198	0.38	0.22	...
120121251	120121C	< 1.648	0.310 ± 0.027	37.121 ± 11.876	-23.877	49.992	0.28	0.09	...
120122300	120122A	0.576 ± 0.147	0.310 ± 0.027	16.701 ± 1.881	-8.264	24.968	0.48	0.26	...
120129312	120129B	0.276 ± 0.030	0.130 ± 0.011	1.280 ± 0.689	-1.274	1.274	1.05	0.49	...
120129580	120129A	0.047 ± 0.015	0.011 ± 0.001	3.072 ± 0.362	-0.870	4.913	0.15	0.04	...
120130699	120130A	0.168 ± 0.027	0.092 ± 0.008	27.777 ± 0.694	-7.181	40.844	0.44	0.24	...
120130906	120130B	0.354 ± 0.135	0.219 ± 0.019	3.584 ± 1.379	-3.056	3.961	0.51	0.32	...
120130938	120130C	< 1.482	0.369 ± 0.032	38.913 ± 7.455	-24.417	52.994	0.30	0.15	...
120203812	120203A	1.382 ± 0.211	0.439 ± 0.038	10.240 ± 2.429	-9.933	10.445	0.80	0.25	...
120204054	120204A	< 0.213	0.078 ± 0.007	49.089 ± 0.429	-14.128	83.542	0.05	0.04	...
120205285	120205A	0.121 ± 0.055	0.078 ± 0.007	0.576 ± 0.272	-0.864	0.284	0.96	0.61	...
120206949	120206A	0.074 ± 0.015	0.039 ± 0.003	9.472 ± 3.338	-4.951	13.875	0.33	0.17	...
120210650	120210A	0.084 ± 0.024	0.039 ± 0.003	1.344 ± 0.264	-0.731	1.949	0.48	0.22	...
120212353	120212B	0.050 ± 0.015	0.023 ± 0.002	0.864 ± 0.577	-1.262	0.458	0.93	0.43	...
120212383	120212A	1.378 ± 0.169	0.522 ± 0.045	9.216 ± 0.724	-6.618	11.690	0.66	0.25	...
120213606	120213B	0.116 ± 0.025	0.065 ± 0.006	13.824 ± 3.328	-9.917	17.585	0.53	0.30	...
120217808	120217A	0.415 ± 0.060	0.155 ± 0.013	5.888 ± 2.862	-3.431	8.271	0.59	0.22	...
120217904	120217B	< 0.050	0.011 ± 0.001	2.624 ± 0.300	-1.525	3.689	0.29	0.12	...
120218276	120218B	0.991 ± 0.330	0.620 ± 0.054	256.260 ± 5.221	-212.996	61.708	0.45	0.28	...
120219563	120219B	< 0.690	0.439 ± 0.038	8.128 ± 0.429	-5.179	10.979	0.61	0.69	...
120220210	120220A	< 2.436	1.043 ± 0.090	21.248 ± 1.639	-15.898	26.370	0.40	0.39	...
120222021	120222A	0.042 ± 0.014	0.019 ± 0.002	1.088 ± 0.143	-0.607	1.359	0.29	0.13	...
120222119	120222A	5.529 ± 0.464	1.755 ± 0.152	29.440 ± 5.382	-19.576	39.009	0.78	0.25	...
120223933	120223A	< 1.565	0.184 ± 0.016	14.336 ± 2.360	-7.616	20.880	0.85	0.19	...
120224282	120224B	< 0.957	0.261 ± 0.023	60.929 ± 3.093	-28.461	79.976	0.34	0.22	...
120224898	120224C	< 0.207	0.078 ± 0.007	29.184 ± 4.222	-14.192	43.876	0.65	0.55	...
120226447	120226B	0.074 ± 0.016	0.046 ± 0.004	14.592 ± 3.916	-10.493	18.521	0.70	0.44	...
120226871	120226A	0.147 ± 0.055	0.078 ± 0.007	52.993 ± 0.572	-15.347	83.726	0.17	0.09	...
120227391	120227A	0.106 ± 0.036	0.065 ± 0.006	19.712 ± 1.717	-10.531	28.671	0.93	0.57	...
120227725	120227B	0.175 ± 0.061	0.092 ± 0.008	17.408 ± 0.810	-8.365	26.261	0.27	0.14	...
120302080	120302A	< 1.418	0.261 ± 0.023	80.384 ± 16.927	-29.100	120.406	1.18	0.69	...
120302722	120302B	< 0.134	0.046 ± 0.004	1.600 ± 0.779	-0.856	2.264	0.86	0.74	...
120304061	120304A	0.677 ± 0.014	0.130 ± 0.011	9.984 ± 1.055	-5.200	14.660	0.50	0.10	...
120304248	120304B	0.018 ± 0.005	0.010 ± 0.001	5.376 ± 0.572	-2.925	7.795	0.62	0.33	...
120308588	120308B	< 0.311	0.078 ± 0.007	25.600 ± 1.557	-27.529	16.759	0.56	0.20	...
120312671	120312A	1.314 ± 0.587	0.738 ± 0.064	13.312 ± 3.167	-8.643	17.823	0.55	0.31	...
120314412	120314A	< 0.201	0.078 ± 0.007	1.280 ± 1.086	-1.914	0.634	0.65	0.51	...
120316008	120316A	< 0.155	0.027 ± 0.002	26.624 ± 0.362	-11.645	41.329	0.73	0.25	...
120319983	120319A	< 0.741	0.219 ± 0.019	72.448 ± 7.832	-9.467	91.224	0.66	0.49	...
120323162	120323B	< 0.275	0.065 ± 0.006	4.352 ± 0.724	-2.928	5.752	0.53	0.24	...
120323507	120323A	0.013 ± 0.001	0.004 ± 0.001	0.448 ± 0.091	-0.285	0.608	0.27	0.08	...
120326056	120326A	0.974 ± 0.140	0.219 ± 0.019	11.776 ± 1.810	-6.176	16.285	0.38	0.08	1.798
120327418	120327B	0.026 ± 0.012	0.016 ± 0.001	0.256 ± 1.319	-0.320	0.192	0.77	0.48	...
120328268	120328B	0.094 ± 0.045	0.055 ± 0.005	29.697 ± 1.056	-2.055	48.104	0.09	0.05	...
120331055	120331A	0.015 ± 0.005	0.007 ± 0.001	16.384 ± 10.367	-5.031	21.668	0.62	0.28	...
120402669	120402B	< 0.624	0.110 ± 0.010	20.224 ± 0.810	-12.093	28.145	0.45	0.11	...
120403857	120403B	< 1.345	0.261 ± 0.023	4.288 ± 1.935	-6.095	2.423	1.30	0.42	...
120410585	120410A	< 0.059	0.014 ± 0.001	1.088 ± 1.180	-1.567	0.604	0.87	0.37	...
120411925	120411A	0.060 ± 0.018	0.033 ± 0.003	38.912 ± 1.493	-19.133	58.278	0.81	0.44	...
120412055	120412A	< 2.242	0.522 ± 0.045	9.728 ± 3.566	-8.915	10.427	0.85	0.42	...
120412920	120412B	< 0.476	0.130 ± 0.011	101.182 ± 4.871	-0.743	151.027	0.39	0.18	...
120415076	120415A	0.978 ± 0.116	0.369 ± 0.032	12.544 ± 4.128	-6.723	18.231	0.57	0.21	...

Continued on Next Page...

Table B.1 – Continued

Trigger ID	GRB Name	$\Delta t_{\rm min}$ (s)	$\Delta t_{\rm S/N}$ (s)	T_{90} (s)	$T_{100}^{\rm start}$ (s)	$T_{100}^{\rm stop}$ (s)	$\sigma_{X,t_{\rm min}}$	$\sigma_{X,t_{\rm S/N}}$	z
120415891	120415B	< 0.046	0.014 ± 0.001	0.960 ± 0.264	-0.731	1.179	0.52	0.44	...
120415958	120415C	1.156 ± 0.777	0.620 ± 0.054	12.544 ± 1.717	-10.563	14.391	0.41	0.22	...
120420249	120420A	2.318 ± 0.291	0.738 ± 0.064	25.600 ± 4.419	-3.712	37.504	0.57	0.18	...
120420858	120420B	1.615 ± 0.698	0.877 ± 0.076	254.913 ± 4.222	-21.676	296.948	0.38	0.21	...
120426090	120426A	< 0.192	0.027 ± 0.002	2.880 ± 0.181	-1.202	4.530	0.27	0.05	...
120426585	120426B	1.620 ± 0.878	0.738 ± 0.064	30.973 ± 3.620	-15.423	46.187	0.35	0.16	...
120427054	120427A	< 0.894	0.110 ± 0.010	5.632 ± 0.572	-0.964	8.702	0.54	0.09	...
120427153	120427B	2.693 ± 0.710	1.476 ± 0.128	22.784 ± 1.999	-9.939	31.748	1.01	0.55	...
120429003	120429A	< 0.182	0.092 ± 0.008	1.664 ± 0.968	-1.018	2.302	0.49	0.53	...
120429484	120429B	< 0.773	0.130 ± 0.011	15.360 ± 1.619	-5.555	21.939	0.52	0.27	...
120430980	120430A	< 1.624	0.439 ± 0.038	14.592 ± 2.172	-9.533	19.481	0.85	0.46	...
120504468	120504A	3.667 ± 0.553	1.755 ± 0.152	41.985 ± 2.673	-12.406	62.318	0.53	0.25	...
120504945	120504B	0.120 ± 0.026	0.065 ± 0.006	5.760 ± 0.779	-5.155	6.307	1.06	0.58	...
120506128	120506A	0.675 ± 0.175	0.369 ± 0.032	2.304 ± 1.379	-1.933	2.666	0.76	0.41	...
120509619	120509A	< 0.027	0.014 ± 0.001	0.704 ± 1.404	-0.542	0.766	0.75	0.79	...
120510900	120510B	< 7.403	1.241 ± 0.108	62.465 ± 3.908	-29.160	82.643	0.65	0.23	...
120511638	120511A	< 0.528	0.130 ± 0.011	45.249 ± 2.940	-22.414	67.613	0.75	0.43	...
120512112	120512A	0.123 ± 0.048	0.078 ± 0.007	18.176 ± 1.350	-2.265	27.517	0.18	0.12	...
120513531	120513A	0.348 ± 0.121	0.219 ± 0.019	23.808 ± 0.923	-12.301	35.061	0.67	0.42	...
120519721	120519A	0.060 ± 0.026	0.033 ± 0.003	0.960 ± 0.202	-0.603	1.307	0.39	0.21	...
120520949	120520A	0.398 ± 0.090	0.184 ± 0.016	5.760 ± 1.356	-7.587	3.875	0.70	0.32	...
120521380	120521B	3.757 ± 1.182	1.755 ± 0.152	91.134 ± 4.222	-26.803	136.302	0.62	0.29	...
120522361	120522B	0.239 ± 0.090	0.130 ± 0.011	28.160 ± 8.039	-12.922	30.445	0.26	0.14	...
120524134	120524A	0.024 ± 0.004	0.014 ± 0.001	0.704 ± 0.466	-0.478	0.921	0.81	0.46	...
120526303	120526A	< 0.327	0.055 ± 0.005	43.649 ± 1.002	-2.392	68.305	0.44	0.23	...
120528442	120528A	< 0.682	0.219 ± 0.019	16.384 ± 5.177	-8.880	23.716	0.26	0.19	...
120530121	120530A	< 1.136	0.219 ± 0.019	77.054 ± 1.810	-2.763	115.108	0.36	0.15	...
120531393	120531A	< 6.901	1.241 ± 0.108	25.344 ± 7.186	-15.363	35.063	0.98	0.36	...
120603439	120603A	0.030 ± 0.021	0.019 ± 0.002	0.384 ± 0.345	-0.252	0.511	0.40	0.26	...
120604220	120604A	0.143 ± 0.017	0.065 ± 0.006	10.496 ± 5.615	-3.094	12.836	0.92	0.42	...
120604343	120604B	4.706 ± 0.283	1.476 ± 0.128	12.032 ± 3.278	-8.522	15.398	0.89	0.28	...
120605453	120605A	0.461 ± 0.029	0.130 ± 0.011	18.112 ± 1.086	-1.466	26.407	0.69	0.19	...
120608489	120608A	< 0.066	0.039 ± 0.003	0.960 ± 1.611	-0.667	1.243	0.53	0.53	...
120608777	120608B	0.278 ± 0.088	0.184 ± 0.016	24.832 ± 3.840	-24.250	22.907	0.47	0.32	...
120609580	120609A	0.243 ± 0.152	0.155 ± 0.013	1.792 ± 0.810	-1.661	1.917	0.50	0.32	...
120611108	120611A	< 0.444	0.046 ± 0.004	49.921 ± 1.639	-21.305	54.573	1.11	0.27	...
120612680	120612B	1.587 ± 0.654	1.043 ± 0.090	63.232 ± 7.886	-27.128	67.702	0.54	0.35	...
120612687	120612C	0.060 ± 0.012	0.027 ± 0.002	0.256 ± 0.453	-0.320	0.192	0.70	0.32	...
120616630	120616A	0.006 ± 0.003	0.004 ± 0.001	0.048 ± 0.484	-0.072	0.024	0.74	0.53	...
120618128	120618A	1.323 ± 0.146	0.439 ± 0.038	17.600 ± 1.820	-8.840	26.184	0.44	0.15	...
120618919	120618B	0.142 ± 0.061	0.078 ± 0.007	47.616 ± 12.299	-33.467	42.693	0.65	0.36	...
120619884	120619A	< 0.454	0.092 ± 0.008	0.960 ± 0.960	-0.731	1.179	1.18	0.40	...
120624309	120624A	< 0.016	0.003 ± 0.001	0.640 ± 0.160	-0.381	0.893	0.27	0.13	...
120624933	120624B	< 0.129	0.033 ± 0.003	271.364 ± 4.580	-257.028	148.171	0.19	0.10	...
120625119	120625A	< 0.149	0.039 ± 0.003	7.424 ± 0.571	-3.933	10.833	0.21	0.12	...
120629565	120629A	0.147 ± 0.027	0.078 ± 0.007	0.704 ± 1.026	-0.734	0.665	0.94	0.50	...
120701654	120701B	< 0.224	0.130 ± 0.011	1.024 ± 1.451	-1.469	0.571	0.83	0.97	...
120703417	120703B	< 1.189	0.219 ± 0.019	64.513 ± 3.083	-24.555	85.095	0.28	0.09	...
120703498	120703C	2.220 ± 0.413	1.043 ± 0.090	77.568 ± 2.187	-30.871	96.327	0.65	0.30	...
120703726	120703A	0.058 ± 0.043	0.033 ± 0.003	8.960 ± 1.379	-3.667	14.163	0.16	0.09	...
120707800	120707A	0.061 ± 0.025	0.039 ± 0.003	40.960 ± 4.238	-18.276	62.825	0.17	0.11	...
120709883	120709A	< 0.069	0.014 ± 0.001	27.328 ± 0.958	-13.933	40.707	0.55	0.17	...

Continued on Next Page...

Table B.1 – Continued

Trigger ID	GRB Name	$\Delta t_{\rm min}$ (s)	$\Delta t_{\rm S/N}$ (s)	T_{90} (s)	$T_{100}^{\rm start}$ (s)	$T_{100}^{\rm stop}$ (s)	$\sigma_{X,t_{\rm min}}$	$\sigma_{X,t_{\rm S/N}}$	z
120710100	120710A	0.670 ± 0.517	0.439 ± 0.038	131.840 ± 1.056	-7.875	155.607	0.22	0.15	...
120711115	120711A	< 0.075	0.011 ± 0.001	44.033 ± 0.724	57.830	128.262	0.50	0.13	...
120711446	120711C	1.139 ± 0.260	0.522 ± 0.045	87.552 ± 3.874	-32.427	123.394	0.90	0.41	...

The redshift values marked with $\star$ are taken from `http://www.mpe.mpg.de/~jcg/grbgen.html`.

APPENDIX C

(U)LIRGS SN RATE ESTIMATIONS USING THE PTF

Table C.1: (U)LIRGs SN Rate Estimations Using the PTF

Optical ID	IRAS Name	RA (J2000)	Dec (J2000)	D_L (Mpc)	$\log_{10}(\frac{L_{ir}}{L})$	Observed Rates						Predicted Rates		
						IIP	IIL	IIn	Ibc	ST (days)	CT (yr^{-1})	F_ν(FUV) ($\frac{erg}{s\ cm^2\ \AA}$)	$\sigma_{\rm FUV}$ ($\frac{erg}{s\ cm^2\ \AA}$)	SN rate (yr^{-1})
05083+2441	05083+2441	77.85783	24.75508	99.20	11.26	1.000	0.965	1.000	1.000	149	0.407	2.00e-16	2.00e-16	0.001
05129+5128	05129+5128	79.23375	51.53236	120.00	11.42	0.711	0.599	0.732	0.631	908	1.683	5.33e-16	3.00e-16	0.005
NGC2342	07063+2043	107.32533	20.63597	78.00	11.31	0.507	0.372	0.548	0.448	1443	1.898	2.54e-14	6.00e-16	0.100
NGC34	F00085-1223	2.77729	-12.10731	84.10	11.49	0.220	0.145	0.244	0.187	1870	1.053	1.53e-14	4.00e-16	0.070
Arp256	F00163-1039	4.71046	-10.36922	117.50	11.48	0.326	0.185	0.354	0.226	1537	1.191	2.65e-14	2.00e-16	0.237
NGC232	F00402-2349	10.69092	-23.56136	95.20	11.44	0.581	0.340	0.651	0.477	396	0.579	2.65e-15	2.00e-16	0.016
MCG9	F00506+7248	13.51504	73.08661	69.80	11.5	1.000	1.000	1.000	1.000	1115	3.055	3.60e-16	3.00e-16	0.001
NGC0317B	F00548+4331	14.41854	43.79225	77.80	11.19	0.848	0.546	0.922	0.729	265	0.575	2.36e-15	3.00e-16	0.009
IC1623	F01053-1746	16.94658	-17.50703	85.50	11.71	1.000	1.000	1.000	1.000	10	0.027	6.40e-14	2.00e-16	0.303
MCG-21	F01076-1707	17.53733	-16.85272	144.00	11.65	1.000	1.000	1.000	1.000	10	0.027	3.63e-15	5.00e-17	0.049
CGCG436-030	F01173+1405	20.01133	14.36192	134.00	11.69	1.000	1.000	1.000	1.000	92	0.252	6.42e-15	6.00e-17	0.075
F01364-1042	F01364-1042	24.72050	-10.45317	210.00	11.85	1.000	1.000	1.000	1.000	36	0.099	2.50e-16	3.00e-17	0.007
NGC695	F01484+2220	27.80933	22.58236	139.00	11.68	0.778	0.592	0.818	0.616	1550	3.017	4.96e-15	6.00e-17	0.062
UGC1385	F01519+3640	28.72412	36.91794	79.80	11.05	0.542	0.385	0.579	0.479	1607	2.256	1.09e-14	4.00e-16	0.045
NGC877	F02152+1418	34.49850	14.54406	54.60	11.1	0.638	0.455	0.687	0.558	1871	3.082	2.81e-14	2.00e-16	0.054
MCG-37	F02203+3158	35.84163	32.19708	145.00	11.64	0.501	0.378	0.534	0.390	786	0.980	2.29e-15	2.00e-16	0.031
NGC958	F02281-0309	37.67846	-2.93900	80.60	11.2	0.900	0.727	0.951	0.826	916	2.174	1.41e-14	1.00e-16	0.059
NGC1068	F02401-0013	40.66963	-0.01328	15.90	11.4	0.926	0.742	0.950	0.856	1556	3.797	2.86e-13	5.00e-16	0.047
UGC2238	F02435+1253	41.57288	13.09567	92.40	11.33	0.308	0.204	0.340	0.263	1247	0.983	1.42e-15	7.00e-17	0.008
NGC1275	F03164+4119	49.95067	41.51169	75.00	11.26	0.915	0.759	0.950	0.863	2067	5.036	1.78e-14	5.00e-17	0.065
F03359+1523	F03359+1523	54.69458	15.54861	152.00	11.55	0.255	0.138	0.289	0.148	927	0.537	9.11e-16	3.00e-16	0.014
CGCG465-012	F03514+1546	58.56700	15.92872	94.30	11.2	0.334	0.208	0.375	0.276	1638	1.383	3.49e-16	3.00e-16	0.002
UGC2982	F04097+0525	63.09354	5.54739	74.90	11.2	0.453	0.296	0.500	0.385	1254	1.450	4.51e-16	4.00e-16	0.002
ESO550-IG25	F04191-1855	65.33342	-18.81322	138.50	11.51	1.000	1.000	1.000	1.000	69	0.189	2.68e-15	3.00e-16	0.033
NGC1961	F05365+6921	85.51938	69.37844	59.00	11.06	0.973	0.888	0.987	0.953	1503	3.958	2.86e-14	1.00e-16	0.064
UGC3410	F06052+8027	93.62346	80.44989	59.70	11.1	0.735	0.498	0.787	0.644	1496	2.832	3.20e-15	3.00e-16	0.007
NGC2146	F06107+7822	94.65712	78.35703	17.50	11.12	1.000	1.000	1.000	1.000	851	2.332	1.39e-14	1.00e-16	0.003
NGC2388	F07256+3355	112.22267	33.81908	62.10	11.28	0.600	0.433	0.653	0.527	2078	3.229	2.96e-14	2.00e-16	0.074
MCG-21	F07329+1149	113.93071	11.70931	72.80	11.13	1.000	1.000	1.000	1.000	86	0.236	1.16e-14	4.00e-16	0.040
NGC2623	F08354+2555	129.60033	25.75461	84.10	11.6	0.584	0.471	0.619	0.535	1667	2.567	5.44e-15	8.00e-17	0.025
F08572+3915	F08572+3915	135.10579	39.06511	264.00	12.16	0.098	0.080	0.213	0.095	1690	0.491	1.39e-15	6.00e-17	0.063

Continued on Next Page...

Table C.1 – Continued

Optical ID	IRAS Name	RA (J2000)	Dec (J2000)	D_L (Mpc)	$\log_{10}(\frac{L_{ir}}{L})$	Observed Rates						Predicted Rates		
						IIP	IIL	IIn	Ibc	ST (days)	CT (yr^{-1})	F_ν(FUV) ($\frac{erg}{s\ cm^2\ \mathring{A}}$)	$\sigma_{\rm FUV}$ ($\frac{erg}{s\ cm^2\ \mathring{A}}$)	SN rate (yr^{-1})
UGC4881	F09126+4432	138.97962	44.33169	178.00	11.74	0.348	0.263	0.403	0.276	1867	1.643	2.52e-15	4.00e-17	0.052
UGC5101	F09320+6134	143.96521	61.35314	177.00	12.01	0.441	0.330	0.539	0.344	2138	2.383	8.91e-16	5.00e-17	0.018
MCG-23	F09333+4841	144.15496	48.47436	117.00	11.34	0.498	0.346	0.522	0.395	1763	2.185	9.76e-15	4.00e-16	0.086
Arp303	F09437+0317	146.58629	3.05847	92.90	11.23	0.852	0.664	0.882	0.776	1184	2.644	4.65e-15	3.00e-16	0.026
NGC3110	F10015-0614	151.00879	-6.47478	79.50	11.37	0.760	0.573	0.817	0.680	1835	3.640	1.80e-14	6.00e-16	0.074
F10173+0828	F10173+0828	155.00088	8.22606	224.00	11.86	0.188	0.156	0.321	0.165	798	0.414	5.87e-18	3.00e-17	0.0005
NGC3221	F10196+2149	155.58325	21.56958	65.70	11.09	0.701	0.543	0.751	0.631	2146	3.939	7.79e-15	4.00e-16	0.022
F10565+2448	F10565+2448	164.82558	24.54286	197.00	12.08	0.123	0.077	0.181	0.080	1796	0.538	4.00e-16	4.00e-17	0.010
MCG-35	F11011+4107	165.97167	40.84917	158.00	11.62	0.547	0.396	0.591	0.406	1389	1.863	7.27e-15	3.00e-16	0.117
NGC3690	F11257+5850	172.13438	58.56222	50.70	11.93	0.353	0.212	0.397	0.292	1457	1.300	1.19e-13	1.00e-15	0.198
F12112+0305	F12112+0305	183.44167	2.81056	340.00	12.36	0.254	0.239	0.546	0.306	1971	1.607	1.46e-15	3.00e-17	0.109
CGCG043-099	F12592+0436	195.46167	4.33333	175.00	11.68	0.777	0.712	0.818	0.720	1867	3.867	1.69e-15	2.00e-16	0.033
MCG-133	F12596-1529	195.58208	-15.76750	78.70	11.17	1.000	1.000	1.000	1.000	70	0.192	5.51e-15	4.00e-16	0.022
ESO507-G070	F13001-2339	195.71812	-23.92158	106.00	11.56	0.887	0.754	0.921	0.812	628	1.469	2.02e-15	9.00e-17	0.015
UGC8387	F13182+3424	200.14725	34.13950	110.00	11.73	0.732	0.512	0.790	0.597	1172	2.163	4.13e-15	3.00e-16	0.032
NGC5104	F13188+0036	200.34617	0.34242	90.80	11.27	1.000	1.000	1.000	1.000	10	0.027	2.97e-15	2.00e-16	0.016
MCG-101	F13197-1627	200.60192	-16.72858	82.20	11.28	0.866	0.708	0.913	0.798	1029	2.354	3.13e-15	3.00e-16	0.014
NGC5135	F13229-2934	201.43358	-29.83367	60.90	11.3	1.000	1.000	1.000	1.000	17	0.047	1.80e-14	6.00e-16	0.043
IC4280	F13301-2356	203.22250	-24.20714	82.40	11.15	1.000	1.000	1.000	1.000	5	0.014	9.92e-15	4.00e-16	0.044
NGC5256	F13362+4831	204.57300	48.27686	129.00	11.56	0.539	0.374	0.575	0.411	1114	1.479	1.02e-14	4.00e-16	0.110
Arp240	F13373+0105	204.97917	0.83528	108.50	11.62	0.510	0.308	0.561	0.393	977	1.227	3.94e-14	7.00e-16	0.300
UGC8739	F13470+3530	207.30804	35.25744	81.40	11.15	0.750	0.533	0.818	0.655	1902	3.686	6.46e-15	4.00e-16	0.028
NGC5331	F13497+0220	208.06787	2.10472	155.00	11.66	0.880	0.829	0.895	0.833	1374	3.239	5.21e-15	6.00e-17	0.081
Arp84	F13564+3741	209.64921	37.43897	58.70	11.08	0.762	0.545	0.829	0.666	1902	3.747	7.52e-15	4.00e-16	0.017
CGCG247-020	F14179+4927	214.93021	49.23658	120.00	11.39	0.589	0.377	0.631	0.436	1701	2.437	4.67e-16	2.00e-16	0.004
NGC5653	F14280+3126	217.54342	31.21550	60.20	11.13	0.405	0.291	0.436	0.359	1161	1.219	1.84e-14	6.00e-16	0.043
VV340a	F14547+2449	224.25283	24.61742	157.00	11.74	0.796	0.617	0.849	0.632	734	1.467	5.72e-15	6.00e-17	0.091
CGCG049-057	F15107+0724	228.30454	7.22550	65.40	11.35	0.560	0.352	0.620	0.476	1821	2.601	7.87e-17	2.00e-16	0.0005
VV705	F15163+4255	229.52617	42.74478	183.00	11.92	0.706	0.602	0.787	0.616	1822	3.363	5.23e-15	3.00e-16	0.113
F15250+3608	F15250+3608	231.74750	35.97708	254.00	12.08	0.318	0.285	0.519	0.305	1961	1.767	2.42e-15	2.00e-16	0.101
NGC5936	F15276+1309	232.50350	12.98931	67.10	11.14	0.446	0.295	0.490	0.381	763	0.870	2.38e-14	6.00e-16	0.069
UGC9913	F15327+2340	233.73800	23.50319	87.90	12.28	0.633	0.435	0.689	0.553	1887	3.080	2.02e-15	3.00e-16	0.010

Continued on Next Page...

Table C.1 – Continued

Optical ID	IRAS Name	RA (J2000)	Dec (J2000)	D_L (Mpc)	$\log_{10}(\frac{L_{ir}}{L})$	Observed Rates						Predicted Rates		
						IIP	IIL	IIn	Ibc	ST (days)	CT (yr^{-1})	F_ν(FUV) ($\frac{erg}{s\,cm^2\,\mathring{A}}$)	$\sigma_{\rm FUV}$ ($\frac{erg}{s\,cm^2\,\mathring{A}}$)	SN rate (yr^{-1})
NGC5990	F15437+0234	236.56821	2.41547	64.40	11.13	0.449	0.305	0.492	0.388	1416	1.635	1.08e-14	4.00e-16	0.029
NGC6052	F16030+2040	241.30437	20.54239	77.60	11.09	0.947	0.823	0.971	0.910	1935	4.919	3.71e-14	8.00e-16	0.145
NGC6090	F16104+5235	242.91958	52.45667	137.00	11.58	0.944	0.800	0.977	0.829	507	1.244	1.38e-14	1.00e-16	0.168
F16164-0746	F16164-0746	244.79912	-7.90078	128.00	11.62	1.000	0.935	1.000	0.952	1063	2.849	1.51e-15	1.00e-16	0.016
CGCG052-037	F16284+0411	247.73558	4.08289	116.00	11.45	0.287	0.164	0.314	0.201	1780	1.219	1.55e-15	2.00e-16	0.013
NGC6240	F16504+0228	253.24537	2.40094	116.00	11.93	0.226	0.119	0.250	0.152	21	0.011	6.39e-15	5.00e-16	0.056
NGC6286	F16577+5900	254.63075	58.93625	85.70	11.37	0.599	0.471	0.629	0.548	1938	3.051	7.32e-15	3.00e-16	0.035
F17132+5313	F17132+5313	258.58333	53.17500	232.00	11.96	0.350	0.322	0.477	0.336	1948	1.891	1.44e-15	4.00e-17	0.050
F17207-0014	F17207-0014	260.84146	-0.28358	198.00	12.46	0.181	0.137	0.265	0.141	1071	0.502	1.19e-17	4.00e-17	0.0005
NGC6621	F18131+6820	273.23046	68.36344	94.30	11.29	0.546	0.342	0.609	0.454	894	1.237	5.64e-15	3.00e-16	0.032
NGC6670	F18329+5950	278.39963	59.88894	129.50	11.65	0.759	0.495	0.797	0.575	453	0.842	3.06e-15	6.00e-17	0.033
NGC6907	F20221-2458	306.27771	-24.80931	50.10	11.11	0.752	0.522	0.815	0.660	776	1.508	8.18e-14	3.00e-16	0.133
NGC6926	F20304-0211	308.27546	-2.02750	89.10	11.32	0.977	0.902	0.999	0.944	1039	2.738	1.41e-14	5.00e-16	0.072
CGCG448-020	F20550+1655	314.34958	17.12750	161.00	11.94	0.370	0.266	0.398	0.277	1238	1.125	1.64e-14	6.00e-16	0.275
ESO602-G025	F22287-1917	337.85617	-19.03447	110.00	11.34	0.772	0.490	0.819	0.630	452	0.875	3.63e-15	4.00e-16	0.028
UGC12150	F22389+3359	340.30108	34.24917	93.50	11.35	0.741	0.578	0.787	0.671	551	1.070	9.13e-17	2.00e-16	0.001
F22491-1808	F22491-1808	342.95525	-17.87319	351.00	12.2	1.000	1.000	1.000	1.000	18	0.049	1.89e-15	6.00e-17	0.151
NGC7469	F23007+0836	345.81508	8.87400	70.80	11.65	0.959	0.802	1.000	0.893	464	1.180	4.50e-14	1.00e-16	0.146
CGCG453-062	F23024+1916	346.23554	19.55222	109.00	11.38	0.532	0.376	0.573	0.439	1265	1.704	7.51e-16	2.00e-16	0.006
IC5298	F23135+2517	349.00292	25.55669	119.00	11.6	0.652	0.450	0.689	0.518	1436	2.334	2.21e-15	3.00e-16	0.020
NGC7592	F23157-0441	349.59250	-4.41600	106.00	11.4	0.517	0.292	0.579	0.387	1224	1.545	2.32e-14	6.00e-16	0.169
NGC7674	F23254+0830	351.98633	8.77903	125.00	11.56	0.953	0.752	0.982	0.803	732	1.781	1.42e-14	1.00e-16	0.144
F23365+3604	F23365+3604	354.75529	36.35242	287.00	12.2	0.283	0.242	0.516	0.287	435	0.360	6.02e-16	5.00e-17	0.032
MCG-83	F23394-0353	355.50354	-3.61517	100.00	11.27	0.487	0.349	0.535	0.419	2007	2.517	7.28e-15	9.00e-17	0.047
Arp86	F23444+2911	356.75708	29.47119	73.60	11.07	0.639	0.459	0.696	0.560	1894	3.132	1.02e-14	1.00e-16	0.036
NGC7771	F23488+1949	357.85367	20.11183	61.20	11.4	0.527	0.385	0.571	0.464	1934	2.642	3.39e-14	8.00e-17	0.082
MRK331	F23488+2018	357.86167	20.58608	79.30	11.5	0.589	0.447	0.633	0.527	1307	2.010	2.91e-15	1.00e-16	0.012

Column (1): Original IRAS source, where an "F" prefix indicates the Faint Source Catalog and no prefix indicates the Point Source Catalog. Column (2): Optical cross-identification, where available from NED. For many cases where the IRAS source corresponds to a pair of optically identified galaxies, we adopt the system name instead of pair components. For example, IRAS F00163-1039 is identified in GOALS as Arp 256 rather than "MCG–02-01-051/2" as in Sanders et al. 2003. Column

(3): The best available source right ascension (J2000) in NED as of 2008 October. Column (4): The best available source declination (J2000) in NED as of October. Column (5): The luminosity distance in Mpc reported in [Armus et al. (2009)]. Column (6): The total infrared luminosity in $\log_{10}$ Solar units computed using the *IRAS* flux densities reported in the RBGS and the luminosity distances in Armus et al. (2009). Columns (7-10): The probabilities of SN detections given cadence for various types of CCSNe, IIP, IIL, IIn, IIb+Ib/c. Column (11): Survey Time (ST), the period of surveillance in days. Column (12): Control-Time (CT), the calculated control-time as discussed in the paper. Column (13): *GALEX* FUV flux density in units of erg s^{-1} cm^{-2} $Å^{-1}$. Column (14): *GALEX* FUV flux density uncertainty. Column (15): The SN rate estimation using *SB99* model and the FUV flux measurement.

APPENDIX D

THE CONTROL-TIME METHOD

Here we describe the control-time methodology used in our SN rate calculations. The concept of control-time is introduced by Zwicky (1942) first, and since then, some minor modifications have been made to the method. We implement the following formalism for the control-time calculation.

Let $C_j = \{t_0, t_1, t_2, ..., t_{\rm i}, ..., t_{\rm N}\}$ be the N epochs of observations belong to a given Cadence (C_j), so $\Delta t_i = t_i - t_{i-1}$ is the time interval between observations $i-1$ and i. For a possible SN in the jth galaxy in the Survey $S_G \in \{G_1, G_2, ..., G_j, ..., G_M\}$ and corresponding $S_C \in \{C_1, C_2, ..., C_j, ..., C_M\}$, the control-time can be evaluated by calculating the interval of time during which a particular SN stays brighter than the limiting magnitude of the observation. Obviously, $T_{\rm L}^{\rm k}$ depends on the adopted peak magnitude of the SN, the light curve shape of the SN and the limiting magnitude of the observation.

The probability of detecting an SN given a Cadence can be calculated as follows:

$$\tilde{\rm T}_{\rm C} = \sum_{i=1}^{N} {\rm u}\big(\Delta {\rm t_i} - {\rm T_L^k}\big) \times (\Delta {\rm t_i} - {\rm T_L^k}) \tag{D.1}$$

$$\Pr\big((\mathrm{SN} \geq 1)|\,\mathrm{C}\big) = 1 - \frac{\tilde{\rm T}_{\rm C}}{T_{\rm C}^{\rm G} + T_{\rm L}^{\rm k}} \tag{D.2}$$

where u represents the unit step function with unit value if its argument is positive and zero otherwise; and k is a subtype from CCSNe set: $k \in \{IIP, IIn, IIL, IIb, Ib/c\}$. $\tilde{\rm T}_{\rm C}$ is total number of days when we are not able to discover an SN and $T_{\rm C}^{\rm G}$ depicts cadence coverage for a particular galaxy in days. We use subscripts C for Cadence, L for limiting-magnitude and superscript G for Galaxy.

The rate of observed SN given the total counts of SN detection, $N_{\rm SN}$, can be calculates as:

$${\rm r_{SN}} = \frac{N_{\rm SN}}{\Pr \times T_{\rm C}^{\rm G}} \tag{D.3}$$

APPENDIX E

THE EXPECTED VALUE OF SN RATE

In order to estimate the expected value of SN rate, we assume that SN explosions within a galaxy and also among galaxies occur independently of one another, with a mean value of r. Under these assumptions, the events may be described by a Poisson distribution for a galaxy and multiplication of N Poisson distributions for multiple galaxies in a sample. Given some control-time τ, the probability of observing k events is:

$$\Pr(r_{\rm SN}) = \prod_{i=1}^{N} \Pr(r|k_i\,\tau_i) \equiv \prod_{i=1}^{N} \frac{(r\,\tau_i)^{k_i}}{k!\,e^{r\tau_i}} = \prod_{i=1}^{N} \frac{r^{k_i}\tau_i^{k_i}}{k!\,e^{r\tau_i}} \tag{E.1}$$

$$\Rightarrow \ln\,\Pr(r) = \ln \prod_{i=1}^{N} \frac{r^{k_i}\tau_i^{k_i}}{k!\,e^{r\tau_i}} = \sum_{i=1}^{N} \ln\left(\frac{r^{k_i}\,\tau_i^{k_i}}{k!\,e^{r\tau_i}}\right)$$

$$= \underbrace{\sum_{i=1}^{N} \ln\left(\frac{\tau_i^{k_i}}{k!}\right)}_{A} + \sum_{i=1}^{N} \ln\left(\frac{r^{k_i}}{e^{r\tau_i}}\right)$$

$$= A + \sum_{i=1}^{N} \ln(r^{k_i}) - \sum_{i=1}^{N} \ln(e^{r\tau_i})$$

$$= A + \sum_{i=1}^{N} k_i\,\ln(r) - \sum_{i=1}^{N} r\tau_i$$

$$= A + \ln(r)\,\sum_{i=1}^{N} k_i - r\,\sum_{i=1}^{N} \tau_i$$

$$\Rightarrow \frac{\rm d}{\rm dr}\Pr(r) = \frac{1}{r}\sum_{i=1}^{N} k_i - \sum_{i=1}^{N} \tau_i = 0 \tag{E.2}$$

$$\Rightarrow r_{\rm SN} = \frac{\sum_{i=1}^{N} k_i}{\sum_{i=1}^{N} \tau_i} \tag{E.3}$$

APPENDIX F

OBSERVATIONS LOG

Table F.1: Observations Log

#	RA (J2000)	DEC (J2000)	20151023 total exp. (sec)		20151024 total exp. (sec)		20151025 total exp. (sec)	
			r-band	i-band	r-band	i-band	r-band	i-band
1	0.493792	-15.461389	480.0	480.0	560.0	560.0	720.0	720.0
2	2.485667	-24.963111	480.0	480.0	480.0	480.0	640.0	720.0
3	3.516292	-23.182111	240.0	240.0	320.0	400.0	720.0	640.0
4	3.855459	-21.444805	480.0	480.0	240.0	240.0	480.0	400.0
5	4.797917	-22.668389	480.0	480.0	240.0	320.0	480.0	480.0
6	8.70375	7.450389	720.0	720.0	960.0	960.0	...	...
7	10.765958	-22.246806	240.0	240.0	480.0	480.0	640.0	640.0
8	11.785666	-20.760389	480.0	480.0	400.0	240.0	720.0	560.0
9	11.888083	-25.288805	240.0	240.0	240.0	240.0	480.0	480.0
10	12.338083	-18.075889	480.0	480.0	240.0	400.0	720.0	720.0
11	12.457792	-21.012194	720.0	720.0	480.0	480.0	800.0	800.0
12	12.60225	-19.906194	720.0	720.0	480.0	480.0	960.0	960.0
13	12.800083	12.024611	1200.0	1200.0	880.0	800.0	1200.0	880.0
14	16.225667	2.133305	1200.0	1200.0	960.0	960.0	1200.0	1200.0
15	16.943708	1.0635	1200.0	1200.0	960.0	960.0	1200.0	1120.0
16	20.3295	12.411694	1440.0	1440.0	880.0	880.0	1200.0	1200.0
17	22.828792	7.787694	1440.0	1440.0	960.0	960.0	1200.0	1200.0
18	352.150792	14.743	480.0	480.0	480.0	480.0	720.0	720.0
19	7.464167	-16.165111	480.0	480.0	480.0	480.0	640.0	640.0
20	6.54525	-11.053889	480.0	480.0	640.0	640.0	...	...
21	5.965667	-24.705111	480.0	480.0	400.0	400.0	480.0	480.0
22	2.30025	-26.161111	240.0	240.0	320.0	320.0	480.0	400.0
23	5.173792	8.615389	720.0	720.0	960.0	720.0	...	...
24	13.197917	-26.59	480.0	480.0	320.0	320.0	560.0	560.0
25	346.6845	12.771889	480.0	480.0	480.0	480.0	720.0	720.0
26	347.1105	-15.611389	240.0	240.0	...	...	480.0	480.0